CHARACTERISATION OF III-V QUATERNARY MULTILAYER SEMICONDUCTOR DEVICE MATERIALS BY X-RAY DIFFRACTION

A thesis submitted to the University of Warwick
for the degree of Doctor of Philosophy

by

S.Swaminathan

Department of Engineering

University of Warwick

February, 1985

SUMMARY

Optoelectronic devices find extensive use in optical fibre communication systems as infrared sources, in view of a relatively low attenuation of the optical fibres for such sources in the spectral range 1.0 - 1.4 μm. In the study of optoelectronic device materials, minute variations in the lattice parameter of different layers cause lattice strain, which, along with other factors namely thermal gradients, a high density of recombining carriers in the active layer promote the motion, multiplication and growth of defects into network clusters.

In this thesis a double crystal plane wave synchrotron radiation technique has been found to be capable of accurately characterizing individual layers in a multilayer structure such as in an opto-electronic device consisting of many layers of InGaAs, InGaAsP and InP grown over an InP substrate. This non-destructive method can separate images of the ternary and quaternary layers from the substrate (InP) thereby identifying the location of any defects as well as detailed identification of dislocation-type defects. The observed presence of a cross hatch pattern of interfacial misfit dislocations has been strongly correlated to the degradation of the device. The technique also enables a very precise plot of the rocking curves which provides invaluable information about the assessment of the thickness, compositional variation in the ternary or quaternary epitaxial layers and also of their crystalline perfection. The technique is capable of mapping lattice parameter differences of the order of 10^{-8}. A fairly accurate assessment of the inhomogeneity and non uniformity of quaternary multilayers grown by liquid phase epitaxy has been made by this technique. About 54% variations in the total quaternary layer thickness was observed for a double heterostructure laser and about 39% for a thick graded single layer quaternary specimen.

For multilayer structures showing complicated rocking curves, it has been demonstrated that a selective etching of the layers in sequence helps identify the individual layer characteristics. A theoretical calculation of rocking curves from heteroepitaxial layers is presented. Initial data from experimental rocking curves are used to calculate rocking curves for the multilayer structure and then compared with experimental curves. The input data are slightly adjusted about their initial values until a reasonable fit with experimental curves is achieved. The initial data consist of the knowledge of the thickness and mismatch variations of each layer in the multilayer structure. The mismatch variations for the layers as obtained by selective etching have been effectively used to simulate experimental rocking curves. An accurate interpretation of layer characteristics from such a simulated fit has thus been made possible. Simulation studies have thus been found to offer a powerful and non-destructive method of a detailed and accurate assessment of layer thickness and compositional variations by comparison with experimental rocking curves. Studies on a number of specimens have shown satisfactory agreement: the predicted thicknesses have been found to be generally of the same order as reported by Plessey, Caswell, where the devices were grown, and in cases where the data were either disputed or not available, experimental verification of the layer thickness made by selective etching, was found to be in agreement with the thickness predicted by the simulated studies.

CONTENTS

Page No.

LIST OF FIGURES

Page No.

10.7. (a to l) Comparison of the experimental and simulated rocking curves for the specimen M979. Emission wavelength for the active layer = 1.31μm. Energy band gap for the quaternary cap is 1.24 eV. Mismatch levels are as indicated in the insets in the graph. The simulated layer thicknesses (μm) for the various graphs are as follows

	n-InP	Q-Active	p-InP	Q-cap	
a	2	0.25	2	0.6	235
b	2	0.25	2	0.6	235
c	2	0.25	2	0.3+0.3	236
d	2	0.50	2	0.3+0.3	236
e	2	0.25	2	0.2+0.5	237
f	2	0.25	2	0.2+0.7	237
g	2	0.25	2	0.2+0.8	238
h	2	0.25	2	0.2+0.9	238
i	2	0.25	2	0.3+0.8	239
j	2	0.25	2	0.3+0.7	239
k	2	0.25	2	0.4+0.8	240
l	2	0.25	2	0.4+0.7	240

10.7m Thickness of the ternary cap as measured at three regions using the Talysurf, are 0.95μm, 0.90μm and 0.90μm respectively, giving an average thickness of 0.92μm 241

Page No.

10.10. (a to h) Comparison of the experimental and simulated rocking curves for the specimen VS296A. Emission wavelength for the active layer is λ = 1.31μm. Energy bandgap of the cap layer is 1.24 eV. Mismatch levels are as indicated in the insets in the graphs. Simulated layer thicknesses (μm) for various graphs as as follows

	N-InP	Q-Active	p-InP	Q-cap	
a	2	2	1	0.25	261
b	2	2	1	0.25	261
c	2	2	1	0.50	262
d	2	2	1	0.25	262
e	2	2	1	0.50	263
f	2	2.5	1	0.50	263
g	2	2.5	1	0.50	264
h	2	2.5	1	0.50	264

LIST OF TABLES

ACKNOWLEDGEMENTS

I would like to express my gratitude to Dr. H.V. Shurmer and Dr. D.K. Bowen for their constant guidance, inspiration and supervision throughout the course of this work.

I am grateful to Dr. S.T. Davies for many helpful discussions and assistance in connection with the preparation of the thesis.

I wish to thank my colleagues Mr. M.J. Hill and Mr. S.J. Barnett for assistance at various stages of the experimental work at Daresbury.

The research project was with the active collaboration of Allen Clark Research Centre, Plessey Research Limited, Caswell. I am extremely grateful to Dr. M. Harding and Dr. D. Darby for many useful discussions regarding interpretation of the experimental results obtained on a number of devices and material supplied by them.

Thanks are due to Dr. D.G. Chetwynd for assistance in thickness measurements, Mr. C. Bidmead for technical assistance and Mr. G. Cunham for help with photography.

My deep sense of gratitude is to the Chairman of the Department of Engineering and the Commonwealth Scholarship Commission in the U.K. for providing financial assistance during my stay in this

Special mention is made to Mrs. Hazel Taylor for her neat and efficient typing of the manuscript. I thank her for the same.

I am ever grateful to my parents for their constant source of inspiration. And last, but not least, my profound thanks are to my wife for her forbearance during my frequent trips to Daresbury as a part of my experimental work.

ACKNOWLEDGEMENTS

I would like to express my gratitude to Dr. H.V. Shurmer and Dr. D.K. Bowen for their constant guidance, inspiration and supervision throughout the course of this work.

I am grateful to Dr. S.T. Davies for many helpful discussions and assistance in connection with the preparation of the thesis.

I wish to thank my colleagues Mr. M.J. Hill and Mr. S.J. Barnett for assistance at various stages of the experimental work at Daresbury.

The research project was with the active collaboration of Allen Clark Research Centre, Plessey Research Limited, Caswell. I am extremely grateful to Dr. M. Harding and Dr. D. Darby for many useful discussions regarding interpretation of the experimental results obtained on a number of devices and material supplied by them.

Thanks are due to Dr. D.G. Chetwynd for assistance in thickness measurements, Mr. C. Bidmead for technical assistance and Mr. G. Cunham for help with photography.

My deep sense of gratitude is to the Chairman of the Department of Engineering and the Commonwealth Scholarship Commission in the U.K. for providing financial assistance during my stay in this

Special mention is made to Mrs. Hazel Taylor for her neat and efficient typing of the manuscript. I thank her for the same.

I am ever grateful to my parents for their constant source of inspiration. And last, but not least, my profound thanks are to my wife for her forbearance during my frequent trips to Daresbury as a part of my experimental work.

1

INTRODUCTION

INTRODUCTION

III-V compound semiconductors, have, over the last several years, aroused great interest, owing to their importance in the development of microwave and optoelectronic devices. GaAs, for example, is already well known as a highly efficient converter of minority carriers into photons, and as a light emitting diode, can provide a powerful infrared light source. In the field of optical fibre communication systems, the attenuation of optical fibres is relatively low for sources emitting radiation in the spectral region 1.0 to 1.4 μm. Hence it is most important to look for efficient and reliable sources in the above spectral range. More commonly, laser diodes and LEDs use InGaAs or InGaAsP for the 1.0 to 1.4 μm spectral region. The fabrication of these diodes involves epitaxial growth of III-V compounds by various methods, including liquid-phase epitaxy, chemical vapour deposition and molecular beam epitaxy, of which liquid phase epitaxy is the most widely used technique.

In a 'heterojunction' diode, a heterojunction is formed by joining two layers of semiconductors with different band gap energies. When the layers have the same conductivity type, an isotype heterojunction is formed whereas in an anisotype heterojunction, the layer conductivity type differs. A typical diode would consist of combinations of heterojunctions that serve three basic functions:

i) anisotype (n-p) heterojunction increase the carrier injection efficiency from a high-band gap region into a low-band gap one

ii) isotype (n-n or p-p) heterojunctions provide a potential barrier to confine minority carriers within a low-band gap region

iii) both isotype and anisotype heterojunctions produce a difference in refractive index across the junction.

Sometimes a fourth function is commonly provided by an isotype heterojunction - the contact resistance to the device is reduced by growing a surface layer (cap) having a lower band gap than in the underlying material.

A typical GaInAsP/InP heterostructure laser therefore consists of four layers of GaInAsP and InP grown over an InP substrate, as shown in Figure 1.1. The basic structure giving rise to injection luminescence is that of a p-n junction, operated under forward bias. The injected minority carriers are confined to the active layers by the energy gap step and the refractive index differences between the layers. These injected carriers undergo radiative recombination giving rise to photon emission from the active layer. The recombination process can be understood from the energy band structure for a typical III-V compound, as illustrated for GaAs in Figure 1.2. The electron energy is plotted as a function of crystal momentum wave vector $\underline{k}$. There is a direct conduction band minimum at Γ_6 and indirect minima at X_6 and L_6 along the [100] and [111] directions. In the direct energy gap material, an electron can make a direct transition between Γ_6 and Γ_8 from the conduction to valence band, or vice versa, by emission or absorption of a photon. For an indirect transition such as between X_6 and Γ_8 or

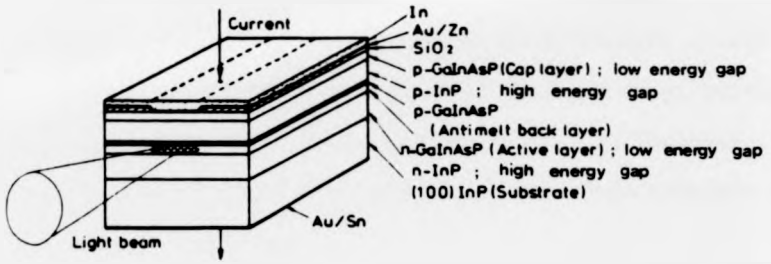

FIG 1.1 A schematic diagram of a typical GaInAsP/InP heterostructure laser. The oxide-stripe geometry and the antimeltback layer are for the 1.5 - 1.67 μm wavelength emission.

FIG 1.2 The energy band structure of GaAs with energy E plotted as a function of momentum wavevector k along [100] and [111] directions.

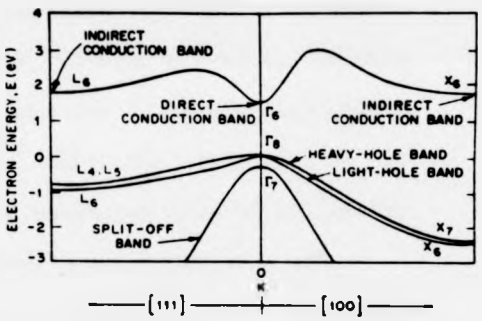

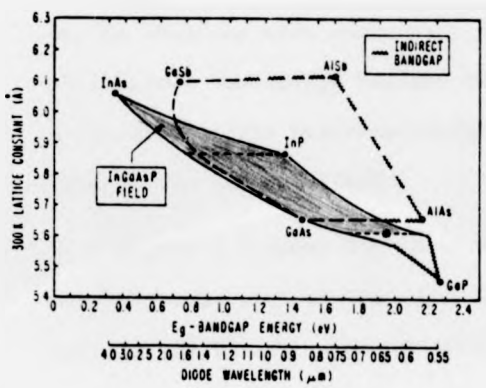

FIG 1.3 Latice constant variation with bandgap energy for various III-V alloys. The shaded region represents the quaternary field.

L_6 and Γ_8, conservation of momentum would require either an absorption or emission of a phonon. Because three particles are now involved in the recombination process, an indirect transition giving rise to radiative recombination is less probable than for the direct transition.

With III-V heterostructure lasers, however, the performance of the device depends not only upon the energy gap Eg and refractive index discontinuities at the heterojunctions that provide carrier and optical confinement, but also on the structural quality of the heterojunction interface and of the epitaxial layers. A lattice mismatch that may occur, during growth, between the layers forming the heterojunction, results in the formation of lattice defects, particularly, dislocations, which may reduce the efficiency of radiative recombination and also, the operating life of the device. In III-V systems the ability to achieve a heterojunction of sufficiently high quality for lasers, thus appears to be strongly dependent upon the achievement of a close lattice match between the heterojunction layers.

An added degree of freedom in lattice matched heterostructures may be obtained with quaternary alloys of the type $In_{1-x}Ga_xAs_{1-y}P_y$. This allows the energy bandgap of the active layer to be varied while keeping the heteroepitaxial layers lattice-matched with that of the InP substrate.

Figure 1.3 shows the lattice constant variation with bandgap energy for several of the important III-V alloys. The boundaries joining the binary compounds give the ternary energy gap and

lattice constant, while the quaternary field is indicated by the shaded region. We note that the energy of an emitted photon E is limited by the energy gap Eg for the active layer; the limiting wavelength of emission is therefore given by

$$Eg = hc/\lambda \quad \text{or} \quad Eg(eV) = 1.24/\lambda(\mu m) \qquad ...(1.1)$$

Figure 1.3 also shows that for quaternary alloys that are lattice matched to InP, emission wavelengths from 0.92 μm to 1.65 μm are possible.

The thickness of the active region in a GaInAsP/InP heterostructure laser is determined from its threshold current density consideration. The current density has been observed[1,2] to be directly proportional to the active layer thickness d, for $d > 0.2$ μm. Values of J_{th}/d are typically around 4-6 KA $cm^{-2}\mu m^{-1}$[3], with a minimum threshold current density of around 1.0 KA/cm^2 for d between 0.1 and 0.2 μm. The threshold increases when the thickness is less than 0.07 μm or greater than about 0.20 μm. Figure 1.4 shows the dependence of threshold current density on thickness d of the active layer[2], where experimental data compares reasonably with theoretical curves calculated on the basis of laser parameters such as loss coefficients.

In ternary heterostructure lasers, an intermediate layer is sometimes included between the substrate and the heterostructure wherein the composition is graded so that the active layer and the adjacent layer have the same lattice constant at the interface. This has the effect of reducing the threshold current density which

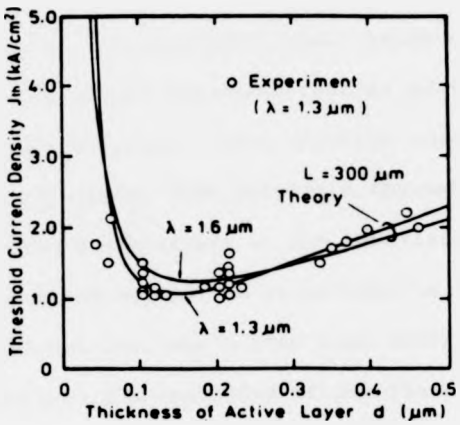

FIG 1.4 Dependence of the threshold current density on thickness of the active layer. The experimental points are from the data of Itaya et al (2)

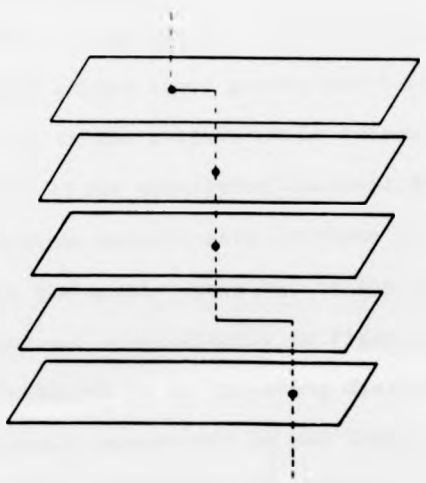

FIG 1.5 Schematic representation of misfit dislocations.

is otherwise large[4]. Experimental observation of highly mismatched layers grown by LPE has shown that in addition to edge dislocations in the interface, there are high concentrations of dislocations (of all types) that penetrate through the grown structure. The edge dislocations in the interface are parallel to the growth plane and may not be as serious as the penetrating or 'inclined' dislocations, which have been observed to have severe degradation effects on the operation of the lasers. Furthermore, layers with dislocations that result from lattice mismatch have been found to have reduced luminescent efficiency in the region of dislocations[5]. Compositional grading, does not however prevent the formation of dislocations, because lattice mismatch does occur and this must be accommodated by means of edge dislocations or the edge component of mixed dislocations. Dislocations that contribute to strain accommodation are referred to as misfit dislocations. According to the models of Abrahams et al[6] and Matthews et al[7], as the graded layer grows, the lattice parameter change increases and the strain introduced is accommodated by the motion, in continuation, of the underlying inclined dislocations. The result is a dislocation network with portions of a component or a component of each dislocation parallel to the interfacial plane. This is illustrated schematically in Figure 1.5 and the defects are commonly referred to as threading dislocations. If the mismatch at the growth temperature is too large, a cross-hatch network of threading dislocation is observed.

To improve the quality of devices, a better approach would be to employ the quaternary alloy $In_{1-x}Ga_xAs_{1-y}P_y$ where the band-gap and lattice constant can be independently adjusted over a useful range. The growth technology of course becomes a bit more complicated but the extra degree of freedom permits the fabrication of strain free heterojunction devices. Because of a differential thermal expansion coefficient for InP and GaInAsP, a lattice matched structure at growth temperature to minimize misfit dislocations, may still result in a residual mismatch at room temperature and most lasers are designed for CW operation at room temperatures. The typical lattice parameter mismatch at room temperature is of the order of 10^{-4} or even less. Such closely matched layers call for more complex growth technology and therefore require assessment on the uniformity of the epitaxial layers. Thus there is an urgent requirement for non-destructive methods to ascertain that compositional and thickness variations are within specified tolerances and also to evaluate lattice parameter mismatches of the order of 10^{-5}. Also required are methods that would image any defects in the multilayer structure and at the same time identify the origin of these defects.

In this thesis, an X-ray double axis diffractometry technique, which has been successfully employed to meet the abovementioned objectives for ternary and quaternary III-V multilayer devices grown by liquid phase epitaxy is described. This work has been made possible with the active collaboration of Plessey Research Limited at Caswell who supplied the specimens to meet the various

requirements. Use of the SERC facility of the Synchrotron Radiation Source at Daresbury is also duly acknowledged.

In brief, the technique involves the study of defect type and distribution in LPE grown double heterostructure lasers and multilayer structures by plane-wave synchrotron radiation topography. A double axis diffractometer designed for the purpose, permits separation of the images from the substrate (InP) and epilayers (GaInAsP or GaInAs) and hence a precise location of defects, as well as detailed identification of dislocation type defects. It also enables a very precise plot of the rocking curves which provides a feast of information including an assessment of the thickness, compositional variation in the ternary or quaternary epitaxial layers, and also of the crystalline perfection of the layers. The technique is capable of mapping lattice mismatch parameters, of the order of 10^{-8}, even though of the experimental samples considered, a lowest mismatch of $M = 100$ parts per million only could be detected. The experimental arrangement and the results obtained on several of the specimens have been presented in detail in Chapters 5-9.

In Chapter 10, a computer simulation of rocking curves from heteroepitaxial layers is presented. Initial data from experimental rocking curves are used to calculate rocking curves for the multilayer structure concerned and then comparod with the experimental curves. Input data are then slightly adjusted about their initial values until a reasonable fit with experimental curves is achieved. From this, the actual thicknesses of the

layers and their exact compositional variations used in the simulation can be predicted. Simulation studies have thus been found to offer a powerful method of detailed interpretation of experimental rocking curves, and since the experimental arrangement for plotting rocking curves is non destructive, we virtually have a powerful, non destructive and an accurate method of assessment of layer thicknesses and compositional variations. The predicted thickness of layers by simulation studies have been verified by other experimental methods in some cases. Simulation studies on a number of specimens have shown a satisfactory agreement: the predicted thicknesses have been found to be generally of the same order as reported by Plessey, and in cases where the data was either disputed or not available, experimental verification of the thickness was made by selective etching. The results in these cases were found to be in agreement with the thickness predicted from the X-ray measurements.

The thesis concludes with a general discussion on the various aspects of the experimental results and on the interpretation of calculated rocking curves from multilayer devices.

References

1. NAHORY, R.E. and POLLACK, M.A., 'Threshold dependence on active layer thickness in InGaAsP/InP DH lasers', Electron. Lett., 14, 727 (1978).

2. ITAYA, Y., SUEMATSU, Y., KATAYEMA, S., KISHINO, K. and ARAI, S., 'Low threshold current density (100) GaInAsP/InP DH lasers for wavelength 1.3 μm', Jpn. J. Appl. Phys., 18, 1795,(1979).

3. ARAI, S., SUEMATSU, Y. and ITAYA, Y., '1.11 - 1.67 μm (100) GaInAsP/InP injection lasers prepared by LPE', IEEE J. Quantum Electron. QE-16, 197 (1980).

4. NAHORY, R.E., POLLACK, M.A., BEEBE, E.D. and DeWINTER, J.C. and DIXON, R.W., 'Continuous operation of 1.0 μm - wavelength $GaAs_{1-x}Sb_x/A\ell_yGa_{1-y}As_{1-x}Sb_x$ DH injection lasers at room temperature', Appl. Phys. Lett., 28, 19 (1976).

5. BLACK, J.F., SUMMERS, C.J. and SHERMAN, B., 'Spatial variation of radiative recombination in GaAsP wafer revealed by photoluminescence image', Appl. Phys. Lett., 19, 28 (1971)

6. ABRAHAMS, M.S., WEINSBERG, L.R., BUIOCCHI, C.J. and BLANC, J., 'Dislocation morphology in graded heterojunctions : $GaAs_{1-x}P_x$', J. Mater. Science. 4, 223 (1969).

7. MATTHEWS, J.W. and BLAKESLEE, A.E., 'Defects in Epitaxial Multilayers', J. Cryst. Growth 27, 118 (1974).

2

REVIEW OF THE METHODS OF ASSESSMENT OF III–V SEMICONDUCTOR DEVICE MATERIALS

2.1. Introduction.

Assessment of the quality of a crystal is vital to both the crystal grower and the consumer. From the manufacturer's point of view, the results of the assessment are used to modify the growth techniques so that any structural imperfections detected in the assessment are brought to a minimum. The consumer is equally interested in purer and more perfect crystals so that he can determine whether the material is capable of being employed in devices which, otherwise, are known to exhibit performance characteristics dependent on structural properties of the material in the device.

The earliest work on the investigation of crystallographic defects in III-V materials was started in the early 1960's and has continued since then, with considerable interest. Observation of etch pits, correlated to edge dislocations in GaAs was made as early as 1959 by Abrahams and Ekstrom[1].

In this chapter, an attempt is made to review some of the most common methods to date, of assessment of crystalline perfection, and the application of these methods to InP based devices is referred to, wherever possible.

Determination of the elemental composition of quaternary semiconductor materials used as active layers in double heterostructure lasers and LEDs is as important as the study of microstructure of the active layers. Some of the methods that can provide qualitative and quantitative analysis of microstructural features are also briefly reviewed in this chapter.

2.2. Assessment of Microstructures.

The methods available for detecting structural imperfections can be broadly divided into four categories

i) Optical Methods

ii) Transmission Electron Microscopy

iii) Scanning Electron Microscopy

iv) X-ray Topography

2.2.1. Optical Microscopy.

This has been the earliest method of assessment and is still considered very important in some investigations. The optical microscope is relatively cheap and easy to operate. The earliest method of assessment is by etching the material by immersing it in an etchant which dissolves the material at a rate which is more rapid at points at which defects intersect the surface of the crystal. Etch pits are thus produced at the points where the dislocation lines meet the surface. Sometimes there may be grooves in the surface resulting from a rapid etch along the line of intersection of grain boundaries and stacking faults with the surface. This etching technique[2] has been first successfully used for Germanium using a CP-4 etchant, wherein etch pits were formed at the dislocations that make up a small angle grain boundary in Germanium. The spacing between the etch pits, agreed with the spacing calculated from a measurement of the angle of misorientation of the grains.

Optical microscopy, as such, is an imaging method with a

resolution of about 0.5μm. The interpretation of images is however usually straight-forward. Contrast in the images can be created by a number of mechanisms based on the reflection, diffraction, interference and polarization of light waves. Interferometric methods are extremely good with optical microscopy and are discussed in detail by Tolansky[3]. The vertical resolution of the image using interferometry is improved to much better than 1000Å. However the lateral resolution is still poor. This therefore limits the application of optical microscopy for studying imperfections. Secondly, only a few materials are transparent to visible light, hence study of imperfections for an opaque material can only be made on its surface using optical methods, otherwise thin layers of the material would have to be successively removed by etching, if the inside of the material is to be probed.

In some transparent materials, certain impurity precipitates can be seen by transmission optical microscopy. In certain cases, these precipitates are arranged along dislocation lines. This effect has been originally used to observe dislocations and grain boundaries in transparent ionic crystals like silver chloride by deliberately introducing impurity precipitates and thereby decorating the dislocation[4]. Dislocations in silicon also used to be studied[5,6] in this way by decorating with copper and heat treating the crystal, and by using infrared transmission microscopy, since silicon is opaque. The more recent methods of electron microscopy and X-ray topography are much superior.

In as far as the study of imperfections in InGaAsP/InP materials is concerned, optical methods have been used as a

supporting tool. Experimental observation of etch pits have invariably been made in addition to using other methods like X-ray topography and scanning electron microscopy. Olsen and Ettenberg[7] compared optical micrographs of top surfaces of VPE InGaAsP/InP DH lasers and observed that the presence of lattice mismatch can sometimes be identified by the appearance of a surface cross-hatched pattern. The cross-hatched pattern is the result of some perturbations during growth and is caused by the presence of interfacial misfit dislocations. InGaAsP/InP alloys seem to accommodate higher amounts of elastic strain without forming misfit dislocations (probably due to smaller elastic constants of InP compared to GaAs). Hence an absence of misfit dislocation network would not necessarily mean perfect lattice match. Nakajima et al[8] observed that for an LPE grown InGaAsP/InP heterostructure wafers, the dislocation-free regions determined by the etch pit observation of InP alone was found to correspond to regions where dislocations form in neither InP nor $In_xGa_{1-x}As_{1-y}P_y$ (as observed by X-ray transmission topograph for the InGaAsP/InP wafers) and concluded that dislocations are not introduced into $In_xGa_{1-x}As_{1-y}P_y$ wherever dislocations do not form in InP. Since some of the dislocations in the substrate necessarily propagate through the epilayer and reach the surface, it is significant that the dislocation free region of InP is determined by etch pit observation.

A more general and detailed discussion on optical microscopy is made by Richardson[9]. Shirafuji et al[10] have analyzed photomicrographs of as-grown, as well as chemically etched surfaces of InGaAsP/InP LPE grown samples to observe cross-hatched patterns

the surface for samples whose ($\Delta a/a$) exceeds 0.3%. The results are in general agreement with those of Feng et al[11] (± 0.2%) but deviates from those of Oe et al[12] (± 0.5%). This shows that the lattice mismatch limits needed to give acceptable surface morphology is indeed a function of the thickness of the epilayer grown. Shirafuji used a thickness of 3-5μm for the epilayer, compared to 3-4μm used by Feng and only 0.4μm used by Oe.

Hsieh[13] used the Nomarski and Mirau techniques of optical interference-contrast microscopy to examine surface morphology of GaAs layers grown by LPE under different conditions to observe discrete features like pits and hillocks with the Nomarski technique and assess surface flatness from the fringe patterns produced by the Mirau technique. Layers with a smooth and flat surface, as thick as 26μm could be grown by the super cooling technique. Step cooling also gives identical, if not slightly better results, but for thin layers of about 0.5μm thickness.

2.2.2. Transmission Electron Microscopy.

Imaging methods by TEM are superior to optical methods in the sense that since electrons can penetrate into materials more easily than visible light, a three dimensional microstructure of an opaque material may be observed without etching in succession. The depth of penetration depends on the material and the electron energy and specimen thicknesses of roughly about 0.3μm at 100 KeV and about 1μm at 1 MeV, depending on the material, can be analyzed. Using a high electron energy 100 KeV - 1 MeV makes the wavelength very short and consequently a high resolution is achieved, about 1.5Å.

the surface for samples whose ($\Delta a/a$) exceeds 0.3%. The results are in general agreement with those of Feng et al[11] (± 0.2%) but deviates from those of Oe et al[12] (± 0.5%). This shows that the lattice mismatch limits needed to give acceptable surface morphology is indeed a function of the thickness of the epilayer grown. Shirafuji used a thickness of 3-5μm for the epilayer, compared to 3-4μm used by Feng and only 0.4μm used by Oe.

Hsieh[13] used the Nomarski and Mirau techniques of optical interference-contrast microscopy to examine surface morphology of GaAs layers grown by LPE under different conditions to observe discrete features like pits and hillocks with the Nomarski technique and assess surface flatness from the fringe patterns produced by the Mirau technique. Layers with a smooth and flat surface, as thick as 26μm could be grown by the super cooling technique. Step cooling also gives identical, if not slightly better results, but for thin layers of about 0.5μm thickness.

2.2.2. Transmission Electron Microscopy.

Imaging methods by TEM are superior to optical methods in the sense that since electrons can penetrate into materials more easily than visible light, a three dimensional microstructure of an opaque material may be observed without etching in succession. The depth of penetration depends on the material and the electron energy and specimen thicknesses of roughly about 0.3μm at 100 KeV and about 1μm at 1 MeV, depending on the material, can be analyzed. Using a high electron energy 100 KeV - 1 MeV makes the wavelength very short and consequently a high resolution is achieved, about 1.5Å.

Electron microscopy basically involves scattering processes that take place when the electron beam travels through the specimen. The scattering processes may be divided into two categories: elastic and inelastic. Elastic scattering involves interaction of the electrons and the effective field potential of the nuclei, with no energy losses. Inelastic scattering involves interaction of electrons with electrons in the specimen and results in energy losses. Diffraction patterns produced by elastic scattering form the basis for studying imperfections in materials. Inelastic scattering, however, also produces informative diffraction effects i.e., Kikuchi patterns, but they are more readily used to analyse spectroscopic data resulting from characteristic energy losses and emissions due to absorption effects of the inelastic scattering. These include Auger Spectroscopy and X-ray fluorescence.

A detailed account of the electron optics and electron microscopy are available in many standard texts[14, 15, 16] while a more concise account is given in Bowen and Hall[17].

The advantages of high resolution in a TEM will have to be weighed against the high cost of the instrument. Economic utilization means that most TEM work is concentrated on specimens known to have high density of dislocations and very rarely on highly perfect crystals like Si. Secondly, the accessible thickness of the specimen is roughly up to 1μm and if one utilizes the high resolving power of the TEM to record a micrograph at a high magnification, the information on the micrograph would actually be resulting from a very tiny volume element of the specimen. Specimens are normally in the form of foils,

about 1μm thick. Transmission electron microscopy essentially operates in the transmission mode while optical microscopy can also be in the reflected mode. A TEM can very easily produce the micrograph and the electron diffraction pattern for the same area of the specimen. Essentially the formation of micrographs and diffraction patterns in a TEM can be explained as follows. Figure 2.1 shows a simple sketch of a vertical cross-section of a TEM, which consists of an electron gun to inject an electron beam and a number of electron lenses, which act in much the same way as optical lenses for visible light, a fluorescent screen to observe the diffraction pattern and a photographic plate to record the image.

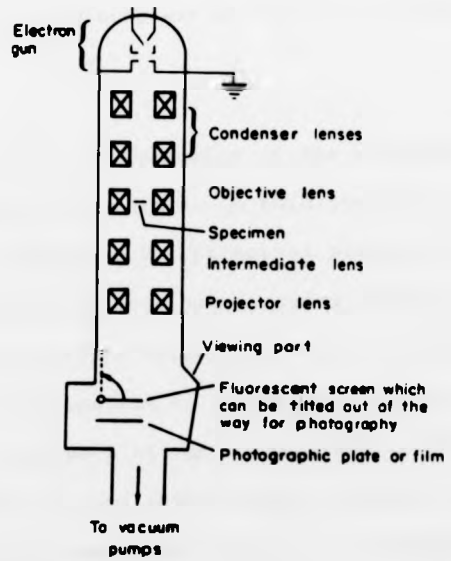

FIG 2.1 A sketch of a vertical cross-section of a TEM [after Holt (49)]

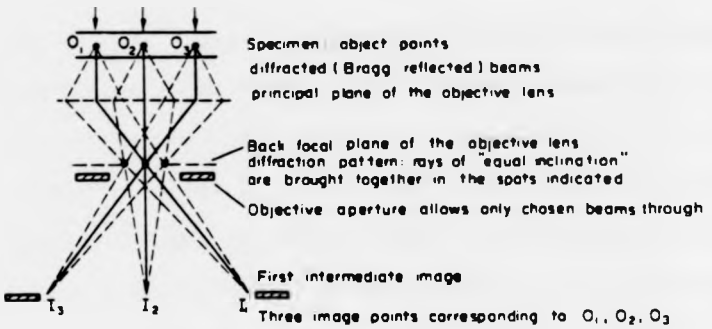

FIG 2.2 Formation of a micrograph and diffraction pattern in a TEM.

Figure 2.2 gives an idea of formation of the micrograph and diffraction pattern of a specimen. A thin specimen placed inside the objective lens and above the principal plane of the lens, diffracts the incoming electron beam passing through it. These diffracted beams are further deflected by the lens in such a way that rays of equal inclination to the vertical axis at the principal plane of the lens intersect at the focal plane to form the diffraction pattern. Rays from the same object point, however, intersect in the conjugate plane to produce a real image. An intermediate lens is used to alter the focal length of the objective lens and can thereby focus either the diffraction pattern or the image on a viewing screen or a photographic plate.

Application of this method to InGaAsP/InP layers has not been widely reported, the one drawback being to etch the specimen to up to 1μm thick for defect analysis.

Ueda et al[18] report studying the nature of dark defects in InGaAsP/InP LEDs grown by LPE, by transmission electron microscopy and other related methods. Electron micrographs of a part of the active region obtained by (220), (2$\bar{2}$0), (400) and (040) reflections were shown to exhibit two sets of misfit dislocations lying in two equivalent directions of (110) and (1$\bar{1}$0). The five types of dark defects observed in the experiment, namely a) cross hatched dark line defect, b) regular tetragonal DLD, c) regularly distributed dark spot defects, d) dark band defects and e) a DSD whose circumference is bright, were considered to originate from i) misfit dislocations ii) stacking faults between the epilayer and substrate interface iii) precipitates iv) mechanical damages and v) crystallographically anomalous region due to the penetration of the p-electrode in the LED structure, respectively. From the study of the contrasts in the transmission electron micrographs showing misfit dislocations under four different reflections, the dislocation dipoles were observed to be associated with Burgers vectors of the type a/2 (101) and a/2 (011) as evidenced in a more recent paper of the same author[19]. Olsen[20] has observed from two cross-sectional TEM micrographs of InGaAsP/InP DH lasers grown by VPE that conditions during a preheat process prior to growth of the epilayer has effects on interfacial defects.

High resolution transmission electron microscopy has made it possible to study interfaces using lattice imaging. In the case of epitaxial semiconductor multilayer structures like InGaAsP/InP which contain similar materials in its layers, it is sometimes difficult to get a good contrast, between the layers, from the axial high resolution TEM images of these structures. This lack of contrast sometimes makes it difficult to observe atomic height steps at the interface. Hetherington et al[21] have devised a "near axial lattice imaging" technique to overcome the lack of contrast between layers of similar materials and have applied this technique to GaAlAs/GaAs multilayers to study interfacial steps and the roughness of each interface as well as the determination of the widths of each layer to an accuracy of about 1Å. High resolution electron microscopy has been widely applied to silicon. Smith et al[22] have observed changes in the morphology of silicon-on-sapphire films that were Si implanted and electron-beam annealed. A comparison of a high resolution lattice image of an as-grown Si-on-sapphire with the one after annealing the sample has shown that defects like stacking faults and micro-twins are removed. Some of the recent studies of semiconductor interfaces made by Sinclair[23] using HREM, include correlation of the fine structure of interfaces with the materials processing and the physical properties of the materials.

In a multilayer structure, high resolution TEM is thus extremely useful for seeing sharpness of interface, dislocations generated from interface, inclusions etc., and steps in the interface.

2.2.3. Scanning Electron Microscopy

The scanning electron microscope is a much more versatile instrument than the TEM. It can in fact provide a whole range of techniques. Basically, in an SEM, a fine high energy beam of electrons from an electron gun are focussed by magnetic lenses so as to produce a point electron source (as small as 50Å in diameter) on a specimen surface. The beam is additionally guided by an objective lens containing scanning coils so that it scans line by line a TV type raster, over the specimen surface. By the impact of the electron beam on the specimen surface, other forms of energy are dissipated from the specimen (thus giving rise to various modes of operation of the SEM). Any of these can be collected and converted into an electrical signal and amplified. A CRO, scanned in synchronism with the electron beam scanning, would convert this electrical signal into a suitable video display. Any variation in the strength of the signal scattered from a specimen point would result in a variation in the intensity at a corresponding point on the CRO display. These give rise to contrasts in the SEM micrographs. The magnification of the micrograph is given by the ratio of the side lengths of the area scanned on the CRO to the side length of the area scanned on the specimen and is in general variable from 20X to about 100000X. Figure 2.3 gives a schematic diagram of a scanning electron microscope.

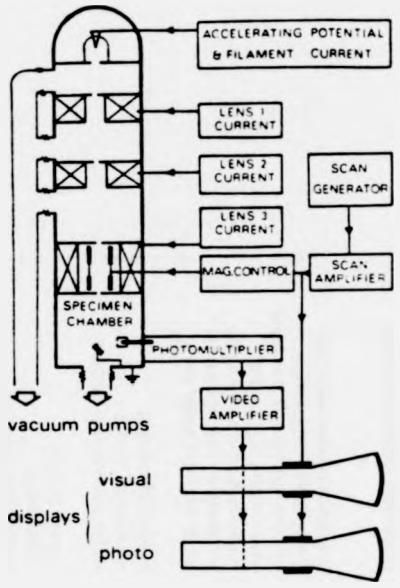

FIG 2.3 Schematic diagram of a scanning electron microscope. [after Bowen and Hall (17)]

A detailed treatment of the various aspects of scanning electron microscopy is given by Oatley[20], Thornton[21], Holt et al[22] while a concise account of the same is given by Bowen and Hall[17].

As mentioned before, the energy of impact of the electron beam on the specimen surface is dissipated into other forms of energy. These are represented schematically in Figure 2.4. Utilizing each form of dissipated energy constitutes an operating mode of the SEM. These are conveniently summarized in Table 2.1. (after Bowen and Hall[17]).

FIG 2.4 The various types of energy dissipation constituting different operating modes of an SEM.

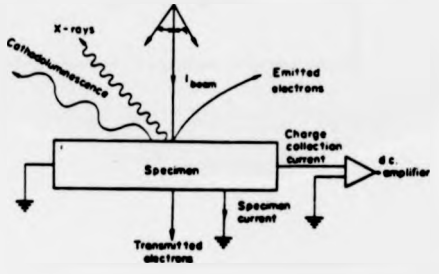

Table 2.1 Information available from various operational modes of SEM.

Mode	Modulation effect	Modulation device	Best resolution	Information available
Emissive	Secondary electrons	Electron collector	5–15 nm	Topographic Work function Surface potential and field (hence electronic device operation) Magnetic field Chemical analysis of surface layer using Auger electrons
Reflective	Backscattered primary electrons	Electron collector	50–250 nm	Topographic Atomic number
Transmitted	Transmitted primary electrons	Electron collector (beneath specimen)	0.5 nm	As for transmission electron microscopy; image processing possible
Absorptive (Specimen current)	Specimen-to-earth current	Specimen current amplifier	5–15 nm	As for emissive mode, but topographic contrast partially suppressed (also used for high beam current or if normal detector obscured by specimen)
Conductive	Excess carriers generated by primary beam	Current through specimen from external source is amplified	$> 1\ \mu m$	Conductivity and impurity variations in semiconductors
Cathodoluminescent	Photons in visible band	Photomultiplier	$> 1\ \mu m$	Qualitative chemical analysis for some materials
X-ray	Photons in X-ray band	X-ray spectrometer	$> 1\ \mu m$	Semi-quantitative chemical analysis for $Z \geq 10$
Crystallographic	Angular variation of electron channelling	(Emissive or absorptive mode)	0.05° from 1 μm selected area	Crystal orientation Lattice parameter Qualitative information on defect density and magnetic fields

The resolution of the SEM, which cannot be less than the electron probe size d, is limited by three basic factors:

i) Lens astigmatism, mechanical vibrations and stray field, which can however be controlled to a reasonable extent.

ii) Spreading of the beam that takes place within the specimen after the electron probe strikes the surface.

iii) In order to obtain the minimum probe current necessary to reveal a particular image, it is often necessary to increase the probe size d to a value considerably larger than the minimum possible.

The actual factors limiting the resolution depends on the operating mode of SEM. In general, a resolution of 50Å or less can be obtained. For the transmission mode and thin specimens, spreading effects are small and a resolution of 1-5Å can even be achieved.

Studies on surface morphology, epilayer and substrate imperfections have been widely made on III-V semiconductor materials and multilayer specimens using some of the operating modes of the SEM. It has become a standard practice to determine thicknesses of epilayers from a SEM micrograph of a stained cleaved edge of the specimen.

Jones and Gopinath[27] were one of the first to report some applications of SEM in the luminescent mode (cathodoluminescence) in InP and GaAs. Since energy is transferred from the electron beam to luminescent centres which are impurity atoms, they are raised to an excited state from where they relax emitting a photon. Alternatively, as in the case of semiconductors, the energy transfer

involves raising an electron from the valence band to conduction band and a photon is emitted after a radiative recombination. From the spectral distribution of the intensity, the emission wavelength corresponding to the peak intensity could be observed. This relates to the band gap of the semiconductor by

$$Eg\ (eV) = \frac{1.24}{\lambda(\mu m)} \qquad \ldots(2.1)$$

This technique is therefore made use of to determine the band gap of the active region of a DH laser or LED. SEM of cathodoluminescence from the impurity centres will be bright at regions where the concentration of that impurity is high and dark where the concentration is low. Casey and Kaiser[28] made measurements on the main cathodoluminescence peak to obtain the photon energy of the peak and the peak half-width and showed that these could be used to measure the impurity concentration in n-GaAs.

2.2.4. X-ray Topography

The advantages of X-ray topography are that the apparatus is relatively inexpensive in general compared to a TEM and specimens can be examined non-destructively. The higher penetrative power of X-rays (lower atomic scattering factors relative to electrons) enables thicker samples to be studied even in the transmission mode. But exposure times for such transmission topographs may be large with laboratory X-ray sources. A great many types of inhomogeneities and crystal defects like dislocations, stacking faults and mis-orientations can be revealed. The disadvantages are that the limit

of resolution is much higher (about 1μm) than that for a TEM and only crystalline specimens can be examined. Diffraction images are formed when a specimen illuminated by an X-ray beam, has a set of crystal planes that satisfies the Bragg condition of diffraction and the X-ray beam gets reflected. A suitable photographic plate placed to receive the diffracted beam would show intensity distributions coming from various sections of the reflecting planes within the crystal. Defects within the crystal alter the orientation and spacing of the planes thus producing local fluctuations in the diffracted intensity. This is seen as a contrast on the photographic plate.

Many experimental arrangements for X-ray topography are possible. These are reviewed in detail by Lang[29]. Tanner[30] also provides a detailed account of the various methods of X-ray topography. The methods are broadly classified into three categories

a) Berg-Barrett Method

b) Lang Method

c) Double-Crystal Method

The Lang method has played an important role in the characterization of defects in crystals. It is essentially a transmission technique (Figure 2.5) and is sensitive to both extinction and orientation contrast. The beam is collimated to avoid doublets in the source emission wavelengths. The Berg-Barrett method (Figure 2.6) is used in reflection mode. Due to the use of an extended source and short film - specimen distances orientation contrasts are not as sensitive as in the Lang method. The double crystal technique (Figure 2.7) uses two crystals, one of which is the reference crystal and the

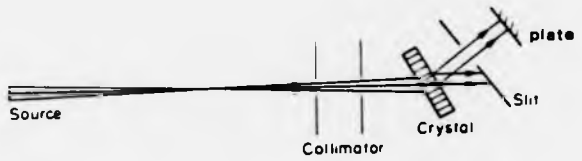

FIG 2.5 Lang's method for a transmission topograph.

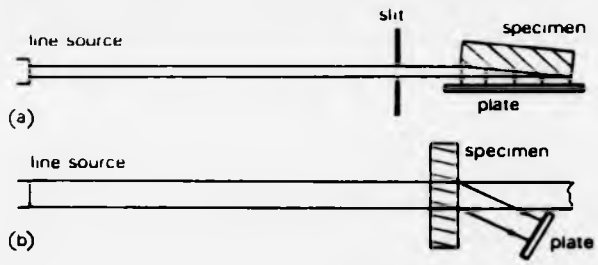

FIG 2.6 Parallel monochromatic beam methods : a) the Berg-Barrat reflection technique, and (b) the Barth-Hosemann transmission technique.

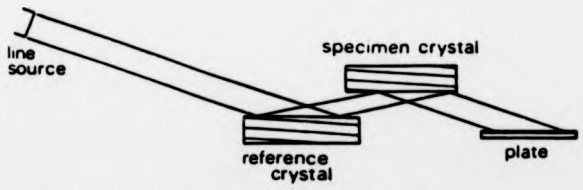

FIG 2.7 A double crystal technique in the (+-) or parallel setting.

other, the specimen. This technique is due to Bond[31] and Bonse and Kappler[32] and uses Bragg reflections from a perfect reference crystal to be incident on the specimen adjusted to either the Bragg or the Laue case. Reflection from the reference crystal essentially produces a non-dispersive wave with an extremely small divergence, in a practical case, usually of a second of arc. This makes the orientation contrast extremely high and the width of rocking curve obtained when one of the two crystals is rotated, is very narrow, if both the reference and specimen crystals are near perfect. The rocking curve, in fact, is the convolution of the reflecting curves of the two crystals. An advantage of the double crystal method is that asymmetric reflections can be used, if necessary. A wider area of the specimen can thus be covered. Since the sensitivity to orientation of the second crystal is high, the specimen must be set extremely precisely.

Using synchrotron radiation X-rays, the time of exposure can be reduced considerably compared to the exposure times with laboratory sources. Tuomi et al[33] were the first to demonstrate this feature.

One of the important contributions made in the application of X-ray topography to misfit dislocation imaging in III-V $Ga_{1-x}Al_xAs_{1-y}P_y$/GaAs heterojunctions was by Petroff et al[34] who separated the images of the quaternary epilayer and the GaAs substrate and by Riglet et al[35] who theoretically simulated dislocation images and compared them with the experimental images obtained by Petroff et al[34]. Assessment of epitaxial layers in terms of their lattice mismatch with the substrate have also been

studied using the double crystal technique for obtaining the rocking curves. With an order-sorting monochromator in the first axis of the double crystal camera which enables monochromatic plane wave to be incident on the specimen, the lattice mismatch of the epitaxial layer with respect to the substrate is

$$\frac{\Delta d}{d} = - \Delta\theta . \cot\theta_B \qquad \ldots(2.2)$$

Thus if the specimen has Bragg planes with two different lattice parameters, the convolution of the reflection curves from the perfect reference crystal and from the specimen would give rise to a rocking curve which has two separate peaks. The separation of the peaks ($\Delta\theta$) determined from the rocking curve would thus enable the lattice mismatch to be calculated using equation (2.2). This is one of the standard techniques for testing lattice matching of the epilayer with the substrate. A typical rocking curve at a point for a quaternary layer InGaAsP grown by LPE over InP substrate, using the synchrotron radiation source at Daresbury is shown in Figure 2.8. A great deal of work on the analysis of rocking curves from hetero-epitaxial layers of InGaAs/InP and InGaAsP/InP has been done by Halliwell[36,37,38,39]. This includes computer simulations of rocking curves from epitaxial/substrate structures and assessment of the quality of epilayers by observing rocking curves at various positions. An important conclusion drawn from the simulation studies was that for epitaxial layers showing compositional variations with thickness, the epilayer intensity profile may consist of one or more secondary peaks and the number of maxima in the calculated curves is not necessarily equal to the number of distinct d spacings present.

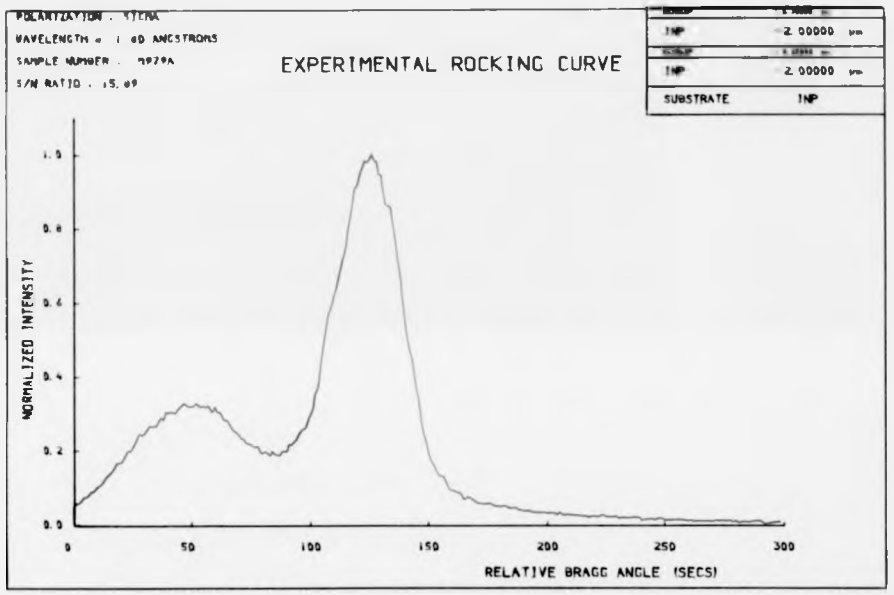

Figure 2.8. Double crystal rocking curve from a multilayer InGaAsP/InP specimen. First axis silicon monochromator, wavelength 1.8Å and for a 400 reflection

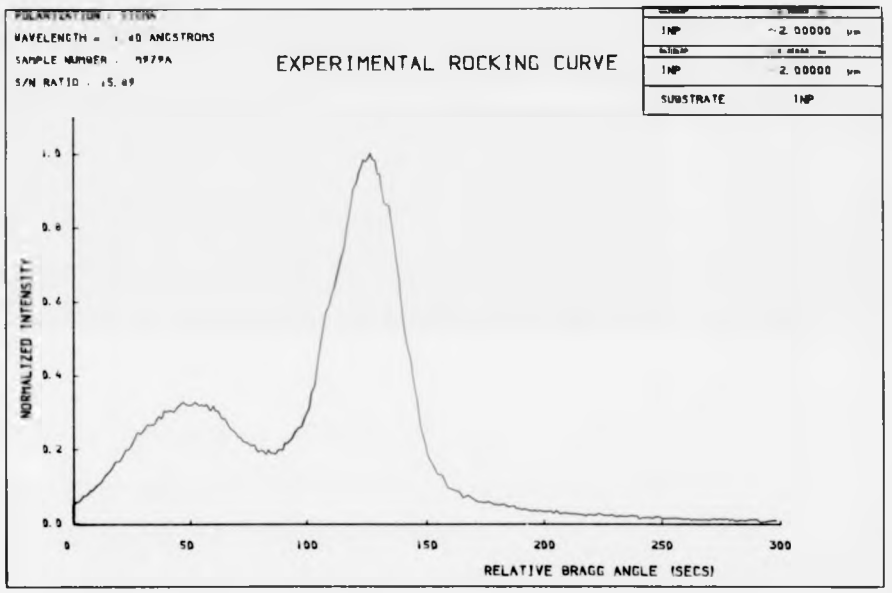

Figure 2.8. Double crystal rocking curve from a multilayer InGaAsP/InP specimen. First axis silicon monochromator, wavelength 1.8Å and for a 400 reflection

A detailed account of the simulation procedures is given in Chapter 10.

Bartels[40] suggests the use of a four-crystal monochromator to characterize thin epitaxial layers grown on perfect crystals.

X-ray topography has thus opened up a wide range of applications in the evaluation of imperfections and material properties of semiconductor heteroepitaxial structures.

2.3. Microanalytical Techniques

The methods that can provide qualitative and quantitative analysis of microstructural features can be broadly divided into the following categories:

i) Electron-probe microanalysis

ii) Auger electron spectroscopy

iii) Secondary ion mass spectrometry

2.3.1. Electron-probe microanalysis

This microprobe or the microanalyzer is basically an extra operating mode of the scanning electron microscope. The method is based on the measurement of characteristic X-rays emitted by elements in the specimen when excited by electrons. It is possible to excite a localised area of a sample surface by a finely focussed electron beam, or probe, giving a resolution of about 1μm. The characteristic X-rays should be of sufficient intensity for reasonably accurate measurements. This requires a higher beam current and higher accelerating voltage than that ordinarily used in scanning electron

microscopy. An arrangement to view the specimen during the analysis would be extremely useful. The X-ray geometry and the specimen position must be carefully designed to ensure good spectrometer performance. These minor differences between the microprobe and a scanning electron microscope require a redesign of the electron-optical, column and the specimen chamber. For optimum performance, separate instruments are therefore used for the microanalysis and microscopy work.

The essential feature of the microanalyzer is the localised excitation of a small area of the sample surface by a finely focussed electron beam, or probe. The practical realisation of this principle was first reported by Castaing and Gruinier[41].

A schematic diagram of a typical electron probe microanalyzer is shown in Figure 2.9. A beam of electrons of appropriate energy is brought to a fine focus on the specimen surface. The X-radiation excited in the specimen is analysed in a spectrometer. In effect, this consists of collecting the X-rays and using an efficient counter to measure the X-ray intensity. The pulses from the counter are normally passed through a pulse height analyzer to reject signals from X-rays of different wavelengths and then to a ratemeter, or preferably a counter which can accurately count the number of pulses received in a given time. A concise account of the design of the electron microprobe can be found in Bowen and Hall[17]. For the quantitative analysis, the concentration of an element is, in principle, determined by comparison of the intensity of a particular characteristic line from the sample to that of a

known standard, usually the pure element, under identical experimental conditions. Experimental errors in the determination of the ratio of the intensities, k can be quite considerable and may arise from the following factors

1. fluctuations in the probe current
2. shifts in the probe position
3. effect of specimen roughness
4. inhomogeneity of standards
5. back scattering of electrons from the surface
6. fluorescence effects

Comprehensive treatments for the correction factors to be applied to k can be found in Duncomb and Shields[42], Martin and Poole[43] and Beauman and Isasi[44]. A review of the methods of correction is given in Renter[45] and a detailed comparison made by Poole[46].

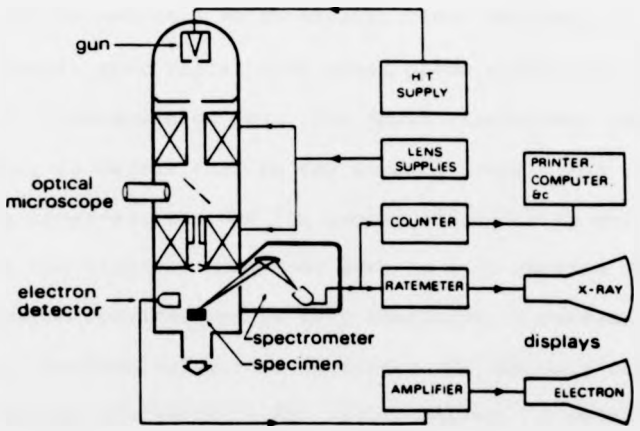

FIG 2.9 A schematic diagram of an electron-probe microanalyzer. [after Bowen and Hall (17)]

2.3.2. Auger Electron Spectroscopy

Auger spectroscopy can be applied as a microanalytical technique to provide information about the chemical composition of a surface. A sample is mounted in a high vacuum and irradiated with mono-energetic electrons, allowing interaction of the incident electrons with surface atoms, due to which electrons are emitted by the Auger process from the surface. It is therefore necessary to have suitable detectors to analyse the energies of the emitted electrons and be able to separate the weak Auger signal from the general secondary electron signal. Because there are normally a number of Auger transitions with characteristic energies, shapes and patterns, the elemental resolution is good. Since electron beams are normally used, spatial resolution in the plane of surface is also good. Standard instruments are available with minimum electron beam size of 500Å. Since Auger signal comes entirely from atoms within a few nanometers of the specimen surface, an ultra high vacuum chamber is essential to maintain an atomically clean surface. This also helps to obtain good signal with small probe diameters using high-brightness field-emission gun. The depth resolution, normal to the surface, is better than in the surface plane. The inelastic scattering cross-section for low energy electrons in solids is so large that the electron mean free path is only about a 10Å. Therefore Auger electron spectroscopy is very sensitive to surface region of the solid. Cylindrical mirror analyzers are the most commonly used electron energy analyzers in AES spectrometers. A detailed account of the theory, experimental techniques and applications of Auger

electron spectroscopy can be found in Brundle and Baker[47]. The most important applications of Auger spectroscopy at present, however, are in the study of surfaces.

2.3.3. Secondary Ion Mass Spectrometry

In this technique, a high energy primary ion beam incident on a specimen surface sputters secondary ions from the surface. A small sample of the surface, is in effect, carried as secondary ions. The primary ion source is usually of A^+, O^- or O_2^- ions and of energy about 10-15 KeV. The secondary ions, after being accelerated by an electric field enter a mass spectrometer. The ions are separated according to their e/m ratio and the beam may be tuned to a particular e/m ratio to pass one isotope only. The depth of analysis is only a few atomic layers and an ultra high vacuum system is essential. The design of very high performance mass spectrometers is possible, hence the ion microscope can be built to have the highest sensitivity, although, of course, it would prove to be the most expensive.

The method is destructive, as the surface is eroded during the analysis. The change in composition with depth in the specimen can however be studied by etching off the layers.

A general review of ion microscopes is given in Socha[48].

2.4. Discussions

A comparison of the microanalytical methods is listed in Table 2.2. All the methods could be applied to III-V materials of the type InGaAsP/InP. The electron microprobe is however the most versatile

instrument that has been widely used for both qualitative and quantitative analysis. In the Auger method light elements emit Auger electrons much more efficiently than X-ray emission in the electron microprobe. The ion microscope has the best detectability limits but causes damage to the specimen. Both the Auger and ion microscope require an ultra high vacuum, which is in fact a disadvantage for routine analysis of materials. Furthermore the ion microscope is comparatively more expensive than the electron probe or the Auger spectrometer.

Of the methods for the assessment of structural imperfections, the optical microscopy has the advantages of being relatively inexpensive, quick and easy to use and fairly easy to interpret. But its main limitation is that its lateral resolution is very poor and is therefore inadequate for studying many effects occurring on a very fine scale in materials. Secondly, only a few materials are optically transparent, hence, in order to observe a detailed in-depth assessment of microstructure of an opaque material, successive sectioning must be used to etch off layers. Transmission electron microscopy on the other hand has an extremely high resolution, but the specimens have to be very thin and thin foils of a sample sometimes behave very differently from the bulk. Noting that the width of a dislocation image is roughly 50Å, allowing electron microscopes to work at very low magnifications, one cannot resolve the dislocations, while when set at extremely high magnification to resolve the same, a very small fraction of the total specimen volume can only be analysed. The lower limit of dislocation

density that can reasonably be studied in the transmission electron microscope is about 10^4 mm^{-2}. III-V semiconductor materials for use in lasers employ high quality epitaxial layers and substrate as far as possible and hence they are supposed to contain very few no dislocations at all. To understand and control the growth of such materials, one requires techniques which will reveal the degree of pefection over a large area of the specimen.

In the X-ray technique, the higher penetrative power of X-rays resulting from lower scattering factors of atoms for X-rays relative to electrons means that the thickness of the semiconductor specimens that can be studied can be from, say, 10μm and upwards depending upon various factors. Another advantage with X-ray topography is that several methods of analysis are available. Double crystal X-ray topography is now a very powerful tool to assess lattice mismatch and imperfections in thin epitaxial layers and quantum well structures and also provide invaluable information about their thickness and composition. The X-ray method allows a non-destructive examination of the specimen and the apparatus is relatively inexpensive. The chief drawback of the X-ray method is the limit of resolution ($\sim$ 1μm) is much poorer than that for the TEM (1Å). Scanning electron microscopy, has a whole range of techniques suitable for a wide range of purposes as listed in Table 2.1, but is highly expensive. Ideally, no one technique will serve all purposes and it is best to have them all available and to know which one to call upon for any particular purpose. But X-ray topography, in view of

its applicability to the whole bulk specimen as grown, its non-destructiveness and its acceptable levels of resolution and detailed interpretability and its inexpensive cost, is a valuable assessment technique readily available.

Table 2.2. A comparison of microanalytical techniques.

Factor	Electron Microprobe	Ion Microscope	Auger Spectrometer
Spatial resolution of analysis, μm	0.5-1	∿1	<0.1
Depth of analysis, μm	0.5-2	<0.005	<0.005
Minimum mass of sampled volume, g	10^{-12}	10^{-13}	10^{-16}
Detectability limits, (1) mass, g	10^{-16}	$<10^{-19}$	10^{-18}
(2) conc. wt. ppm.	50-1000	0.01-100	10-1000
Elements analysable	$Z \geq 4$	All elements	$Z \geq 3$
Performance for $Z < 10$	Poor	Good	Good
Vacuum required, torr	10^{-5}	10^{-8}	10^{-10}
Damage to specimen	Yes, in poor thermal conductors	Sampled volume destroyed	Rare
Approx. exposure for point analysis, seconds	100	0.05	1000
Comparative cost (units)	1	1	1

References

1. ABRAHAMS, M.S. and EKSTROM, L., 'Etch pits, deformation and dislocations in GaAs', Metallurgical Society Conference on Properties of Elemental and Compound Semiconductors, Boston, Massachusetts, August 31 - September 2 (1959)

2. VOGEL, F.L., PFANN, W.G., COREY, H.E., and THOMAS, E.E. 'Observations of dislocations in lineage boundaries in germanium', Phys. Rev., 90, 489 (1953).

3. TOLANSKY, S., 'An introduction to interferometry', Longmanns, Green, London, (1973).

4. AMELINCKX, S. and DEKEYSER, W., 'The structure and properties of grain boundaries', Solid State Phys. 8, 325 (1959).

5. DASH, W.C., 'The observation of dislocations in silicon', Dislocations and mechanical properties of crystals, Wiley, N.Y. (1957).

6. DASH, W.C., 'The growth of silicon crystals free from dislocation', Growth and Perfection of Crystals, Wiley, N.Y. (1958).

7. OLSEN, G.H. and ETTENBERG, M., 'Growth effects in the hetero-epitaxy of III-V compounds' Crystal Growth, Theory and Technique, Vol.II, ed. C.H.L. Goodman, Plenum Press, London (1978).

8. NAKAJIMA, K., YAMAZAKI, S., KOMIYA, S. and AKITA, K., 'Misfit dislocation free $In_{1-x}Ga_xAs_{1-y}P_y$/InP heterostructure wafers grown by liquid phase epitaxy', J. Appl. Phys, 52, 4575 (1981).

9. RICHARDSON, J.H., 'Optical microscopy for the materials sciences', Marcel Dekker Inc., N.Y. (1971).

10. SHIRAFUJI, J., TAMURA, A., INOUE, M. and INIUSHI, Y., 'Influence of lattice-mismatch on properties of $In_xGa_{1-x}As_{1-y}P_y$ layers epitaxially grown on InP substrates', J. Appl. Phys., 52, 4704 (1981).

11. FENG, M., TASHIMA, M.M., WINDHORN, T.H. and STILLMAN, G.E., 'Composition dependence of the influence of lattice mismatch on surface morphology in LPE growth of InGaAsP on (100) - InP', Appl. Phys. Lett., 33, 533 (1978).

12. OE, K., SHINODA, Y. and SUGIYAMA, K., 'Lattice deformations and misfit dislocations in GaInAsP/InP double-heterostructure lasers', Appl. Phys. Lett., 33, 962(1978).

13. HSIEH, J.J., 'Thickness and surface morphology of GaAs LPE layers grown by super cooling, step-cooling, equilibrium-cooling and two-phase solution techniques', J. Cryst. Growth, 27, 49 (1974).

14. KLEMPERER, O. and BARNETT, M.E., 'Electron Optics', Cambridge Univ. Press (1971).

15. HAWKES, P.W., 'Electron Optics and Electron Microscopy', Taylor and Francis (1972).

16. THOMAS, G. and GORINGE, M.J., 'Transmission Electron Microscopy of materials', John Wiley & Sons (1979).

17. BOWEN, D.K. and HALL, C.R., "Microscopy of Materials', MacMillan Press, (1975).

18. UEDA, O., UMEBU, I., YAMAKOSHI, S. and KOTANI, T., 'Nature of dark defects revealed in InGaAsP/InP double heterostructure light emitting diodes aged at room temperature', J. Appl. Phys., 53, 2991 (1982)

19. UEDA, O., WAKAO, K., YAMAGUCHI, A., KOMIYA, S., ISOZUMI, S., NISHI, H. and UMEBU, I., 'Study of defects in a rapidly degraded InGaAsP/InGaP DH laser grown by liquid phase epitaxy', Appl. Phys. Lett., 44, 861 (1984).

20. OLSEN, G.H., 'Vapour phase growth of (In,Ga) (As,P) Quaternary Alloys', IEEE J. Quantum Electronics, QE-17, 128 (1981).

21. HETHERINGTON, C.J.D., BARRY, J.M., BI, J.M., HUMPHREYS, C.J., GRANGE, J. and WOOD, C., 'High resolution electron microscopy of semiconductor quantum well structures' Materials Research Society, Boston, 1984, Fall Meeting Abstracts, 119 (1984)

22. SMITH, D.J, FREEMAN, L.A., McMAHON R.A., AHMED, H., PITT, M.G. and PETERS, T.B., 'High resolution electron microscopy of Si-implanted and electron-beam annealed Silicon-on-Sapphire', Microscopy of Semiconductor Mat. Conf., Inst. Phys. Conference Series No. 67, 83 (1983).

23. SINCLAIR, R., 'Recent studies of semiconductor interfaces by HREM', Materials Research Society, Boston, 1984, Fall Meeting Abstracts, 142 (1984).

24. OATLEY, C.W., 'Scanning Electron Microscopy', Cambridge University Press, (1972).

25. THORNTON, P.R., 'Scanning Electron Microscopy' Chapman & Hall, London (1968).

26. HOLT, D.B., MUIR, M.D., GRANT, P.R. and BOSWARVA, I.M. (eds) Quantitative Scanning Electron Microscopy, Academic Press, London (1974).

27. JONES, G.A.C. and GOPINATH, A., 'Some applications of Cathodoluminescence in direct band gap semiconductors', SEM : Systems and Applications, Inst. of Phys. Conf. Ser. No. 18, 266 (1973).

28. CASEY, H.C. and KAISER, R.H., 'Analysis of n type GaAs with electron beam excited radiative recombination', J. Electrochem. Soc., 114, 149 (1967).

29. LANG, A.R., 'Modern Diffraction and Imaging Techniques in Materials Science' (eds. Amelinckx, S. et al.), North Holland (1970).

30. TANNER, B.K. 'X-ray Diffraction Topography', Pergamon Press, Oxford (1976).

31. BOND, W.L. 'A double-crystal X-ray goniometer for accurate orientation determination', Proc. Inst. Radio Engrs., 38, 886 (1950).

32. BONSE, U. and KAPPLER, E., "Rontgenographische Abbildung des Verzerrungsfeldes einzelner Vertsetzungen in germanium - Einkristallen', Z. Naturforschung, 13a, 348 (1958).

33. TUOMI, T., NAUKKARINEN, K, and RABE, P., 'The use of Synchrotron radiation in X-ray diffraction topography', Phys. Stat. Sol (a), 25. 93 (1974)

34. PETROFF, J.F., SAUVAGE, M., RIGLET, P and HASHIZUME, H., 'Synchrotron radiation plane-wave topography : I Application to misfit dislocation imaging in III-V heterojunctions', Phil. Magazine A, 42, 319 (1980).

35. RIGLET, P., SAUVAGE, M., PETROFF, J.F. and EPELBOIN, Y., 'Synchrotron-radiation plane-wave topography : II Comparison between experiments and computer simulations for misfit-dislocation images in III-V heterojunctions'. Phil. Magazine A, 42, 339 (1980).

36. HALLIWELL, M.A.G., 'X-ray measurements of lattice mismatch in heteroepitaxial layers', Microscopy of Semiconducting Materials, Inst. Phys. Conf. Series No. 60 : Sec. 5, 271 (1981).

37. HALLIWELL, M.A.G., JULER, J. and NORMAN, A.G., 'Measurement of grading in heteroepitaxial layers', Microscopy of semi conducting materials, Inst. of Phys. Conf. Ser. No.67 : Sec. 7, 365 (1983)

38. HALLIWELL, M.A.G, and LYONS, M.H. and TANNER, B.K., 'Assessment of Epitaxial layers by automated scanning double axis diffractometry', J. Cryst. Growth, 65 672 (1983).

39. HALLIWELL, M.A.G. and LYONS, M.H. and HILL, M.J., 'The interpretation of X-ray rocking curves from III-V semiconductor device structures', J. Cryst. Growth, 68, 523 (1984).

40. BARTELS, W.J., 'Characterization of thin layers on perfect crystals with a multipurpose high resolution X-ray diffractometer', J. Vac. Sc. Technology B 1, 338 (1983)

41. CASTAING, R, and GRUINIER, A., Proceedings of the conference on electron microscopy, Delft, 1949, The Hague, 70 (1950).

42. DUNCOMB, P. and SHIELDS, P.K., 'The present state of quantitative X-ray microanalysis, Part I : Physical Basis' Br. J. Appl. Phys. 14, 617, (1963).

43. MARTIN, P.M. and POOLE, D.M., 'Electron-probe microanalysis : The relation between intensity ratio and concentration', Metals and Materials, 5, 19, (1971).

44. BEAMAN, D.R. and ISASI, J.A., Electron Beam Microanalysis, ASTM Special Publication No. 506, ASTM, Philadelphia, (1972).

45. RENTER, W., 'Electron probe microanalysis', Surface Science, 25, 80, (1971).

46. POOLE, D.M., 'Quantitative Electron Probe Microanalysis' Ed. Heinrich, K.F.J., NBS Special Publication 298, Washington 93, (1968).

47. BRUNDLE, C.R. and BAKER, A.D. (ed)., Electron Spectroscopy : Theory, Techniques and Application', Academic Press, London, Vol. 4, (1981).

48. SOCHA, A.J., 'Analysis of surfaces utilizing sputter ion source instruments', Surface Science, 25, 147 (1971).

49. HOLT, D.B. in 'Crystal Growth' ed. Pamplin, B.R., Pergamon Press, Oxford (1980).

3

EPITAXIAL GROWTH OF GaInAsP/InP SYSTEMS

3.1. Introduction

In the quaternary GaInAsP system, single-phase solid solutions exist throughout the whole range of compositions[1] and it is possible to epitaxially grow lattice matched layers on InP substrates over a wide range of band gaps. InP fuses at 1070°C. This is high enough for conveniently growing an epitaxial layer, as the growth temperatures are much below this, thereby preventing substrate degradation. GaInAsP, on the other hand, is chemically stable in the atmospheric environment unlike alloys containing Aℓ, where surface oxidation is a problem. Complicated multilayer structures of GaInAsP/InP can thus be easily prepared.

There are four processes of epitaxial growth of GaInAsP alloys - liquid phase epitaxy (LPE), vapour-phase epitaxy (VPE), Metal-organic chemical vapour deposition (MOCVD) and the molecular beam epitaxy (MBE). All the epitaxial processes are briefly outlined and reviewed in the following sections, with a special emphasis on the liquid phase epitaxy process which has been used to grow GaInAsP/InP multi-layer structures and devices for subsequent defect analysis by double-crystal X-ray methods to be discussed in the forthcoming chapters.

3.2. Liquid Phase Epitaxy

The most widely used method for making heterojunction devices is liquid phase epitaxy. In liquid phase epitaxy, thin epitaxial layers are grown on a single crystal substrate from supersaturated melts. To grow, for example, an InP epilayer on InP substrate, first, a liquid metal such as In is saturated with a compound

semiconductor such as InP at an elevated temperature. A single crystal substrate of InP is also heated to the same temperature as the melt until the solute is uniformily distributed in the melt. Next, contact is established between the substrate and the melt. If the substrate and the melt are not isothermal, part of the substrate dissolves into the melt or part of the solute precipitates over the substrate. Epitaxial deposition is initiated by cooling the melt and substrate simultaneously. As cooling proceeds, the melt gets supersaturated in P atoms and hence phosphorus precipitates as InP. Ideally this takes places over the substrate, which is already in contact with the melt and an LPE layer is thus grown. The growth can be terminated by mechanically separating the substrate from the melt.

To produce GaInAsP/InP heterostructures by LPE growth, an accurate Ga-In-As-P equilibrium phase diagram is required. An experimental determination of the equilibrium phase diagram for the growth of lattice matched GaInAsP/InP heterostructures at 600° and 650°C was made by Nakajima et al[2]. The commonly used temperature range for the growth is between 600° and 650°C. Growth above 650°C rapidly increases thermal etching of the InP surface[3] while at temperatures below 600°C, a depletion of P in the growth solution[4] results in a variation in the composition of the epitaxial layers grown.

Liquidus data for the phase diagram are generally determined by the seed dissolution technique[5], which in this case can be done by saturating a ternary undersaturated Ga+In+As solution

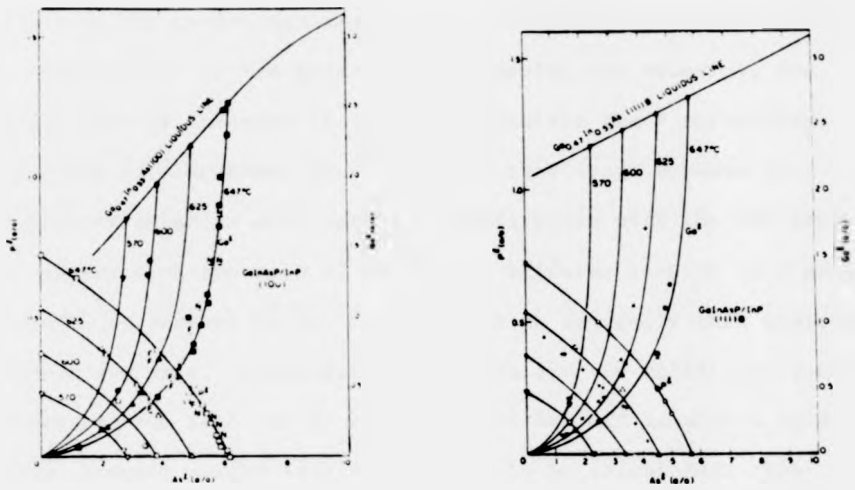

FIG 3.1 Composition of the liquidus that yield lattice matched GaInAsP alloys by growth at four different temperatures on (a) (100) InP substrates, and (b) (111) B InP substrates. The symbols refer to the data of the following references : F [Feng et al (7)], N [Nagai and Noguchi (8)], O [Oe and Sugiyama(9)] x and + [Perea and Fonstad (15)]. [after Hsein (6)]

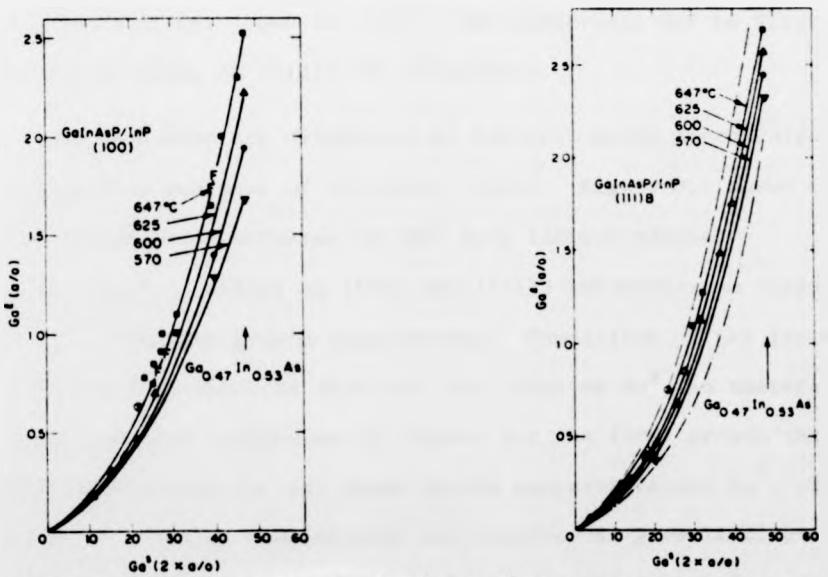

FIG 3.2 The relation between Ga^l and Ga^s for growth of lattice-matched GaInAsP alloys at four different temperatures on (a) (100) InP substrates, and (b) (111)B InP substrates. The broken lines are those calculated by Perea and Fonstad (15).

with P at the growth temperature by allowing the solution to come in contact with an InP seed. After removing the solution, the weight loss of the seed is noted to calculate the P solubility. There are some problems encountered at this stage because the Ga+In+As+P solution will not be in equilibrium with the InP seed, so contact with the seed of Ga+In+As+P solution results in a steady state being reached by the formation of an extremely thin quaternary film on the seed. Fortunately this film and the solidified solution adhered to the seed can be completely etched off in nitric acid to allow accurate weight loss of the seed to be calculated. The experimental observation of Hsieh[6], Feng et al[7] and Nagai and Noguchi[8] and Oe and Sugiyama[9] permits the liquidus isotherms for P^{ℓ} and Ga^{ℓ} to be drawn as functions of As^{ℓ} at four different growth temperatures, as shown in Figure 3.1a, for lattice matched quaternary alloys grown on (100) - InP substrates and in Figure 3.1b for alloys grown on (111)B InP substrates.

Solidus data are determined by electron-probe microanalysis performed on surfaces of epitaxial layers. Figure 3.2 shows the solid solubility isotherms for Ga^{s} into lattice matched $Ga_xIn_{1-x}As_yP_{1-y}$ alloys on (100) and (111)B InP substrates respectively, at four different growth temperatures. Comparison of the isotherms in Figures 3.2a and 3.2b show that the value of Ga^{s} and therefore the Ga distribution coefficient is higher for the (100) growth than for the (111)B growth for any given growth temperature and Ga^{ℓ}. Thus different solution compositions are required to grow lattice-matched layers on both (100) and (111)B substrates. Figures 3.2a and 3.2b

also show that the quaternary alloy $In_xGa_{1-x}As_yP_{1-y}$ can be grown over InP over the entire range of lattice-matched compositions $1 \geq x \geq 0.53$, $0 \leq y \leq 1.0$.

Several theoretical methods[10,11,12] have been derived to predict the III_1-III_2-V_3-V_4 phase diagram, the most extensive, and the one pertinent to the In-Ga-As-P system that we are interested in, being that of Jordan and Ilegems[12] who presented a rigorous and unified thermodynamic treatment of solid-liquid equilibria in quaternary systems. A generalised liquidus equation of a quaternary system was derived by the method of chemical potentials[13]. Vieland's heat of fusion thermodynamic liquidus equation for binary compounds[14] was extended, with relatively simple models to obtain solidus and liquidus surfaces for the case of a quaternary solid solution of the form $In_xGa_{1-x}As_yP_{1-y}$. These solidus and liquidus functions involve a large number of binary or ternary interaction parameters whose values are derived from curve fitting with the binary or ternary experimental phase diagrams. Lack of experimental data for the binary and ternary compounds at all the temperatures and compositions relevant to the quaternary, makes an extrapolation, to obtain the interaction parameters, only approximate. The thermodynamic treatment is however generalised in that it predicts the solidus and liquidus functions for the quaternary from the data of the appropriate ternary systems. The calculated liquidus isotherm shows reasonable agreement with experimental results while the solidus isotherm shows slight departures (Figure 3.4).

With a modified calculation for growth of lattice-matched quaternary on a (111)B InP substrate, the results of Perea and Fonstad[15] have shown reasonably good agreement with the experimental data of Hsieh[6] as is evident in Figure 3.2.

3.2.1. The Apparatus

The LPE apparatus, appears in general, as shown schematically in Figure 3.3a, and essentially consists of a pure graphite boat placed in a quartz tube. The boat, in effect, has a melt holder, a base and a sliding platform carrying the substrate (Figure 3.3b). The melt holder carries with it, five melt bins. The slider and the upper part of the melt holder can be moved from outside the quartz tube by using thin quartz rods. In the system such as the one used at Plessey, Caswell, where most of the device materials analysed in this thesis were grown, a computer controlled stepper motor was used to move the slider on to or out of the melt very quickly and is particularly suitable for controlling thermal gradient effects on the epilayer growth.

Before heating the quartz tube, it is flushed with purified hydrogen in order to prevent oxidation in growth melts. A diffusion furnace heats the quartz tube. Extreme care is taken to see that the furnace has a uniform temperature in its centre zone wherein the graphite boat is positioned. The Plessey system also employs a temperature control unit and also continuously monitors the temperature of the graphite boat. A flat temperature profile, to an accuracy of $\pm$ 0.1°C over the length of the boat could thus be provided by the furnace.

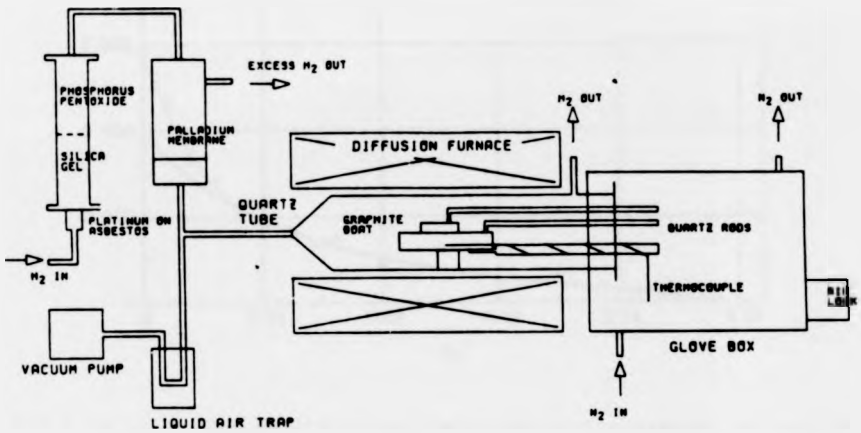

Figure 3.3a. Schematic diagram of the LPE apparatus

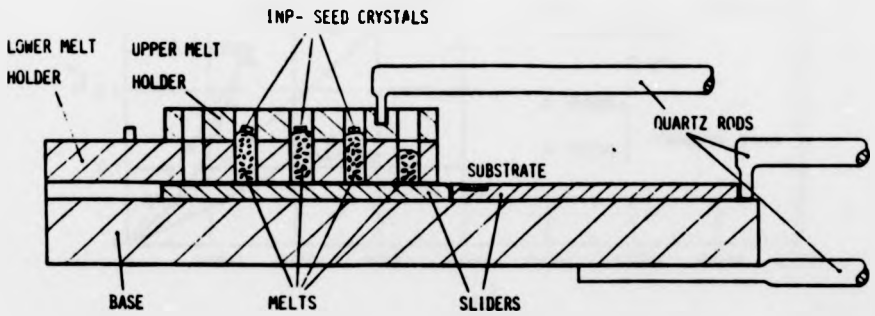

Figure 3.3b. The graphite boat with the various melts[44].

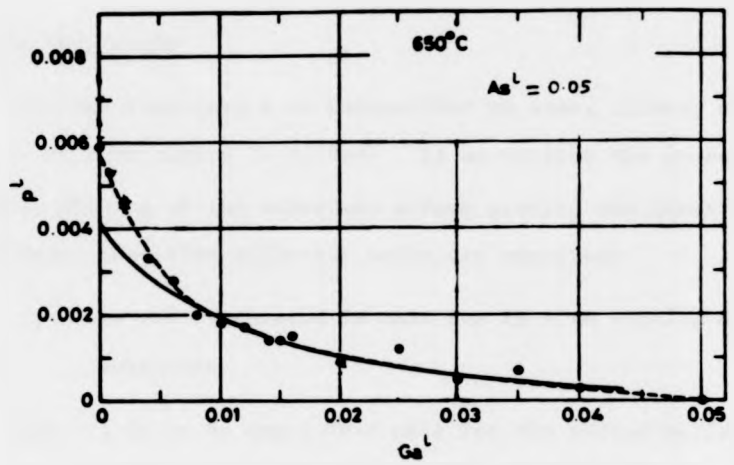

FIG 3.4a Liquidus isotherm for the In-Ga-As-P system at $As^l = 0.05$

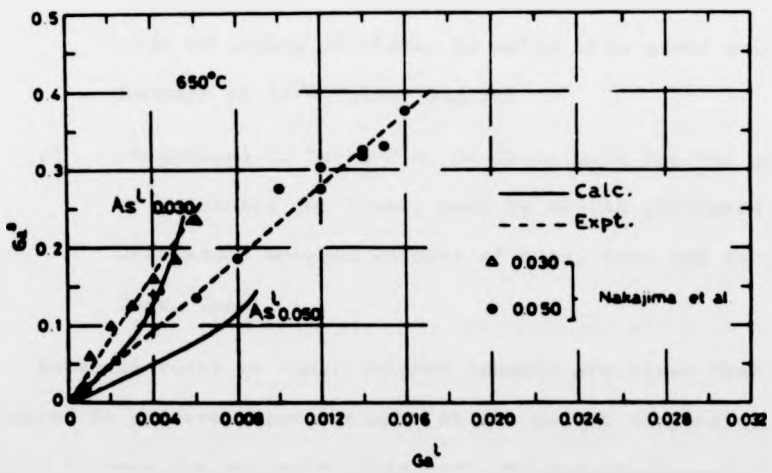

FIG 3.4b Solid solubility isotherm for Ga at $As^l = 0.03$ and 0.05. The full curves in both the figures are the calculated isotherms while the broken lines are the experimental curves obtained from the data of Nakajima et al (2,4).

3.2.2. The Growth

For the fabrication of GaInAsP/InP DH laser diodes, epitaxial growth of four layers is needed. If we include the process of an in situ etching of the substrate before growing the first epilayer, this means that five different melts are required:

i) an undersaturated In melt for in situ etching of the substrate

ii) a Ge or Sn doped In-P melt for the n-type buffer layer made by adding prebaked In melts with added weighed amounts of Ge or Sn and InP

iii) a nominally undoped Ga-In-As-P melt for the growth of the active layer, made by adding pre-baked In-melts with added weighed amounts of GaAs, InAs and InP

iv) a Zn-doped In-P melt for the p-type cladding layer made by adding pre-baked In melts with added weighed amounts of In+Zn alloy and InP

v) an undoped Ga-In-As-P or Ga-In-As melt for the quaternary or a ternary cap layer, made by adding pre-baked In melts with added weighed amounts of GaAs, InAs and InP or GaAs, InAs.

These mixtures in their weighed amounts are those that are required to produce saturated melts at the growth temperature of 650^{o}C and to achieve the estimated thickness and composition of the epilayers. Epilayer growth is achieved through the following steps:

1) A thoroughly clean graphite boat is baked in the quartz tube for several hours at over 700^{o}C under steady hydrogen flow, then cooled.

2) Weighed amounts for the various melts are loaded into the appropriate wells of the high purity graphite boat, and a (100) - oriented InP substrate, chemically polished with a 1% Br-methanol solution, is placed in the slider.

3) After purging the system with Pd diffused high purity hydrogen to remove oxygen and water vapour, the temperature is raised from room temperature to 670^{o}C. The melts are maintained at 670^{o}C for 45 minutes to ensure that the components are completely melted and then the melt temperature is reduced to 650^{o}C, the saturation temperature, in 10 minutes.

4) During the period between raising the temperature of the system from room temperature to 670^{o}C and cooling it subsequently to 650^{o}C, the InP substrate is kept covered by the graphite boat. In spite of this protection, there is considerable thermal decomposition of the substrate surface and this damage is removed by sliding the substrate under a pure In melt in the first well of the boat for a period of 10-20 secs . This process etches the substrate.

5) Immediately after the substrate etching, the n-type InP buffer layer, the GaInAsP active layer, the p-type InP cladding layer and the GaInAsP capping layer are grown by sliding the substrate under other wells in sequence, while

at the same time employing a supercooling of 1-5°C for the melt. Typical growth times for a 5°C supercooling are 10 minutes (n-InP, 2.5μm), 15 secs (GaInAsP active, 2000Å), 10 minutes (p-InP, 2.1μm) and 15 seconds (GaInAsP cap, 2000Å)

3.2.3. Features of the Growth

Using the step cooling technique[16] typical growth rates of 0.4μm/min and constant composition quaternary layers upto several microns thick have been reported[16,17,18]. The distribution coefficient, growth rate and surface morphology are strongly dependent on the crystallographic orientation of the substrate. The maximum layer thickness which can be obtained by the step cooling technique is limited due to nucleation in the highly supercooled solution. Any growth technique involving growth with changing temperature may result in graded alloy compositions of the epitaxial layers.

In the growth of DH laser structures at wavelengths beyond 1.4μm, after the appropriate GaInAsP active layer is grown and while attempting to grow the next InP layer, there is a serious problem of dissolution of the GaInAsP layer on bringing the In-P solution into contact with it because of the larger As solubility in the solution in equilibrium with the longer wavelength layer[8]. As a result of this, compositional gradients in InP/GaInAsP interface have been observed[19] which have been found to be significant with even a small amount of lattice mismatch for the active layer. A close lattice matching is therefore essential for the fabrication of GaInAsP/InP heterostructure lasers. Several methods have been suggested to prevent the dissolution. One way is to reduce the growth temperature of the InP layer on top of

the GaInAsP active layer, to about 600°C[20,21,22], or to grow a thin anti-meltback GaInAsP layer over the active layer, prior to growing the InP layer[23,24]. The anti-meltback layer should of course have a lower fraction of As, than in the active layer.

3.3. Vapour Phase Epitaxy

Vapour phase epitaxial growth of GaInAsP is done by either 1) the 'trichloride' or 2) the 'hydride' method. In the trichloride method a stream of $AsC\ell_3$ or $PC\ell_3$ is passed over In or Ga so as to form metal chlorides - or passed over binary source wafers such as GaAs or InP. In the hydride method. $HC\ell$ is passed over hot In or Ga to form metal chlorides, and combined with hydrides of arsenic and/or phosphorus. The trichloride method gives the purest InP or GaAs, so most microwave devices employ this method of growth. However, a majority of optoelectronic devices have been successfully synthesised by the hydride method. A detailed account of the hydride method of growth of (Ga,In) (As,P) alloys is given by Olsen and Zamerowski[25,26]. Deposition of the epitaxial layer is initiated by passing $HC\ell$ over In and/or Ga which are in the furnace and held at 850-900°C. Metal chlorides are formed. Arsine and/or phosphine are brought in through a separate pipe and mixed with the metal chlorides in a mixing zone. If a p-doping is needed, then Zn is vaporised separately and carried by H_2 in a separate pipe. For n-type doping H_2S is used. All the input reactant flows are controlled by electronic mass-flow controllers. Meanwhile the substrate held on a rotatable sample holder is cleaned by a flush of hydrogen in a separate compartment in the furnace, and then pushed into a pre-heat zone

containing an atmosphere of AsH_3 and/or PH_3. Then the substrate is heated to about 900°C and inserted into the growth zone where the reaction of various gases results in the deposition of the epitaxial layer on the substrate. The substrate is rotated slowly during the growth, in order to smooth out any non uniformity in temperature or gas flow. Growth is terminated by withdrawing the substrate to its own compartment. If more layers are to be grown, the substrate with the grown layer is brought back to its own compartment while the reactant flows are changed to allow a different type of layer to be grown. The process is repeated until all the layers for the device are grown. Several versions of the VPE apparatus have been reported[27,28,29,30,31], each one having a particular advantage, but principally they are similar. Modern VPE reactors have sophisticated automated growth systems.

The chief drawback of the VPE process is that the epitaxial layers grown have a potential for hillock and haze formation and interfacial decomposition during the 'preheat' stage. A dual-growth-chamber VPE reactor has been suggested[32] for the growth of GaInAsP/InP. In this, two conventional VPE reactors, placed in parallel, feed into a single growth chamber. Different gases can be made to flow through each tube so that multilayer structures of GaInAsP/InP can be grown by switching the substrate on to the relevant flow tube, thus removing the need for a preheat cycle and thereby avoiding the introduction of interfacial defects.

3.4. Metal Organic Chemical Vapour Deposition

In this method, known amounts of group III alkyls (e.g. $Ga(CH_3)_3$, $In(C_2H_5)_3$ and the group V hydrides (e.g. AsH_3,PH_3) are introduced into a quartz reactor tube which contains the substrate placed on an RF heated carbon susceptor. The gaseous products decompose in the reactor and growth is initiated on this hot substrate surface.

The growth of III-V compounds which contain Indium (InAs, InP, etc) is complicated. Indium organometallic compounds react very easily at room temperature with hydrides leading to the formation of additive compounds and rapid transformation to the vapour phase, resulting in fumes. Several remedies have been suggested, notable among these being the proposal to use group V alkyls instead of hydrides as the group V sources. Growth of GaInAs[33] has been reported using this technique. Thus the co-pyrolysis of $In(C_2H_5)_3$ and $P(C_2H_5)_3$ could avoid the formation of strongly reacting additive compounds.

The growth by MOCVD can be explained as follows

i) The gas molecules diffuse across a thin layer adjacent to the substrate surface.

ii) At the hot surface, the metal alkyls and hydrides are decomposed. Group III and V elemental species are thus produced.

iii) The elemental species move about on the hot surface of the substrate until they nucleate on a lattice site where the growth occurs.

Under normal operating conditions the growth is only diffusion limited

and temperature independent. This gives a much more precise control over the uniformity and composition of the grown layers. It has been demonstrated that metalorganic CVD can be used to produce $Ga_{0.47}In_{0.53}As$ lattice matched to InP, with electronic properties comparable to other epitaxial techniques. Furthermore the advantages of a larger area grown, better uniformity of thickness and composition, good surface flatness and excellent morphology make this method much superior in applications where a high yield and large surface area are important. More details of the MOCVD technique can be found in Duchemin et al[34], Manasevit and Simpson[36] and Yoshino et al[35].

For GaInAsP epilayers lattice-matched to InP, the growth characteristics are observed to be generally the same, as long as the sum of partial pressures of arsine and phosphine does not exceed a critical value. The growth rate is proportional to the sum of the partial pressures of triethylgallium and triethylindium and is independent of the partial pressures of arsenic or phospherus. Typical growth rates are of the order of 0.03μm/min. However, if the sum of the partial pressures of arsenic and phosphorus exceeds the critical value the epilayer growth no longer is diffusion limited and becomes strongly temperature dependent. Under this condition, the growth material for a critical composition range corresponding to λ_g between 1.35 and 1.45μm has been found to be highly mismatched with dislocations, and to exhibit poor photoluminescent and electrical properties.

3.5. Molecular Beam Epitaxy

In this technique separate sources carrying the constituent species of a resultant quaternary material, are simultaneously evaporated onto the growth surface which is the InP substrate. In order to minimize the growth contamination resulting from unintentional adsorption processes, an ultra high vacuum environment is necessary for the growth. Present day MBE systems use a vacuum of the order of 10^{-11} - 10^{-12} torr. The evaporation sources are normally contained in a pyrolitic boron nitride crucible. This is essential to keep the highly reactive species like Ga, Aℓ or In. The crucible is housed in a temperature controlled chamber. The MBE system uses a multiport evaporation shroud where the sources are isolated by a water cooled shroud and then surrounded by a liquid nitrogen reservoir and each source is individually shuttered. The close to unity sticking coefficients for the group III elements at typical growth temperatures[37] makes it easy to grow alloys of the type III_A-III_B-V with predetermined composition, while a non-unity sticking coefficient of group V fluxes makes it difficult to control growth of alloys of the form III-V_A-V_B or III_A-III_B-V_C-V_D. $Aℓ_nGa_{1-n}As$ have been widely studied and used for the fabrication of DH lasers[38]. The growth phenomenon in an MBE is treated in detail by Bacharach[39] and various techniques for the growth reviewed by Cho[40]. A wide variety of surface analysis tools can be incorporated in an MBE system like Auger Electron Spectroscopy, Secondary Ion Mass Spectrometry, high energy electron diffraction, photo emission spectroscopy etc., to analyse, in situ, the composition and surface morphology of the MBE growth.

Controlled growth of ultra thin layers is possible leading to growth of superlattice structures like - $GaAs_n$ - $GaAlAs_m$ - where n and m are the number of the relevant atomic layers[41,42,43].

Thus the MBE technique gives an excellent control over the growth but the technique is not yet fully developed for quaternary growth of InGaAsP/InP, mainly because of the non-unity sticking coefficients of the group V element fluxes.

3.6. Discussion

Liquid phase epitaxy is a relatively simple and inexpensive process. Good overall device results achieved to date have been with LPE material. Drawbacks of the LPE process are nonuniform growth, terracing effects, melt carry over etc. The conventional VPE process has good control over thickness and compositional uniformity of the epilayer as well as on the compositional grading. Growth of Al and Sb are however difficult by this process. MOCVD, in addition to having all the advantages of a conventional VPE, has the ability to grow Al and Sb alloys. Its main drawback is the formation of addition compounds with the InP - bearing alloys. Possibilities of organic contamination also exist. MBE has a very clean growth environment with excellent control and uniformity in growth. It is however a very expensive and complicated process and presents certain difficulties with p-type doping and with the growth of P-bearing alloys (it is reported that phosphorus clogs the vacuum pump)

In conclusion, the LPE apparatus is usually minimal, consisting of a quartz reactor tube with metering valves for purging H_2 through

the system. Few changes are required to achieve mixed alloy and multilayer growths and unlike the vapour or the molecular beam technique, the apparatus does not 'grow' with increasing alloy complexity.

References

1. MULLER, E.K. amd RICHARDS, J.L., 'Miscibility of III-V semiconductors studied by flash evaporation', J.Appl. Phys., 35, 1233 (1964).

2. NAKAJIMA, K., KUSUNOKI, T., AKITA, K, and KOTANI, T., 'Phase diagram of the In-Ga-As-P quaternary system and LPE growth conditions for lattice matching on InP substrates', J. Electochem, Soc., 125, 123 (1978).

3. PAK, K., NISHINAGA, T. and UCHIYAMA, S., 'Thermal etching effect of InP substrate in LPE saturation process', Jpn. J. Appl. Phys. 14, 1613 (1975).

4. NAKAJIMA, K., YAMAGUCHI, A., AKITA, K. and KOTANI, T., 'Composition dependence of the band gaps of $In_{1-x}Ga_xAs_{1-y}P_y$ quaternary solids lattice matched on InP substrates', J. Appl. Phys., 49, 5944 (1978).

5. ILEGEMS, M. and PANISH, M.B., 'Phase diagram of the system Aℓ-Ga-P', J. Cryst. Growth, 20, 77 (1973).

6. HSIEH, J.J., 'Phase diagram for LPE growth of GaInAsP layers lattice matched to InP substrates', IEEE J. Quantum Electron, QE-17, No.2, 118 (1981).

7. FENG, M., WINDHORN, T.H., TASHIMA, H.M. and STILLMAN, G.E., 'Liquid phase epitaxial growth of lattice matched InGaAsP on (100) - InP for the 1.15 - 1.31μm spectral region', Appl. Phys. Lett., 32, 758 (1978).

8. NAGAI, H. and NOGUCHI, Y., 'InP-$Ga_xIn_{1-x}As_yP_{1-y}$ double hetero-structure for 1.5μm wavelength', Appl. Phys. Lett., 32, 234 (1978).

9. OE, K. and SUGIYAMA, K., 'Orientation effects in the LPE growth of GaInAsP quaternary alloys', Appl. Phys. Lett., 33, 449, (1978).

10. ILEGEMS, M. and PANISH, M.B., 'Phase equilibria in III-V quaternary systems - Applications to Al-Ga-P-As', J. Phys. Chem. Solids, 35, 409 (1974).

11. STRONGFELLOW, G.B., 'Calculation of ternary and quaternary III-V phase diagrams', J. Cryst. Growth, 27, 21 (1974).

12. JORDAN, A.S. and ILEGEMS, M., 'Solid-liquid equilibria for quaternary solid solutions involving compound semiconductors in the regular solution approximation', J. Phys. Chem. Solids, 36, 329 (1975).

13. JORDAN, A.S., 'The liquidus surfaces of ternary systems involving compound semiconductors : I. General Thermodynamic analysis', Met. Trans., 2, 1959 (1971).

14. VIELAND, L.J., 'Phase equilibria of III-V compounds', Acta Met., 11. 137 (1963).

15. PEREA, E.H. and FONSTAD, C.G., 'Phase diagram calculations for $In_uGa_{1-u}P_vAs_{1-v}$ lattice matched to (111)B InP, in the temperature range 600-660°C', J.Appl. Phys., 51, 331 (1980)

16. HSIEH, J.J., 'Thickness and surface morphology of GaAs LPE layers grown by supercooling, step cooling, equilibrium cooling and two-phase solution techniques', J. Cryst. Growth, 27, 49 (1974).

17. FENG, M., COOK, L.W., TASHIMA, M.M. and STILLMANN, G.E., 'The influence of LPE growth techniques on the alloy composition of InGaAsP', Appl. Phys. Lett., 34, 292 (1979).

9. OE, K. and SUGIYAMA, K., 'Orientation effects in the LPE growth of GaInAsP quaternary alloys', Appl. Phys. Lett., 33, 449, (1978).

10. ILEGEMS, M. and PANISH, M.B., 'Phase equilibria in III-V quaternary systems - Applications to Al-Ga-P-As', J. Phys. Chem. Solids, 35, 409 (1974).

11. STRONGFELLOW, G.B., 'Calculation of ternary and quaternary III-V phase diagrams', J. Cryst. Growth, 27, 21 (1974).

12. JORDAN, A.S. and ILEGEMS, M., 'Solid-liquid equilibria for quaternary solid solutions involving compound semiconductors in the regular solution approximation', J. Phys. Chem. Solids, 36, 329 (1975).

13. JORDAN, A.S., 'The liquidus surfaces of ternary systems involving compound semiconductors : I. General Thermodynamic analysis', Met. Trans., 2, 1959 (1971).

14. VIELAND, L.J., 'Phase equilibria of III-V compounds', Acta Met., 11. 137 (1963).

15. PEREA, E.H. and FONSTAD, C.G., 'Phase diagram calculations for $In_uGa_{1-u}P_vAs_{1-v}$ lattice matched to (111)B InP, in the temperature range 600-660°C', J.Appl. Phys., 51, 331 (1980)

16. HSIEH, J.J., 'Thickness and surface morphology of GaAs LPE layers grown by supercooling, step cooling, equilibrium cooling and two-phase solution techniques', J. Cryst. Growth, 27, 49 (1974).

17. FENG, M., COOK, L.W., TASHIMA, M.M. and STILLMANN, G.E., 'The influence of LPE growth techniques on the alloy composition of InGaAsP', Appl. Phys. Lett., 34, 292 (1979).

18. FENG, M., TASHIMA, M.M., WINDHORN, T.H. and STILLMANN, G.E. 'Composition dependence of the influence of lattice mismatch on surface morphology in LPE growth of InGaAsP on (100) - InP', Appl. Phys. Lett., 33, 533 (1978).

19. FENG, M., COOK, L.W., TASHIMA, M.M., STILLMANN, G.E. and BLATTNER, R.J., 'Auger profile study of the influence of lattice mismatch on the LPE InGaAsP - InP heterojunction interface', Appl. Phys. Lett., 34, 697 (1979).

20. TAKAHEI, T., NAGAI, H. and KAWAGUCHI, H., "Low temperature liquid phase epitaxy growth for room temperature CW operation of 1.55μm InGaAsP/InP double heterostructure laser', Appl. Phys. Lett., 36, 309 (1980).

21. COOK, L.W., FENG, M., TASHIMA, M.M., BLATTNER, R.J. and STILLMAN, G.E., 'Interface grading in InGaAsP liquid phase epitaxy heterostructures', Appl. Phys. Lett., 37, 173 (1980).

22. KAWAGUCHI, H., TAKAHEI, T., TOYOSHIMA, Y., NAGAI, H. and IWANE, G., 'Room temperature CW operation of InP/InGaAsP/InP double hetero-structure diode lasers emitting at 1.55μm', Electron, Lett., 15, 669 (1979).

23. ARAI, S., SUEMATSU, Y., and ITAYA, Y., '1.67μm $Ga_{0.47}In_{0.53}As$/InP DH lasers double cladded with InP by LPE technique', Jpn. J. Appl. Phys., 18, 709 (1979).

24. AKIBA, S., SAKAI, K. and YAMAMOTO, T., '$In_{0.53}Ga_{0.47}As/In_{1-x}Ga_xAs_yP_{1-y}$ double heterostructure lasers with emission wavelength of 1.67μm at room temperature', Jpn. J. Appl. Phys., 17, 1899 (1978).

25. OLSEN, G.H. and ZAMEROWSKI, T.J., 'Vapour-phase growth of (In, Ga) (As, P) quaternary alloys', IEEE J. Quantum Electron, QE-17, 128 (1981)

26. OLSEN, G.H. and ZAMEROWSKI, T.J., 'Crystal growth and properties of binary, ternary and quaternary (In, Ga) (As, P) alloys grown by the hydride vapour phase epitaxy technique', Progress in Crystal Growth and Characterisation, Vol.II. ed. Pamplin, B.R., Pergamon Press, London, 309 (1979).

27. HYDER, S.B., SAXENA, R.R. and COOPER, C.C., 'Vapour-phase epitaxial growth of quaternary $In_{1-x}Ga_xAs_yP_{1-y}$ in the 0.75 - 1.35 eV band-gap range', Appl. Phys. Lett., 34, 584 (1979).

28. ZINKIEWICZ, L.M., LEPOWSKI, T.R., ROTH, T.J. and STILLMAN, G.E., 'Vapour phase growth of InP and InGaAs by the hydride (In-Ga-AsH_3-HCℓ-H_2) technique', Proc. 1980 NATO Conf. on InP, Hanscom Airforce Base, MA, 349 (1980).

29. SUGIYAMA, K., KOJIMA, H., ENDA, H. and SHIBATA, M., 'Vapour phase epitaxial growth and characterisation of $Ga_{1-y}In_yAs_{1-x}P_x$ quaternary alloys', Jpn. J. Appl. Phys., 16, 2197 (1977).

30. ENDA, H., 'Preparation and properties of VPE-grown GaInAsP', Jpn. J. Appl. Phys., 18, 2167 (1979).

31. SUSA, N., YAMAUCHI, Y., ANDO, H. and KANBE, H., 'Vapour phase epitaxial growth of indium gallium arsenide on (100) indium phosphide substrate', Jpn. J. Appl. Phys., 19, L17 (1980).

32. MIZUTANI, T., YOSHIDA, M., USAI, A., WATANABE, H., YUASA, T. and HAYASHI, I., 'Vapour phase growth of InGaAsP/InP DH structures by the dual-growth-chamber method', Jpn. J. Appl. Phys., 19, L113 (1980).

33. COOPER, C., LUDOVIK, M. and MOON, R.A.V., 'The organometallic VPE growth of $GaAsAs_{1-y}Sb_y$ using trimethyl-antimony and $Ga_{1-x}In_xAs$ using trimethyl-arsenic', Electron. Lett., 16, 20 (1980).

34. DUCHEMIN, J.P., BONNET, M., BEUCHET, G. and KOELSCH, F., 'Organometallic growth of device quality InP by cracking of In $(C_2H_5)_3$ and PH_3 at low pressure', Gallium Arsenide and related compounds, 1978, Conf. Ser. No. 45, Inst. of Phys., Bristol, 10 (1979).

35. YOSHINO, J., IWANOT, T. and KUKIMOTO, H., 'Organometallic VPE growth of $In_{1-x}Ga_xP$', J. Cryst. Growth, 55, 74 (1981).

36. MANASEVIT, H.M. and SIMPSON, W.I., 'The use of metal-organics in the preparation of semiconductor materials, V : the formation of In-group V compounds and alloys', J. Electrochem, Soc., 120, 135 (1973).

37. CHO, A.Y. and ARTHUR, J.R., 'Molecular beam epitaxy', Prog. in Solid State Chem., 10, 157 (1975).

38. TSANG, W.T., 'High-through-put, high-yield and high-reproducible (AlGa)As DH laser wafer grown by moleculer beam epitaxy', Appl. Phys. Lett., 38, 587 (1981)

39. BACHARACH, R.Z., "MBE - Molecular Beam Epitaxial Evaporative Growth', Crystal Growth, ed. Pamplin, B.R., Pergamon Press, Oxford (1980).

40. CHO, A.Y., 'Recent developments in molecular beam epitaxy (MBE)', J. Vac. Sci. Technol., 16, 275 (1979).

41. GOSSARD, A.C., PETROFF, P.M, WIEGMANN, W., DINGLE, R. and SAVAGE, A., 'Epitaxial structures with alternate-atomic-layer composition modulation', Appl. Phys. Lett., 29, 323 (1976).

42. GOSSARD, A.C., 'GaAs/AℓAs layered films', Thin Solid Films, 57, 3 (1979).

43. PETROFF, P.M., 'TEM of interfaces in III-V compound semiconductors', J. Vac. Sci. Technol., 14. 973 (1977)

44. NAUKKARINEN, K., AIRAKSINEN, V.-M., LAAKSO, K., -M., LAHTINEN, J.A. and TUOMI, T., "Liquid phase epitaxial growth of GaInAsP/InP laser crystal", Helsinki University of Technology, Laboratory of Physics, Otaniemi, Finland, Report P3 (1982).

4

DYNAMICAL THEORY OF X-RAY DIFFRACTION

4.1. Introduction

When a monochromatic beam of X-rays of wavelength λ is incident at an angle θ_B on a set of lattice planes separated by a distance d in a perfect crystal, a strong diffracted beam would appear at an angle $2\theta_B$ to the incident beam, in accordance with the well known Bragg's law

$$\lambda = 2d \sin\theta_B \qquad \ldots(4.1)$$

If there are perfect and distorted regions in the crystal, equation (4.1) will not be simultaneously satisfied by both the regions. The intensity of the X-rays diffracted from the deformed lattice planes around a defect would differ from the intensity diffracted from the perfect lattice planes surrounding the deformed region. Consequently, a topograph of the diffracted beam would show a contrast in the image between the perfect and distorted areas. Essentially the phenomenon of diffraction is used to probe the internal structure of the crystal. The theory of X-ray diffraction is therefore necessary for a physical understanding of the formation of diffraction topographs - essential in order to be able to interpret the images of any defects in the crystal.

Rocking curves, on the other hand, show one or more peaks, depending upon, in general, one or more sets of lattice planes with different lattice parameters that are presented to the incident X-ray beam. The height, width and shape of the rocking curve are also functions of the thickness of the material and

misorientations of the lattice planes.

The basic theory of X-ray diffraction was developed much before any experiental topographic technique for studying imperfections in nearly perfect crystals was attempted. A detailed treatment of the dynamic theory is available in standard literature[1-4]. The aim of this chapter is to provide an interpretation of contrast of the images in X-ray topography, as well as of the nature of the double-crystal rocking curves, with the help of an elementary dynamic theory of X-ray diffraction.

Two main theories have been developed to interpret the changes in intensities of X-rays diffracted by a crystal. In the kinematical theory, the amplitude of X-rays diffracted from diffracting centres are at all times assumed very small in comparison to the incident wave amplitude. This assumption is based on the fact that the interaction of X-rays with matter is very weak and that the scattering of X-rays by an atom is always very small and is valid for very thin crystals as well as highly deformed crystal. For large crystals, with thickness exceeding a particular limiting value, even if perfect, the amplitude of the X-rays diffracted becomes comparable with the incident wave amplitude. Assuming a kinematical approximation the total intensity diffracted by the crystal is always higher than in the non-kinematical case. A 'reduced' diffracted intensity observed in thick perfect crystals is attributed to what is called extinction effect. In thick perfect crystals interchange of energy occurs between the incident and diffracted beams as they pass through the crystal

and a kinematical theory containing an extinction correction cannot satisfactorily explain the phenomenon; a dynamical theory is therefore called into play, which takes care of all the interactions between the incident and diffracted beams. The analysis of the dynamical theory tends asymptotically towards the kinematical theory in the case of thin perfect crystals.

Since we are considering the propagation of electromagnetic waves in the crystal, Maxwell's equation should be satisfied at every point. The problem for the dynamical theory is in simple terms, to determine solutions of Maxwell's equations in a periodic medium, employing appropriate boundary conditions which are satisfied by matching to solutions which are plane waves outside the crystal.

4.2. The Laue condition

According to the kinematical theory of X-ray diffraction, the wave vectors of the incident and diffracted waves should satisfy the principle of conservation of energy and momentum. Within the crystal, the diffracted beam wave vector $\underline{K}_h$ is related to the incident beam wave vector $\underline{K}_o$ by the Laue equation

$$\underline{K}_h = \underline{K}_o + \underline{h} \qquad \ldots(4.2)$$

where $\underline{h}$ is called the reciprocal lattice vector, $|h| = \frac{1}{d}$.
The refractive index for X-rays is very close to unity, hence

$$|K_o| \approx |K_h| \approx 1/\lambda$$

Equation (4.2) suggests that there are two waves whose difference in wave vectors is equal to the reciprocal lattice vector corresponding to the Bragg reflecting plane.

4.3. The Periodic Complex dielectric constant

The electron density, or the density of scattering matter at any point in the crystal can be expressed as a Fourier sum over the reciprocal lattice as

$$\rho(\underline{r}) = \frac{1}{V} \sum_{h} F_h \exp(- 2\pi i \, \underline{h}.\underline{r}) \qquad \ldots(4.3)$$

where V = volume element of the unit cell

$\underline{h}$ = reciprocal lattice vector

= $h\underline{b}_1 + k\underline{b}_2 + \ell\underline{b}_3$, where h, k, ℓ are the Miller indices of the reflection described by the reciprocal lattice point, and $\underline{b}_1$, $\underline{b}_2$, $\underline{b}_3$ are the reciprocal lattice vectors defining the unit cell in the reciprocal space

F_h = structure factor for the hkℓ reflection.

Assuming that the atoms behave as rigid spheres with respect to their charge densities and neglecting their thermal vibration, the structure factor can be written as

$$F_h = \sum_{n} f_n \exp(2 \, i\pi \underline{h}.\underline{r}_n) \qquad \ldots(4.4)$$

where the summation is over the n atoms in the unit cell.

f_n = atomic scattering factor of the n^{th} atom.

The refractive index according to the classical dispersion theory is given by a relationship[5]

$$n^2 - 1 = \sum_{a} \frac{4\pi\rho'(r)e^2}{m(\omega_a^2 - \omega^2)} \qquad \ldots$$

where the summation is over the number of resonators or absorption bands, or more conveniently

$$n^2 - 1 = - \frac{4\pi e^2 \rho(r)}{m\omega^2} \qquad \ldots(4.5)$$

in most cases of interest, where $(n^2 - 1)$ is proportional to the square of X-ray wavelength.

The polarization $\underline{P}$ is defined by

$$\underline{D} = \underline{E} + 4\pi\underline{P}$$

and the electric displacement $\underline{D} = \varepsilon\underline{E}$.

Since the susceptibility χ is defined by

$$\chi\underline{D} = 4\pi\underline{P} = \frac{\varepsilon-1}{\varepsilon}\ \underline{D}$$

it follows that

$$\chi = \frac{\varepsilon-1}{\varepsilon} = \frac{n^2-1}{n^2}$$

Assuming $\varepsilon \simeq 1$, this means

$$\chi = - \frac{4\pi e^2}{m\omega^2}\ \rho(r) \qquad \ldots(4.6)$$

In a periodic medium. the susceptibility χ is periodic and can be expanded as a Fourier series over the reciprocal lattice as

$$\chi = \sum_h \chi_h \exp(- 2\pi i\ \underline{h}.\underline{r}) \qquad \ldots(4.7)$$

Equation (4.6) is essentially

$$\chi = \varepsilon - 1 = -\frac{e^2\lambda^2}{\pi mc^2 V}.\sum_h f_h \exp(-2\pi i\, \underline{h}.\underline{r}) \qquad \ldots(4.8)$$

Comparing equations (4.7) and (4.8)

$$\chi_h = -\frac{e^2\lambda^2}{\pi mc^2 V} F_h \qquad \ldots(4.9)$$

The quantity e^2/mc^2 is the classical electron radius

$r_e = 2.818 \times 10^{-13}$ cm

4.4. Solutions of Maxwell's equations

Assuming that the electrical conductivity is zero at X-ray frequencies and that the magnetic permeability μ is unity, Maxwell's equation, in CGS Gaussian units can be written as

$$\nabla \times \underline{E} = -\frac{1}{c}\frac{\partial \underline{B}}{\partial t}$$

$$\nabla \times \underline{H} = \frac{1}{c}\frac{\partial \underline{D}}{\partial t}$$

or using $\underline{D} = \varepsilon\, \underline{E}$ and $\varepsilon \simeq 1 + \chi$ the above equations reduce to

$$\nabla \times \nabla \times \underline{D} = -\frac{(1+\chi)}{c^2}\frac{\partial^2 \underline{D}}{\partial t^2} \qquad \ldots(4.10)$$

As χ is very small in the X-ray region, typically of the order of 10^{-5}, equation (4.10) can be written as

$$\nabla \times \nabla \times (1-\chi)\underline{D} = -\frac{1}{c^2}\frac{\partial^2 \underline{D}}{\partial t^2} \qquad \ldots(4.11)$$

For the solution of the Bragg reflection problem, in the dynamical case, which must yield the same results as the kinematical theory in the limit of thin crystals, we may expect the solutions to Maxwell's equations to consist of sums of plane waves for which the allowed wave vectors are related to one another by the Laue condition.

We accordingly look for solutions for $\underline{D}$ of the form

$$\underline{D} = \sum_h \underline{D}_h \exp(-2\pi i \underline{K}_h \cdot \underline{r}) \exp(i\omega t) \qquad \ldots(4.12)$$

Substituting equations (4.12) and (4.7) into (4.11) we finally get

$$\sum_h \left[\chi_h (\underline{K}_h \cdot \underline{D}_h) \underline{K}_h - \chi_h (\underline{K}_h \cdot \underline{K}_h) \underline{D}_h\right] = \left[k^2 - \underline{K}_h \cdot \underline{K}_h\right] \underline{D}_h \qquad \ldots(4.13)$$

where $k = \frac{f}{c} = \frac{1}{\lambda}$ is the vacuum wave number.

Equations (4.12) and (4.13) are the fundamental equations of the dynamical theory and are the vector-form equivalent to the electron diffraction case obtained by solving Schrodinger's equation in a periodic medium. For the X-ray case, in general, only one reciprocal lattice point provides a diffracted wave of appreciable amplitude. We thus need to consider only two waves to have appreciable amplitude in the crystal - the incident wave and the diffracted wave from a reciprocal lattice vector $\underline{h}$. Equation (4.13) then becomes

$$\chi_h (\underline{K}_h \cdot \underline{D}_o) \underline{K}_h - \chi_h (\underline{K}_h \cdot \underline{K}_h) \underline{D}_o + \chi_o (\underline{K}_h \cdot \underline{D}_h) \underline{K}_h$$

$$- \chi_o (\underline{K}_h \cdot \underline{K}_h) \underline{D}_h = (k^2 - \underline{K}_h \cdot \underline{K}_h) \underline{D}_h \qquad \ldots(4.14)$$

and

$$\chi_h^-(\underline{K}_o\cdot\underline{D}_h)\underline{K}_o - \chi_h^-(\underline{K}_o\cdot\underline{K}_o)\underline{D}_h + \chi_o(\underline{K}_o\cdot\underline{D}_o)\underline{K}_o$$

$$- \chi_o(\underline{K}_o\cdot\underline{K}_o)\underline{D}_o = (k^2-\underline{K}_o\cdot\underline{K}_o)\underline{D}_o \qquad \ldots(4.15)$$

Making the substitutions

$$C = \underline{D}_o\cdot\underline{D}_h = 1 \text{ for } \sigma \text{ polarization}$$

$$= \mathrm{Cos}2\theta_b \text{ for } \pi \text{ polarization}$$

$$\alpha_o = \frac{1}{2k}\left[\underline{K}_o\cdot\underline{K}_o - k^2(1+\chi_o)\right]$$

$$\alpha_h = \frac{1}{2k}\left[\underline{K}_h\cdot\underline{K}_h - k^2(1+\chi_o)\right]$$

a non-trivial solution of equations (4.14) and (4.15) gives

$$\alpha_o\alpha_h = \frac{1}{4}k^2C^2\chi_h\chi_h^- \qquad \ldots(4.16)$$

Equation (4.16) is an important relation linking $\underline{K}_o$ and $\underline{K}_h$ in the crystal and describes a dispersion surface, drawn in Figure 4.1.

OO and HH are sections of segments of spheres of radius k drawn with centres at O and H respectively of the reciprocal lattice. In the absence of a Bragg reflection, the situation inside the crystal is that since $\underline{D}_h = 0$,

$$|K_o| \simeq k(1+\chi_o/2)$$

The wave vectors now start on spheres O'O" and H'H" which have radii equal to $k(1+\chi_o/2)$. In effect, the wave vector is corrected for the refractive index.

As χ_o is small, $|K_o| \simeq |K_h| \simeq k$

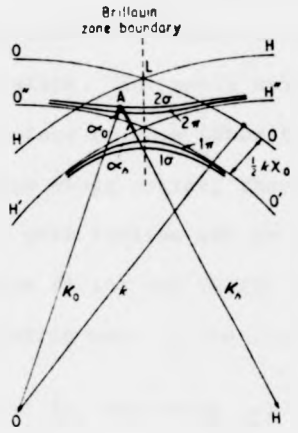

FIG 4.1 Construction of a dispersion surface showing the loci of tie points like A , which define wave vectors whose real parts satisfy both Maxwell's equation and the Laue equation when there are only two strong waves.

The Laue condition is satisfied only at, or close to the intersection of the two spheres and a strong diffraction would then occur.

In the absence of a diffracted wave, the tail of the wave vector $\underline{K}_o$ in the crystal will fall on the sphere O'O" about O, far from the Laue point L. When strong diffraction occurs, $\underline{K}_o$ and $\underline{K}_h$ are governed by equation (4.16) and the tail can no longer lie on the spheres. In Figure 4.1, α_o and α_h correspond to the perpendicular distances of a point A to the spheres O'O" and H'H". The distances are small compared to the radii of the spheres, so the section of the spheres can be approximated to a plane while calculating the perpendicular distance. The equation (4.16) for the dispersion surface is a hyperboloid of revolution with axis OH.

Figure 4.1 shows a section of the hyperboloid : a hyperbola asymptotic to O'O" and H'H". There are four branches, two for each polarization state. For small Bragg angles the dispersion surfaces are very close to each other for the two polarization states, but at large Bragg angles, they show significant deviation and the effects of polarization are to be taken into account. $\underline{D}_o$ and $\underline{D}_h$ from equation (4.14) and (4.15) can be substituted in (4.12) to give the propagating wave in the crystal an amplitude

$$\underline{D} = \exp(i\omega t)\ [\underline{D}_o \exp(-2\pi i \underline{K}_o.\underline{r}) + \underline{D}_h \exp(-2\pi i \underline{K}_h.\underline{r})] \qquad ...(4.17)$$

The amplitude ratio

$$\xi = \underline{D}_h/\underline{D}_o = 2\alpha_o/Ck\chi_{\bar{h}} = Ck\chi_h/2\alpha_h$$

$$\text{and } \xi^2 = \alpha_o\chi_h/\alpha_h\chi_{\bar{h}}$$

Thus the dispersion surface not only determines the wave vectors from the position of the point A, but also the ratio of the amplitudes of the waves.

The diameter of the hyperbola of Figure 4.1 is approximately $10^{-5}k$. Figure 4.1 is therefore intentionally magnified around L.

Assuming that there is no absorption, χ_o is therefore real and $\chi_h = \chi^*_{\bar{h}}$, or in other words $\chi_h\chi_{\bar{h}}$ is real. We see that the right hand side of equation (4.16) is real. Two types of solutions are therefore possible.

If α_o and α_h are both real, then $\underline{K}_o$ and $\underline{K}_h$ are also both real and the appropriate solutions of equation (4.16) are represented

by the four branches of the hyperboloid as already discussed and a section of which is shown in Figure 4.1. The factor C (= 1 for α polarized state and = $|\cos 2\theta_B|$ for the π polarized state) arises from the dependence of the scattering amplitude on the polarization of the wave. Since α_o and α_h are known at each point on the dispersion surface, ξ is also known and so a solution of the Maxwell's equation is possible to give a complete specification of the waves in the crystal. α_o and α_h are positive for branch 2; hence if χ_h and $\chi_{\bar{h}}$ are real, so that $\chi_h = \chi_{\bar{h}}$, and negative, ξ is negative. The two waves are opposite in phase.

If α_o and α_h are complex conjugates, it directly follows from the definition of α_o and α_h that

$$\underline{K}_o \cdot \underline{K}_o = (\underline{K}_h \cdot \underline{K}_h)^*$$

$$\text{or} \quad |K_o| = |K_h^*|$$

The real part of $\underline{K}_o$ and $\underline{K}_h$ are thus equal, hence it follows that the tail of the wave vectors $\underline{K}_o$ and $\underline{K}_h$ end on the Brillouin zone boundary. We see that ξ is a complex quantity, the relative phase of the two waves in the crystal thus being determined by α_o.

Assuming χ_h to be real, with $\chi_{\bar{h}} = \chi_h$, we obtain

$$|\xi^2| = 1$$

We can thus summarize the results as follows: If the point A moves from near O" towards H", then ξ, starting from a small negative value near O", passes through - 1 at the Brillouin zone boundary

and approaches a large negative value near H''. For the pair of dispersion surfaces in branch 1, ξ starts from $+\infty$ near H', then through +1 at the Brillouin zone and approaches +o near O'. When there is absorption in the crystal, χ_o is no longer real and the allowed solutions are complicated. The real parts of the wave vector remain the same but the amplitudes of the waves are changed.

4.5. Boundary Conditions for Solutions of Maxwell's Equations

Considering that the waves inside the crystal are induced by plane waves incident on the crystal from outside, all necessary boundary conditions must be satisfied.

For a plane polarized incident wave of amplitude

$$\underline{D} = \underline{D}_i \exp(-2\pi i \, \underline{k}_e . \underline{r})$$

incident on the surface of a crystal, the Bloch waves in the crystal can be considered as a superposition of plane waves such as

$$\underline{D} = \sum_h \underline{D}_h \exp(-2\pi i \, \underline{K}_h . \underline{r})$$

Continuity of the wave vector across the boundary requires

$$\exp(-2\pi i \, \underline{k}_e . \underline{r}) = \exp(-2\pi i \, \underline{K}_h . \underline{r})$$

for each plane wave (corresponding to the incident and diffracted components outside the crystal).

Thus wave vectors inside the crystal differ from that outside only by a vector normal to the crystal surface

$$\underline{K}_{oi} - \underline{k}_e = \underline{K}_{hi} - \underline{k}_e = \delta\underline{n} \qquad \ldots(4.18)$$

where $\hat{n}$ is a unit vector normal to the surface and i = 1 or 2 depending on the branch of the dispersion surface. Equation (4.18) means that a plane incident wave excites two tie points on the dispersion surface that are given by the points of intersection of the unit vector $\hat{n}$ with the dispersion surface. The vector $\hat{n}$ is drawn normal to the crystal surface from the tip of the wave vector $\underline{k}_e$ of the incident wave. In the Laue transmission geometry, these tie points lie on the opposite branches of the dispersion surface whereas in the Bragg reflection case, they lie on the same branch of the dispersion surface. The two tie points represent the tip of the two pairs of wave vectors $(\underline{K}_{o1}, \underline{K}_{h1})$ and $(\underline{K}_{o2}, \underline{K}_{h2})$, certain complex situations are possible in the Laue case where the waves that exit from the lower surface of the crystal that is not parallel to the entrance surface need to satisfy a separate boundary condition involving an additional unit vector $\hat{n}$ normal to the lower surface. The same is true for the Bragg case where the waves can reach the back surface of the crystal and then return to the front surface and the two surfaces are not parallel.

4.6. Pendellösung

For a plane wave incident on a crystal there are two Bloch waves within the crystal with two different wave vectors, whose difference leads to a difference in propogation velocity. Fringes are therefore expected to occur in wedge shaped crystals due to interference effects between the Bloch waves.

For a symmetric Laue geometry, it can be shown that the intensity of both the diffracted and transmitted beams exhibits a periodic variation with crystal thickness. The period is given by the depth

$$\xi_d = \left[\Lambda_o \left(1 + \eta^2\right)^{1/2}\right]^{-1} \qquad \ldots(4.19)$$

where Λ_o = dispersion surface diameter given by

$\Lambda_o^2 = \mathrm{Sec}^2\theta_B k^2 C^2 \chi_h \chi_{\bar{h}}$

and η = deviation parameter

$= 2\sin\theta_b k\Delta\theta/\Lambda_o$

η is proportional to the angular deviation from the Bragg condition.

ξ_d has a maximum value at $\eta = 0$, and this is the exact Bragg condition. The extinction depth is then given by

$$\xi_g = \Lambda_o^{-1} = \cos\theta_B / Ck\left(\chi_h \chi_{\bar{h}}\right)^{1/2}$$

$$\xi_g = \frac{\pi V_o \cos\theta_B}{r_e \lambda C \left(F_h F_{\bar{h}}\right)^{1/2}} \qquad \ldots(4.20)$$

For $\eta \neq 0$, $\xi_g' = \xi_g / \left(1 + \eta^2\right)^{1/2}$

As $\eta \to \infty$, $\xi_g' \to 0$, only one wave is excited within the crystal and no interference occurs. The transmitted and diffracted intensities are given by

$$I_o = \cos^2 \left[\pi \Lambda_o t \left(1 + \eta^2\right)^{1/2}\right] / \left(1 + \eta^2\right)$$

$$I_h = \sin^2 \left[\pi \Lambda_o t \left(1 + \eta^2\right)^{1/2}\right] / \left(1 + \eta^2\right) \qquad \ldots(4.21)$$

In simple terms, a plane wave incident on a crystal excites a diffracted wave in the crystal as it is transmitted through it. Effectively energy is passed from the transmitted to the diffracted beam as the wave passes through the crystal and this phenomenon is called Pendellosung in analogy with coupled pendulum. The diffracted and transmitted intensities are complementary.

Since the intensity of both the diffracted and transmitted beams exhibits a periodic variation with the crystal thickness, if the crystal is wedge-shaped, then in the thin region the two wavefields cannot separate enough and Pendellosung interference occurs. In the thicker regions, the wavefields diverge and interference is not observed.

The symmetrical Bragg case geometry can also be used similarly to obtain interference effects in thin crystals.

When the crystal is thick, it can be shown that the intensity in the diffracted beam becomes for the Bragg case,

$$I_h = \left[\, |\eta| - \left(\eta^2 - 1\right)^{1/2} \right]^2 \qquad \ldots(4.22)$$

for a non-absorbing crystal. The intensity is thus independent of the crystal thickness.

4.7. Rocking Curve Profile

When a perfect crystal is rotated through the Bragg angle, the intensity of the diffracted beam, as given by equations (4.21) and (4.22) for both the Laue and Bragg cases, which is a function of the deviation parameter η, thus varies. This plot of the diffracted intensity against angular deviation from the Bragg condition is called the rocking curve. It is the convolution of the perfect crystal reflection curve given by equations (4.21) and (4.22) and the divergence of the incident X-ray beam. Assuming that the incident beam is a plane wave, the rocking curve is given simply by these equations.

Equation (4.21) can be simplified for thick crystals to

$$I_h = (1 + \eta^2)^{-1} \qquad \ldots(4.23)$$

Equation (4.23) shows that the rocking curve is symmetric. If absorption is included, they tend to become asymmetric. The full width at half maximum intensity is at

$$\Delta\eta = 2$$

This corresponds to an angle

$$\Delta\theta \Big|_{1/2} = \frac{2}{h\xi_g} \qquad \ldots(4.24)$$

where $h = \frac{1}{d}$ = magnitude of the reciprocal lattice vector

ξ_g = extinction distance

Rocking curve widths of perfect crystals are of the order of a few seconds of arc.

Both h and ξ_g increase with the increasing order of reflection, weak reflection means large extinction depths, hence higher order, weak reflections have extremely narrow rocking curve widths.

Equation (4.22) plots the rocking curve for the symmetric Bragg case. As can be seen, for values of $|\eta| < 1$, the term under square root is negative. Physically, no wavefields can be excited in the crystal and total reflection occurs. The range of total reflection is again $\Delta\eta = 2$ and is given by equation (4.24).

For a double crystal arrangement, in a non-dispersive setting, it can be shown[3] that the rocking curve for the intensity when the second crystal is rotated is the convolution of the reflectivity functions $R_1(\theta)$ and $R_2(\theta)$of the two crystals

$$I(\theta) = \int_{-\infty}^{\infty} R_1(\alpha) \; R_2(\alpha - \theta) \, d\theta$$

This means that even if the incident beam is not a plane wave, if both the crystals are perfect, the rocking curve is highly symmetrical; but if one of the crystals is distorted, the rocking curve would be asymmetric.

4.8. Distorted Crystals

The simple classical theory of Section 4.4 does not explain the diffraction processes in a distorted crystal. Several theories have been proposed and one of the most successful has been that of Takagi[6].

The wave equation for the electric displacement $\underline{D}$ induced by X-rays in a crystal should satisfy

$$\text{div } \underline{D} = 0$$

It is assumed that the wave inside the crystal is of the form

$$\underline{D} = \underline{D}(r) \exp(i\omega t)$$

where

$$\underline{D}(r) = \sum_h D_h(r) \exp(-2\pi i \, \underline{K}_h . \underline{r})$$

$D_h(r)$ is now considered to be a slowly varying function of position instead of being constant and $\underline{K}_h = \underline{K}_o + \underline{h}$

A more convenient expansion is

$$D(r) = \sum_h D'_h(r) \exp(-2\pi i \, S_h(r))$$

with $S_h(r) = \underline{K}_h \cdot \underline{r} - \underline{h}.\underline{u}(r_o)$

where $\underline{r} = \underline{r}_o + \underline{u}(r_o)$

and $K'_h = \text{grad } S_h(r) = \underline{K}_h - \text{grad } (\underline{h}.\underline{u})$

= wave vector of the h^{th} component wave.

We define a local reciprocal lattice vector in the vicinity of r in distorted crystal by

$$\underline{h}' = \underline{h} - \text{grad } (\underline{h}.\underline{u}(r_o))$$

and $\underline{K}'_h = \underline{K}_o + \underline{h}'$

That $D_h(r)$ and $D_h'(r)$ are now variable allows an ambiguity in the definitions of $\underline{K}_o$; the effect of any slight change ΔK_o in K_o can be compensated by multiplying a factor $\exp(2\pi i \Delta\underline{K}_o . \underline{r})$ to $D_h(r)$ or $D_h'(r)$ without affecting the macroscopic character, as long as $\Delta\underline{K}_o$ is sufficiently smaller than any reciprocal lattice vector.

We initially choose $\underline{K}_o$ such that $|K_o| = K = nk$, n = mean refractive index. Substitution of the expression for $\underline{D}$ in Maxwell's equation and neglecting second order effects gives

$$\frac{(\underline{K}_h \cdot \text{grad})\underline{D}_h'}{k^2 - k_h^2} + i\pi \underline{D}_h' + \frac{i\pi K_h^2}{k^2 - K_h^2} \sum_{h' \neq h} \chi_{h-h'} \underline{D}_h = 0 \qquad \ldots(4.25)$$

In the case of two strong waves, i.e. the case where only the transmitted and one one diffracted wave have appreciable amplitudes each of the above equation reduces to a set of two equations with two unknown functions:

$$\frac{\partial D_o'}{\partial S_o} = - i\pi k C \chi_{\bar{h}} D_h'$$

$$\frac{\partial D_h'}{\partial S_h} = -i\pi k C \chi_h D_o' + 2\pi i\, k\beta_h' D_h' \qquad \ldots(4.26)$$

where $\hat{S}_o$ and $\hat{S}_h$ are unit vectors parallel to $\underline{K}_o$ and $\underline{K}_h$ that is, to the incident and diffracted beam directions and

$$\beta_h' = \frac{K_h^2 - K_o^2}{2k^2} = \frac{K_h - K_o}{k}$$

$$= \frac{K_h - k(1 + \chi_o/2)}{k} \qquad \text{in a non absorbing case}$$

When $\beta_h' = 0$ i.e. for a perfect crystal, equations (4.26) reduce to a simple form where they can be solved analytically.

When $\beta_h' \neq 0$, numerical integration must be performed. In any case, equations (4.26) are the basic set of equations to be solved. Taupin[7] has extended the theory of Takagi to obtain the change in the ratio of the diffracted to the incident beam amplitudes as a function of the depth below the surface.

The incident and diffracted beam amplitudes D_o and D_H can be expressed in a differential form[7]

$$i \frac{\lambda}{\pi} \nu_H \frac{\partial D_H}{\partial Z} = \psi_o D_H + \psi_H D_o - \alpha_H D_H \qquad \ldots(4.27)$$

$$i \frac{\lambda}{\pi} \nu_o \frac{\partial D_o}{\partial Z} = \psi_o D_o + \psi_H D_H \qquad \ldots(4.28)$$

where

$$\nu_H = \eta . S_H = - \sin\theta_B$$

$$\nu_o = \eta . S_o = + \sin\theta_B$$

(assuming a symmetric Bragg case)

with η = unit vector normal to the surface of entrance

S_o = unit vector along the incident beam direction

S_H = unit vector along the reflected beam direction

θ_B = Bragg angle

λ = wavelength of the X-ray beam

D_o = complex amplitude of the incident beam at a depth Z

D_H = complex amplitude of the reflected beam at the depth Z

$$\psi_H = \frac{-\lambda^2 R_e}{\pi V} F_h \qquad \ldots(4.29)$$

$$\psi_o = \frac{-\lambda^2 R_e}{\pi V} F_o \qquad \ldots(4.30)$$

with R_e = classical electron radius = 2.817×10^{-13} cm

V = volume of the unit cell

F_o = complex structure factor in the incident direction

and F_h = complex structure factor for the reflected direction

$$\alpha_H = \lambda^2 \left(\frac{1}{d_H^2} - \frac{2 \operatorname{Sin}\theta_B}{\lambda d_H} \right)$$

with d_H = lattice plane spacing assumed a function of depth Z. A polarization factor c = 1 has been used. For any c, ψ_H will be replaced by $c\psi_H$.

The ratio χ, (D_H/D_o), is related to the reflection of the system

$$\frac{dX}{dZ} = \frac{i\pi}{\lambda \operatorname{Sin}\theta_B} \left[c\psi_H \chi^2 + \{2\psi_o - \alpha_H(Z)\}\chi + c\psi_H \right] \qquad \ldots(4.31)$$

By varying $\alpha_H(Z)$ symmetrically and on calculating the value of χ at the surface of the specimen, at every instant, using numerical solutions of equation (4.31), we can compute the graph of the reflectivity for the arrangement.

In a double crystal arrangement, assuming that the first crystal is perfect, we can carry out the product of the convolution of this reflectivity for the specimen with the graph of theoretical reflectivity calculated for the perfect crystal with absorption.

The absorption effects are duly taken care of by using complex structure factors in calculations. The resultant convoluted reflectivity is the double crystal rocking curve.

4.9. Discussion

The application of the dynamical theory, for distorted crystals, has been briefly outlined. The amplitude of the wave field has been considered to be a slowly varying function of position. The solution of Maxwell's equations provides an expression for the ratio of the amplitudes of the diffracted to the incident wave fields as a function of position within the crystal. This expression would be used to calculate the rocking curves, and the approach adopted to simulate rocking curves of multilayer laser structures is outlined in Chapter 10.

References

1. BATTERMAN, B.W. and COLE, H., 'Dynamical diffraction of X-rays by perfect crystals', Rev. Mod. Phys., 36, 681 (1964).

2. AZAROFF, L.V., KAPLOW, K., KATO, N., WEISS, R.J., WILSON, A.J.C. and YOUNG, R.A., 'X-ray diffraction', McGraw Hill, New York (1974).

3. JAMES, R.W., 'The optical principles of the diffraction of X-rays', Bell, London (1948).

4. AUTHIER, A., 'Contrast of Images in X-ray Topography', Modern Diffraction and Imaging Techniques in Material Science , Ed. Amelinckx, S., et al, North Holland, Amsterdam, 481 (1970).

5. BORN, M. and WOLF, E., Principles in Optics, Pergamon Press, London, (1959).

6. TAKAGI, S., 'A dynamical theory of diffraction for a distorted crystal', J. Phy. Soc. Jpn., 26. 1239 (1969).

7. TAUPIN, D., Bull. Soc. Fr. Mineral Cristallogr., 87, 469 (1964).

5

DOUBLE CRYSTAL

EXPERIMENTAL METHODS

5.1. Introduction

A detailed description of the experimental methods employed to obtain double crystal topographs and rocking curves of single and multilayer III-V GaInAsP/InP structures will be given in this chapter. The experimental arrangement, in its simplest form, consists of a beam conditioner, which selects a particular wavelength from the white radiation synchrotron beam. This 'monochromatic' beam is then allowed to fall on the experimental specimen which may be an InP substrate with an epitaxial layer of GaInAsP grown over it. For any chosen plane of reflection, the Bragg angle for a particular incident wavelength will be different for the epilayer and substrate, if they have different lattice parameters. So by allowing the specimen to be positioned at these two Bragg angles, two separate topographs, one corresponding to the epilayer and another corresponding to the substrate can be obtained. Alternatively, a rocking curve could be plotted by rotating the axis carrying the experimental specimen so as to pass through the two Bragg angles and having a scintillation counter instead of a photographic plate, to record the intensity of the diffracted beam as the Bragg angle is changed. Both the rocking curve and topographs give valuable information for characterizing the materials. Various aspects of the experimental method will be briefly discussed in the following sections.

5.2. The Source

Synchrotron radiation has been used as an X-ray source for topography since 1974. The main advantage of such a source over ordinary laboratory sources is that the synchrotron source is more intense. Some of the characteristics[1] of the synchrotron source at Daresbury are shown in Figure 5.1. Synchrotron radiation,

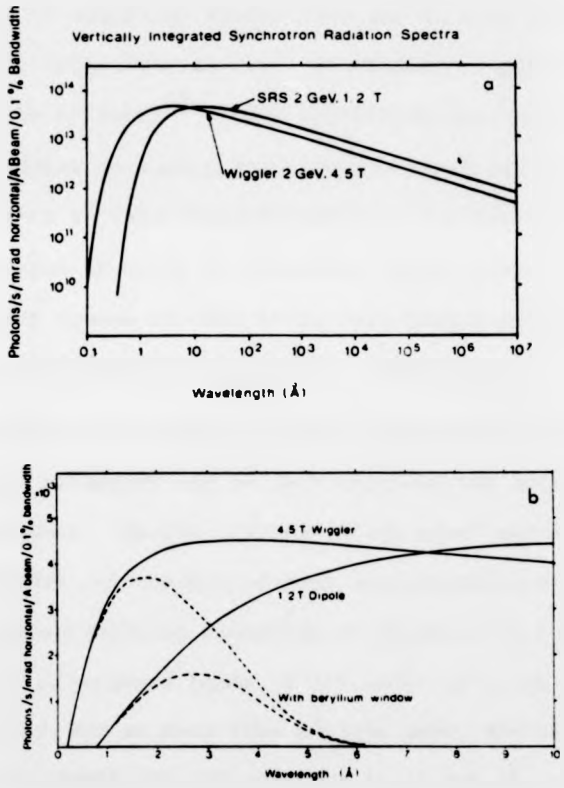

FIG 5.1 (a) Spectral curves from a normal bending magnet (1.2T) and from a 4.5T wiggler magnet, for a 2 GeV, 1 A beam in the Synchrotron Radiation Source at Daresbury. (b) Spectral curves transmitted through a 380 μm thick Be window on X-ray beam line.

generated by the radial acceleration of electrons by means of a bending magnet that keeps the electron orbit in a circular arc, exhibits a spectrum that consists of this r.f. frequency and harmonics that are too closely spaced to resolve, upto the X-ray region (Figure 5.1). To get a comparative idea with a laboratory source, we see from Figure 5.1a, at 1.5Å for example, the brightness is 1-2 orders of magnitude higher than the K_α peak obtained from a rotating anode laboratory source. A detailed comparison of various sources is made by Bonse[2]. The continuous spectrum gives the synchrotron radiation source an extremely important feature that, when used with a suitable monochromator, a tunable line source, which is powerful as well, is obtained. Other characteristics of the synchrotron source is that it is very highly polarized in the plane of the electron orbit, and has a low divergence.

In the study of electronic device materials, minute variations in the lattice parameter can be very critical for satisfactory device performance. Double crystal 'plane wave' synchrotron radiation methods are capable of such characterization. The ability of the synchrotron radiation to produce, at reasonable intensity, low divergence beams of the order of a fraction of an arc second which act as much like a plane wave, and to have a control of wavelength and polarization state are the natural advantages of synchrotron radiation double crystal cameras.

5.3. Beam Conditioner

Presently, large perfect crystals of Silicon and Germanium are commercially available. These are believed to be almost undamaged by X-radiation and would therefore be ideally suited for X-ray diffraction. When such perfect crystals satisfy the Bragg condition, they reflect the X-rays with a very high efficiency. Multiple Bragg reflections from multiple crystal systems can thus be used without serious loss of intensity, in a number of arrangements which can lead to a control of the properties of the incident beam.

One of the beam conditioners, to be described briefly below, and which was used in the double crystal camera at Daresbury, was designed and constructed by M. Hart at King's College, London[3]. It comprises a pair of separate (111) Si crystals, symmetric cut and mounted on an aluminium framework. A sketch of its layout is shown in Figure 5.2. For a narrow beam, the range of Bragg angles available is from about 6.0° to 76.5° corresponding to input

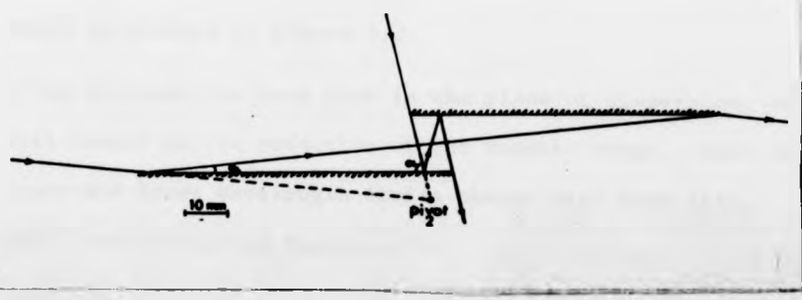

FIG 5.2 A schematic diagram of the (111) silicon monochromator. The low and high angles of incidence are 6.05 and 76.6 degrees respectively.

wavelengths from about 0.66Å to 6.0Å. For wider beams, the range is still more limited. Stepper motor controls are provided to set the crystals parallel, mainly by rotating the first crystal about pivot 1 (not shown). A solenoid arrangement is also used for a finer setting and also for harmonic control. Pivot 2 is at the 'Rodrigues point' which is the point of intersection of the highest and lowest possible angles of incidence (for Bragg reflection) of an X-ray. The entire system rotates about an axis (on the goniometer) passing through this point. This controls the wavelength. Finer adjustments of the tilt between the two crystals are made by rotating the crystal 2 about an axis parallel to its long dimension. This is done with the help of pivot 3 (not shown) which is a manual screw arrangement.

Some of the details of the monochromator have been worked out:

i) Selection of wavelength is performed by a selection of the incident Bragg angle

For (111) Si, for n = 1

$$\lambda = 6.2706 \sin\theta \ (\text{Å})$$

which is plotted in Figure 5.3.

If we increase the beam size in the plane of dispersion, this will result in the reduction of the tunable range. Both the upper and lower wavelength limits change with beam size. These are plotted in Figure 5.4.

The vertical displacement of the beam increases as the Bragg angle is decreased according to the expression $2t \cos\theta$, where t is the separation between the crystals.

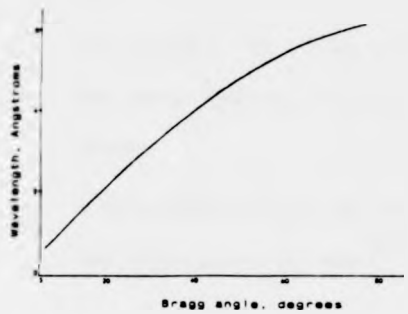

FIG 5.3 The relation between wavelength and incident Bragg angle for the silicon monochromator.

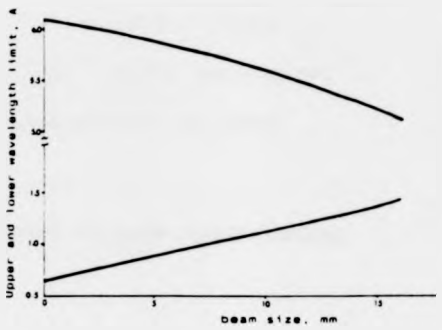

FIG 5.4 Change in upper and lower wavelength limits with beam size for the silicon monochromator.

ii) Control of harmonics is achieved by slightly misaligning the two crystals so that the broad fundamental reflections still partially overlap but the narrower harmonics no longer overlap. Thus, in the presence of harmonics a diffraction topograph will consist of a series of superimposed images with intensity ratios proportional to $F_h\ n^{-2}$, where F_h is the structure factor for the Bragg reflection. It can be shown[9] that about two-thirds of the total intensity is expected from a given reflection and the rest are due to higher order Bragg reflections.

Thus about one third of the intensity contributions are from the harmonics. For laboratory sources at high energies, the intensity in the source is as such reduced, leading to a preferential suppression of higher harmonics; so is the case

with a reduced structure factor for the higher order reflection. To have complete control of the harmonics, one has, however, to use a monochromator as outlined above.

A detailed account of the principles of beam conditioning has been given by Hart[4].

5.4. The Double Crystal Camera

The double crystal camera (DCC) intended for a wide variety of experimental measurements, including rocking curve and topographic studies, has been designed by Bowen et al[5]. An outline of the drawing of the DCC is shown in Figure 5.5 and a photograph of the camera used in an experiment, in Figure 5.6. The camera has four axes. The two fine axes are each driven by a stepper motor through a 100:1 gearbox, micrometer screw and a tangent arm to give a basic step of 0.2 arc-seconds. The axis separation is 308mm, thus allowing plenty of room for mounting large crystals and monochromators. The fine axis closer to the source carries the beam conditioner or a reference 'first' crystal. The experimental specimen which is the 'second' crystal, is mounted on the other fine axis.

The rings around the fine axes are capable of carrying slits and detectors as extra accessories. The main detector axis however, is coincident with the second fine axis of the goniometer and has a step length of 1 arc-minute. The axis is strong enough to hold an X-ray TV imaging camera or a scintillation counter. The main camera axis GM2 is coincident with the first fine axis. The

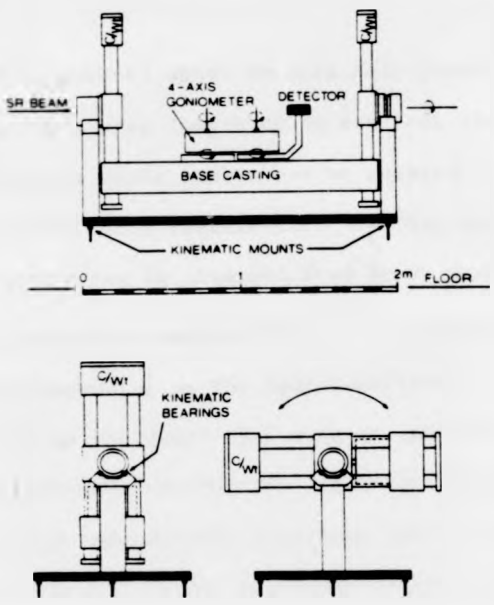

FIG 5.5 Outline of the double crystal camera.

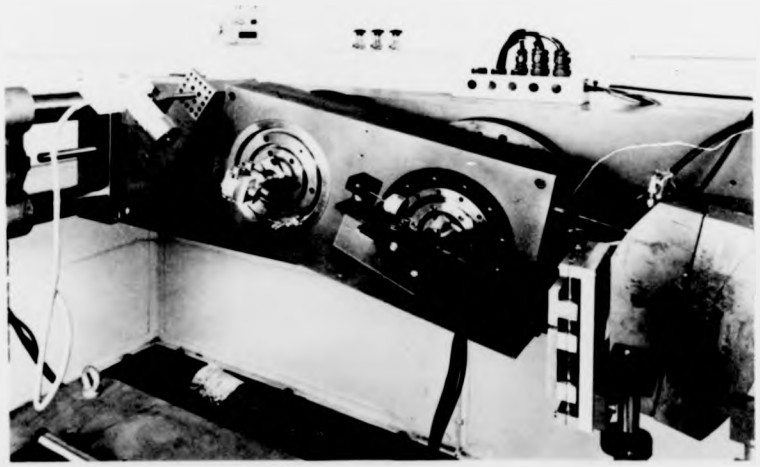

FIG 5.6 Photograph of the double crytal camera in an experimental set-up. An order sorting beam conditioner is mounted on the right hand fine axis while a test specimen is mounted on a goniometer on the left hand fine axis.

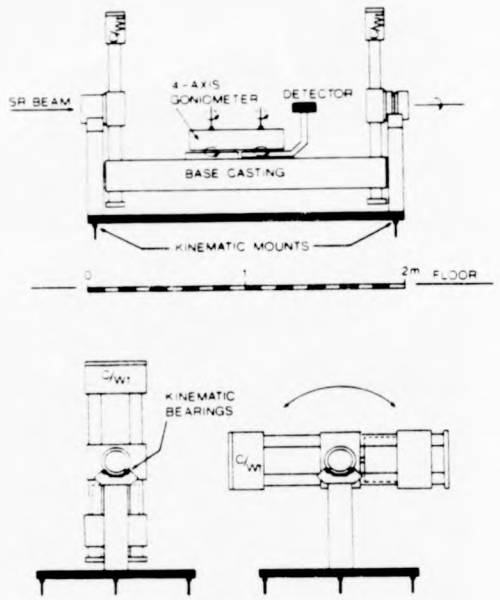

FIG 5.5 Outline of the double crystal camera.

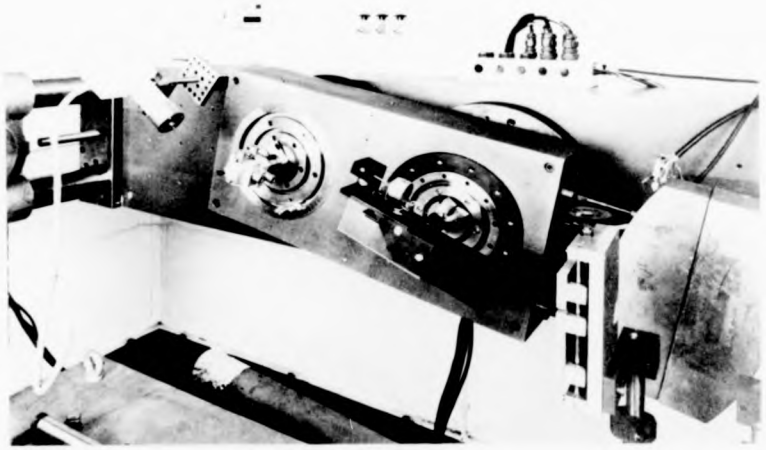

FIG 5.6 Photograph of the double crytal camera in an experimental set-up. An order sorting beam conditioner is mounted on the right hand fine axis while a test specimen is mounted on a goniometer on the left hand fine axis.

whole goniometer can be rotated about an axis coincident with the first fine axis with a step length of 16 arc secs through a 200 : 1 gearbox, while the whole camera can be rotated to choose the plane of dispersion without restriction. Further details of the double crystal camera can be obtained from Bowen and Davies[6].

Two types of experimental methods can now be followed:
a) one in which a monochromator or the beam conditioner described in Section 5.2 is used as the first fine axis of the DCC. We then have monochromatic plane wave synchrotron radiation topography,
(b) where a near perfect commercially available InP is used on the first fine axis. The situation is similar to the ordinary double crystal arrangement available with laboratory sources and shown in Figure 2.7. It can be seen that the first crystal does not act as a monochromator since the line source is not collimated. For a high resolution, the incident radiation must have an extremely low beam divergence, otherwise a point on the specimen crystal will result in being recorded as a line on the photographic plate depending upon the range of wavelengths getting through. In theory, an incident wave can only be approximated to a plane wave, if its divergence is much less than the width of the rocking curve of the crystal, which is about 5×10^{-5} radians. We therefore seek a source whose divergence is say about 5×10^{-6} radians or less. Laboratory sources of say 0.4mm source-width will have to be about 100 metres away from the experimental specimen to satisy this requirement. The intensity at this point is as such very much reduced. Hence for all practical purposes, for laboratory

sources, the divergence is limited to first being able to separate the $K\alpha_1$ and $K\alpha_2$ lines.

A very low divergence can however be obtained by the use of multiple crystal monochromators. For the synchrotron radiation source, the source size is 0.3mm at a distance of 60 metres; hence the divergence of the source as seen from a point on the specimen in the plane of dispersion is 5×10^{-6} radians. This is about an order of magnitude less than the rocking curve width. The synchrotron beam is as such very intense and the available intensity is concentrated within a small solid angle, with a vertical divergence of $\theta_v = 0.5$ mrad.

When a multilayer device is presented for defect analysis by X-ray methods and providing that the radiation is able to penetrate through all the layers, the Bragg condition would be simultaneously satisfied by any particular plane of reflection for different incident wavelengths, if the incident radiation is a white beam, and a topograph in such a situation would only give an overall picture of the whole multilayer structure. From this it would be difficult to predict the origin of any identified defects. Experimental methods with a double crystal camera eliminates the problem of separating the images of the substrate from that of the epitaxial layer.

In a typical experimental arrangement, shown in Figure 5.7, a white synchrotron beam A passes through a horizontal slit B and a vertical slit C and on to a beam conditioner or a reference InP crystal D mounted on the first axis of the goniometer of the

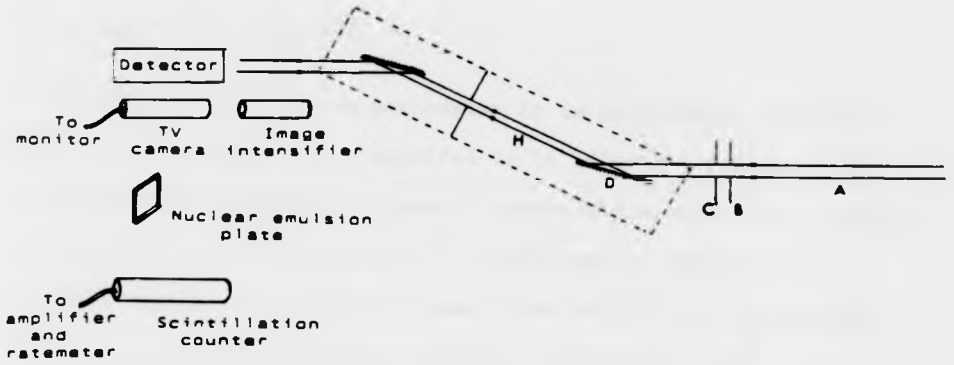

FIG 5.7 A sketch of a typical double crystal experimental arrangement.

double crystal camera. The slits B and C are only to localize the area on the specimen. If the reference crystal is a (100) InP, a 400 reflection is the most convenient to consider, as the structure factors are otherwise too low for a 200 reflection and zero for a 100 reflection. Furthermore the angular spread of double crystal rocking curves for higher order reflection is larger and therefore it is more convenient to separate the substrate and epilayer peaks in a rocking curve. The Bragg angle corresponding to a wavelength λ for a 400 reflection is

$$\theta_B = \mathrm{Sin}^{-1} (2\lambda/5.86875)$$

The reference crystal surface is aligned at an angle θ_B with respect to the incoming beam. If however, a silicon monochromator is mounted on the 1st axis, it is aligned for a 111 reflection at a wavelength λ, the Bragg angle for which is

$$\theta_B = \sin^{-1} (\lambda/6.27)$$

From the geometry of the goniometer it is possible to calculate the angle at which it is required to be adjusted to ensure that the diffracted component H heads towards the second axis. Mounted on this axis is the specimen. All the samples considered for double crystal analysis have been grown on (100) InP substrates. Hence a symmetric 400 double crystal arrangement in the (+, -) or the parallel setting is the most appropriate to consider for the present case. The specimen is now roughly adjusted to the required Bragg angle for a 400 reflection. It is now necessary to rotate the specimen about the initial setting in order to locate the substrate and epilayer peaks of the specimen. Adequate software routines have been provided to accurately control the rotation of the camera axes. A detecting system is now necessary to locate the position of the intensity maxima for the substrate and epilayers. These are described in the next section.

5.5. Detectors and Counters for topography and rocking curves

Detectors are needed to help find the diffracted beam and thereby adjust the specimen for the maximum intensity. Primary X-ray photon detectors are based on the principle of conversion of the X-ray photon into ionization in a gaseous, liquid or solid medium or into a number of low energy photons corresponding to visible or ultraviolet radiation. Gas filled counters are divided into ionization chambers, proportional counters and Geiger Counters.

The total energy in an X-ray photon, being large, can produce a large number of charged ion pairs in a gas filled counter and a still larger number in a Ge semiconductor detector. Phosphors which convert X-rays into visible radiation are convenient to use like NaI(Tℓ) used in scintillation counters and ZnS phosphors used in fluorescent screens as well as X-ray image intensifiers. Gas filled ionizations counters are rarely used in X-ray work, as they are not compact, and do not have a uniform absorption efficiency for all the X-ray wavelengths used in X-ray topography. A scintillation counter is generally considered best suited for topographic needs. These consist of a scintillator crystal which is sensitive to X-ray photons, along with a photomultiplier and produce a pulse proportional to the initial photon energy. A standard commercially available hermetically sealed NaI(Tℓ) scintillator crystal with Be windows facing the X-rays is used in the present experimental arrangement. The pulses from the detector must now be counted. The normal process is to pass the energy-proportional pulses through a pulse height analyzer to reject signals from X-rays of different wavelengths, then to a rate meter or a counter. A low detector background is necessary when looking for weak reflections, but a minimum background scatter from the specimen and from the air path of the X-ray beam is always likely to be present. By using a simple discriminator to cut off small pulses it is possible to reduce the background and improve the signal to background ratio by narrowing the window between the upper and lower discriminator levels, thereby shaping the pulse height distribution.

The probability of counting an average number of pulses N in a given time t is given by the Poisson's distribution

$$P(n) = \frac{N^n \exp(-N)}{n!}$$

where n is the actual number for an interval t. This distribution has a standard deviation $\sqrt{N}$, while the fractional precision in counts is given by $1/\sqrt{N}$. If counting losses due to the 'dead time' of the detector are large, serious error in the counting rates will occur. A scintillation counter has a typical dead time of 1 μsec compared to about 100 μsec for the Geiger counter. Locating the peak is a much easier job with a more efficient detector.

In the present experimental arrangement an image intensifier in combinations with a TV camera has been found to be very convenient for an initial location of the peaks on a TV monitor. It is necessary to open the slits to the size of the specimen. Once the peaks are located, the image intensifier and TV camera system is replaced by a scintillation counter for an accurate quantitative estimate of the counting rate, thus enabling a precise location of various peaks.

5.5.1. Plot of Rocking Curves

After the initial alignment and the location of the peaks for a particular hkl reflection from the specimen, extreme care is taken to reduce the background by providing lead shielding at appropriate places. A slit 100 x 500 μm is used to define a point on the specimen where rocking curves are taken. In some cases the beam conditions are such that the count rate is too low thus increasing

the counting time and hence the time for the experiment. In such cases the slit is slightly widened (100 μm x 1 mm) without much loss of resolution.

Adequate software routines have been provided to facilitate a quick setting up of the double crystal experiment including an automatic peak search routine, collection and display of counting data, followed by a plot of the rocking curve. A simple block diagram of the experimental system is shown in Figure 5.8. A pocket terminal

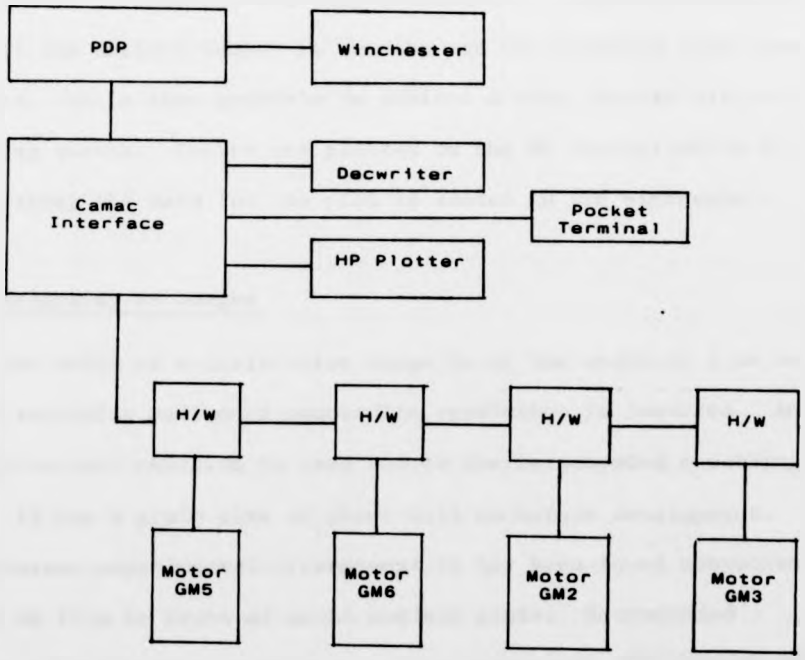

FIG 5.8 Block diagram of the control system for a rocking curve plot.

to control the movements of various stepper motors, an HP Plotter and a Decwriter are interfaced to the PDP through a CAMAC interface, while the stepper motors are connected through highway interfaces to a multiplexer. One single step on the stepper motor on the fine axis carrying the specimen corresponds to a rotation of 0.2 arc seconds, so the angular accuracy in the rocking curve plot is ± 0.1 arc seconds.

Software routines are provided for a counting accuracy that is basically determined by the counting precision needed for the plot. The total number of counts needed to achieve a certain precision can be calculated[7]. Photons are thus counted for a varying period of time until the desired number is counted and the counting rate then determined. It is thus possible to achieve a very precise plot of the rocking curves. Curves are plotted on the HP Plotter while at the same time, the data for the plot is stored in the Winchester.

5.5.2. Recording of Images

As the width of a dislocation image is of the order of 1 μm and above, a recording medium of comparable resolution is required. An Ilford L4 nuclear emulsion is used and is the recommended recording medium. It has a grain size of about 0.15 μm before development. In the present experimental arrangement it has been found convenient to use a D4 film in front of an L4 nuclear plate. Recommended thickness of the nuclear emulsion for the wavelength of interest is 25 μm. Processing instructions are given by Lang[8]. The basic steps for the processing are:

1. The developer 'D19' is used diluted (1 : 3).
2. The nuclear plate is soaked in water for a sufficient time for the emulsion to swell so that the developer can diffuse into it subsequently.
3. The plate is developed in a refrigerator maintained at 0^{o} - 5^{o}C. At higher temperatures, control of the development is difficult.
4. After developing the plate is kept in a stop bath for about 5 minutes and then fixed (Kodax fixer diluted 1 : 6) for at least 1½ times the time required to clear the emulsion.
5. The plate is subsequently washed for about 1 hour, and
6. Dried slowly at room temperature.

5.6. Discussion

Unlike the SEM, no magnification is possible while recording the topographs. The topographs can only be subsequently enlarged optically. Extreme care is taken in mounting the specimen so as to avoid tilt, and if detected, these are adjusted prior to recording the rocking curves and topographs. In recording topographs, a slit size not more than the size of the specimen is used, while for rocking curves slit sizes of 100 μm x 500 μm are normally used whereas in exceptional cases about 100 μm x (1-2)mm or so is allowed to define points on the specimen.

Some of the results of the experiment with various samples along with an interpretation of their rocking curves and topographs are presented in the next chapter.

References

1. LEA, K.R. and MUNRO, I.H., 'The Synchrotron Radiation Source at Daresbury Laboratory', Daresbury Laboratory Report, Warrington, U.K. (1980).

2. BONSE, U., In 'Characterization of Crystal Growth defects by X-ray methods' eds. Tanner B.K. and Bowen D.K., Chapter 11, New York, Plenum., 298 (1980).

3. HART, M. and RODRIGUES, A.R.D., 'Harmonic free single crystal monochromators for Neutrons and X-rays', J. Appl. Cryst., 11, 248 (1978).

4. HART, M., in 'Characterization of crystal growth defects by X-ray methods', eds. Tanner, B.K. and Bowen D.K., Plenum, New York, 241 (1980).

5. BOWEN, D.K., CLARK, G.F., DAVIES S.T., NICHOLSON, J.R.S., ROBERTS, K.J., SHERWOOD, J.N. and TANNER, B.K., 'The X-ray topography station at Daresbury Laboratory', Nucl. Instr. and Methods, 195, 227 (1982).

6. BOWEN, D.K. and DAVIES, S.T., 'The double crystal X-ray camera at Daresbury Laboratory', Nucl. Instr. and Meth., 208, 725 (1983).

7. BOWEN, D.K. and HALL, C.R.,'Microscopy of Materials', Macmillan, London, 86 (1975).

8. LANG, A.R., in 'Modern diffraction and imaging techniques in material science', eds. Amelinckx, S., et al, North Holland, Amsterdam, 407 (1970).

9. HART, M., 'Synchrotron radiation - its application to high speed, high resolution X-ray diffraction topography', J. Appl. Cryst., 8, 436 (1975)

6

DOUBLE CRYSTAL ROCKING CURVES AND TOPOGRAPHS OF OPTO-ELECTRONIC DEVICES AND MULTILAYER STRUCTURES AND THEIR INTERPRETATION

6.1. Introduction

Details of a typical double crystal experimental set up were discussed in the previous chapter. In this chapter, we will analyze some of the experimental results that were obtained on a wide variety of specimens.

6.2. Characteristics of the Silicon Monochromator

The silicon monochromator was meant to deliver a monochromatic plane wave to be incident on the specimen. It was therefore found essential to study the topographic features of the monochromator. Features of a double crystal topograph of a specimen essentially includes that of the monochromator or a reference crystal used on the first axis of the double crystal camera. A topograph of a 111 reflection from the monochromator set for 1Å, did not apparently show any feature but when highly magnified, showed fine grains running horizontally (Figure 6.1). The grains are too closely

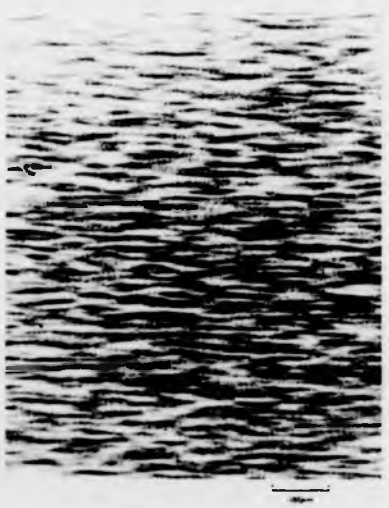

FIG 6.1 Topograph of the silicon monochromator aligned for 111 reflection at 1.0 A wavelength.

6.1. Introduction

Details of a typical double crystal experimental set up were discussed in the previous chapter. In this chapter, we will analyze some of the experimental results that were obtained on a wide variety of specimens.

6.2. Characteristics of the Silicon Monochromator

The silicon monochromator was meant to deliver a monochromatic plane wave to be incident on the specimen. It was therefore found essential to study the topographic features of the monochromator. Features of a double crystal topograph of a specimen essentially includes that of the monochromator or a reference crystal used on the first axis of the double crystal camera. A topograph of a 111 reflection from the monochromator set for 1Å, did not apparently show any feature but when highly magnified, showed fine grains running horizontally (Figure 6.1). The grains are too closely

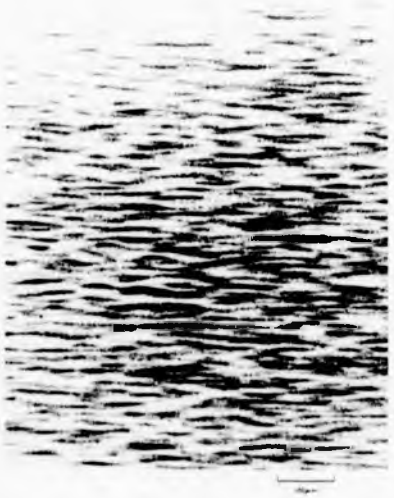

FIG 6.1 Topograph of the silicon monochromator aligned for 111 reflection at 1.0 A wavelength.

spaced for the nuclear plate to resolve. Deterioration of the surface requiring a polishing of the crystals is thought of as one of the reasons for this effect, as the monochromator had been in constant use. Surface damage due to beam heating is also a possibility. The monochromator has a fairly complicated design and has been built with precision engineering. It was therefore not possible to dismantle the crystals easily for etching purposes. This has however been planned for the near future. A double crystal topograph obtained using the monochromator as the first crystal would therefore show these grains on top of the topographic features for the specimen, and one has to take due account of this when interpreting such a double crystal topograph.

6.3. Experimental results

A light emitting diode, VS296A (Figure 6.2), was one of the first specimens chosen for the double crystal experiment. The first crystal was a Si monochromator. Both the monochromator and the specimen were aligned for an incident wavelength 1.0Å and for a 400 reflection from the specimen. Two peaks were observed and

GaInAsP cap	~ .25 μm
p-InP	~ 1 μm
GaInAsP active	~ 2 μm
n-InP	~ 2 μm
InP substrate	

FIG 6.2 A schematic diagram of the light emitting diode, VS 296A

topographs were taken in the vicinity of the peaks. Since the active layer is of comparable thickness with respect to the InP layers, reflection from the quaternary layers on the whole, will be equally comparable, if one neglects absorption effects. Relative thickness of the quaternary layers in comparison with the InP layer participating in the reflection will depend on the penetration depth of X-rays, discussed in Chapter 4. The ratio of the integrated intensity of the quaternary and InP peaks in a rocking curve will give an approximate estimate of the relative layer thicknesses of the two materials. If the penetration depth for the wavelength and reflection concerned is determined, the peaks can be identified. In Chapter 10, a method for a theoretical calculation of rocking curves has been discussed in detail, using which, an experimental rocking curve can be simulated and the exact layer thickness determined. The extinction depth is typically 5-10 μm, for InP, hence for thin active layers, the quaternary peak can be identified straight away. In this case, for the specimen VS296A, the quaternary peak was located at a higher Bragg angle than the InP peak, or in other words, the quaternary layer lattice mismatch is negative. Double crystal topographs corresponding to the InP and quaternary peaks were taken with the specimen positioned in two perpendicular directions.

These are shown in Figures 6.3 and 6.4. Both the figures clearly show a cross-hatch pattern of misfit dislocations in their corresponding quaternary topographs, (Figures 6.3b and 6.4b) whereas they are less prominent on the InP topographs (Figures 6.3a and 6.4a).

(a) Topograph corresponding to the InP peak

1 mm

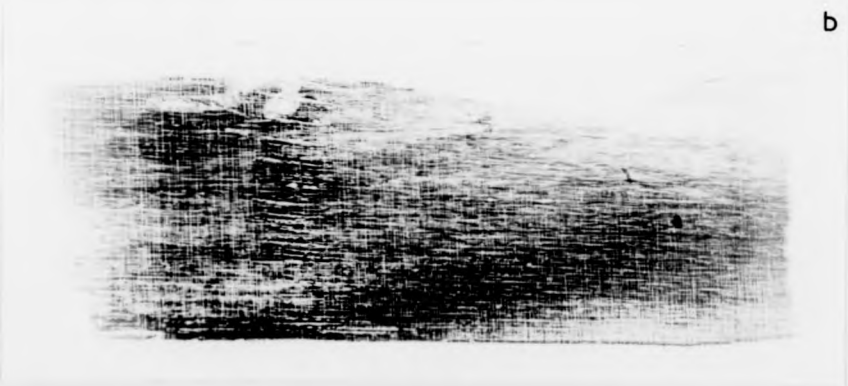

(b) Topograph corresponding to the quaternary layer peak.

1 mm

FIG 6.3 Double crystal reflection topographs for the specimen VS 296A. Wavelength : 1.0 A, 400 reflection.

a

(a) Topograph corresponding to the InP peak

1 mm

b

(b) Topograph corresponding to the quaternary layer peak.

1 mm

FIG 6.3 Double crystal reflection topographs for the specimen VS 296A. Wavelength : 1.0 A, 400 reflection.

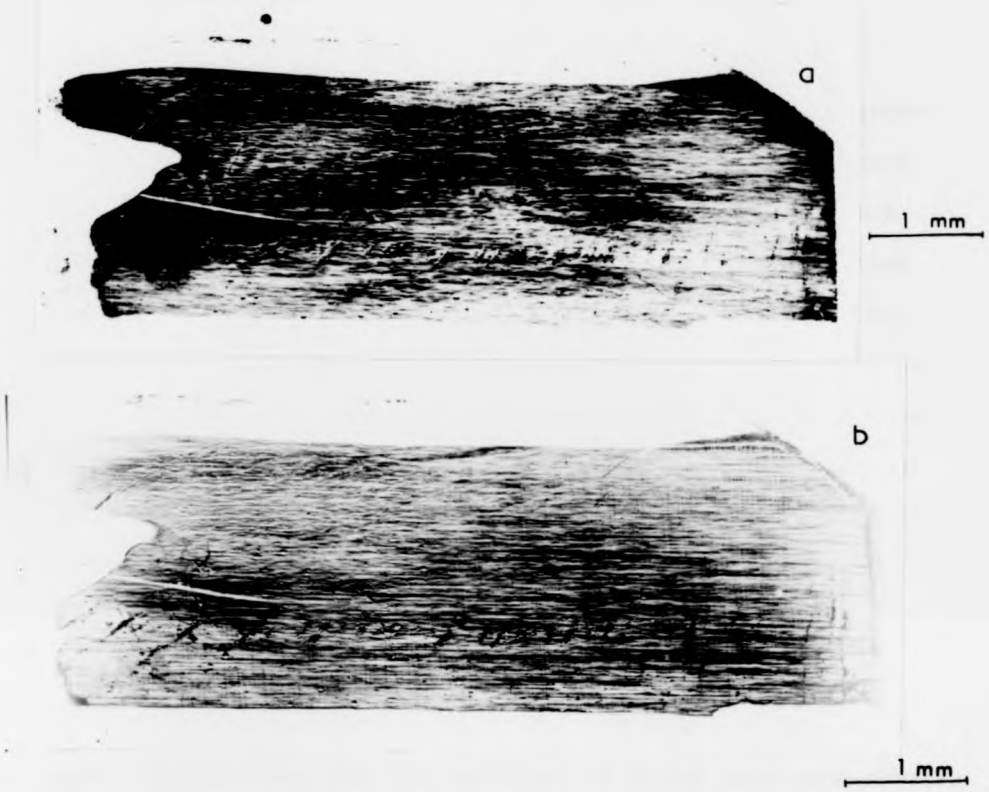

FIG 6.4 (a) InP and (b) quaternary topographs of the specimen VS 296A rotated 90 degrees in its plane. 1.0 A wavelength, 400 reflection.

FIG 6.5 White radiation topograph of the InP reference crystal, 400 reflection

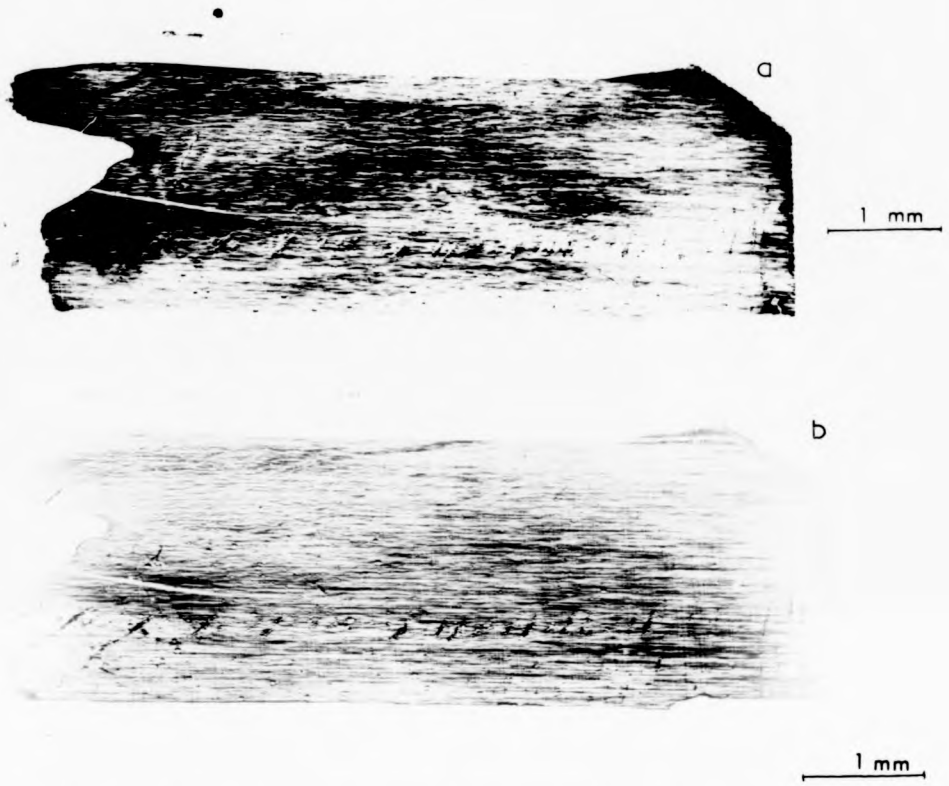

FIG 6.4 (a) InP and (b) quaternary topographs of the specimen VS 296A rotated 90 degrees in its plane. 1.0 A wavelength, 400 reflection.

FIG 6.5 White radiation topograph of the InP reference crystal, 400 reflection

Some scratch marks on the specimen have appeared on the topographs as a series of contrasting features running vertically in Figure 6.3 and horizontally in Figure 6.4. Some growth striations are detected in the Figure 6.4a. The double crystal method has thus made it possible to separate the images from the quaternary and InP layers. The topographs of Figure 6.3b and 6.4b correspond to a combined effect of the active and capping layers, since in this case, only one quaternary peak was observed. Similarly the other two topographs of Figures 6.3a and 6.4a are representative of the layers n-InP, p-InP and InP substrate.

Separation of images from each quaternary layer would be possible if they had different lattice mismatch. The peak separation as observed using an ionization chamber to locate the peaks in this case, had been estimated as 92 arc secs corresponding to a mismatch m = 1240 ppm approximately.

In a separate experiment, using an InP first crystal and aligned for 400 reflection at 1.5Å wavelength, a double crystal rocking curve at a point on the specimen VS296A was plotted. The InP reference crystal had been considered to be near perfect. Figure 6.5 shows a white radiation topograph of the reference crystal for a 400 reflection. The topograph is almost uniform with negligible features. The double crystal rocking curve for the specimen, shown in Figure 6.6 indicates a peak separation of about 141 arc seconds corresponding to a lattice mismatch of 1190 ppm. The quaternary peak width is about 36 arc seconds while that of InP is about 53 arc seconds. The wide InP peak indicates that the

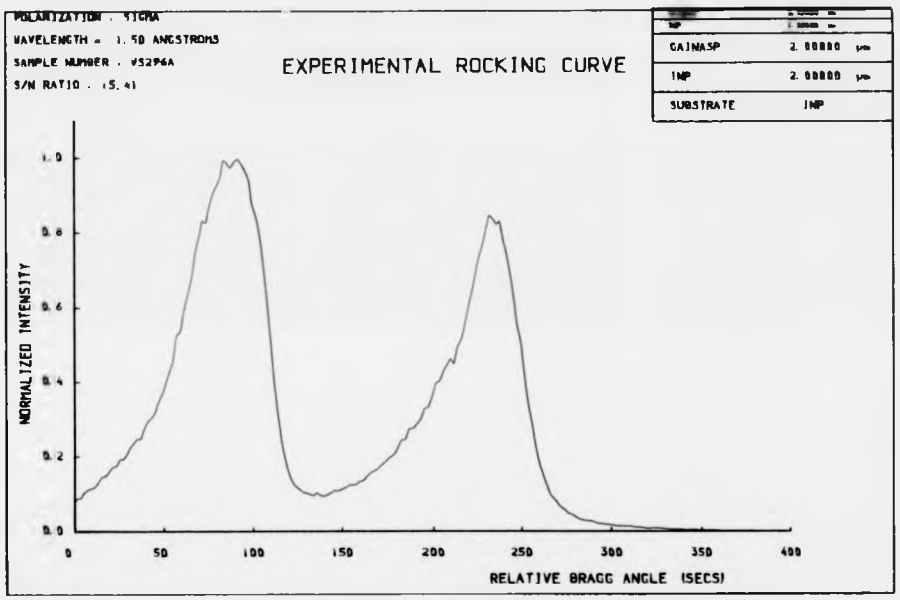

Figure 6.6. Double crystal rocking curve for the specimen VS296A. First axis : InP, 400 reflection and slit size : 100µm x 2mm

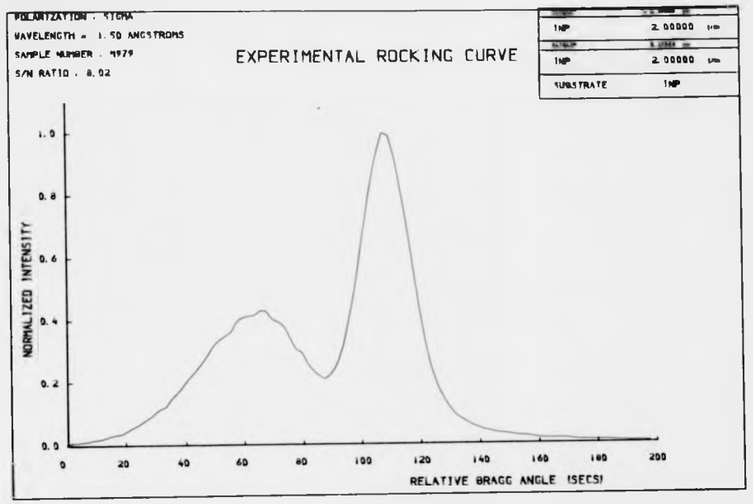

Figure 6.7

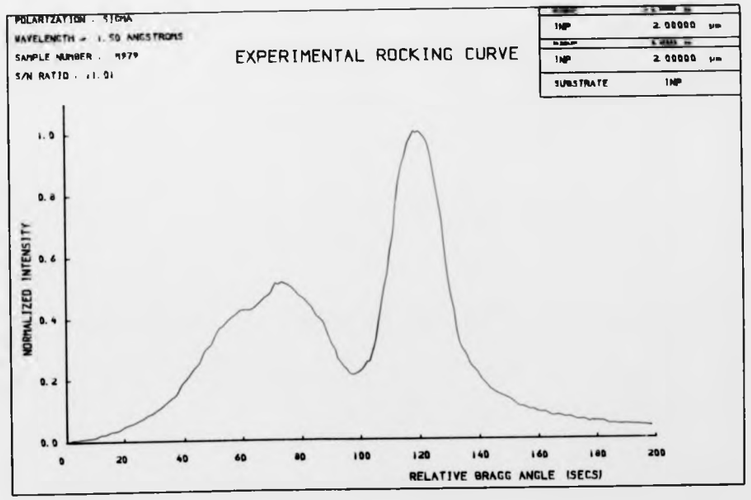

Figure 6.8

specimen is probably curved. A 100 μm x 2mm horizontal slit was used in the rocking curve measurements. If the sample is curved vertically then a wide rocking curve is expected due to a finite beam size. The curvature may be due to the high amount of lattice mismatch introduced in the quaternary layers.

Both the silicon monochromator and an InP reference crystal had been used to plot double crystal rocking curves. A comparison of the rocking curves for a 400 reflection from a specimen obtained by using a Silicon monochromator as well as an InP reference crystal is made from Figure 6.7 and Figure 6.8. The specimen was a double heterostructure laser, M979. Layer characteristics of the specimen as reported by Plessey are shown in Figure 6.9. The incident wavelength was 1.5Å. An aperture of 100 μm x 500 μm was used to define a point on the specimen.

GaInAsP cap	> 0.3 μm
p-InP	~ 2 μm
GaInAsP active	~ .25 μm
n-InP	~ 2 μm
InP substrate	

FIG 6.9 Schematic diagram of a double heterostructure laser, M979

The peak widths and peak heights as well as the peak separation are compared in Table 6.1.

Table 6.1 Comparison of rocking curve characteristics for a double heterostructure laser for different incident beam wavelengths and different reference crystals on the first axis of the double crystal camera.

First Crystal	Wave length Å	Quaternary Layer		InP			Mismatch (ppm) m
		Peak height (arbitrary)	Peak width arc secs	Peak height (arbitrary)	Peak width arc secs	Peak separation arc secs	
Silicon Monochromator	1.5	0.4	46	1	20	41.6	350
InP	1.5	0.51	47.9	1	21.5	46.1	375
Silicon Monochromator	1.8	0.34	48	1	35.1	57	356

The quaternary peak is wider and bigger with the InP first crystal than with the silicon monochromator. Using a silicon monochromator in the double crystal arrangement, we can assume that the beam incident on the specimen is a monochromatic plane wave. Accordingly the rocking curve for the specimen should be similar to the Darwin-Prins curve. Compared with an ordinary double crystal arrangement, the rocking curve width using the Silicon monochromator is about a factor of 1.32 lower than the peak width for the ordinary double crystal arrangement in the parallel setting[1]. This holds for small glancing angles, less than about 10°. At larger glancing angles, the ratio of the peak widths becomes less than 1.32. A comparison of Figures 6.7 and 6.8 shows that the peak widths of the quaternary and InP layers in Figure 6.7 are only slightly narrower than the corresponding quantities for

Figure 6.8 by a factor of 1.05. In Chapter 7 the effect of inhomogeneity and non uniformity of a specimen on rocking curves is discussed. We shall later see that under identical conditions, different positions on the specimen show different rocking curve characteristics, due to compositional and thickness variation of the active or the cap layer. Hence the difference shown in Table 6.1 may not be entirely due to a different reference crystal. A comparison of rocking curves for a point on the specimen for two different incident wavelengths can be made from Figures 6.7 and 6.10. The silicon monochromator was used on the first of the double crystal camera. The peak separation increases with wavelength of the incident beam, as expected, but the derived lattice mismatch is similar. Results of the comparison are also shown in Table 6.1.

Rocking curves and topographs from a set of three edge emitting LED structures similar to that shown in Figure 6.9 but which had ceased to operate were compared to see of there was any correlation with their degradation. Double crystal rocking curves for a 400 reflection from the three specimens M952, M949 and M777 were plotted for an incident wavelength 1.5Å and with a silicon monochromator on the first axis of the double crystal camera. These are shown in Figure 6.11. The rocking curve of Figure 6.11a corresponding to M952 shows two peaks. The quaternary peak appears to be graded in mismatch. Detailed discussion on the effect of grading on a rocking curve shape is discussed in Chapter 10. The mismatch is positive. Figures 6.11b and 6.11c corresponding to specimens M949

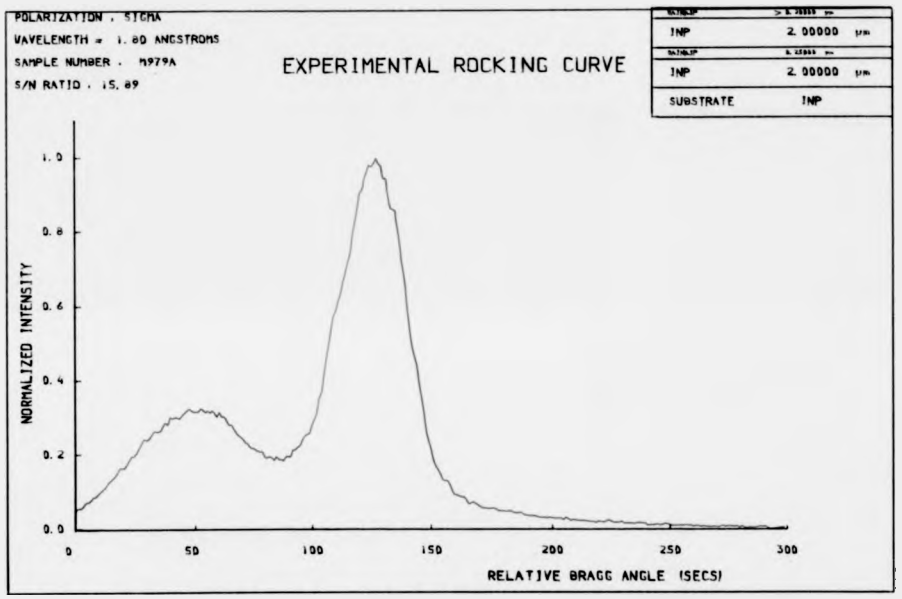
POLARIZATION : SIGMA
WAVELENGTH = 1.80 ANGSTROMS
SAMPLE NUMBER . M979A
S/N RATIO . 15.89
EXPERIMENTAL ROCKING CURVE
INP 2.00000 µm
INP 2.00000 µm
SUBSTRATE INP
NORMALIZED INTENSITY
1.0
0.8
0.6
0.4
0.2
0.0
0
50
100
150
200
250
300
RELATIVE BRAGG ANGLE (SECS)

Figure 6.10

(a) specimen M952 shows a quaternary layer peak whose mismatch is graded and is positive.

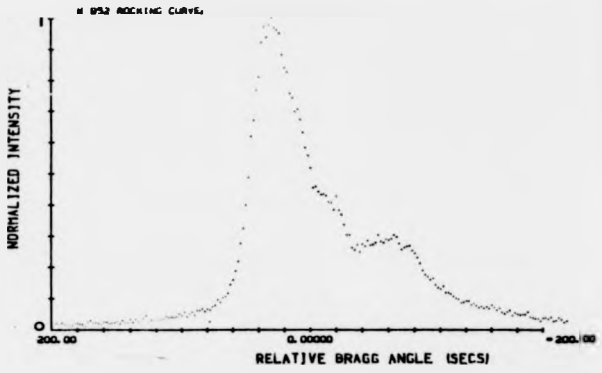

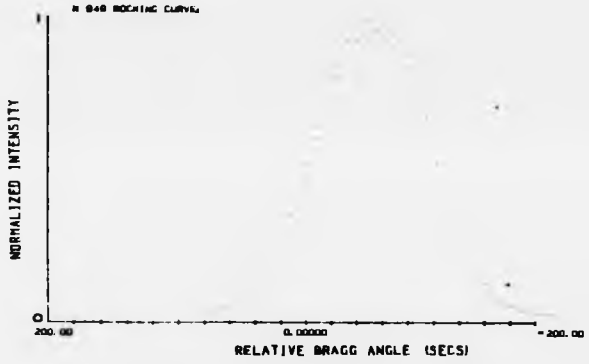

(b) specimen M949 shows only one peak and is therefore lattice-matched. The peak is however broad.

(c) specimen M777 also shows only one peak but the peak is much narrower.

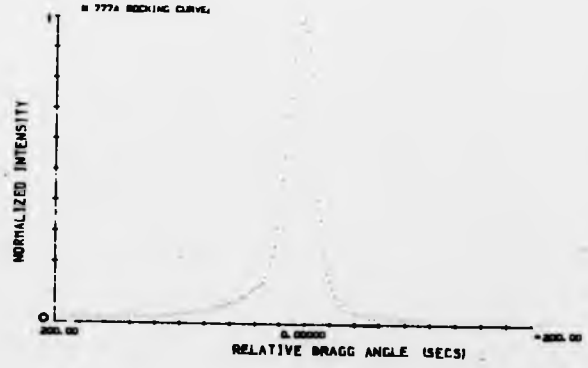

FIG 6.11 Double crystal rocking curves for a set of three edge emitting LEDs that had shown degradation effects. First crystal : Si monochromator. Input wavelength: 1.0 A. Slit size : 100μmx500μm.

and M777 show only one peak. The peak for M979 is broad while the other peak is much narrower. The peak width, peak separation and the mismatch for the three specimens are tabulated in Table 6.2.

Table 6.2 Comparison of InP and quaternary layer characteristics for a set of three edge emitting LEDs from their corresponding rocking curves of Figure 6.11.

Specimen	Peak height arbitrary		Peak width arc secs		Peak separation arc secs	Mismatch m (ppm)
	InP	Quaternary	InP	Quaternary		
M952	1	0.3	20	60	93	760
M949	1	-	70	-	-	-
M777	1	-	20	-	-	-

The rocking curve of M777 shows a better characteristic than those of the other two specimens. In Figure 6.12, double crystal topographs of the three specimens are compared. Figures 6.12a and 6.12b correspond to the InP and quaternary peak positions respectively of specimen M952 while Figures 6.12c and 6.12d correspond to the only peak observed for the other two specimens. The topographs of Figure 6.12a and 6.12b do not apparently show any cross hatch pattern. Scatter from a patch of Indium sticking on a small portion of the specimen results in a blurred image on the topograph corresponding to that region. There are however some fine features running horizontally along the specimen as well as inclined across the

(a) Topograph of the InP peak for M952

(b) Topograph of the quaternary peak for M952

(c) Topograph of the only observed peak for M949

(d) Topograph of the only observed peak for M777

FIG 6.12 Double crystal topographs for the three specimens M952, M949 and M777. Wavelength : 1.0 A, 400 reflection, First axis: silicon monochromator.

(a) Topograph of the InP peak for M952

(b) Topograph of the quaternary peak for M952

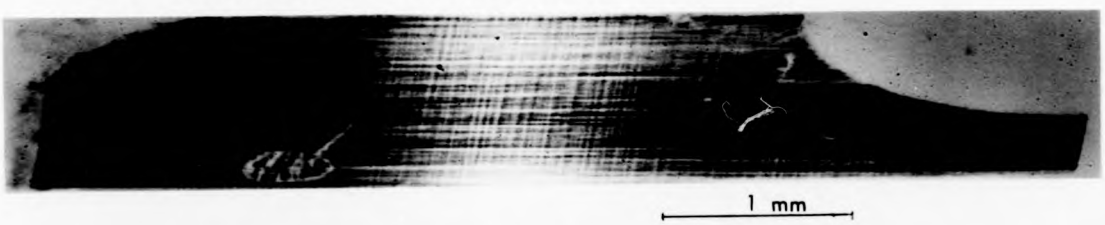

(c) Topograph of the only observed peak for M949

(d) Topograph of the only observed peak for M777

FIG 6.12 Double crystal topographs for the three specimens M952, M949 and M777. Wavelength : 1.0 A, 400 reflection, First axis: silicon monochromator.

specimen in both the topographs. The effect of the silicon monochromator topograph of Figure 6.1 is however not likely to cause features as prominent as in Figures 6.12a and 6.12b. The topograph of Figure 6.12a and 6.12b can be considered as due mainly to the specimen, with very little of the monochromator contribution. The topograph about the only peak observed in M949 shows a distinct cross hatch pattern of misfit dislocation while that of M777 shows a comparatively better topograph. The fine structures running horizontally all over the topograph in Figure 6.12d are probably due to the Silicon monochromator. It is interesting to note that the topograph of M949 (Figure 6.12c) shows a prominent misfit dislocation network while its corresponding rocking curve shows only one single peak, which is however, very broad. Jesser and Kuhlmann-Wilsdorf[2] have shown that the generation of interfacial misfit dislocations depends on both the lattice mismatch and the layer thickness under a fixed starting growth temperature. From among a series of experiments performed on a wide variety of specimens with different layer thicknesses and mismatch, Nakajima et al[3] were able to determine the conditions for the growth of thick layers without misfit dislocations. Their experimental result is shown in Figure 6.13. For thick layers to be free from misfit dislocations, they must have a negative lattice mismatch at room temperature, so that the differential thermal expansion coefficient of the lattice for InP and InGaAs/InGaAsP would make the layer lattice matched at the growth temperature of about 650^{o}C. For thin layers of 0.4 μm, Oe et al[4] reported

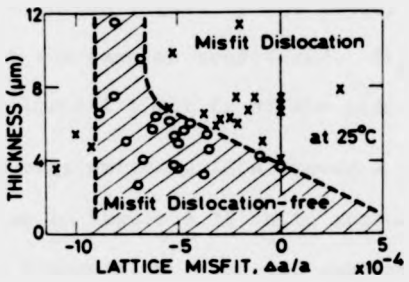

FIG 6.13 Limiting regions for the lattice mismatch and active layer thickness for initiation of misfit dislocations at the interface. Data points o and x are due to Nakajima et al (3) for several GaInAs/InP single layer specimens of different thicknesses. The misfit dislocation-free region is shown by the shaded region.

that misfit dislocations were not found if $\Delta a/a$ was between + .005 and - .005. From the topograph and rocking curve of Figure 6.12c and 6.11b respectively we find that there are misfit dislocations, but room temperature lattice mismatch is zero. Comparing with Figure 6.13 we find that the layer has to be moderately thick for this purpose. The thickness of either the active layer or the cap layer must have been larger than the estimated values. If the active layer thickness increases even slightly, the threshold current density rises leading to degradation. In any case, degradation effects in two of the three samples considered namely M949 and M952 can be linked to topographs with misfit dislocations.

Figure 6.14 shows a rocking curve for a single quaternary layer specimen R296A plotted for a 400 reflection at 1.5Å. The layer is approximately 1 μm thick. The corresponding layer mismatch as measured from the rocking curve is about 220 ppm, which, incidentally has been the lowest mismatch detected, other than

zero. The above quoted figure is the lowest non-zero mismatch that was available in the samples considered. Figure 6.14 shows that the actual experimental limit is of the order of 100 ppm.

One of the edge emitting LEDs showed a rocking curve characteristic as in Figure 6.15 while another had a nature of variation as in Figure 6.16. The two smaller peaks in Figure 6.16 are due to the different mismatch characteristics of the active and cap layers (they are probably graded as well). One of the layers thus has a positive mismatch while the other a negative mismatch. The nature of Figure 6.15 indicates that the two minor peaks probably correspond to layers with different positive mismatch parameters.

Discussion

The double crystal method is thus extremely powerful in providing a lot of information about the characteristics of the layer and the substrate. This non-destructive method can separate images of the layer from the substrate, thereby identifying the location of any defects. Accurate lattice parameter mapping is possible from the precision plot of rocking curves. A lattice mismatch as low as m = 220 ppm has been detected. The actual experimental limit this set up can provide, is about 100 ppm; the method is however capable of mapping lattice parameter changes of the order of 10^{-8}. In the forthcoming chapters a variety of experiments are performed to assess the homogeneity and uniformity of the layers grown by LPE.

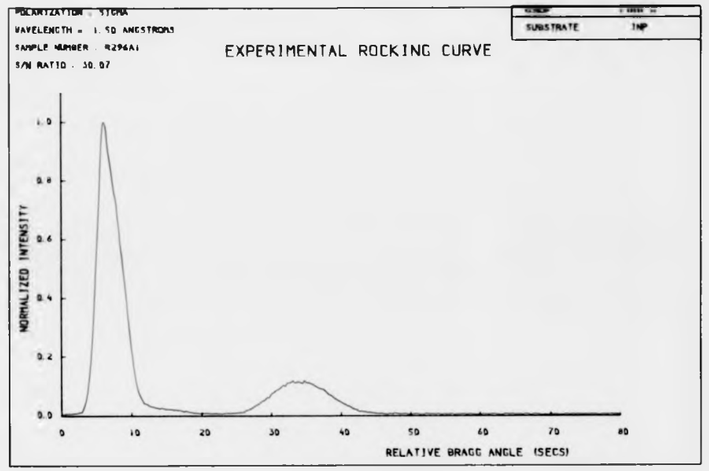

Figure 6.14

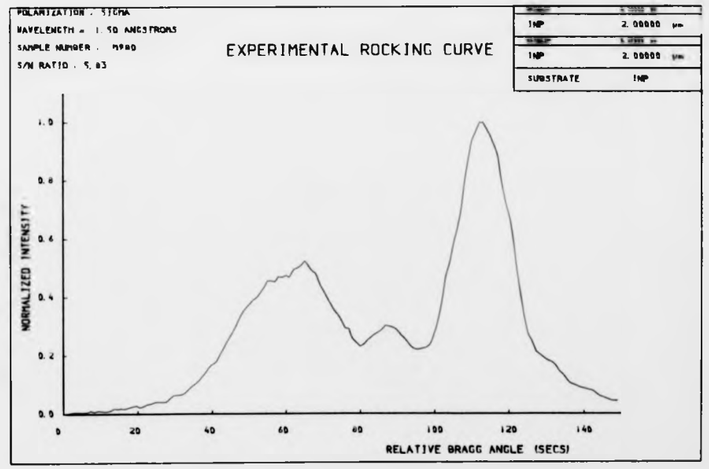

Figure 6.15

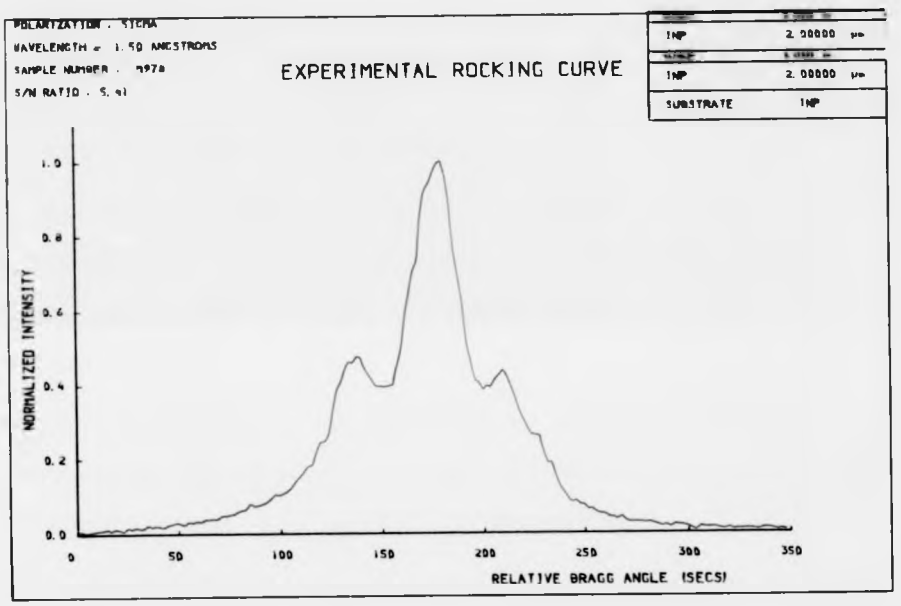
POLARIZATION . SIGMA
WAVELENGTH = 1.50 ANGSTROMS
SAMPLE NUMBER . 7978
S/N RATIO . 5.41
EXPERIMENTAL ROCKING CURVE
INP 2.00000 μm
INP 2.00000 μm
SUBSTRATE INP
NORMALIZED INTENSITY
1.0
0.8
0.6
0.4
0.2
0.0
0
50
100
150
200
250
300
350
RELATIVE BRAGG ANGLE (SECS)

Figure 6.16

References

1. COMPTON, A.H. and ALLISON, S.K., 'X-rays in theory and Experiment', Van Nostrand (1963).

2. JESSER, W.A. and KUHLMANN-WILSDORF, 'On the theory of interfacial energy and elastic strain of epitaxial overgrowths in parallel alignment on single crystal substrates', Phys. Stat. Sol. 19, 95 (1967).

3. NAKAJIMA, K., KOMIYA, S., AKITA, K., YAMAOKA, T. and RYUZAN, O., 'LPE growth of misfit dislocation-free thick $In_{1-x}Ga_xAs$ layers on InP', J. Electrochem. Soc., 127, 1568 (1980).

4. OE, K., SHINODA, Y. and SUGIYAMA, K., 'Lattice deformations and misfit dislocations in GaInAsP/InP double heterostructure lasers', Appl. Phys. Lett., 33, 962 (1978).

7

AREA SCANNING OF ROCKING CURVES

TO ASSESS EPILAYER PROPERTIES

7.1. Introduction

Liquid phase epitaxial growth of InGaAsP/InP multilayer structures for LEDs and lasers require that the active layer be lattice-matched to the InP substrate. The solid composition $In_{1-x}Ga_xAs_{1-y}P_y$ required for the lattice-match could be achieved by choosing the correct melt composition in the graphite boat prior to initiating epitaxial growth. As mentioned in Chapter 3, the surface degradation of InP substrates in the growth reactor prior to epitaxy prevents high quality layers being grown directly on InP substrates. Since the dissocation pressure of InP is high[1] at typical growth temperatures, the InP substrates become thermally etched by the vapourization of P. Growth of GaInAsP on a thermally etched InP surface produces local variations in composition and the resulting variations in lattice constant lead to the formation of misfit dislocations. A number of techniques have generally been used in an attempt to prevent surface degradation of InP substrates, but these do not eliminate the problem altogether. Even if the lattice misfit is nearly zero, it has been found that thick quaternary layers are difficult to grow on (100) InP, with the surface becoming very uneven due to the depletion of P in solution near the growing interface. Secondly, for active layers as thin as 0.2μm, typical growth times are of the order of a few seconds. The controlled growth of sub-micron layers is also an important problem. There is thus an urgent requirement for methods to ascertain that compositional and thickness variations of the epitaxial layer are within specified tolerances. In the next

section, an experimental procedure is described that enables rocking curves to be automatically recorded at various positions on the specimen. A comparison of the rocking curves at various points would provide an assessment of the relative layer thickness, while the shape and width of the epilayer peak would provide information regarding compositional variations at those points. Two specimens were chosen for this purpose.

7.2. A double heterostructure laser, specimen M979

7.2.1. Experimental Procedure

The specimen chosen for investigation is shown schematically in Figure 7.1a. Scanning of the specimen is achieved by placing

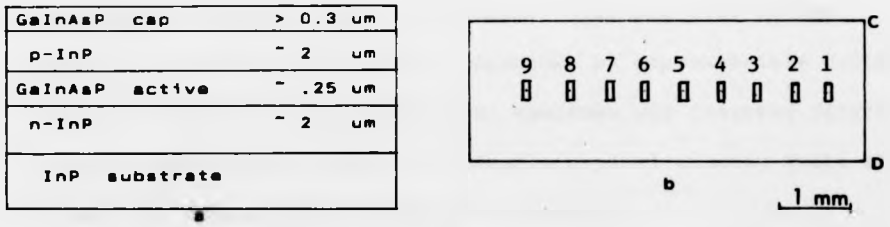

FIG 7.1 (a) Schematic diagram of a double heterostructure laser, M979
(b) Positions on the top surface of the specimen where rocking curves were recorded

the specimen on an XY translation stage, made by Bede Scientific Instruments, and is as shown in Figure 7.2. This 'area scan' goniometer, has stepper motors, enabling the specimen, when placed over the platform A, to move in two perpendicular directions. The stepper motor used in the area scan goniometer

FIG 7.2 X-Y translation and tilting stage used for scanning the specimen area. The specimen is placed on the translation table A. X-Y translation is achieved by the stepper motor and micrometer combination (S1,C1) and (S2,C2) respectively, while tilting is achieved by (S3,Z) through a gear box G. The spindle T slots into the second axis of the double crystal camera.

to displace the specimen along its length AD makes 48 steps per revolution and drives a micrometer C1 which displaces the specimen by 0.5mm for each revolution. Thus one step on the stepper motor would displace the specimen by approximately 0.01mm. The translation stage, carrying the specimen was inserted directly into the second fine axis of the double crystal camera, while the first axis carried the silicon monochromator.

For convenience in the initial location of the peak, it is preferable to have the detector as close to the specimen as possible. In the present case, since the specimen was too small compared to the translation stage platform, and since this stage has stepper motors located at its sides, the detector could not be brought very close to the specimen, unless the detector was at a sufficiently high enough angle.

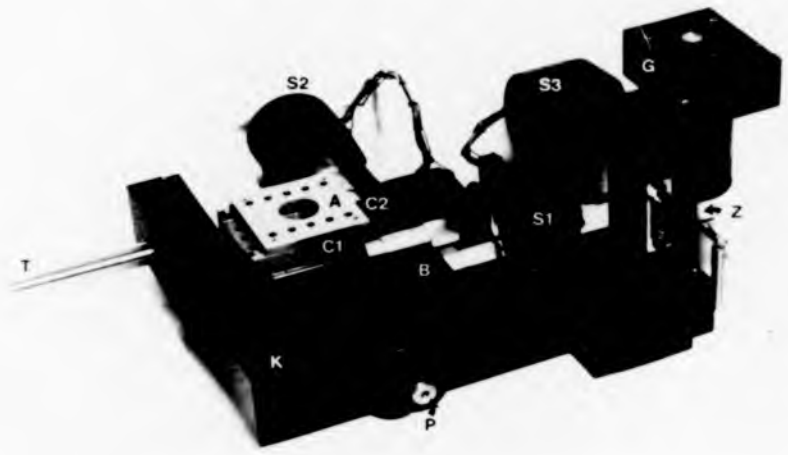

FIG 7.2 X-Y translation and tilting stage used for scanning the specimen area. The specimen is placed on the translation table A. X-Y translation is achieved by the stepper motor and micrometer combination (S1,C1) and (S2,C2) respectively, while titling is achieved by (S3,Z) through a gear box G. The spindle T slots into the second axis of the double crystal camera.

to displace the specimen along its length AD makes 48 steps per revolution and drives a micrometer C1 which displaces the specimen by 0.5mm for each revolution. Thus one step on the stepper motor would displace the specimen by approximately 0.01mm. The translation stage, carrying the specimen was inserted directly into the second fine axis of the double crystal camera, while the first axis carried the silicon monochromator.

For convenience in the initial location of the peak, it is preferable to have the detector as close to the specimen as possible. In the present case, since the specimen was too small compared to the translation stage platform, and since this stage has stepper motors located at its sides, the detector could not be brought very close to the specimen, unless the detector was at a sufficiently high enough angle.

For a 400 reflection, the Bragg angles for InP are

19.92^{o} for $1.0\mathring{A}$

30.74^{o} for $1.5\mathring{A}$

37.83^{o} for $1.8\mathring{A}$

It was found that the detector could be satisfactorily positioned for an input wavelength of $\lambda = 1.8\mathring{A}$ corresponding to an inclination of $2\theta_B = 75.6^{o}$ for the detector, with respect to the direction of the incident beam. For the initial alignment, the camera GM2 was set at an angle 4.69^{o} from the horizontal and the Si-monochromator at an angle 16.88^{o} with respect to the incident beam.

The usual method of placing a polaroid film behind the specimen to assess the location of the incoming beam, could not be employed. Therefore, to check the initial alignment an Industrex film was placed on the platform instead of the specimen, the beam was reduced to the size of the specimen by means of a slit and the film exposed for one minute. The spot when the beam was incident on the translation stage platform was identified and the specimen placed on that spot.

Since the specimen consists of layers of GaInAsP grown over InP, at least two peaks are expected to be observed, unless the quaternary layers are perfectly lattice matched to InP.

After the initial alignment, the specimen surface was roughly adjusted to be at about 38^{o} with respect to the incoming beam and the Image Intensifier/TV camera aligned at an angle of 76^{o} to

receive the reflected beam and placed as close to the specimen as possible. The fine axis goniometer of the double crystal camera, carrying the specimen on the translation stage was slowly rotated until the two rocking curve peaks were located. A 100μm vertical slot was then introduced in the main beam and positioned to be approximately at the mid section of the specimen. The Image Intensifer/TV camera was replaced by a scintillation counter and the presence of the peaks was verified. The stepper motor on the XY stage which displaced the specimen was slowly rotated in small regular steps and the peaks were monitored at the end of each interval, until one edge of the specimen was reached (edge DC). The specimen was next moved in the opposite direction in steps of 0.5mm. Thus nine points on the specimen were made available (Figure 7.1b) and the rocking curve plotted for each position. The counting routine employed for plotting rocking curves was a constant time count with a counting time of one second. The set of rocking curves so obtained are shown in Figure 7.3. The heights, half-widths and separation of the peaks of both the InGaAsP and InP layers are tabulated in Table 7.1. There are however two quaternary layers in the specimen, one being the active layer and the other the capping layer. The secondary peak observed in Figure 7.3 could be due to either the capping layer alone (in which case, the active layer is probably lattice matched) or the active layer alone (in which case the capping layer is probably lattice matched) or both. In Chapter 10, a theoretical calculation of rocking curves from ternary and

The various positions for rocking curves are indicated in Figure 7.1b

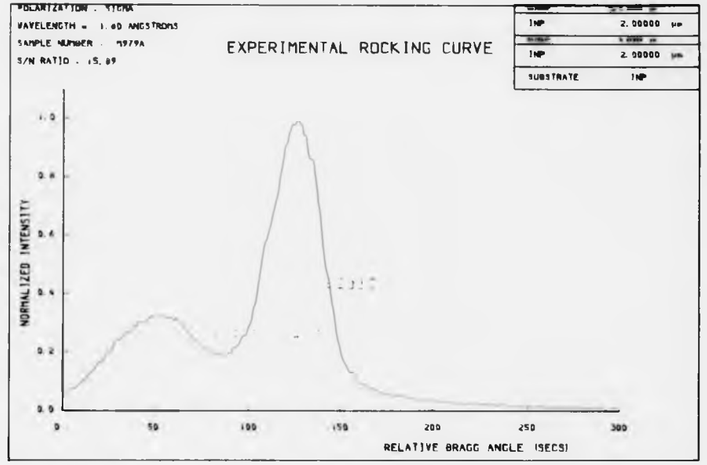

Figure 7.3a

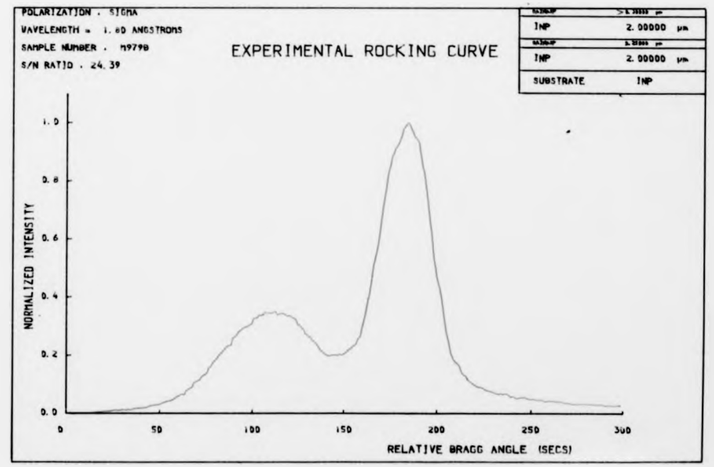

Figure 7.3b

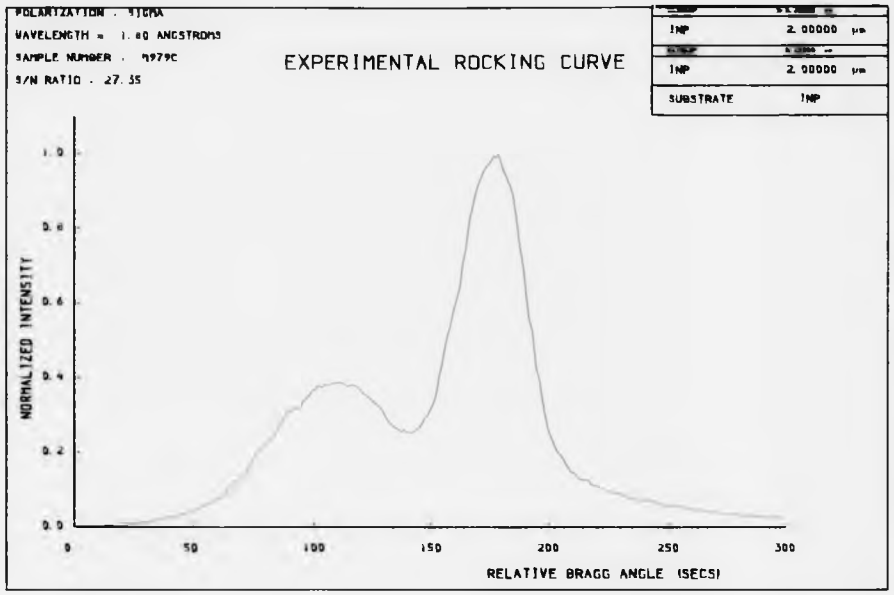

Figure 7.3c

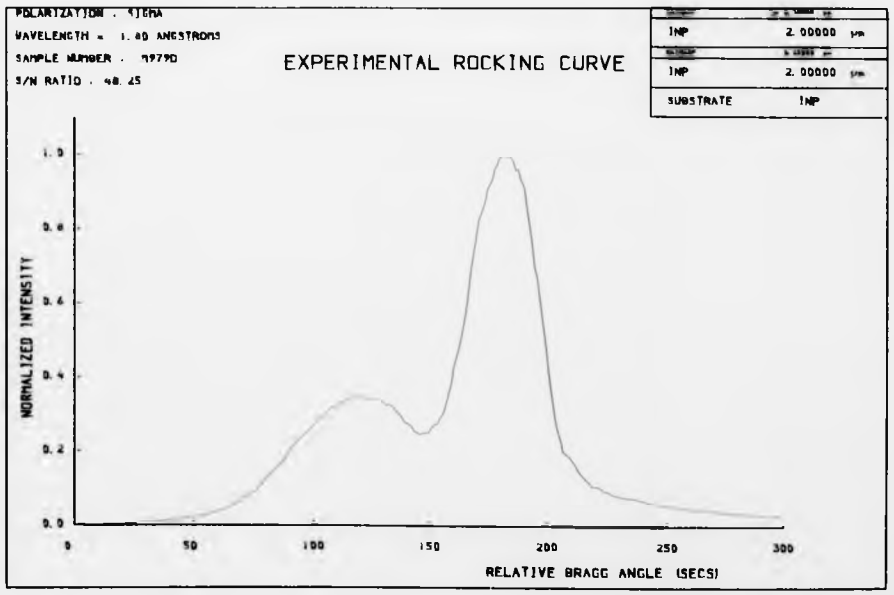

Figure 7.3d

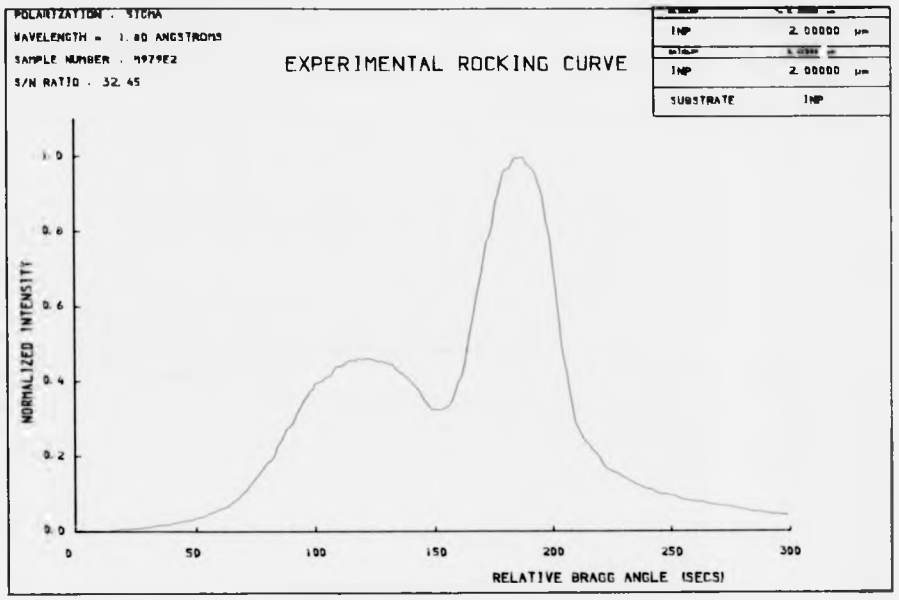

Figure 7.3e

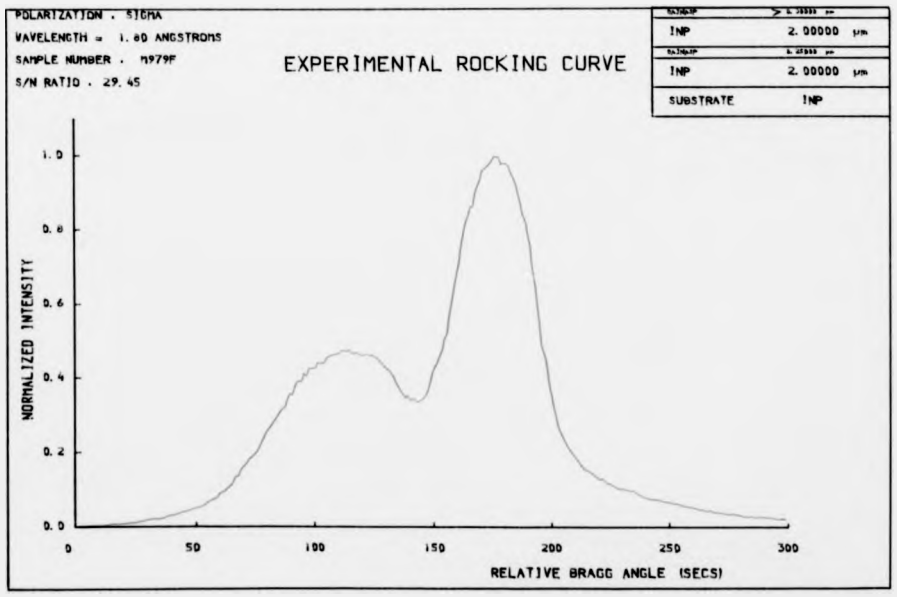

Figure 7.3f

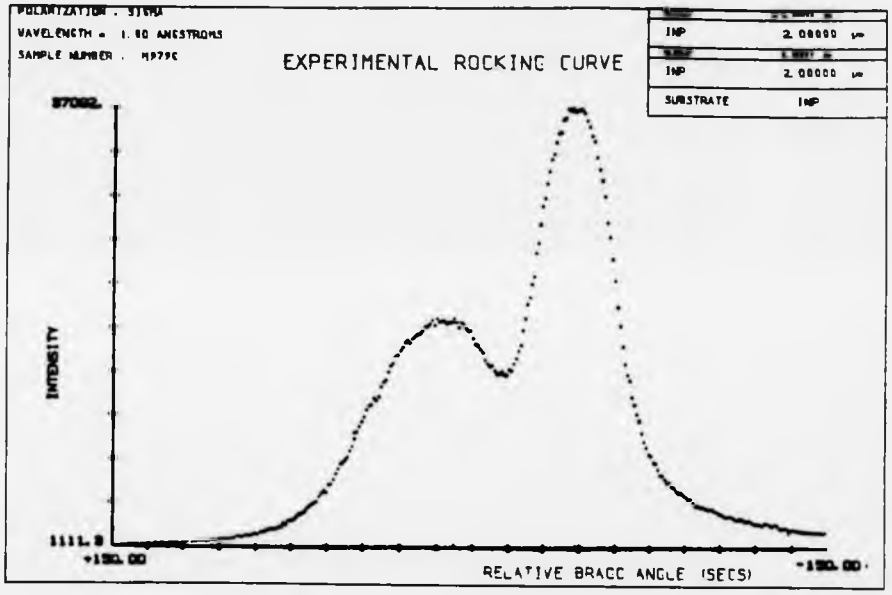
POLARIZATION . SIGMA
WAVELENGTH = 1.80 ANGSTROMS
SAMPLE NUMBER . M979C
EXPERIMENTAL ROCKING CURVE
INP 2.00000 um
INP 2.00000 um
SUBSTRATE INP
87082.
1111.8
INTENSITY
+150.00
-150.00
RELATIVE BRAGG ANGLE (SECS)

Figure 7.3g

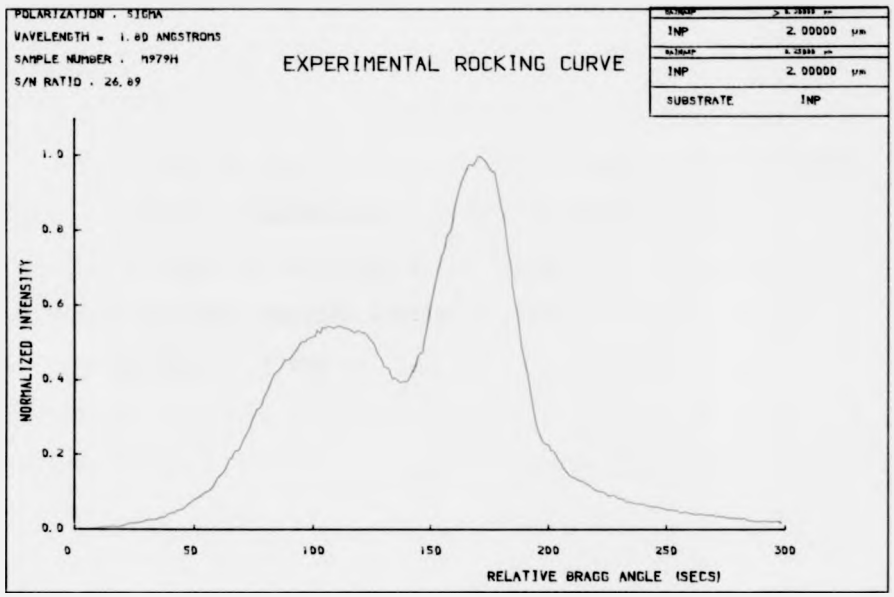

Figure 7.3h

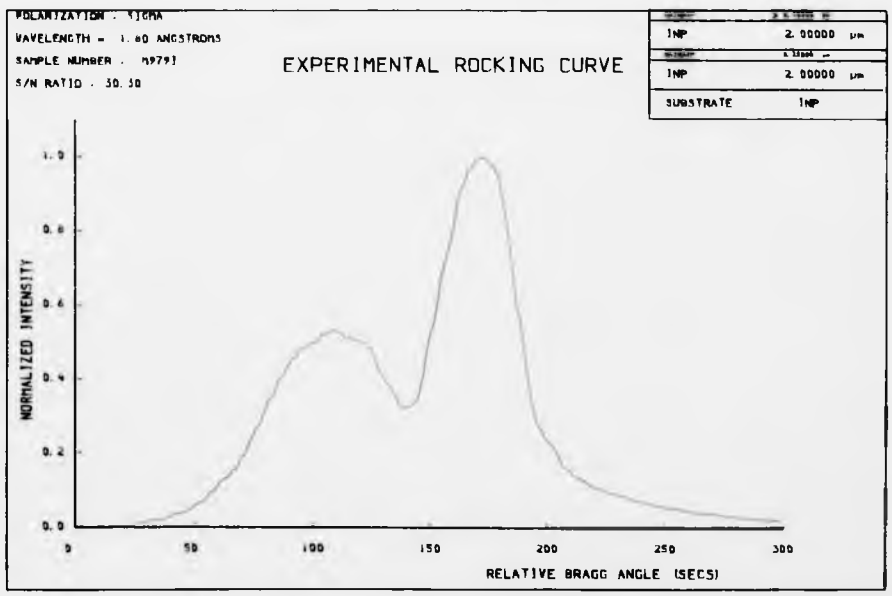

Figure 7.3i

quaternary multilayers has been made from which it is possible to show that the capping layer or the active layer in our present case is too thin to individually provide a secondary peak relatively as high and as broad as in Figure 7.3. The quaternary peak widths and peak heights listed in Table 7.1 also refer to the combined effect of the two layers. The two layers have approximately the same lattice mismatch. The mismatch, m, in parts per million, and shown in Table 7.1, varied slightly between a minimum at position 7 and a maximum at position 1. The peak width of the InP layer is seen from Figure 7.3 to be more uniform and much narrower than for the InGaAsP layer. The advantage of a greater crystalline perfection (narrower peak width) of the InGaAsP layer near position 1 is offset by a larger mismatch in this area. Near positions 4 and 9, both these factors are reasonably low. The lattice mismatch measured from the rocking curves includes the effect of tetragonal distortion. A detailed account of the effect of tetragonal distortion is presented in Chapter 10. Accordingly the mismatch M corresponding to a relaxed layer lattice parameter a_r is related to the measured mismatch m corresponding to the lattice parameter c_ℓ by

$$M = \frac{1 - \nu}{1 + \nu} .m$$

where ν is the Poisson's ratio.

Table 7.1. Characteristics of InP and InGaAsP layers from experimental rocking curves for a double heterostructure laser. Wavelength : 1.8Å, 400 Reflection.

Position	Peak height arbitrary	Peak width, arc secs.		Mismatch m		Relative thickness of InGaAsP layer
	InGaAsP layer	InGaAsP layer	InP layer	arc sec	ppm	
1	50.5	48	35.1	57	356	1.00
2	54.0	50	33.6	55	343	1.08
3	59.5	55	36.1	53	331	1.08
4	54.5	54	35.7	48	299	0.98
5	70.5	60	39.1	52	324	1.30
6	72.5	55	40.8	47	293	1.28
7	78.5	58	40.8	38.5	240	1.51
8	82.5	55	41.0	46.5	290	1.51
9	80.5	52	39.7	48.0	299	1.44

For most materials ν is roughly of the order of 1/3 so that

$$M \simeq m/2$$

For ternary layers, from the value of the lattice mismatch M, a direct evaluation of the composition of the layer could be made. This is done by assuming the lattice parameter of the ternary to vary linearly between their binary limits. In other words, the lattice parameter can be expressed as an empirical function of the composition of the ternary. For quaternary layers however, two variables are involved in the empirical relationship determining the lattice parameter and a direct evaluation of the composition x and y cannot be made from the consideration of lattice parameter alone.

7.2.2. Assessment of Composition

An approximate evaluation of the composition can now be made as follows. The lattice parameter for the quaternary alloy $In_xGa_{1-x}As_yP_{1-y}$ can be expressed as[2].

$$a(x,y) = 5.4512 + 0.41755x + 0.20225y - 0.0125xy \quad ...(7.2)$$

G.H. Olsen et al[3] have presented an empirical relationship for the band gap of the quaternary alloy according to which

$$\begin{aligned} Eg(eV) = {} & 2.75 - 1.33y - 1.4x + 0.33xy \\ & -(0.758 - 0.28y)\, x\, (1 - x) \\ & -(0.21 - 0.109x)\, y\, (1 - y) \end{aligned} \quad ...(7.2)$$

The lattice parameter has been assumed to obey Vegard's law whereas the band gap is assumed to have a quadratic dependence upon composition. The band gap of the quaternary layer can be determined from room temperature photoluminescence measurements. If we assume Eg to be uniform within the layer, we can solve equations (7.1) and (7.2) for an approximate estimate of the compositional variations across the layer. The photoluminescence emission wavelength for the quaternary layer has been reported by Plessey as 1.3μm corresponding to a band gap of 0.954 eV. Solving equations (7.1) and (7.2) for various quaternary lattice parameters obtained from experimental rocking curves corresponding to various positions, the composition x and y can be evaluated. These are listed in Table 7.2.

For nearly lattice matched systems, $a(x,y) = a_{InP}$ and equation (7.1) can be simplified to relate x in terms of y. Equation (7.2) for the band gap, in turn reduces to a function of y alone and would be similar to an empirical fit of Nahory et al[4] according to which

$$Eg = 1.35 - 0.72y + 0.12y^2 \text{ eV}$$

For inhomogeneous quaternary layers with graded composition, the lattice mismatch is in fact a function of layer depth and the experimental rocking curve would give an overall picture for a layer thickness, depending upon its extinction depth. In such cases, an accurate direct estimate of the mismatch variation

for the layer from experimental rocking curves is sometimes difficult.

7.2.3. Assessment of thickness

Assuming that the layer is not thick enough to exceed the extinction depth for the reflection used (i.e. the kinematic approximation), the ratio of the integrated intensities of the two peaks should give a measure of the thickness of one layer relative to the other. The extinction depth, is proportional to $\left[\lambda|F_a|/\mathrm{Cos}\theta_B\right]^{-1}$

where λ is the wavelength of radiation used

F_a is the structure factor for the reflection

θ_B is the Bragg angle

For λ in the 1 - 2Å range and large Bragg angles, the extinction depth is typically 9μm or more. The above condition is thus usually met. Assuming a uniform thickness for the InP layers grown on good quality InP substrates, which is in most cases, a valid assumption, the ratio of the integrated intensities should give a measure of the total thickness of the quaternary layers, though not in absolute units.

For the positions (1) to (9) on the specimen for which rocking curves were recorded, the relative total quaternary layer thickness was calculated. These are listed in Table 7.1. About 54% variation in the total thickness is thus seen. Maximum

Table 7.2. Assessment of x and y compositions for the $In_xGa_{1-x}As_yP_{1-y}/InP$ laser structure : Eg = 0.954 eV

Position	Calculated using equations (7.1) and (7.2)	
	x	y
1	0.7427	0.5621
2	0.7426	0.5622
3	0.7424	0.5623
4	0.7421	0.5627
5	0.7424	0.5624
6	0.7420	0.5627
7	0.7413	0.5633
8	0.7419	0.5628
9	0.7421	0.5627

FIG 7.4 A schematic diagram of the specimen L5. The points G,D,E and F refer to the positions where rocking curves were plotted and compared.

thickness occurs in the region near positions (7) and (8) while the minimum thickness is towards the right half of the specimen. A theoretical calculation of rocking curve profiles, discussed in detail in Chapter 10, would enable a more-or-less accurate assessment of the thicknesses of individual layers.

7.3. A linearly graded quaternary single layer, Specimen L5

In the last chapter experimental rocking curves from a variety of specimens were discussed. Accordingly, we observe that rocking curves from inhomogeneous layers are likely to attain complex shapes in view of the rapid fluctuation in the homogeneity and uniformity of the layer. An asymmetry in the layer peak shape is developed. To facilitiate a detailed assessment of compositional and thickness variations from rocking curves for such a structure, a compositionally graded single quaternary layer, approximately 4.2μm thick and grown by liquid phase epitaxy, was supplied by Plessey. The composition was thought of as being graded in both directions. A schematic diagram of the specimen is shown in Figure 7.4 For the assessment of uniformity of the layer, the same experimental procedure outlined in section 7.2.1 was followed. Scanning of the specimen was achieved by moving a slit 100 x 500μm in front of the beam. On the first axis of the double crystal camera was placed a highly perfect (100) InP crystal. A wavelength of 1.5Å was used. Rocking curves were plotted for a 400 reflection from four points G, D, E and F on the

specimen. These are reproduced in Figure 7.5. The curves show a wide epilayer peak, consisting of another secondary peak. The substrate peak being more symmetric and sharp is easily identified as the one on the far right in Figure 7.5. An idea of the thickness of the layer would also help identify the substrate peak. The limits of mismatch for the graded layer can be determined from the positions of the extreme peaks for the epilayer, such as peaks 1 and 2 in Figure 7.5a. Between peaks 1 and 2, the rocking curve falls off gradually, but with several characteristic features. A relatively higher level for peak 1 indicates that the epilayer has the top surface corresponding to a higher mismatch, which falls off gradually with depth below the surface. One would not then expect a specially resolved peak 2 as we see in Figure 7.5a. It is therefore quite possible that at some intermediate depth, the mismatch either remains constant with depth or increases with depth or is perhaps a mixture of both. The characteristics of the substrate and epilayer peak and the mismatch for the epilayer peak for the four positions, as observed from the rocking curves, are shown in Table 7.3. We see that the mismatch progressively decreases from region G to F, the range of mismatch grading at F being between 660 ppm and 220 ppm approximately. While the substrate width remains almost uniform, the epilayer width changes in an unidentified manner. Calculation of the ratio of the integrated intensities of the epilayer to the substrate peaks shows that the epilayer thickness is largest at D and smallest at G while at E and F they are moderately

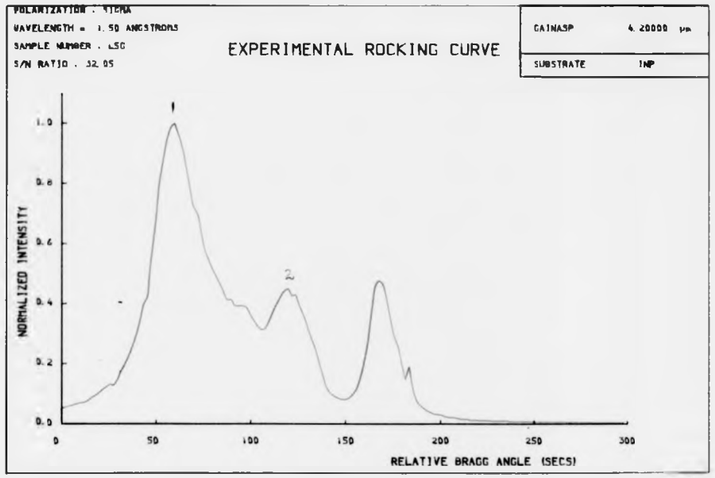

Figure 7.5a

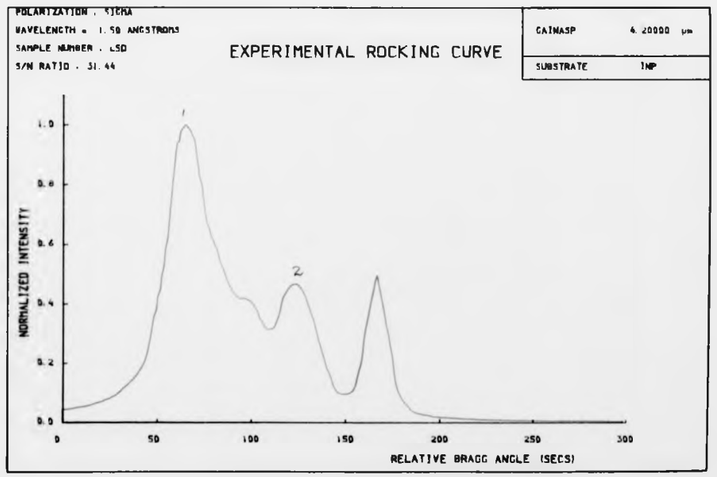

Figure 7.5b

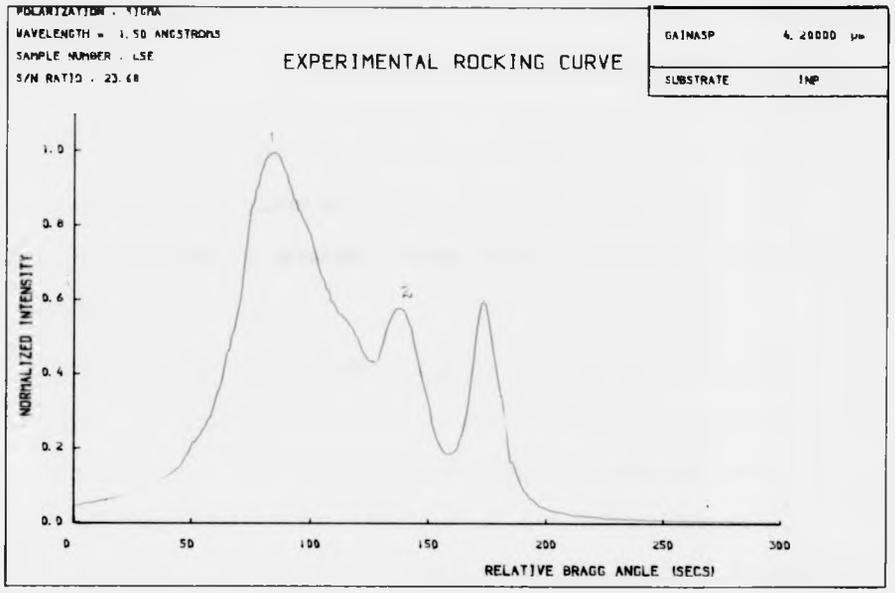

Figure 7.5c

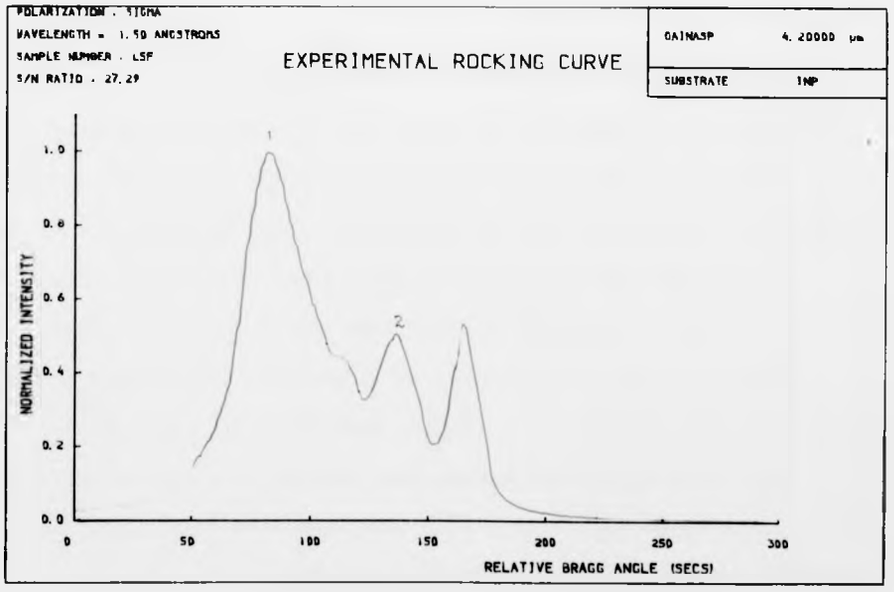

Figure 7.5d

uniform. The relative thicknesses at these points are also listed in Table 7.3. The 400 reflection topographs for the substrate and epilayer peaks are shown in Figure 7.6. The topographs do not show any dislocation network. Some growth striations appear to be present.

Since the lattice mismatch varies between two levels within the layer, an assessment of the limits of compositional variation can only be made. From the reported photoluminescence data for the layer the emission wavelength is λ_g = 1.245μm. Equations (7.1) and (7.2) can be solved, the band gap Eg and the mismatch level being now known. The compositional limits are listed in Table 7.4.

7.4. Discussion

For the assessment of the quaternary layer composition, the lattice mismatch m of the layer as measured from experimental rocking curves are duly corrected for tetragonal distortion to obtain the relaxed layer mismatch M so that equations (7.1) and (7.2) can be solved. According to Table 7.2 the observed variations in x and y are seen only to the order of 10^{-4}. A direct measurement of x and y by electron-microprobe or other methods is accurate to within ± 0.001. Accordingly, the variations observed in x and y for both the double heterostructure laser and single quaternary specimens are only slight and may be treated as insignificant. The quaternary materials are thus fairly uniform

Table 7.3. Characteristics of the substrate and epilayer from experimental rocking curves for a graded quaternary specimen, L5. Wavelength 1.5Å, 400 reflection.

Position	Substrate Peak		Epilayer Peak					Relative thickness of epilayer
			Upper mismatch level			Lower mismatch level		
	Peak height arbitrary	Peak width arc secs	Peak height arbitrary	Peak width arc secs	Mismatch ppm	Peak height arbitrary	Mismatch ppm	
G	.477	18.3	1	34.0	880	.452	400	1
D	.495	15.0	1	33.3	830	.472	365	1.39
E	.593	16.1	1	52.9	720	.577	290	1.28
F	.536	16.0	1	38.1	660	.629	220	1.25

Table 7.4. Assessment of compositional limits for the graded quaternary, L5. Measured bandgap = 0.954 eV

Position on the specimen	Alloy composition for upper mismatch limit		Alloy composition for lower mismatch limit	
	x	y	x	y
G	.7815	.4875	.7758	.4922
D	.7809	.4880	.7754	.4926
E	.7796	.4891	.7745	.4933
F	.7789	.4897	.7737	.4940

(a) Topograph of the substrate peak

(b) Topograph of the epilayer peak

2 mm

FIG 7.6 Double crystal reflection topographs of the specimen L5 400 reflection. Wavelength : 1.5 A

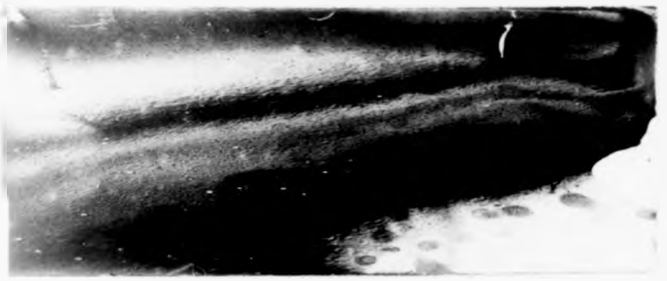

(a) Topograph of the substrate peak

(b) Topograph of the epilayer peak

2 mm

FIG 7.6 Double crystal reflection topographs of the specimen C5
400 reflection, Wavelength : 1.5 A

in composition along the layer. The multilayer laser was chosen as one of the specimens for the assessment of layer thickness and composition, with the idea that if the cap and active layers had different lattice mismatch, then two separate peaks for the quaternary would have been observed and the compositional and thickness variations of each layer could be determined. Unfortunately, both the quaternary layers have about the same lattice mismatch in this case and variations observed and tabulated in Tables 7.1 and 7.2, refer to the combined effect of the two layers. However the experiment conveys the most important fact that there exists non-uniformity and inhomogeneity in the grown quaternary layers.

An accurate assessment of the layer peak width and peak height and hence the area under the peak is possible only if the layer peak is well separated from the substrate/InP peak. The peaks for the graded layer specimen L5 are not well resolved, hence the results tabulated in Table 7.3 are only approximate.

References

1. WEISER, K., "Dissociation pressure and cohesive energy of Indium Phosphide', J. Physical Chem., 61, 513 (1957).

2. MOON, R.L., ANTYPAS, G.A. and JAMES, L.W., 'Bandgap and Lattice constant of GaInAsP as a function of alloy composition', J. Elec. Mater., 3, 635 (1974).

3. OLSEN, G.H., ZAMEROWSKI, T.Z., SMITH, R.T. and BERTIN, E.P., 'InGaAsP quaternary alloys : composition, refractive index and lattice mismatch', J. Elec. Mater., 9, 977 (1980).

4. NAHORY, R.E., POLLACK, M.A., JOHNSTON, W.D. Jr., and BARNS, R.L., 'Bandgap versus composition and demonstration of Vegards law for $In_{1-x}Ga_xAs_yP_{1-y}$ lattice matched to InP', Appl. Phys. Lett., 33, 659 (1978).

8

CHARACTERISATION OF A DOUBLE HETEROSTRUCTURE LASER AND AN EDGE EMITTING LED BY SELECTIVE ETCHING

8.1. Introduction

We have seen in Chapters 6 and 7 that experimental rocking curves of a specimen can provide valuable information about the lattice mismatch, crystallographic quality, compositional or thickness variations of the quaternary layer. This is satisfactory in so far as the growth of single quaternary InGaAsP layer on an InP substrate is concerned. The same is true for a single ternary layer. Even in single layers, if the layers are inhomogeneous, that is, have fluctuations in their lattice parameter across the layer, the rocking curves attain a complex shape, because of the variation of the lattice mismatch, and the extraction of relevant information is not straightforward. The situation is even more complicated in hetero-epitaxial systems where a number of epitaxial layers are grown over an InP substrate. One would presume that rocking curves from such heterostructures as GaInAsP(cap)/p-InP/GaInAsP(active layer)/n-InP/InP substrate would consist of two classes of peaks corresponding to InP and GaInAsP. From a theoretical calculation of rocking curves, it has been pointed out in Chapter 10 that very thin hetero-epitaxial multi-layers, even if homogeneous show peaks at unexpected positions and the interpretation of the experimental rocking curve becomes extremely difficult. Even in the normal case where two classes of peaks corresponding to InP and GaInAsP are expected, characteristics of each individual layer cannot be known from the superimposed curves. That is, one cannot distinguish between a quaternary active layer and a quaternary cap with the analysis so far. If however, the peaks of individual layers are

well separated, then a knowledge of the thicknesses of the layers would make the identification of the peaks simpler, but where layers of comparable thicknesses are present, it would again be difficult to identify. It was therefore necessary to see if it was possible to isolate rocking curve characteristic of each layer in the heterostructure. In order to achieve this, each layer was etched off in sequence and an experimental rocking curve plotted. By comparing these rocking curves, the detailed characteristics of each layer were obtained.

8.2. Experimental Procedure

Two specimens were chosen for this purpose. One of them, a double heterostructure laser, is shown schematically in Figure 8.1.

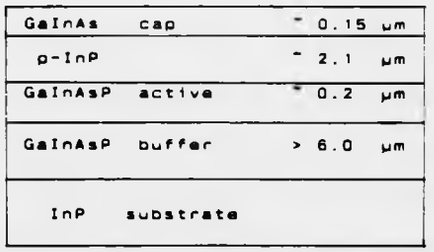

FIG 8.1 A schematic diagram of the double heterostructure laser, R154

It consists of a thick buffer layer of n-InGaAsP, closely approximating in composition to InP, grown over an InP substrate over which is a thin quaternary active layer. This is followed by a p-InP layer and a thin InGaAs ternary capping layer. The layers were grown by liquid phase epitaxy on a (100) InP substrate by Plessey

(Caswell) Limited. The reported thicknesses of the layers are indicated in the figure.

Four windows were created on the upper half of the top surface of the specimen to expose each of the four layers. This was done by selectively etching the layers. Proper selective etchants are available for this purpose[1,4]. For the (100) face the AB etchant (HNO_3 : HF = 5 : 1)[3] and (H_2SO_4 : H_2O_2 : H_2O = 10 : 1 : 1)[2] have been reported to be used to selectively etch off GaInAsP or GaInAs over InP while a mixture of (HBr : HF = 1 : 10)[5] and dilute HCℓ are used to selectively remove InP on GaInAsP. In this case a solution of 3: 1 : 1 H_2SO_4 : H_2O_2 : H_2O was used for the GaInAsP or GaInAs layer while a solution of dil. HCℓ ($4HC\ell + H_2O$) was used for InP layers. Since the entire layer of a particular kind was to be etched, precise control of the etch rate was not found necessary.

The lower half of the top surface was masked by lacomit varnish (black wax can alternatively be used). Next, masking window A (Figure 8.2a), the top ternary cap was etched using the (3 : 1 : 1) etchant, thereby exposing InP. The etching rate was roughly about 1μm/min. at 300°K. So, for the ternary layer of approximately 0.15μm thickness, the etching was carried out for a period of 15 seconds to ensure that the entire ternary layer had been etched. This selective etchant had been considered to have negligible effect on the InP layer[2]. Next window C was also masked and the exposed InP layer removed using the $4HC\ell + 1H_2O$ etchant. Figure 8.3 shows the etching rate in InP using $4HC\ell + H_2O$ solution at 1°C[6]. So an etching time of approx. 2 mins. was

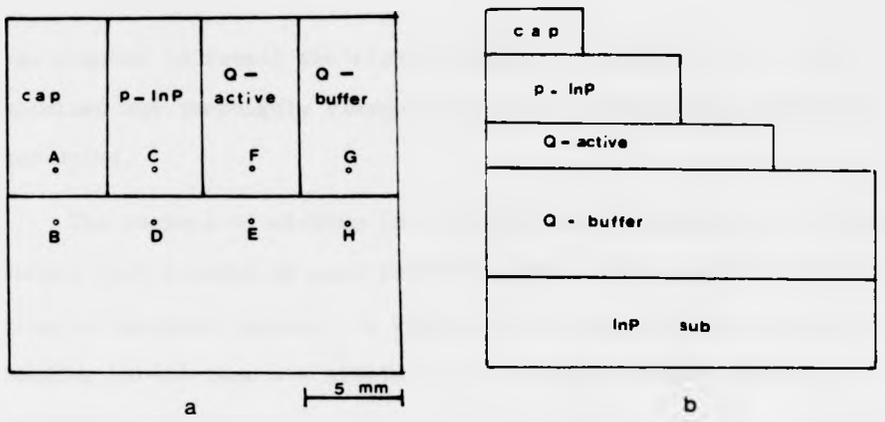

FIG 8.2 (a) etching configuration for the specimen R154. The upper half of the top surface was divided into four sections. (b) By masking each window in turn, and using selective etchants, a portion of each layer of the multilayer structure can be exposed. Vertical height is not to scale

allowed to etch at room temperature, InP layer, 2.1μm thick. The active layer was then exposed in windows F and G. Masking F, the active layer in G was removed to expose the Q-Buffer. The etching period was controlled and set to 12 secs. to ensure that only the active layer was etched. After the etching process, the lacomite

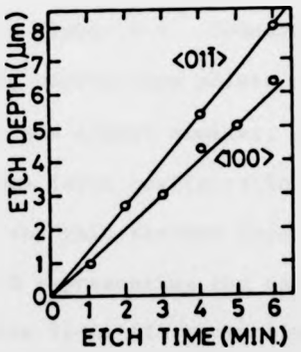

FIG 8.3 Etching rate in InP for the (4HCl + H_2O) etchant at 1°C. [after Arai et al (6)]

was removed to reveal the etched structure (Figure 8.2b). The specimen was thoroughly cleaned in acetone and trichloroethylene and dried.

The purpose of etching is to facilitate a comparison of rocking curves from a point on each etched region of the specimen with that from an unetched region. In view of the changes in the shape of rocking curves that are likely to occur due to composition or thickness variations of the layers from point to point in the specimen, a meaningful comparison would be obtained if the two points in the etched and unetched region are close to each other. Four pairs of points were therefore chosen for rocking curve analysis (Figure 8.2a).

The experimental arrangement for recording rocking curves was essentially similar to that described in Chapter 5. On the first axis of the double crystal camera was a highly polished and perfect (100) InP crystal. The camera was adjusted to record rocking curves for a 400 reflection at 1.5Å wavelength. A 100 x 500μm aperture was used to define points on the specimen where rocking curves were taken. These are reproduced in Figure 8.4. Comparing Figure 8.4a and 8.4b which represent rocking curves from points A and B respectively, we see that the curves are almost similar, since the two points A and B represent the same layer configuration. Comparing Figure 8.4c, for the point C where the thin ternary layer is removed, and Figure 8.4d for point D representing the same unetched configuration, we see that the relative level of the smaller peaks in Figure 8.4c has gone up slightly. By removing a layer from the top, more reflection from the underlying layers is expected, while the

The various points where rocking curves were recorded are shown in Figure 8.2a

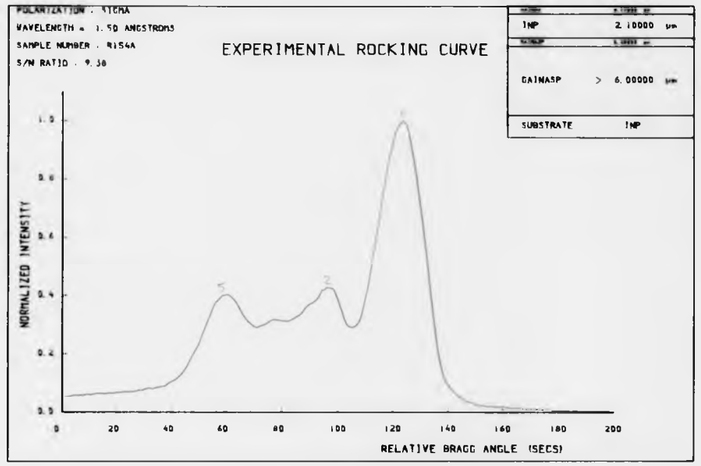

Figure 8.4a

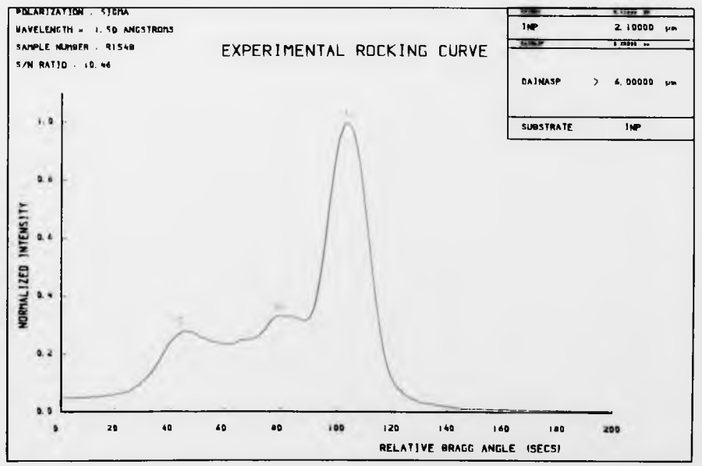

Figure 8.4b

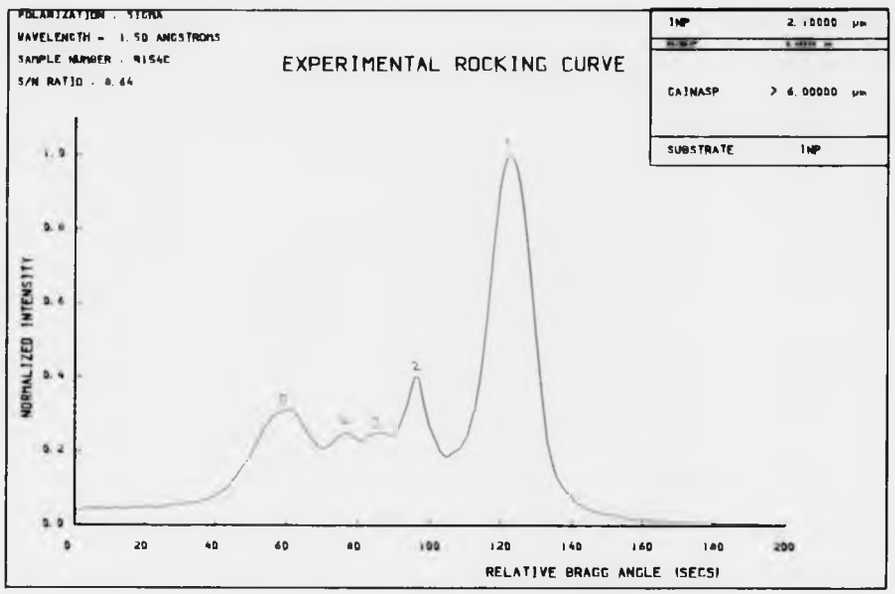

Figure 8.4c

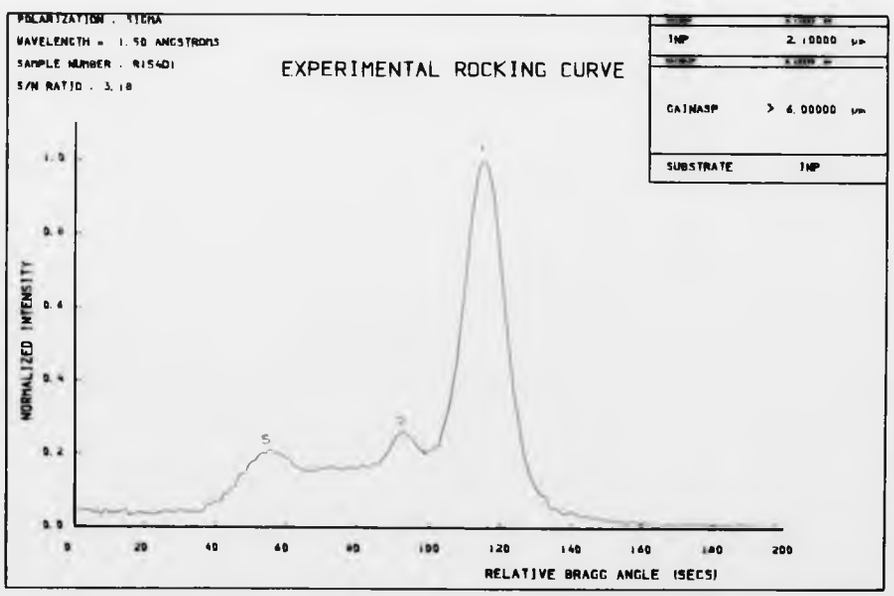

Figure 8.4d

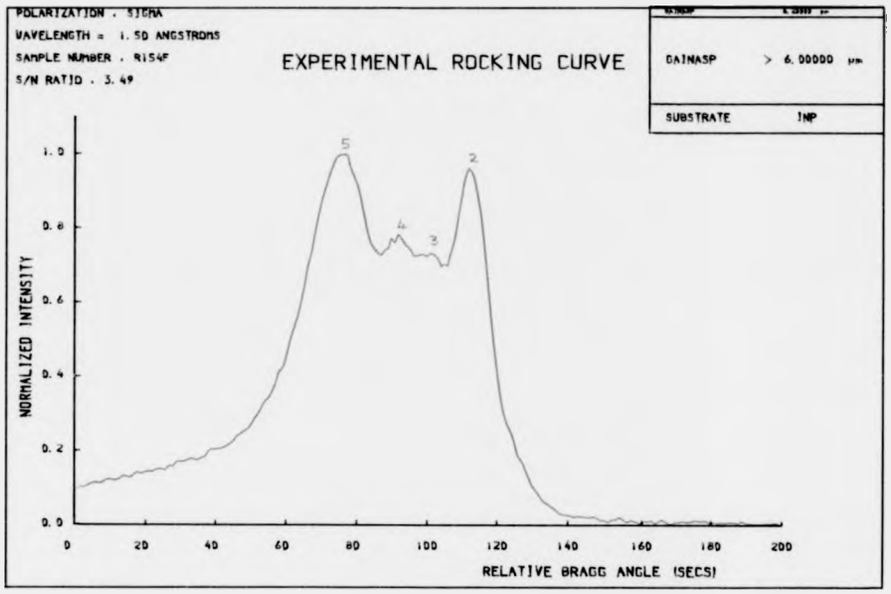

Figure 8.4e

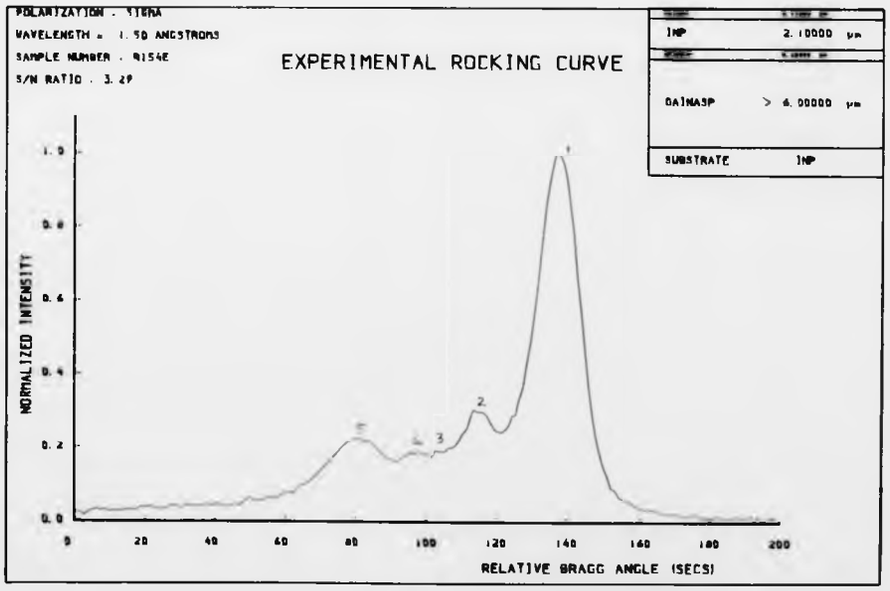

Figure 8.4f

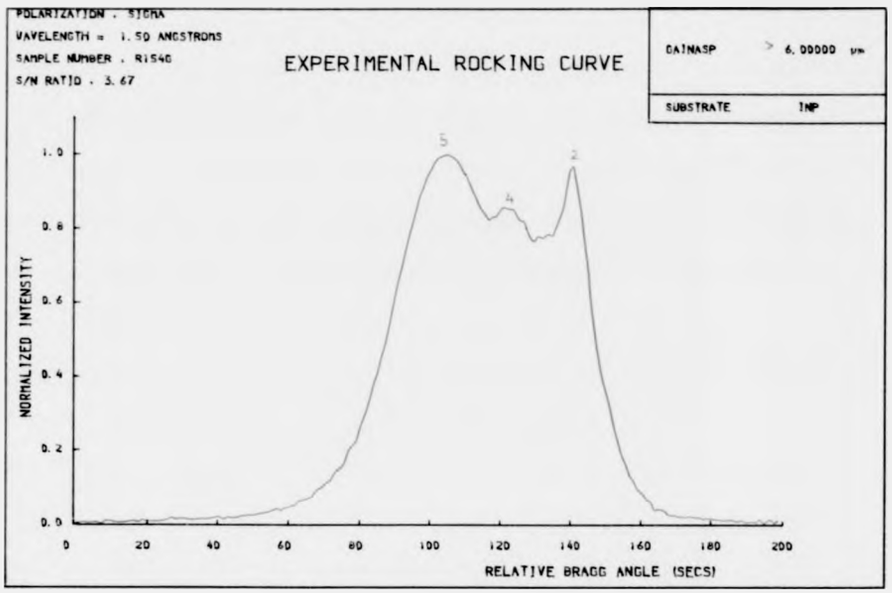

Figure 8.4g

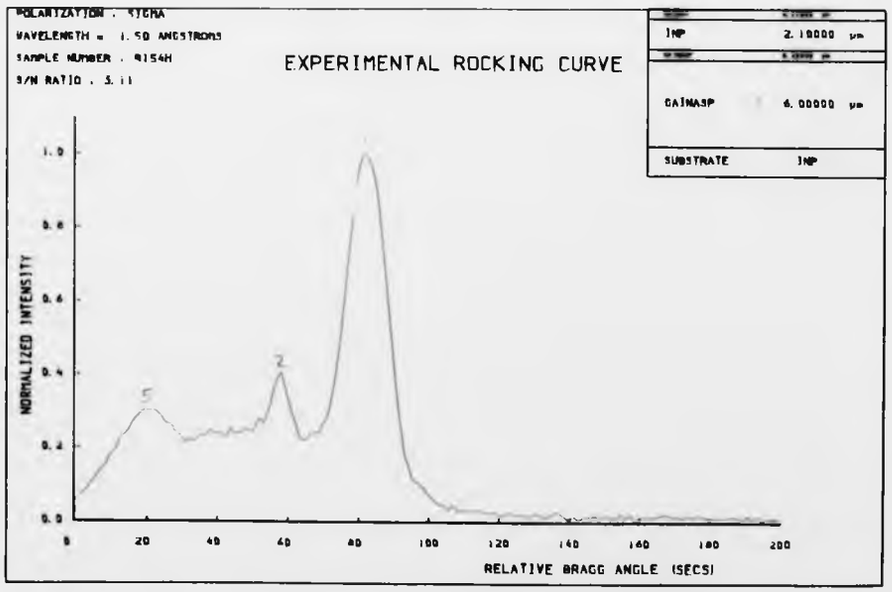

Figure 8.4h

reflection due to the removed layer would be absent. We however, do not see the absence of any peak on Figure 8.4c when compared with Figure 8.4d. It therefore appears that the ternary cap is quite closely matched with InP. Comparing figure 8.4e, for the point F where the InP layer is also removed, and Figure 8.4f for point E representing the unetched configuration, we see that peak 1 (figure 8.4f) is no longer seen in Figure 8.4e. Removal of the InP layer has therefore resulted in the relative levels of the peaks 2,3,4 and 5 going up while the reflection from the layer itself is absent. This is what is also observed in Figure 8.4e. Peak 1 in Figure 8.4f is therefore attributed to the InP layer. Comparing Figure 8.4g, where the active layer is removed with Figure 8.4e which includes the active layer, we find that peak 3 is due to the active layer. The peak is not very prominent as the thickness of the active layer is very small. The rocking curve in Figure 8.4g is for a reflection from the quaternary buffer layer over an InP substrate. Normally peaks corresponding to both the layers would be observed in such a rocking curve. The peak position corresponding to InP, as we note from Figure 8.4f, is about 26 arc secs to the right of the peak 2. Accordingly, in Figure 8.4g, a reflection from the InP substrate, if observed would indicate a peak in the neighbourhood and to the right of peak 2. Since no such peak is observed, it is concluded that the buffer layer is too thick for the X-rays to penetrate to the InP substrate. The reflection from the buffer is therefore comprised of peaks 2,4 and 5. The layer is not homogeneous, and has two distinct sections : one corresponding to a mismatch m = 210 ppm (giving rise to peak 2)

and the other corresponding to a mismatch m = 505 ppm (giving rise to peak 5). The two peaks are not well separated and peak 5 has a gradual fall with a secondary peak 4 before merging with peak 2. Theoretical analysis of rocking curve profiles discussed in Chapter 10 shows that such a shape would be the result of an intermediate section having a graded mismatch grading between the mismatch of 210 and 505 ppm. Table 8.1 gives a list of peak height, peak width and lattice mismatch (m), wherever possible, of all identified peaks in the rocking curves.

The second specimen chosen was an edge emitting LED. A schematic diagram of the LED is shown in Figure 8.5. Its structure

GaInAs	cap	~ 0.20 μm
p-InP		~ 2.5 μm
GaInAsP	active	~ 0.3 μm
GaInAsP	buffer	> 6.0 μm
InP	substrate	

FIG 8.5 A schematic diagram of the edge emitting LED, R249

is essentially the same as the double heterostructure laser except that the thickness of the layers are slightly different.

As before, etched windows were created on the upper half of the top surface using the same selective etchants. Figure 8.6 shows a schematic top and side view of the etching arrangement. A set of rocking curves for a 400 reflection at 1.5Å were taken

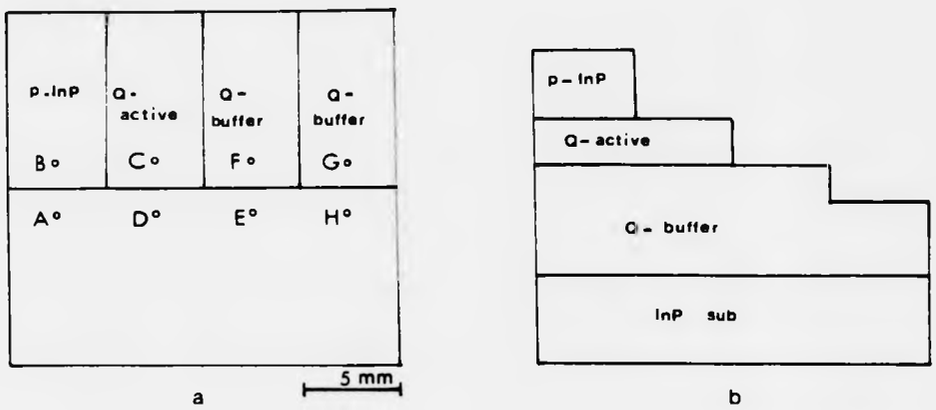

FIG 8.6 (a) etching configuration for the specimen R249. (b) etched layer arrangement, side view. Vertical height is not to scale.

at various points in a similar way. The curves are plotted in Figure 8.7. Figure 8.7a shows the rocking curve at a point for the unetched region of the specimen while Figures 8.7b - 8.7e shows rocking curves from a point on each etched window.

Comparing the rocking curve at point A with that at B (Figures 8.7a and 8.7b) we find that peak 2 of Figure 8.7a corresponds to the ternary cap layer which had been etched off to obtain the rocking curve of Figure 8.7b. Comparing Figure 8.7b with Figure 8.7c which represents the rocking curve with the InP layer removed, we find that peak 1 corresponds to the InP layer. The rocking curve from the point in the region where the quaternary layer was removed is shown in Figure 8.7d. A comparison of Figures 8.7c and 8.7d indicates that the quaternary peak could be the one corresponding to peak 5 in Figure 8.7c. For a similar reasoning as

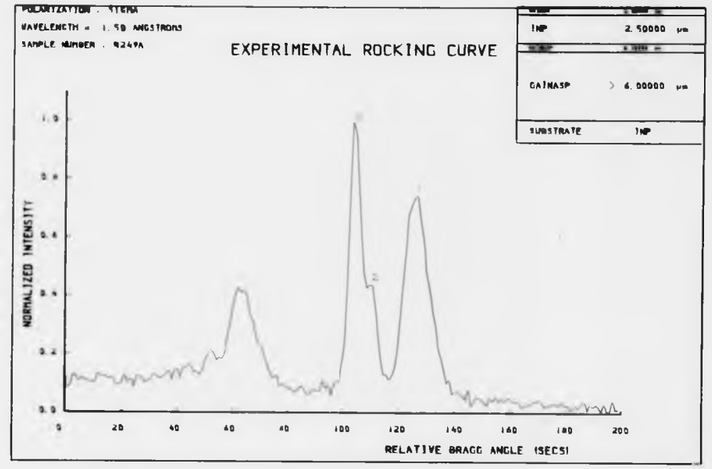

Figure 8.7a

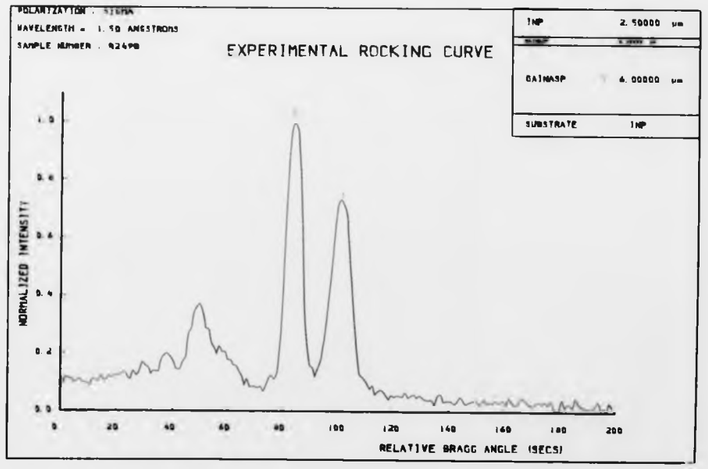

Figure 8.7b

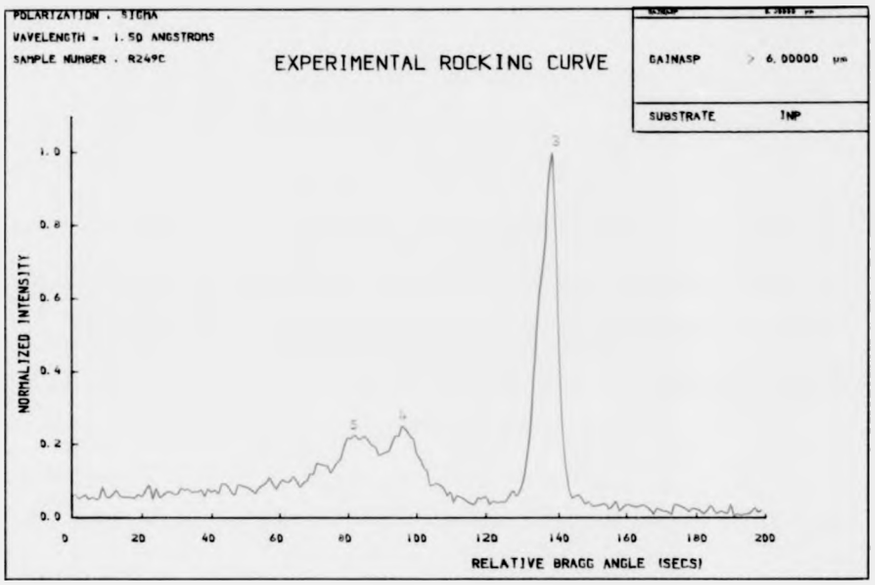

Figure 8.7c

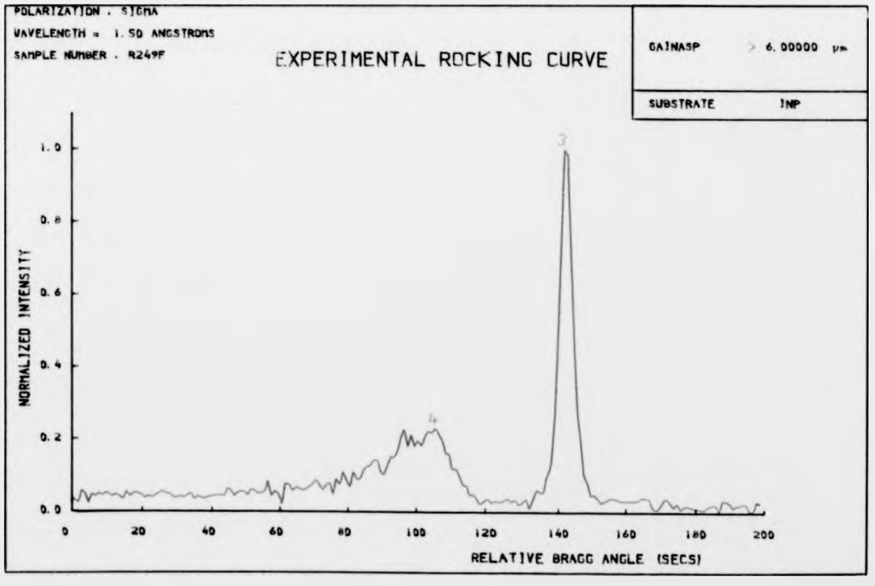

Figure 8.7d

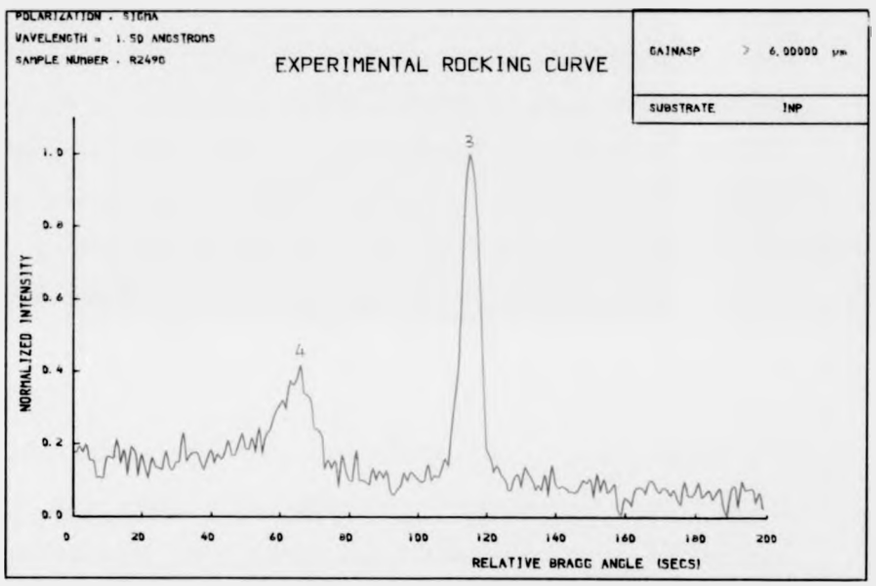
POLARIZATION : SIGMA
WAVELENGTH = 1.50 ANGSTROMS
SAMPLE NUMBER : R2490
EXPERIMENTAL ROCKING CURVE
GAINASP > 6.00000 μm
SUBSTRATE INP
NORMALIZED INTENSITY
1.0
0.8
0.6
0.4
0.2
0.0
0
20
40
60
80
100
120
140
160
180
200
RELATIVE BRAGG ANGLE (SECS)
3
4

Figure 8.7e

before, the reflection from the InP substrate, if permitted, would have indicated a peak on the rocking curve to the right of peak 3, in Figure 8.7d. The absence of such a peak in either Figure 8.7d or Figure 8.7e (where a small thickness of the buffer layer has been etched off) indicates that the buffer layer is again too thick for the X-rays to penetrate to the InP substrate. From the nature of the rocking curve, the buffer layer is thus assumed to consist of two sections, a reasonably thick and more uniform layer (giving rise to peak 3) on top of a relatively thin graded layer (giving rise to peak 4). The peak heights, widths and mismatch of the identified layers have been listed in Table 8.2.

Discussion

Some strain on a layer is relieved by removing a layer on top of it. As a result characteristics of a peak for a layer obtained from the rocking curve measurements under this condition may not correspond exactly with those obtained from rocking curve measurements for the entire hetero-epitaxial structure. This, and the fact that compositional and thickness variations with position may occur for a layer due to unsteady growth conditions, makes it extremely difficult to compare rocking curves on an absolute scale. For example, the separation between peaks 1 and 3 in Figure 8.7a is 22.7 arc secs while the same in Figure 8.7b is 17.3 arc secs, with an angular accuracy of ± 0.1 arc secs. Hence, data for the layer characteristics listed in Tables 8.1 and 8.2 are only approximate.

TABLE 8.1

Layer characteristics of the double heterostructure laser, R154.

	InGaAs Cap	p - InP	Buffer		Q-Active layer
			I	II	
Mismatch (arc secs)	-	-	26.1	62.1	36.9
$m = \Delta a/a$ ($\times 10^4$)	-	-	2.10	5.05	3.00
Peak width (arc secs)	-	14.4	14.4	31.9	-
Peak height (arbitrary unit)	-	150	59.5	47.5	38

TABLE 8.2

Layer characteristics of the edge emitting LED, R249.

	InGaAs Cap	p - InP	Buffer InGaAsP		Q-Active layer
			I	II	
Mismatch (arc secs)	16.0	-	22.4	64.8	78.8
$m = \Delta a/a$ ($\times 10^4$)	1.3	-	1.8	5.3	6.45
Peak width (arc secs)	-	11.3	5.8	14.4	-
Peak height (arbitrary unit)	65.5	111	150	65	32.5

In plotting the intensity for the rocking curves, if the photon counting rate is N per sec and if the counting time is for t secs, the total number of photons counted in time t is Nt and the standard error for the count is $\sqrt{Nt}$ assuming a Poisson's distribution. If however, the signal is mixed with a background noise with a background count rate of N_B per sec then the standard error for the count becomes $\sqrt{(Nt - N_B t)}$. An estimate of the standard error in a count will help identify certain small humps on rocking curves as peaks. For example, peak 2 in Figure 8.7a, though plotted on a normalized scale, had a count rate of about N = 18000 per sec. The counting time was 1 sec while the background count rate was about N_B = 15000 per sec. The standard error is thus 55. The dip in the rocking curve close to peak 2 in Figure 8.7a corresponds to a counting rate of about 17900. The peak at 2 was therefore considered to be just beyond the limits of statistical error and was therefore not considered as merely a fluctuation.

The lattice parameter mismatch as measured from experimental rocking curves relate to the lattice parameter of the layer measured between the Bragg planes. When a layer with a 'relaxed' lattice parameter a_r is grown over a substrate with a lattice parameter a_o, the layer unit cell undergoes a tetragonal distortion and the layer unit cell attains a dimension $a_o \times a_o \times c_\ell$ instead of $a_r \times a_r \times a_r$. X-ray methods determine the mismatch m corresponding to the layer lattice parameter c_ℓ, defined by

$$m = \frac{c_\ell - a_o}{a_o}$$

while the mismatch M corresponding to the relaxed layer parameter a_r is

$$M = \frac{a_r - a_o}{a_o}$$

In Chapter 10 it has been shown that the two mismatch parameters are related by

$$M \simeq m/2$$

The mismatch parameter m obtained from experimental rocking curves can thus be related to the relaxed parameter mismatch.

The method of selective etching has made it possible to identify the approximate positions of the peaks corresponding to each epitaxial layer in the multilayer structure. In Chapter 10, where a rocking curve for a multilayer structure has been theoretically calculated, it has been demonstrated, that the mismatch data for the layers obtained by selective etching can be effectively used as initial input values and thereby obtain detailed characteristics of the layers by a computer simulation of the experimental rocking curves.

Some of the layer peaks in Figures 8.4 and 8.7 are not well separated from the neighbouring peaks; as such an accurate estimate of the peak widths and area under such peaks cannot be made.

The accuracy in the angular position is limited to one step of the stepper motor rotating the specimen. This corresponds to 0.2 arc secs and the angular positions are therefore accurate to within ± 0.1 arc secs.

References

1. PHATAK, S.B. and KELNER, G., 'Material-selective chemical etching in the system InGaAsP/InP', J. Electrochem. Soc., 126. 287 (1979).

2. NELSON, R.J., WRIGHT, P.D., BARNES, P.A., BROWN, R.L., CELLA, T. and SOBERS, R.G., 'High output power InGaAsP (λ = 1.3μm) strip-buried heterostructure lasers', Appl. Phys. Lett., 36, 358 (1980).

3. ABRAHAMS, M.S. and BUIOCCHI, C.J., 'Etching of dislocations on the low index faces of GaAs', J. Appl. Phys., 36, 2855 (1965).

4. KOMIYA, S. and NAKAJIMA, K., 'Multiplication of threading dislocation in the InP/InGaAsP/InP double heterostructure grown on InP (111)B substrate', J. Cryst. Growth, 48. 403 (1980).

5. AKITA, K., KUSUNOKI, T., KOMIYA, S. and KOTANI, T., 'Observation of etch pits produced in InP by new etchants', J. Cryst. Growth, 46, 783 (1979).

6. ARAI, S., ASADA, M., TANBUNEK, T., SUEMATSU, Y., ITAYA, Y. and KISHINO, K., '1.6μm wavelength GaInAsP/InP BH Lasers', IEEE J. Quantum Electron., QE-17, 640 (1981).

9

INVESTIGATION OF THE CHARACTERISTICS OF AN EPITAXIAL LAYER AT DIFFERENT STAGES OF ITS GROWTH

9.1. Introduction

As was pointed out before, in liquid phase epitaxy, controlled growth of submicron layers is extremely difficult, while very thick layers tend to become highly non uniform. It is not clear whether, during an epitaxial growth of a layer, the initial stages of epitaxy show growth characteristics that are in any way different from the bulk. It is therefore interesting to see if there is any experimental evidence distinguishing between the initial and advanced stages of epitaxial growth of a layer. In particular, it would be interesting to know how the mismatch characteristics of a layer varies, as the growth progresses, or in other words, to characterize a layer at different intermediate thicknesses. An attempt was therefore made to see if it would be possible to observe any changes in growth characteristics at different intermediate thicknesses.

9.2. Experimental methods and results

Two methods were followed. In one, samples were grown with the growth terminated at different intermediate stages. These samples, grown by Plessey for this purpose, had thicknesses between a few hundred Angstroms and 2μm. In the other method, a sample, with a thick epitaxial layer was etched off to various thicknesses and characterized at every stage. It was not possible to control the etchant to obtain layer thicknesses as low as a few hundred Angstroms used in the previous method. Hence characterization by etching was done for various layer thicknesses

up to about 2μm or so.

9.2.1. Samples with growth terminated at intermediate stages

A set of three nominally lattice matched layers of different thicknesses were grown at Plessey for this purpose. One of the specimens, VS399B was reported to be grown very thin, showing only island growths. A second specimen, VS399A had an epitaxial layer estimated at approximately a few hundred Å thick, while the third specimen was grown approximately 2μm thick.

Double crystal rocking curves for a 400 reflection were recorded from a point on each of the three samples. A silicon monochromator, set for a wavelength of 1.5Å was used on the first axis of the double crystal camera. An aperture of 100μm x 500μm was used to define the points on the specimen for rocking curve measurements. Figure 9.1 shows the rocking curves for the three samples. For the sample with the thinnest layer the rocking curve appears to show an asymmetric fall towards the right (Figure 9.1a), while the layer of intermediate thickness has a more-or-less symmetric rocking curve, (Figure 9.1b). The 2μm layer shows asymmetry in the rocking curve towards the left. Both the thin layer specimens have about the same rocking curve widths but slightly wider than for the 2μm sample. Reflection from very thin layers is expected to be very low; however, since no separate peak was observed even for the 2μm sample, it appears that the layers are lattice matched with the InP substrate. The asymmetry in the rocking curves for VS397 and VS399B may probably

FIG 9.1 Double crystal rocking curve for a 400 reflection from a point 100x500 μm on a quaternary single layer specimen. First crystal is silicon monochromator. Input wavelength :1.5 A

(a) VS 3998 has slight asymmetry on its right corresponding to a +ve mismatch; could be due to a thin layer.

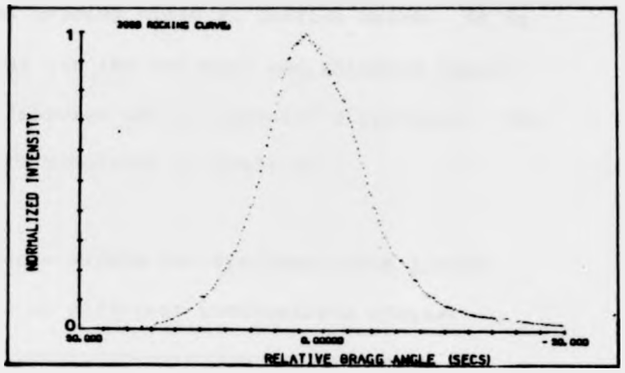

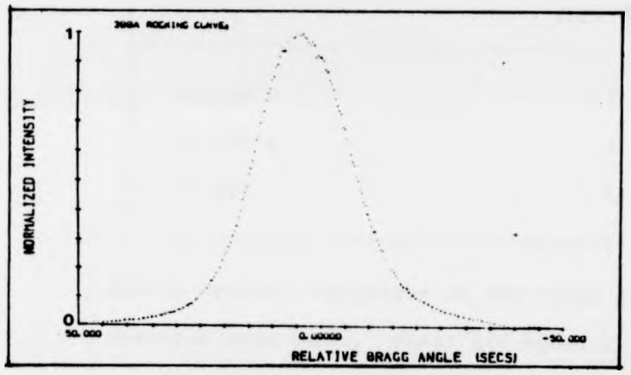

(b) VS 399A, slightly thicker,~500A, has a symmetric rocking curve.

(c) VS 397, around 2μm, has asymmetry to the left corresponding to a negative mismatch.

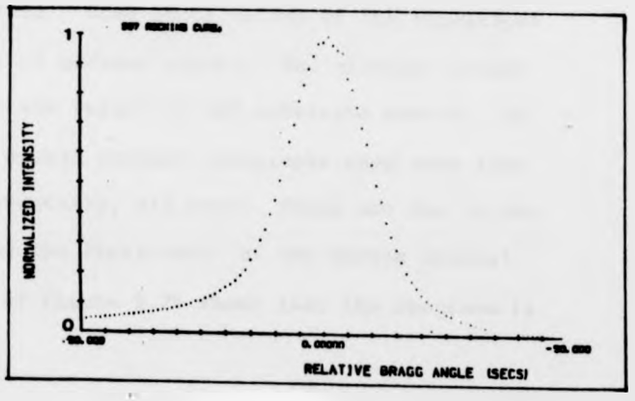

FIG 9.1 Double crystal rocking curve for a 400 reflection from a point 100x500 μm on a quaternary single layer specimen. First crystal is silicon monochromator. Input wavelength :1.5 A

(a) VS 3998 has slight asymmetry on its right corresponding to a +ve mismatch; could be due to a thin layer.

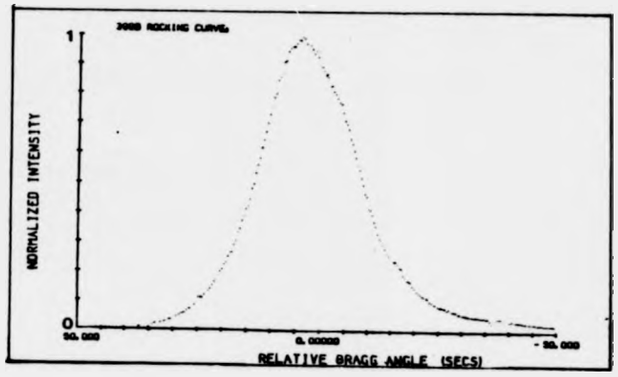

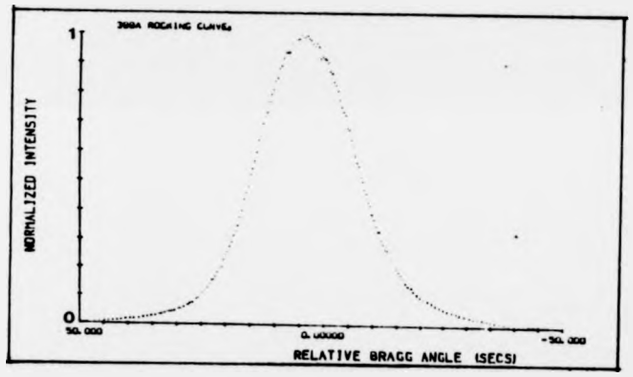

(b) VS 399A, slightly thicker,~500A, has a symmetric rocking curve.

(c) VS 397, around 2μm, has asymmetry to the left corresponding to a negative mismatch.

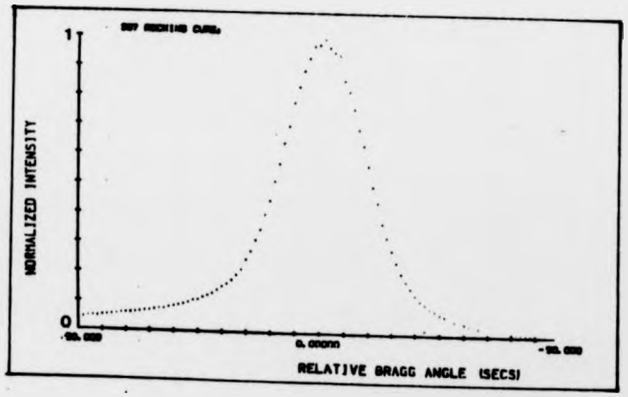

be due to compositional grading close to lattice match. It is interesting to note that for the thickest and thinnest layers the slight asymmetric features are in opposite directions. The rocking curve widths are tabulated in Table 9.1.

Table 9.1. Rocking curve widths for specimens with growth terminated at different intermediate stages.

Sample No.	Rocking curve widths (arc secs)
VS 399 B	20
VS 399 A	20
VS 397	15

Double crystal topographs of the three samples at the only peak observed were taken. These are shown in Figure 9.2. The topographs show no misfit dislocations, however some growth striations appear to be present. Some contrast is seen on the topograph due to the In melt on the surface. Some spots on one of the topographs were due to a bad batch of nuclear plates. The circular growth striations are probably the result of InP substrate growth. In addition to these, the double crystal topographs show some fine structures running horizontally, all over. These are due to the Si-monochromator used on the first axis of the double crystal camera. The topograph of Figure 9.2b shows that the specimen is bent.

(a) Topograph of VS 399B

(b) Topograph of VS 399A

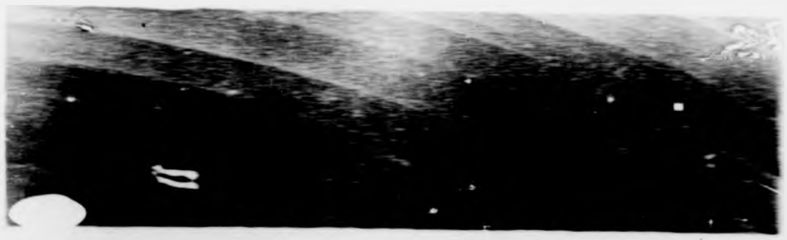

(c) Topograph of VS 397

1 mm

FIG 9.2 Double crystal reflection topographs for three single layer specimens of different thicknesses at the only peak observed for each specimen. Incident wavelength : 1.5 A, 400 reflection

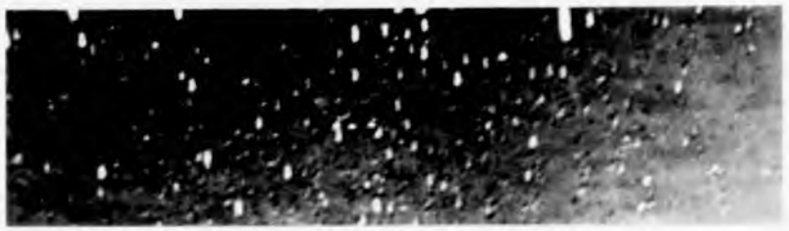

(a) Topograph of VS 399B

(b) Topograph of VS 399A

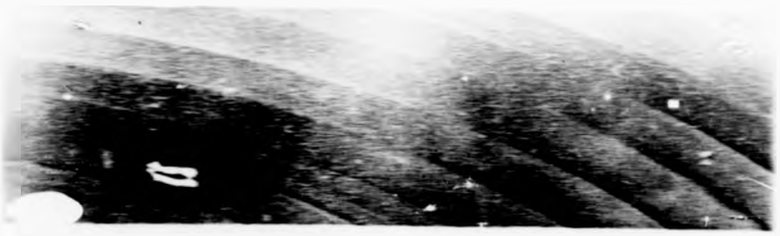

(c) Topograph of VS 397

1 mm

FIG 9.2 Double crystal reflection topographs for three single layer specimens of different thicknesses at the only peak observed for each specimen. Incident wavelength : 1.5 A, 400 reflection

9.2.2. Sample etched off to various thicknesses

A thick quaternary layer grown over an InP substrate was chosen for the purpose. The sample, L5, supplied by Plessey was reported to be around 4.2μm thick and doubly graded in mismatch, that is, the mismatch decreases with depth upto a certain depth and then increases with depth. This was a specimen intentionally grown graded, to test the control of growth.

Etching of the layer was carried out on an small section of the specimen by first dividing the sections into a number of segments and using a mask and a quaternary etchant to etch off progressively the segments to various thicknesses. The experimental arrangement is shown schematically in Figure 9.3a. A 3 : 1 : 1 H_2SO_4 : H_2O_2 : H_2O etchant was used. As already discussed in Chapter 8, the etching rate on a quaternary layer for this etchant at room temperature is approximately 1μm/min. The etching time was therefore set to about 10-15 secs so that about 0.25μm of the layer

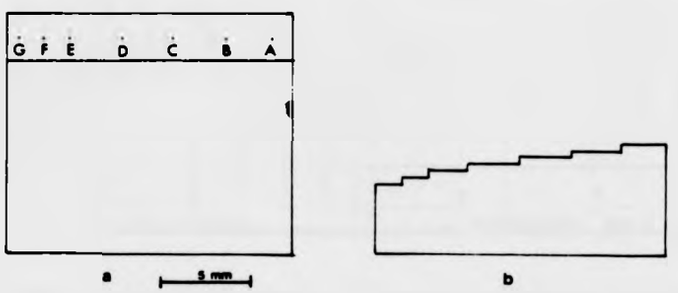

FIG 9.3 Experimental arrangement for etching the layer to various thicknesses.(a) Points A through G refer to the positions on each etched window where rocking curves are plotted. (b) A side view of the etching configuration.

was progressively etched off in each window, leaving a step layer arrangement as shown in Figure 9.3b. An experimental measurement of the step change in thickness of the layer was made using the Talysurf. The positions on the specimen where the thickness changes were measured are indicated in Figure 9.3a. Attempts to level the specimen indicated that the sample was highly non uniform over the right side of the section. The sample is probably slightly bent as well. Hence an appropriate levelling was done over the left half of the specimen; still then, the point C was out of the levelled plane. The results of the experiment are shown in the graph in Figure 9.4. The location of the different points are indicated in the graph. Step changes in thickness are seen in the graph. The graph however dips suddenly in the vicinity of point C and the change in thickness between C and D is also not

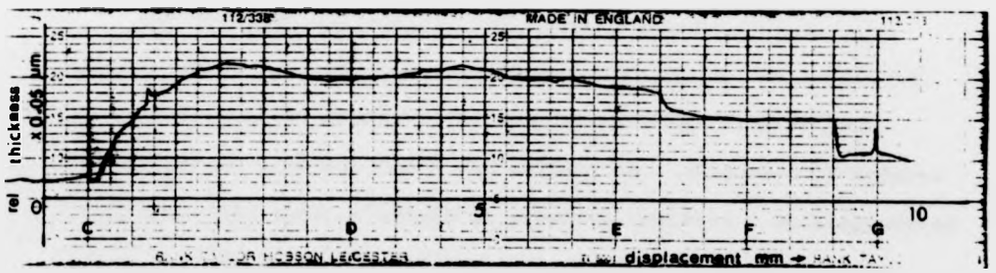

FIG 9.4 Graph showing a variation in the step change in thickness of the layer from one point to another, as plotted by the Talysurf.

properly indicated. The step change between D and E is made up of two steps with a total change of about 2.75 divisions = 0.137μm. Between E and F the change is approximately 3 divisions = 0.15μm while between F and G it is 0.21μm. The thickness changes as measured by the Talysurf are tabulated in Table 9.2 for the points C to G.

Table 9.2. Step change in thickness between adjacent positions on the specimen as measured by the Talysurf.

Position on specimen	C	D	E	F	G
Step change in thickness (μm)	-	.137	0.15	0.21	

The specimen was aligned for double crystal rocking curve measurements. A (100) InP crystal was used on the first axis of the double crystal camera. The camera was aligned for a beam wavelength of 1.5Å and for a 400 reflection. Alignment procedures have been discussed in detail in previous chapters. Rocking curves were recorded for a 400 reflection from a point on each etched window of the specimen. An aperture of 100 x 500μm was used, as before to define the points. Figure 9.5 shows a plot of the rocking curves. The effect of a graded mismatch is responsible

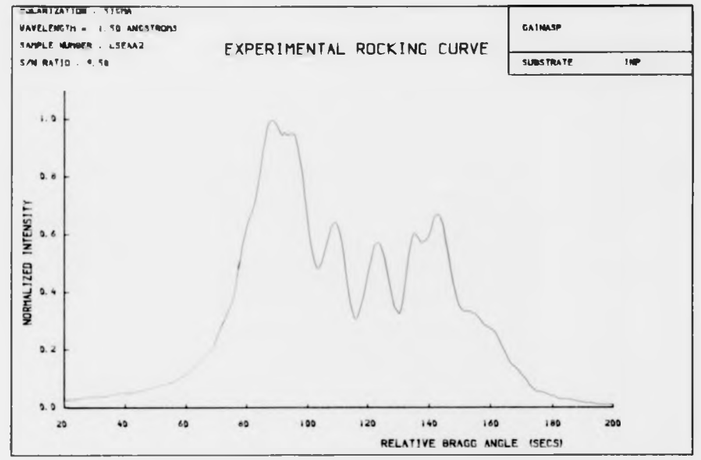

Figure 9.5a

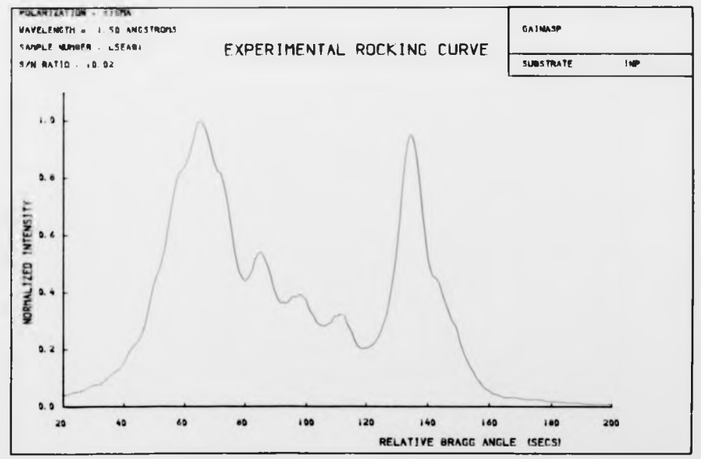

Figure 9.5b

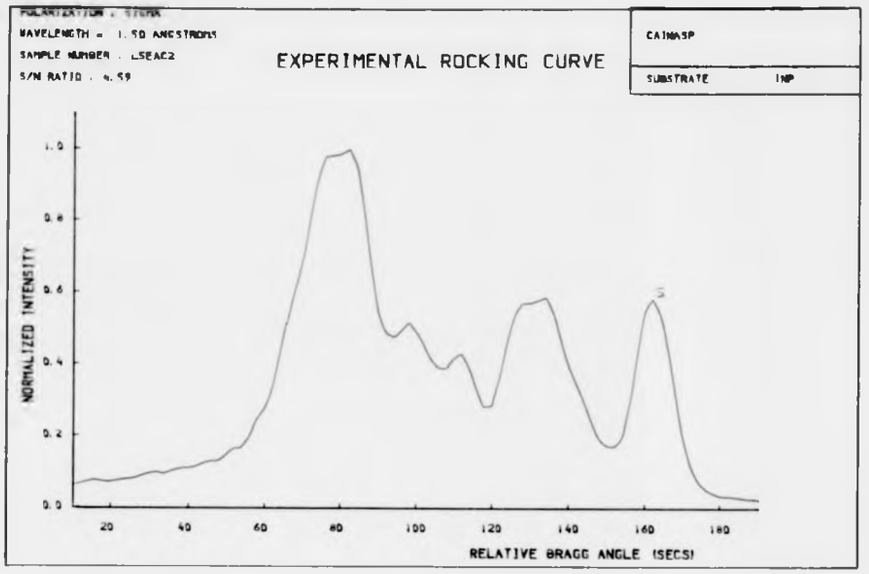

Figure 9.5c

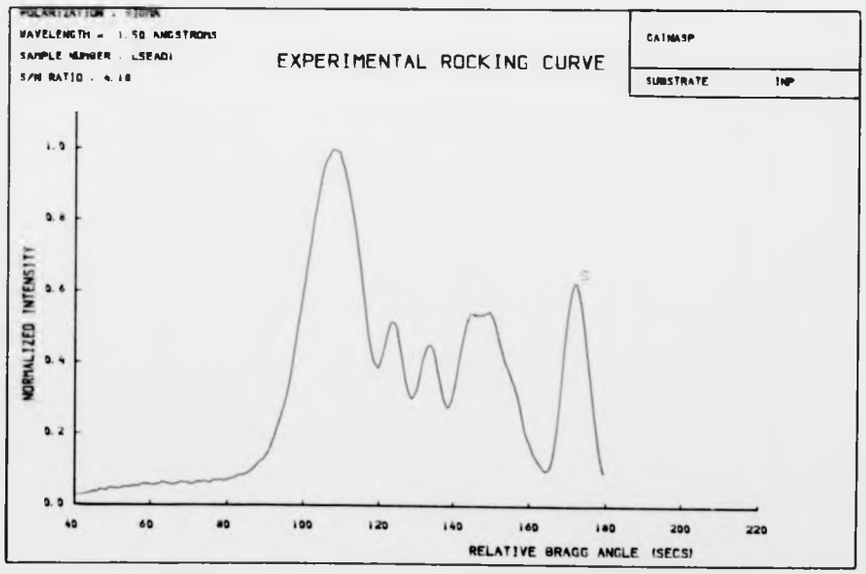

Figure 9.5d

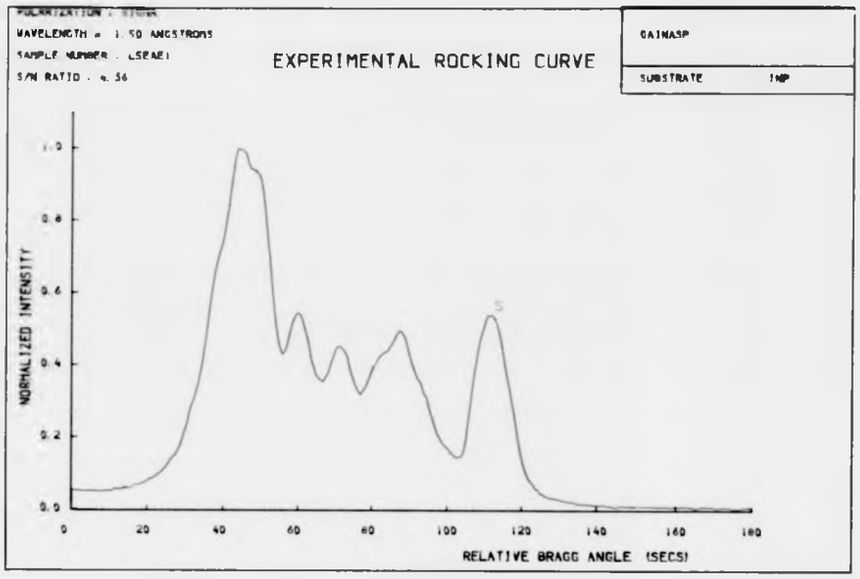

Figure 9.5e

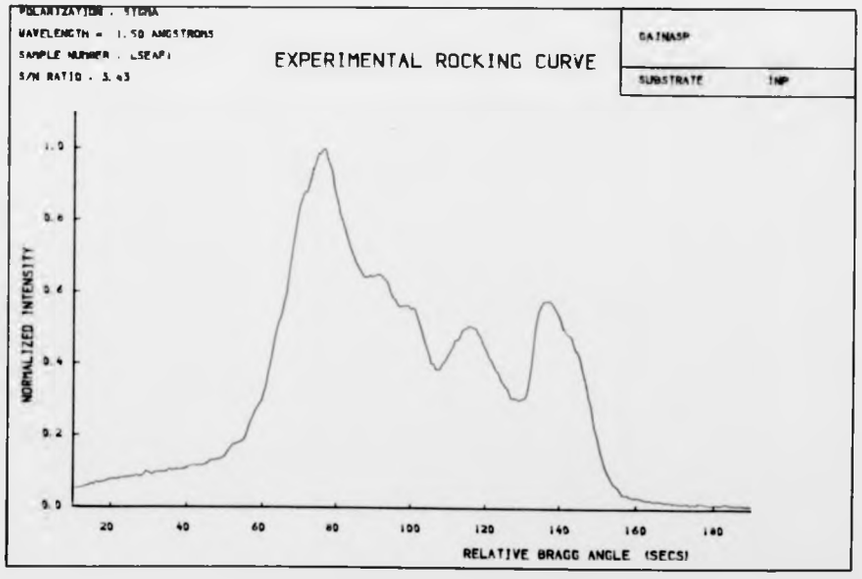

Figure 9.5f

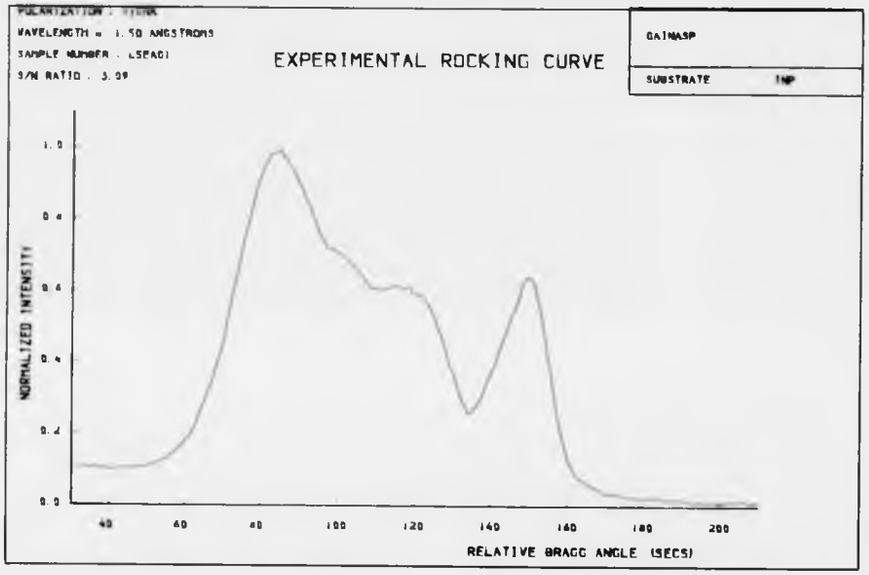
POLARIZATION : SIGMA
WAVELENGTH = 1.50 ANGSTROMS
SAMPLE NUMBER : LSEA01
S/N RATIO : 3.09
EXPERIMENTAL ROCKING CURVE
GAINASP
SUBSTRATE INP
NORMALIZED INTENSITY
1.0
0.8
0.6
0.4
0.2
0.0
40
60
80
100
120
140
160
180
200
RELATIVE BRAGG ANGLE (SECS)

Figure 9.5g

for such a shape in the rocking curve. This has already been discussed in Chapter 7. From a comparison of rocking curves and from a knowledge of the thickness of the layer it would be possible to identify the substrate peak. For instance, in Figure 9.5c, d and e, peak S is symmetric. In other curves, their shape is affected by the grading effects of the layer. The area under this peak in comparison to the area under the rest of the curve indicates that the peak S is due to the substrate, realizing that the extinction depth is roughly about 9μm for a 400 reflection, that is, reflection from the substrate would certainly be available. Ratios of the integrated intensities of the substrate to the layer peak for the various points are compared in Table 9.3.

Table 9.3. Relative layer thickness at the etched windows from the experimental rocking curves.

Position on the specimen	A	B	C	D	E	F	G
Relative layer thickness (approx)	.57	.41	1	.87	.86	.77	.70

Table 9.3 indicates that the relative thicknesses at the points A and B are indeed low. The substrate and layer peaks are not well separated in the rocking curves, hence the estimates for the relative layer thicknesses for the various positions are only

approximate but in any case, would indicate a general nature of thickness variation. Compared with the results of Talysurf measurement, Table 9.3, being only a rough estimate, does not agree very well; however, the variations shown in both Tables 9.2 and 9.3 are in the same direction.

In Chapter 7 a brief description of the nature of the specimen L5 was given. The specimen was grown to provide a test for the control of growth, and was thought of as graded in mismatch. A study on the theoretical calculation of rocking curve shapes, made in Chapter 10 would show that it is possible to simulate the experimental rocking curves and thereby extract details of the layer characteristics from the simulated curve. A satisfactory fit to the experimental curves at position C to G has shown that a linear grading nature of mismatch is more-or-less maintained and that the epilayer also consists of a thin strip of a constant mismatch close to the interface; however the same simulated model has failed to hold for the other two points on the specimen. The right side of the specimen has been found to be highly non uniform as observed both by Talysurf measurements and by experimental rocking curve analysis. It is interesting to note that on this side, in particular, the mismatch grading extends to the negative side. A slight negative mismatch is also seen at the position F, while at other positions the substrate peak is highly symmetrical. Hence it is clear that mismatch characteristics vary with position, and the same growth pattern does not hold for every point on the specimen.

Due to lack of control of etchant, it was not possible to etch the layer to the order of a few hundred Angstrons thick, as used in the previous method. This method does not, therefore, reveal changes in growth characteristics in the very early stages of epitaxy. However, negative mismatch characteristics of the layer are revealed for relatively low layer thicknesses. Hence these features must have been introduced at an initial stage of epitaxy, and that too, only in certain regions of the specimen.

9.3. Discussion

In lattice matched layers, initial stages of epitaxy showing a thin growth do not seem to exhibit a different growth characteristic than in thicker layers. For the specimen showing only island growths, it is possible that only the substrate reflection was observed in the rocking curve.

For the graded layer specimen,the relative thickness of the layers estimated from rocking curves reflect the general variation of the layer thickness and an accurate measure of the same is obtained from the results of the Talysurf experiment. These values, in fact, compare reasonably well with the thickness changes obtained from simulation studies. Thick graded layers show non uniformity in growth characteristics. Positional changes in characteristics are also observed. These fluctuations are found to be introduced in the early or intermediate stages of epitaxy.

10

COMPUTER SIMULATION OF ROCKING CURVES

AND THEIR COMPARISON

WITH EXPERIMENTAL CURVES

10.1. Introduction

From the results on various specimens, we have seen in previous chapters that the experimental X-ray rocking curves are highly sensitive to lattice strain in epitaxial structures. In particular, they are sensitive to lattice mismatch, thickness and uniformity of the epitaxial layers. A quantitative analysis of experimental rocking curves has also been found to provide detailed information on these factors.

In epitaxial layers, the diffraction of X-rays can be modelled fairly accurately by solving Taupin's derivation[1] which gives the ratio of the diffracted to incident beam amplitudes as a function of depth below the surface in accordance with equation (4.31), i.e.,

$$\frac{dX}{dZ} = \frac{i\pi}{\lambda \sin\theta_b} \left[c\psi_H X^2 + \{ 2\psi_o - \alpha_H(Z) \} X + c\psi_H \right] \quad \ldots(10.1)$$

Equation (10.1) is obtained using Takagi's dynamical theory of X-ray diffraction for a distorted crystal[2] and has been outlined briefly in Chapter 4. This method was first applied by Burgeat and Taupin[3] to study reflection profiles from boron diffused silicon and was followed by subsequent studies on diffused and ion implanted layers[4,5], and more recently, by Halliwell et al[6,7] on III-V ternary and quaternary layers. In this chapter simulation of rocking curves for III-V quaternary multilayer device structures using the solutions of Taupin's equation (10.1) is presented along with a comparison with some of the experimental rocking curves. By fitting the experimental curves, the details of the actual thickness

and compositional variation for the layers in the device can be predicted.

10.2. Calculation of Rocking Curves

The approach of Halliwell et al[6] has been adopted to calculate rocking curves for quaternary multilayer specimens. Due acknowledgements are to M.J. Hill[17] on whose earlier work of rocking curve simulation of ternary single layers, the present modification is based.

Equation (10.1) can be written in the form

$$\frac{dX}{dZ} = iA\,(B\,(X^2 + 1) + 2CX) \qquad \ldots(10.2)$$

where $A = \pi/\lambda \mathrm{Sin}\theta_b$

$B = c\psi_H$

and $C = \psi_o - \alpha_H(Z)/2$

where $\alpha_H(Z) = \lambda^2 \left(\frac{1}{d_H^2} - \frac{2\,\mathrm{Sin}\theta_b}{\lambda d_H}\right)$

$$\simeq -\frac{2\lambda}{d_H}\ \mathrm{Cos}\theta_b .\ (\theta - \theta_b)$$

θ being the angle of incidence of the beam with the Bragg plane.

ψ_o and ψ_H are related to the structure factor F by

$$\psi_o = -\frac{\lambda^2}{\pi V} .R_e .F_o$$

and $$\psi_H = -\frac{\lambda^2}{\pi V} .R_e .F_H$$

All the specimens considered for experimental rocking curve analyses were those grown on (100) InP. A symmetrical 400 reflection rocking curve was the most appropriate to observe, as peaks corresponding to small lattice parameter mismatch could be conveniently separated and ideally displayed on the angular scale. Furthermore the structure factors for a 200 reflection are too low while for a 100 reflection they are zero. Rocking curves were therefore simulated for a 400 reflection and for specimens with single or multilayers of InP or GaInAsP grown over (100) InP.

Equation (10.2) has a solution of the form

$$X = \frac{iB \tan \left[AK (Z-Z_o)\right]}{k - iC \tan \left[AK (Z - Z_o)\right]} \qquad \ldots(10.3)$$

for a thick uniform crystal, where the boundary condition is assumed as $X = 0$ at a point deep inside the crystal, and $K = \sqrt{C^2-B^2}$. At the surface of the crystal

$$X(O) = \frac{-C + K \sin \left[Im (K)\right]}{B} \qquad \ldots(10.4)$$

In order to obtain the reflectivity $R_1(\theta)$ of a single uniform thick crystal, X(O) from equation (10.4) is evaluated at different values of C, which in turn, is a function of the angle of incidence, θ, of the beam. For a thick uniform crystal with several epitaxial layers over it, if we assume a boundary condition that $X = X_o$ at $Z = Z_o$, then the solution for equation (10.2) is obtained as

$$X(Z) = \frac{X_o K + i(B + X_o C) \tan \left[KA (Z - Z_o)\right]}{K - i(C + BX_o) \tan \left[KA (Z - Z_o)\right]} \qquad \ldots(10.5)$$

Equation (10.4) is first evaluated for X at the surface of the substrate. This is then matched as a boundary condition with the value of X at the bottom of the first epilayer and using equation (10.5), X at the top of the layer is evaluated. The process is repeated until the amplitude ratio at the surface of the specimen is obtained. The constants B and C involve the structure factors and are considered as complex quantities to take into account the absorption effects. Accordingly the amplitude ratio X is obtained as a complex quantity. The reflectivity ratio R_2 is given by

$$R_2 = |X|^2$$

The reflectivity $R_2(\theta)$ at various angles of incidence can be obtained by following the above procedure for various appropriate values of C, C being a function of the angle of incidence, θ. To get the double crystal rocking curve $R(\theta)$ the reflectivity $R_1(\theta)$ of the first crystal (InP) is convoluted with the reflectivity $R_2(\theta)$ of the specimen[8].

10.3. Determination of Structure Factors

An accurate representation of the structure factors for the elements involved in a layer is essential in order to reflect the accuracy of the calculated curves, as is evident from the definitions of the constants A, B and C.

InP has a zinc blende structure with a face centred cubic lattice, with four equivalent points at 0, 0, 0 ; ½, ½, 0 ; ½, 0, ½; and 0, ½, ½. The structure factor of a material of the type $In_xGa_{1-x}As_yP_{1-y}$,

can be represented in a convenient form

$$F_{400} = 4.0 \quad [f_{In}(x) + f_{Ga}(1-x) + f_{As}y + f_{P}(1-y)] \quad ...(10.6)$$

where f refers to the structure factors for the element concerned. Values of f_{In}, f_{Ga}, f_{As} and f_p can be obtained from standard tables[9] for both the 000 and 400 reflections, and thus F_o and F_H are calculated. We however see from equation (10.6) that a complete knowledge of the composition x and y of the layer is required in order to calculate the structure factor for the compound. Also, f, as obtained from tables, are those calculated on the assumption that the frequency of the incident radiation is large compared with any absorption frequencies of the atom. In practice, the scattering factors will have to be duly corrected for any dispersion effects.

10.3.1. Composition x and y

In simulating a rocking curve, one of the characteristics of the layers that has to be specified, is the mismatch M defined as

$$M = \frac{a - a_o}{a_o}$$

where a = lattice parameter of the layer, and

a_o = lattice parameter of the substrate

= 5.86875Å

The mismatch value for each layer along with its variation within the layer is thus required.

On the other hand, to determine the structure factor for a constituent layer, we require the alloy composition x and y. The alloy compositions are found[10,12] to bear a definite empirical relationship with material parameters of the layer, namely the lattice parameter and the energy band gap.

For alloys of the form $In_xGa_{1-x}As_yP_{1-y}$ the lattice parameter a(x,y) can be expressed[11] as

$$a(x,y) = xy\ a(InAs) + x(1-y)\ a(Inp) + y(1-x)\ a(GaAs) + (1-x)(1-y)\ a(GaP) \quad ...(10.7)$$

by assuming a linear variation between the binary constituents (Vegards law).

Equation (10.7) accordingly becomes

$$a(x,y) = 5.4512 + 0.41755x + 0.20225y - 0.0125xy \quad ...(10.8)$$

The band gap variation is taken from the data of Olsen et al[10]:

$$Eg(x,y) = 2.75 - 1.33y - 1.4x + 0.33xy - (0.758 - 0.28y)\ x(1-x) - (0.21 - 0.109x)\ y(1-y)\ \ eV \quad ...(10.9)$$

To determine x and y, both a and Eg must be known so that equations (10.8) and (10.9) can be solved. For ternary layers like $Ga_xIn_{1-x}As$, y = 1 and the mismatch M, by itself, is sufficient to specify the lattice parameter, a, and hence, x.

10.3.2. Dispersion Corrections for Atomic Scattering Factors

The scattering power of a bound electron of an atom may in an actual case, be more or less than that of a free electron. Furthermore, the phase of the scattered X-rays may be different.

The corrections for the scattering factor thus take the form

$$f = f_a + \Delta f' + i\Delta f'' \qquad \ldots(10.10)$$

where $\Delta f'$ and $\Delta f''$ are the real and imaginary terms accounting for the dispersion correction.

Cromer and Libermann[13] have calculated $\Delta f'$ and $\Delta f''$ using relativistic scattering theory. The correction factors are available for standard X-ray wavelengths. Making use of these data[9] the correction factors for any wavelength λ can be computed using a polynomial approximation:

$$\Delta f' = a_{11} + (\lambda - 2.291)\, a_{12} + (\lambda - 2.291)(\lambda - 1.935)a_{13} + (\lambda - 2.291)(\lambda - 1.935)(\lambda - 1.154056)a_{14} + \ldots\ldots \qquad \ldots(10.10)$$

$$\Delta f'' = a_{21} + (\lambda - 2.291)a_{22} + (\lambda - 2.291)(\lambda - 1.935)a_{23} + (\lambda - 2.291)(\lambda - 1.935)(\lambda - 1.54056)a_{24} + \ldots\ldots \qquad \ldots(10.11)$$

the right-hand side containing as many terms as are correction data available for discrete wavelengths, like Cr Kα, Fe Kα, Cu Kα

etc., the more the number of terms, the wider being the range of application of λ for calculating $\Delta f'$ and $\Delta f''$. The constants a_{ij} are evaluated from the data for known wavelengths.

10.3.3. Atomic Scattering Factors

Following the procedure outlined in the above section, the correction terms for the atomic scattering factors for In, Ga, As and P can be written in the form

$$\Delta(In) = F1 + iF2$$

$$\Delta(P) = F3 + iF4$$

$$\Delta(Ga) = F5 + iF6$$

$$\Delta(As) = F7 + iF8$$

The structure factors f_H and f_o for a 400 reflection and 000 reflection at any wavelength λ, can thus be determined for the elements In, Ga, As or P by substituting the values of f_a from standard tables. Equation (10.6) can now be used to determine F_H and F_o:

$$F_H = 4.0 \left[(f_H)_{In}\, x + (f_H)_{Ga}\, (1-x) + (f_H)_{As}\, y + (f_H)_P (1-y)\right] \quad \ldots(10.12)$$

$$F_o = 4.0 \left[(f_o)_{In}\, x + (f_o)_{Ga}\, (1-x) + (f_o)_{As}\, y + (f_o)_P\, (1-y)\right] \quad \ldots(10.13)$$

F_H and F_o can now be directly employed in equation (10.5) to evaluate X and hence $R_2(\theta)$.

Ideally, the structure factors should be corrected for thermal vibrations by multiplying by a Debye-Waller factor, e^{-M}.

10.4. Effect of tetragonal distortion on the epitaxial layer mismatch

The mismatch parameter of the epitaxial layer used in the calculation of structure factors corresponds to the relaxed lattice parameter a of the layer and is given by

$$M = \frac{a - a_o}{a_o}$$

a_o being the lattice parameter of the substrate. It is assumed that the epitaxial material has a cubic unit cell of dimension a. In actual practice when a thin epitaxial layer is grown over a substrate, lattice accommodation by a tetragonal distortion occurs as a result of which the unit cell for the layer adopts a dimension $a_\ell \times a_\ell \times c_\ell$, where c_ℓ is the unit cell dimension perpendicular to the interface and a_ℓ, the dimension parallel to the interface. For coherent layers $a_\ell = a_o$. The mismatch m measured experimentally corresponds to the lattice parameter c_ℓ of the layer.

$$\text{Hence } m = \frac{c_\ell - a_o}{a_o}$$

Using the theory of elasticity, the stress-strain relations for the present case can be written as

$$\varepsilon_1 = S_{11}\sigma_1 + S_{12}\sigma_2 \qquad \ldots(10.14)$$

$$\varepsilon_2 = S_{12}\sigma_1 + S_{11}\sigma_2 \qquad \ldots(10.15)$$

$$\varepsilon_3 = S_{12}\sigma_1 + S_{12}\sigma_2 \qquad \ldots(10.16)$$

where $\varepsilon_1 = \varepsilon_2 = \frac{a - a_\ell}{a}$

is the strain in the x and y directions parallel to the plane of

the interface.

$\varepsilon_3 = \dfrac{a - c_\ell}{a}$ is the strain in the z direction perpendicular to the interface, $\sigma_1 = \sigma_2$ is the stress in the x or y directions and S_{ij} are the stiffness coefficients.

Equations (10.14) to (10.16) for the present case become

$$\varepsilon_1 = \varepsilon_2 = (S_{11} + S_{12})\,\sigma_1 \qquad \ldots(10.17)$$

$$\varepsilon_3 = 2S_{12}\,\sigma_1 \qquad \ldots(10.18)$$

In terms of the Young's modulus E and Poisson's ratio ν the above stress-strain relations can be written[14]

$$\varepsilon_1 = \varepsilon_2 = \frac{(1 - \nu)}{E}\,\sigma_1$$

$$\varepsilon_3 = -\frac{2\nu}{E}\,\sigma_1$$

Thus $\dfrac{\varepsilon_3}{\varepsilon_1} = -\dfrac{2\nu}{1 - \nu}$ $\qquad \ldots(10.19)$

By definition, $\dfrac{\varepsilon_3}{\varepsilon_1} = \dfrac{a - c_\ell}{a - a_\ell}$ $\qquad \ldots(10.20)$

Equating (10.19) and (10.20), we get

$$\frac{a_\ell - a}{a_\ell - c} = \frac{1 - \nu}{1 + \nu}$$

For coherent layers $a_\ell = a_o$

Hence,

$$\frac{a - a_o}{a_o} = \frac{1 - \nu}{1 + \nu} \cdot \frac{c_\ell - a_o}{a_o}$$

or $$M = \frac{1 - \nu}{1 + \nu} \cdot m \qquad \ldots(10.21)$$

Published data[15], are available for ν corresponding to binary compounds. For ternary and quaternary compounds, an appropriate linear interpolation between the binary constituents is made to calculate the value of ν. In general ν is approximately equal to 1/3. Accordingly $M = m/2$.

The mismatch M corresponding to the relaxed lattice parameter of the layer is thus approximately one half of the mismatch calculated from experimental rocking curves. An experimental rocking curve with a mismatch m can therefore be simulated for a mismatch $M = m/2$. In the following sections, the mismatch referred to is the mismatch M, unless otherwise indicated.

10.5. Rocking Curve Simulation

We have already seen in Section 10.2 that once the reflectivity curves for R_1 and R_2 are determined, the rocking curve for the specimen $R(\theta)$ can be calculated by convoluting $R_1(\theta)$ with $R_2(\theta)$.

It is intended to compare experimental rocking curves from specimens whose layer thicknesses and mismatch variations across the heteroepitaxial layers are not well defined, by simulating a

curve for a similar structure. The layer thickness and mismatch variation parameters are then slightly adjusted about an initially chosen value, until a reasonable agreement with the experimental rocking curve is obtained. The set parameters in the simulated curve will then predict the thickness and compositional variation across the layers in the experimental specimen. A judicious choice of the initial values is needed in order to make the computing time reasonable. One has therefore to take great care in interpreting the initial values from the experimental curves. Etching off each layer in sequence using selective etchants and plotting experimental rocking curves in each case and comparing between them would give the closest possible initial values. Before attempting to simulate rocking curves of experimental specimens, we give below some calculated curves for a wide range of assumed structures.

10.5.1. Single epitaxial layers of uniform composition

Rocking curves were simulated for single ternary and quaternary layers of various thicknesses and mismatch parameters (M). As long as the lattice mismatch is constant throughout the layer, the structure factors F_H and F_o would remain fixed and hence the reflectivity profile for the layer is expected to be sharp. In Figure 10.1 the calculated curves are shown for a ternary GaInAs layer over InP substrate, for a wide range of thicknesses between 0.1 and 5.0μm and mismatch parameters between 100 and 500 ppm. For a layer with a mismatch of 100 ppm, the minimum layer thickness

for which the layer peak could be resolved is about 0.5μm (Figure 10.1a), while for a 0.2μm thick layer, the smallest mismatch for which the layer peak could be resolved is about 400 ppm (Figure 10.1b). Figure 10.2 shows the calculated curves for a quaternary InGaAsP layer with a band gap energy of Eg = 0.996 eV, corresponding to an emission wavelength of 1.245μm. The layer peak height for any mismatch increases with increasing layer thickness, while the substrate peak height decreases accordingly. The peak separation increases with increasing mismatch parameter. The mismatch has been considered as positive, so the layer lattice parameter is larger than that of the substrate, hence for the same incident wavelength, the layer will diffract at a smaller Bragg angle. In other words the layer peak is to the left of the substrate peak in the rocking curve.

Using Bragg's law, the peak separation ($\Delta\theta$) can be related to the mismatch (M) for the present case, by approximately

$$(\Delta\theta)_{secs} = \frac{0.4\lambda}{\sqrt{(8.6-\lambda^2)}} \; M(ppm) \; ; \; \lambda \text{ in Angstroms} \qquad \ldots(10.22)$$

From Figures 10.1 and 10.2 we see that the layer peak width (full width at half maximum) is very large for small layer thicknesses and reduces almost exponentially with increasing thickness, with a limiting value for large layer thicknesses.

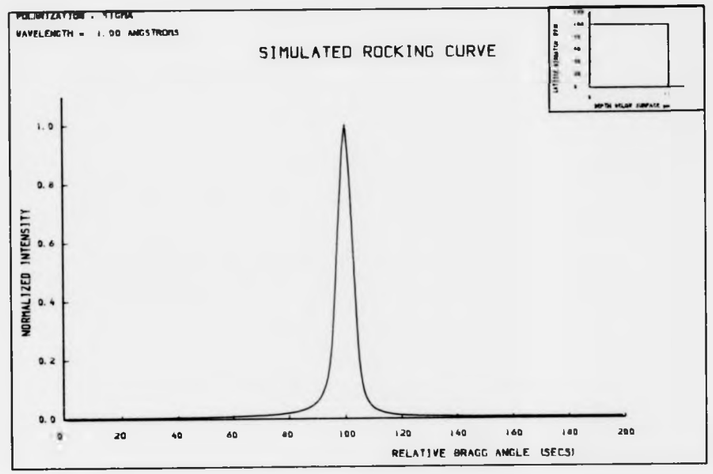

Figure 10.1a - 1

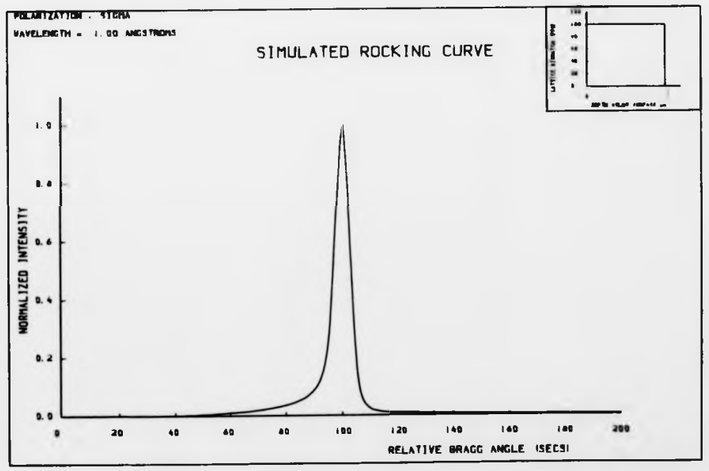

Figure 10.1a - 2

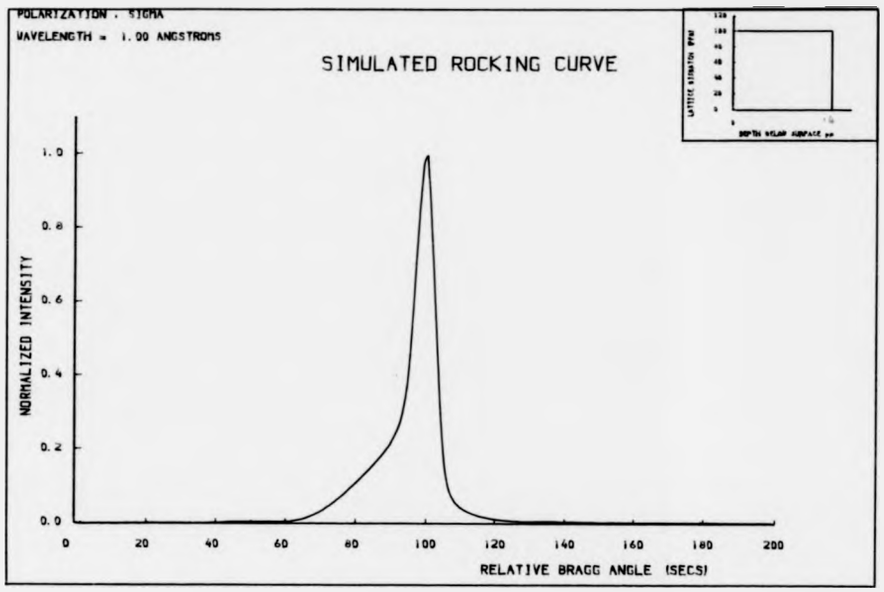

Figure 10.1a - 3

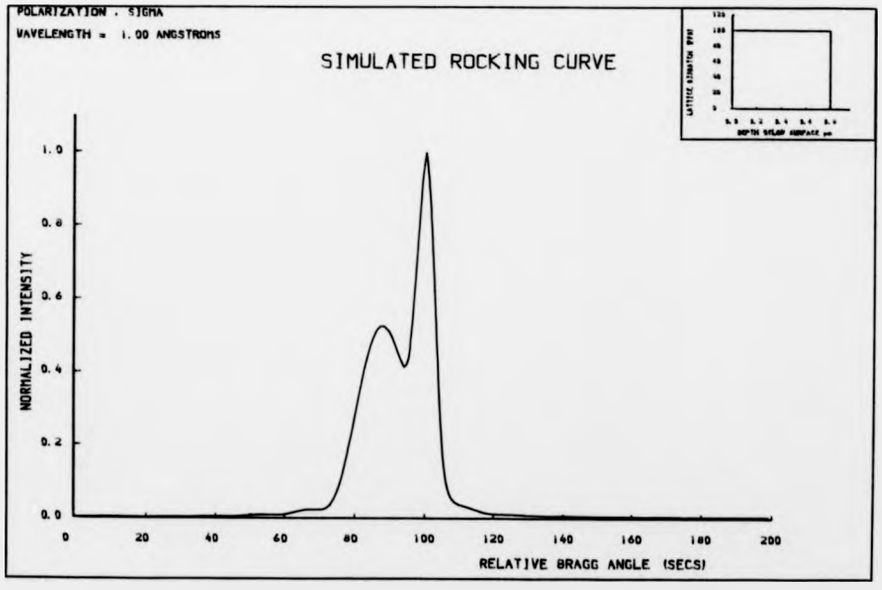

Figure 10.1a - 4

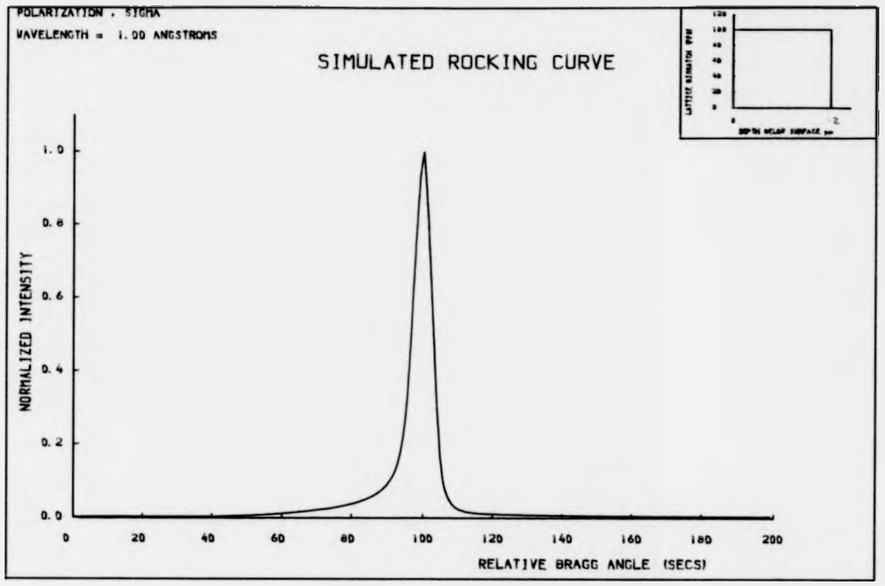

Figure 10.1b - 1

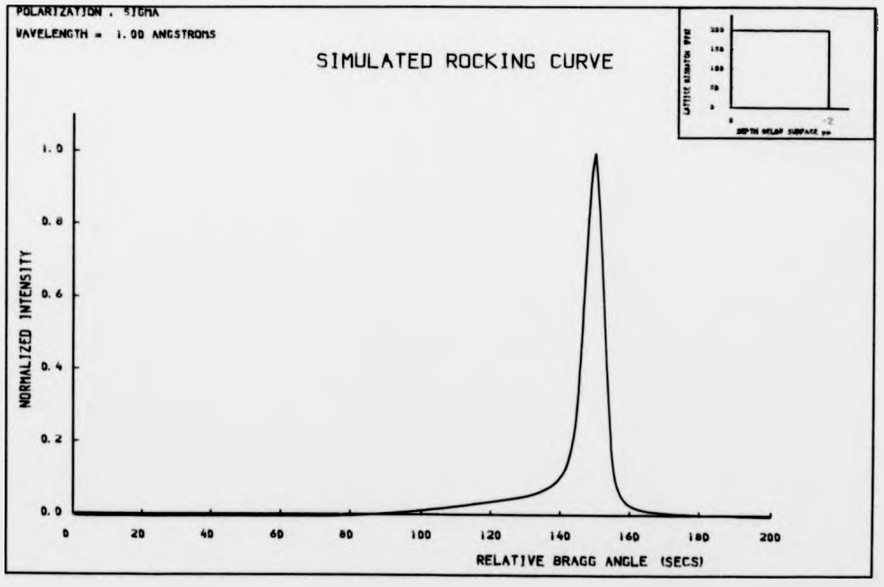

Figure 10.1b - 2

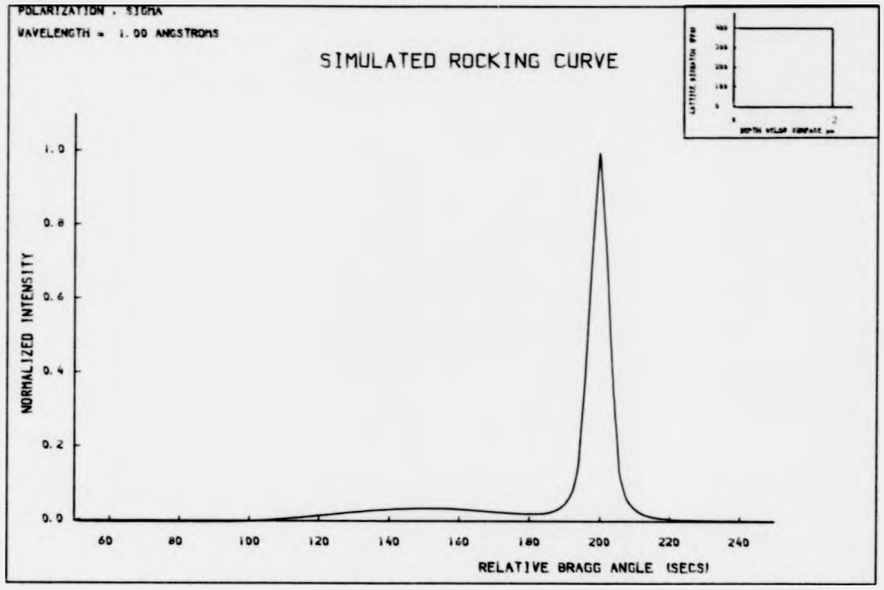

Figure 10.1b - 3

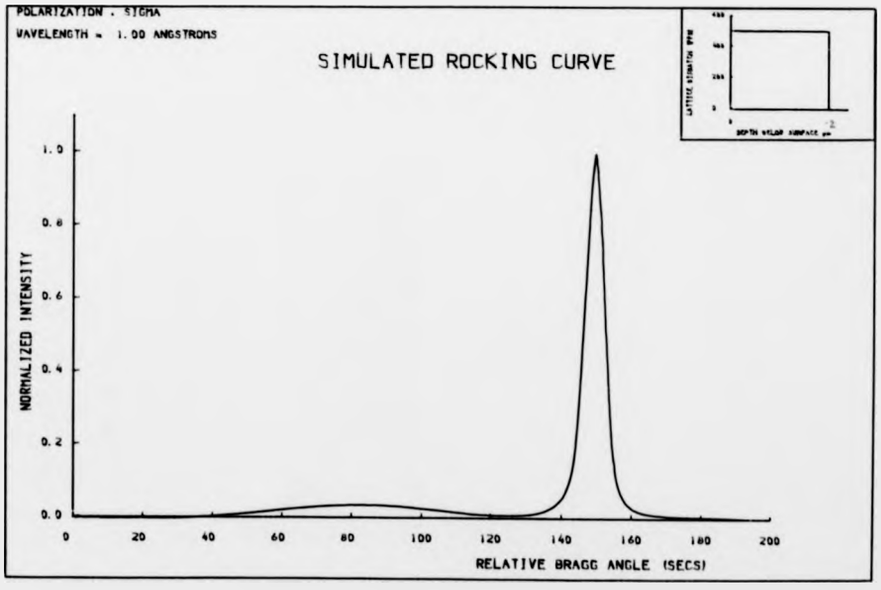

Figure 10.1b - 4

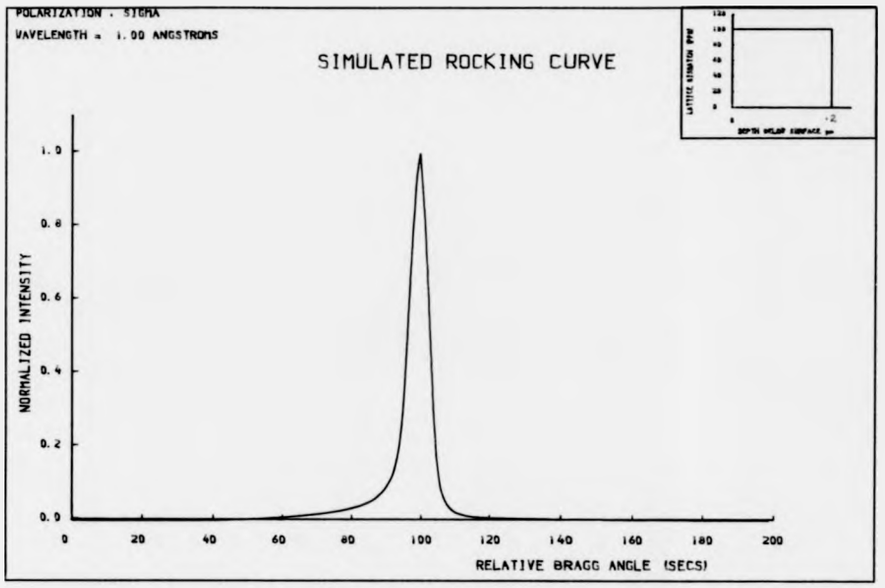

Figure 10.2a - 1

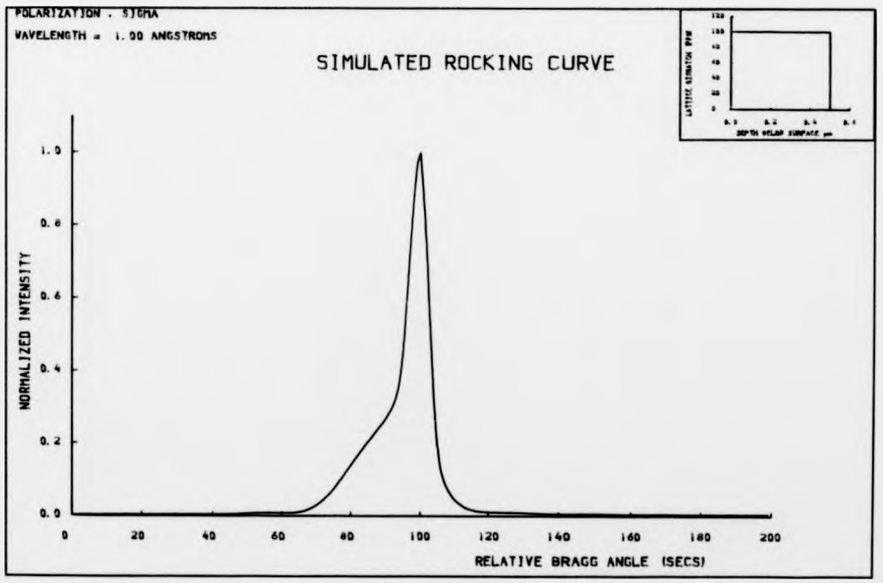

Figure 10.2a - 2

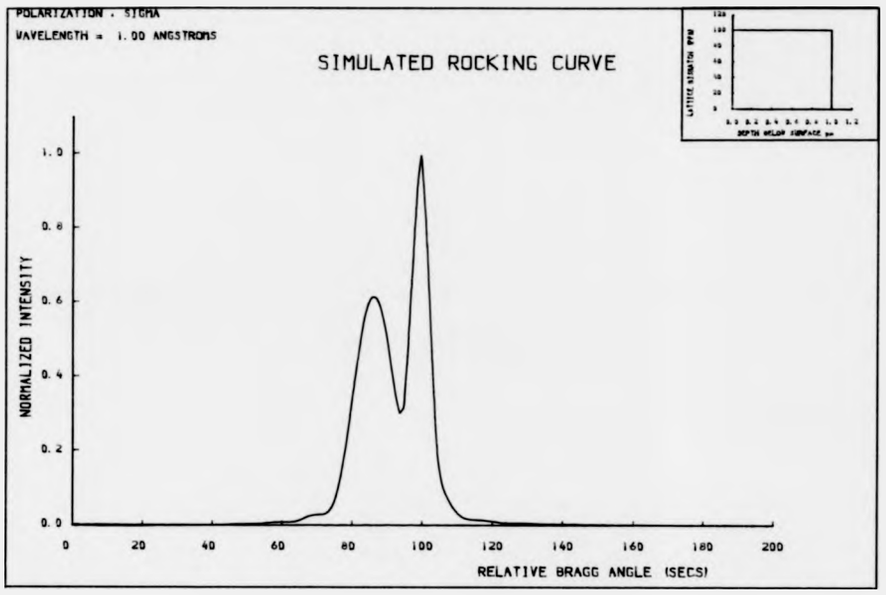

Figure 10.2a - 3

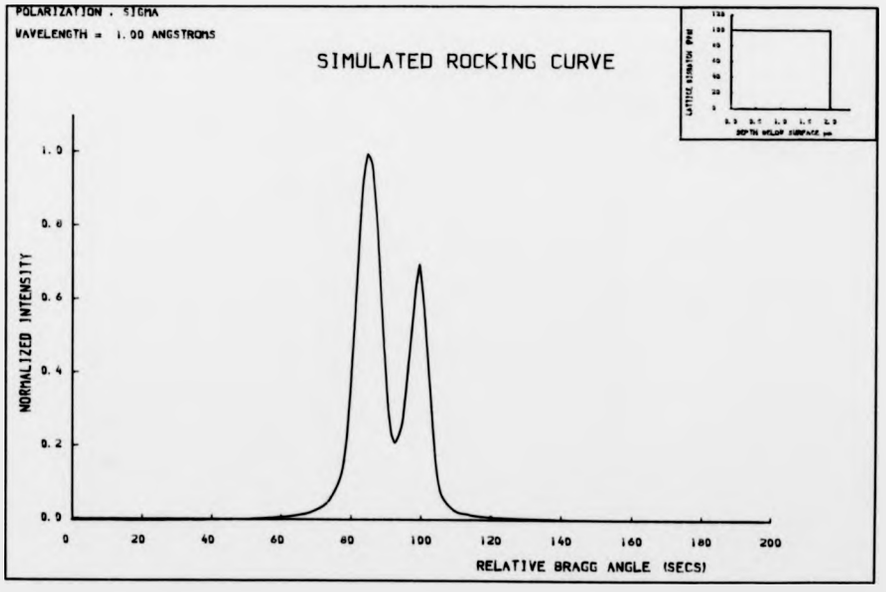

Figure 10.2a - 4

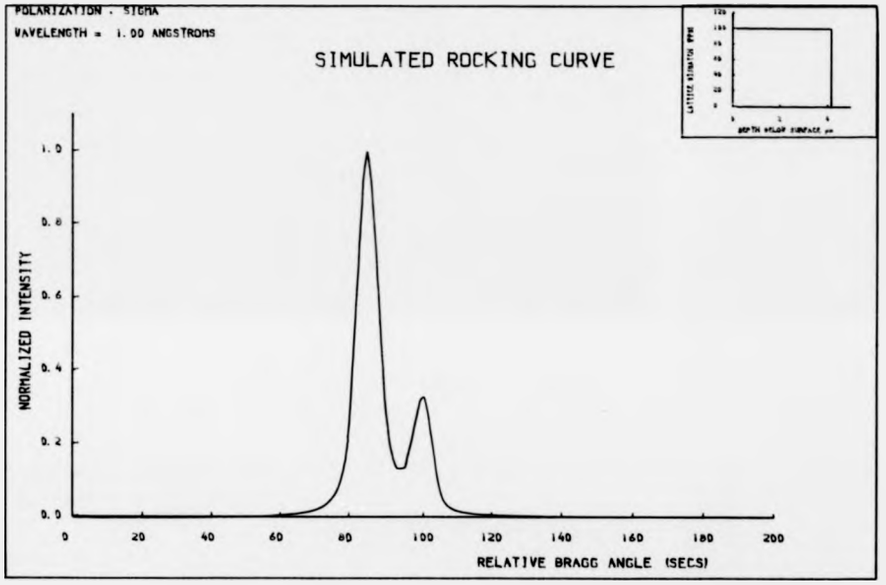

Figure 10.2a - 5

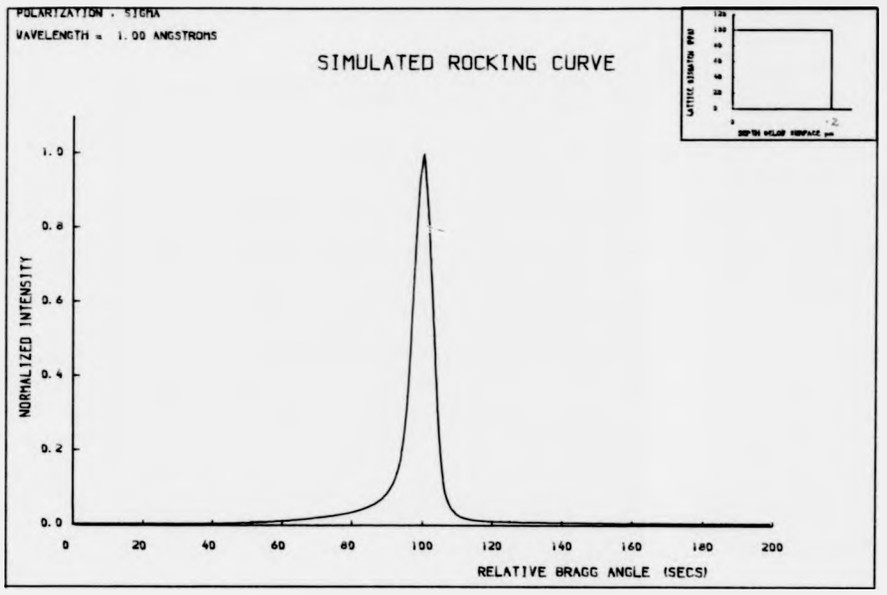

Figure 10.2b - 1

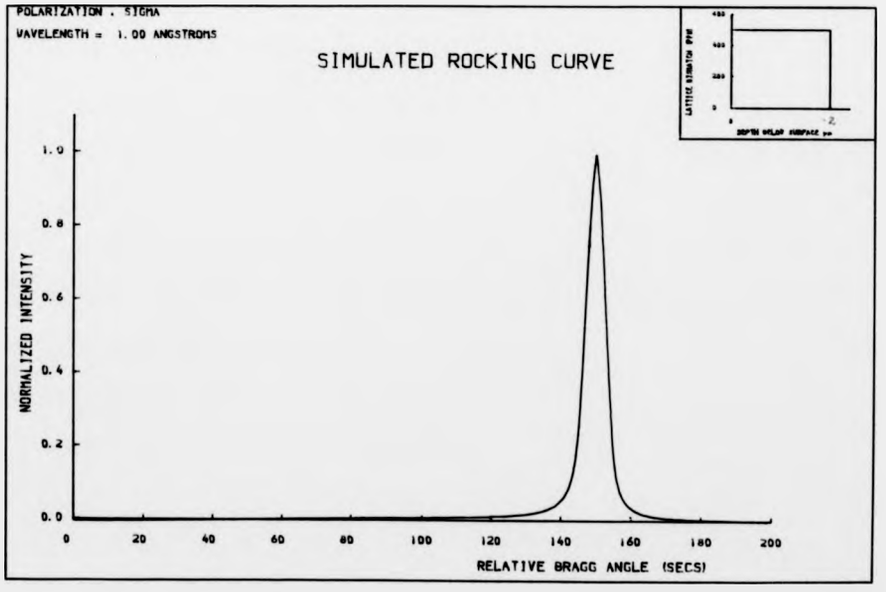

Figure 10.2b - 2

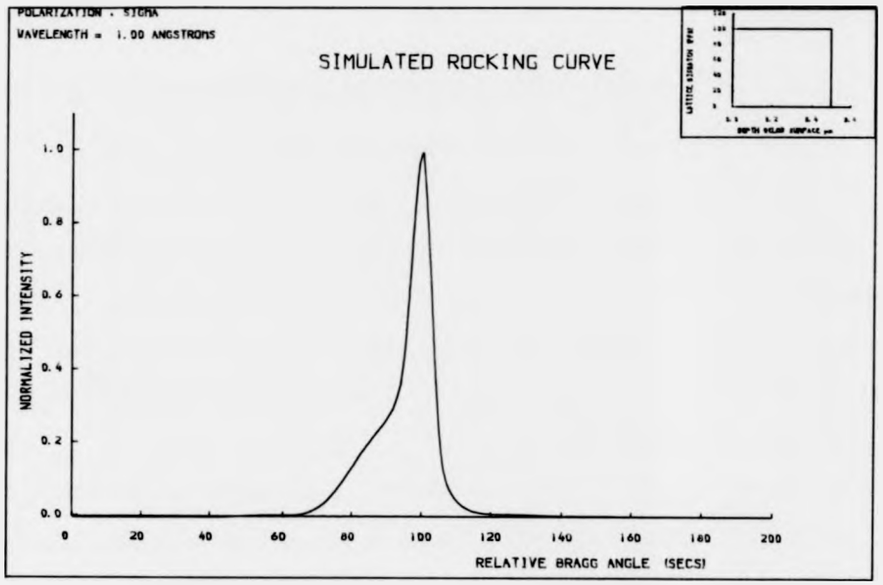

Figure 10.2b - 3

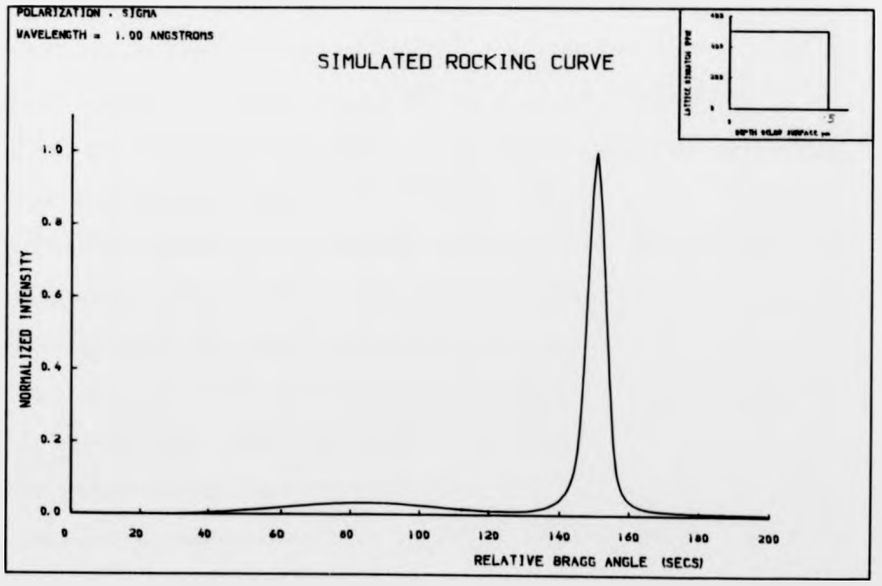

Figure 10.2b - 4

10.5.2. Single epitaxial layers of varying composition

In some ternary heterostructure lasers, the composition is graded in an intermediate layer between the substrate and the heterostructure so as to match the lattice constant at the active layer - heterojunction interface. Even though this is not necessary for quaternary heterostructures, there have been reports[16] of compositionally graded quaternary $Ga_xIn_{1-x}As_{1-y}P_y$ active layers having been grown to achieve emission at wavelengths as short as 0.647μm. It was therefore interesting to see the effects of a graded mismatch on the shape of the simulated rocking curves. Rocking curves were therefore calculated wherein the mismatch parameter was assumed to vary linearly with the layer depth, with a certain slope. In Figure 10.3 the calculated curves are shown for a linearly graded quaternary epitaxial layer for various thicknesses and mismatch gradients. The emission wavelength has been chosen at 1.31μm corresponding to a energy band gap of 0.947 eV. In all the cases the average mismatch for the layer has been assumed constant at 500 ppm. Figure 10.3a shows the effect of changing the mismatch gradient in a layer of constant thickness 2.0μm. We find that the peak separation is no longer well defined, the layer peak height gradually reduces and at the same time the layer peak broadens, forming an increasing number of undulations. With an increase in the mismatch gradient, the thickness of the layer being constant, the mismatch limits are expected to widen around the average value of 500 ppm. This is therefore expected to broaden the epilayer peak. Since the total

integrated intensity from a layer of constant thickness will have to be constant, the layer peak height reduces at the same time as it broadens. In the rocking curve calculations, the epilayer has been assumed to be divided into a large number of lammellae, large enough to assume a gradual change of the mismatch parameter from one lamella to another. The top lamella is assumed to have the largest mismatch. According to this model, a strong but slightly asymmetric peak is expected to start at a position corresponding to the large mismatch due to lamellae at the top. Due to absorption effects of these lamellae, the reflected intensity from the underlying lamellae corresponding to a smaller mismatch, is expected to be slightly reduced. We would therefore expect a wedge shaped layer peak corresponding to the sum of a series of equally spaced peaks of identical half width and a gradually reduced intensity. The calculated rocking curve does not show a wedge shaped epilayer peak in all cases, particularly for epilayer thicknesses less than 1.0μm. Furthermore some of the undulations are rather more sharp than expected. In Figure 10.3b, the effect of changing the thickness of the graded layer for a constant mismatch gradient, is shown.

10.5.3. Epitaxial multilayer structures

As we have seen before, double heterostructure lasers require multilayers of InP and InGaAsP grown over InP substrates. When rocking curves from such multilayer structures are calculated, it is observed that in certain cases, by increasing the number of layers but keeping the total thickness the same, the calculated

curves show peaks at unexpected positions. For example, in Figure 10.4 rocking curves are calculated for a quaternary InGaAsP multilayer structure grown over an InP substrate. A total thickness of 2.0μm for the multilayers is assumed. Initially two epilayer peaks are seen corresponding to two mismatch levels. When the number of layers is increased the peaks separate into several positions while the peak (A) corresponding to an average mismatch level keeps building up. In the limit of a large number of extremely thin layers, a single peak with an average mismatch is what will be observed in the calculated rocking curve for the range of Bragg angles considered.

The situation is similar to that for a superlattice where, in addition to the average lattice reflection, satellite peaks are also observed, for an extended range of Bragg angles, at positions in reciprocal space determined by the period of lattice distortion due to the thin alternate layers of periodically changing composition. In fact,the shape, intensity and location of the average lattice reflection and their satellites allow a characterization of superlattice structure. This has been the subject of recent interest for the characterization of quantum well devices by double crystal rocking profiles[18].

Figure 10.5 shows the effect of increasing the total thickness, keeping the number of layers the same. The splitting of the peaks seen only in Figure 10.5a is therefore dependent on the thickness of each individual layer. In double heterostructure lasers abrupt mismatch changes at short periods seldom occur. The active

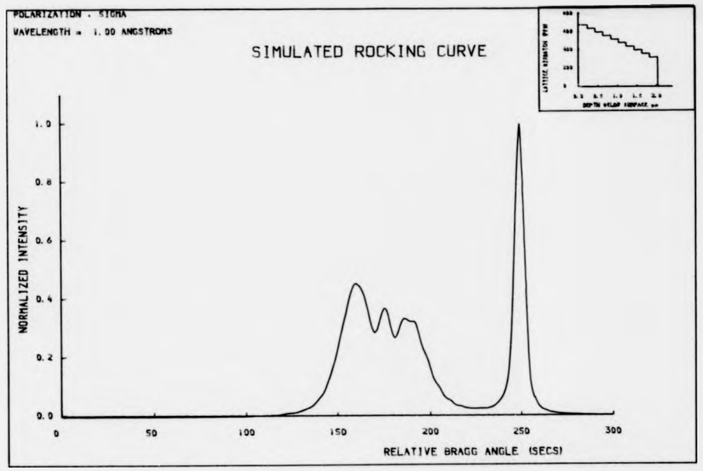

Figure 10.3a - 1

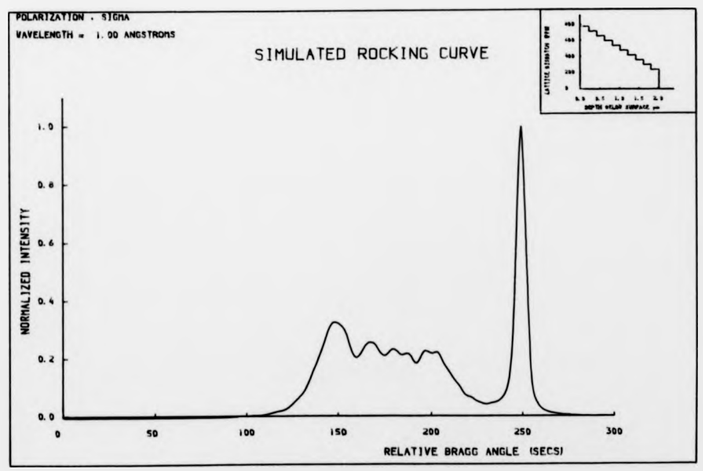

Figure 10.3a - 2

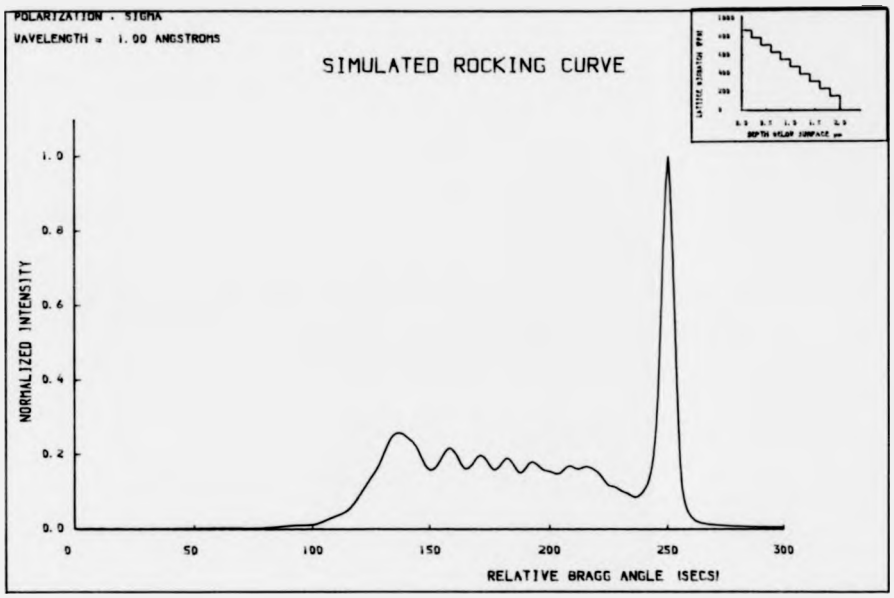

Figure 10.3a - 3

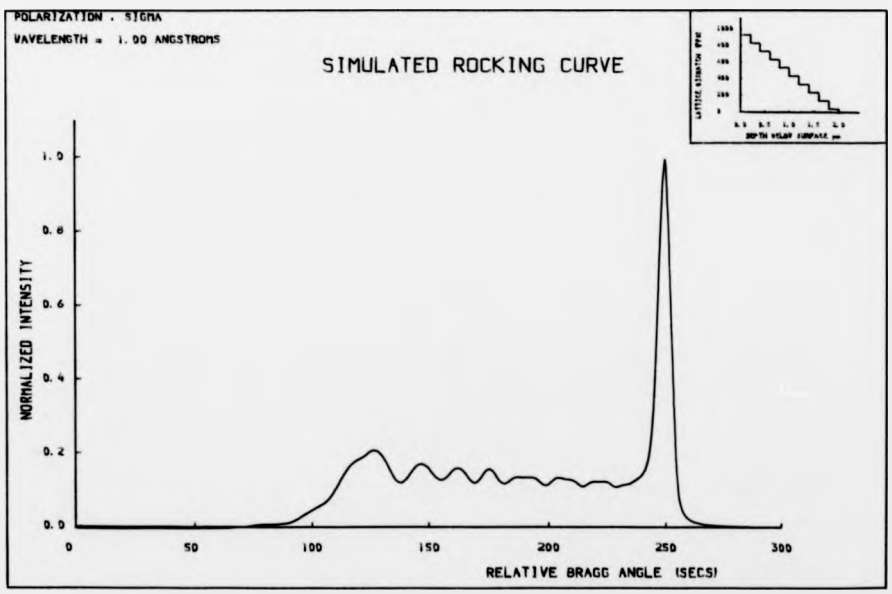

Figure 10.3a - 4

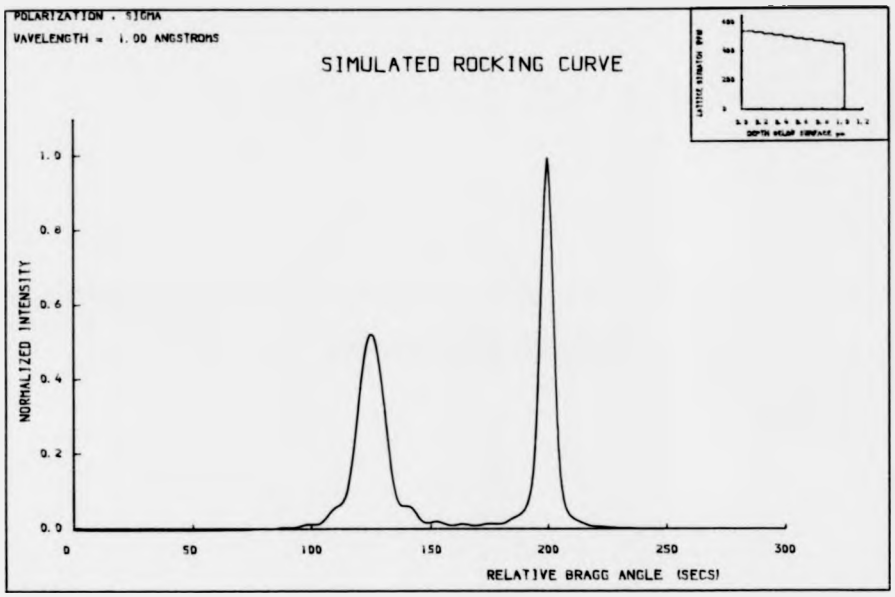

Figure 10.3b - 1

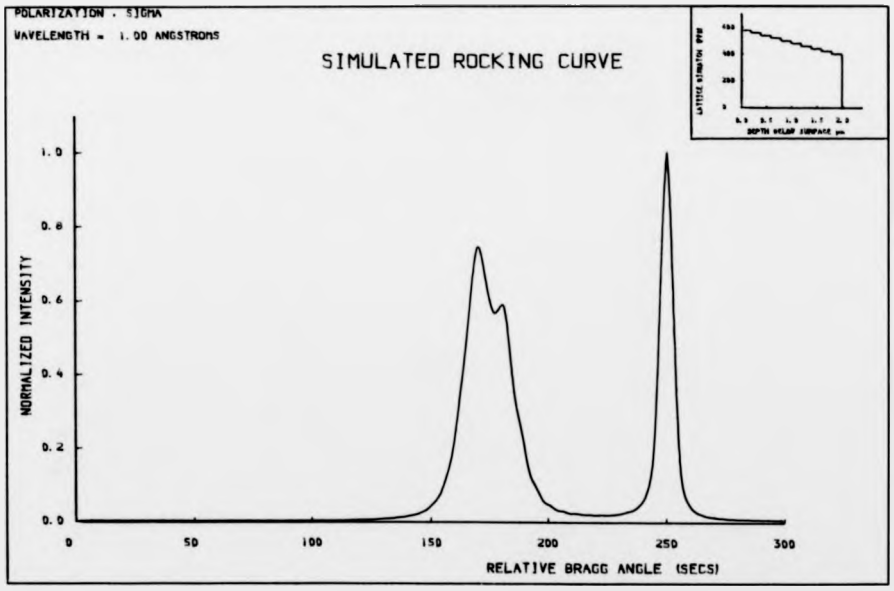

Figure 10.3b - 2

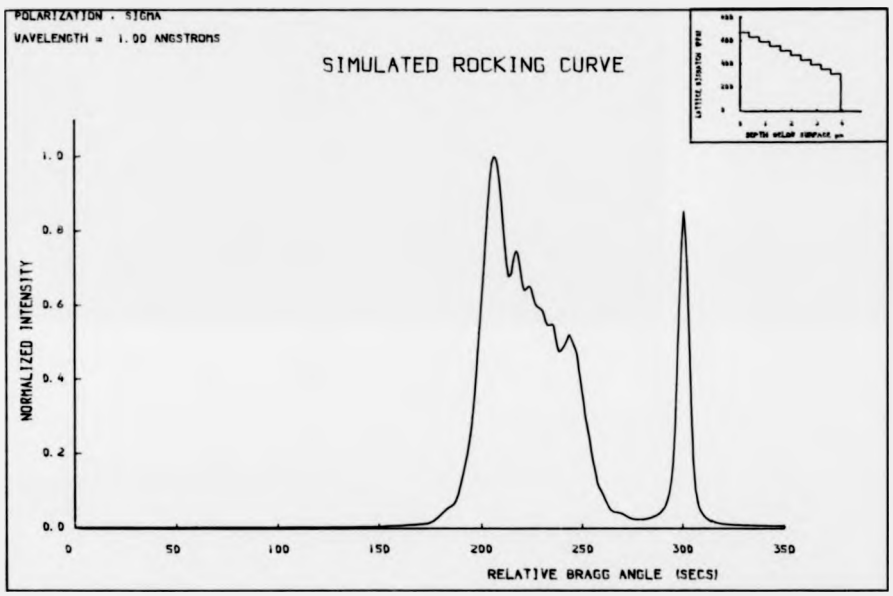

Figure 10.3b - 3

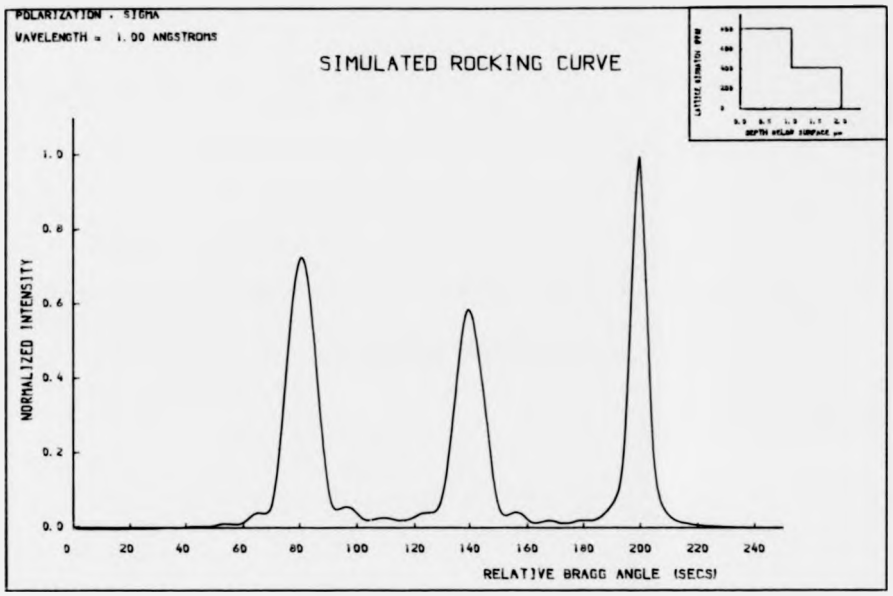

Figure 10.4 - 1

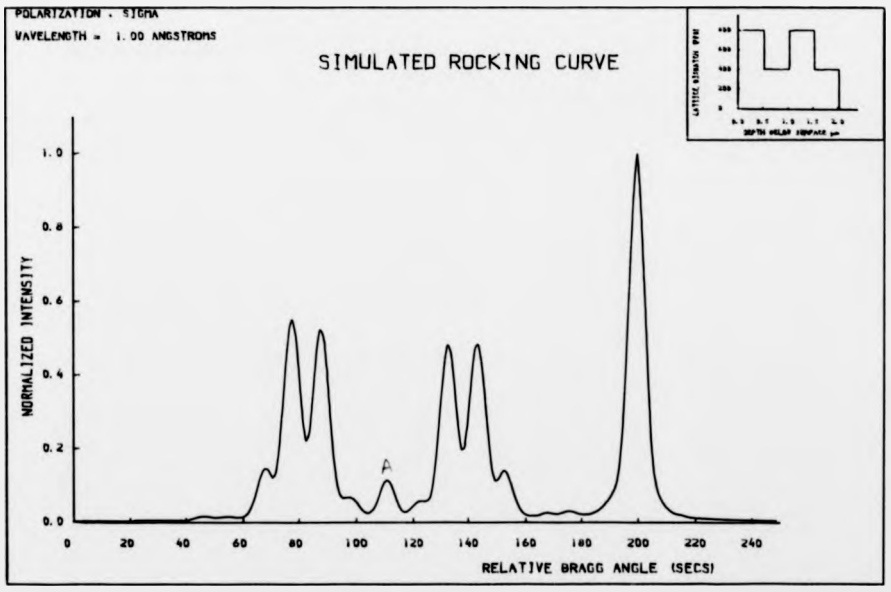

Figure 10.4 - 2

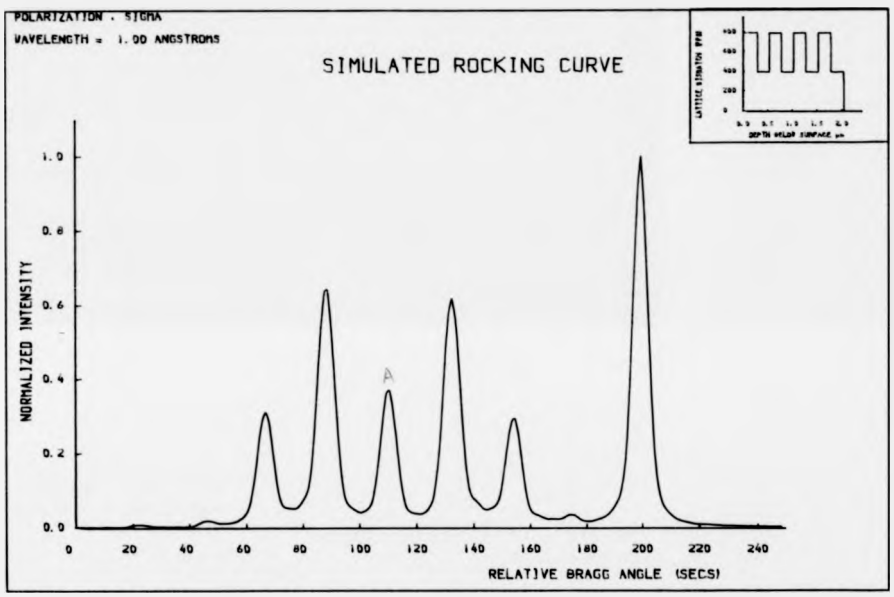
POLARIZATION . SIGMA
WAVELENGTH = 1.00 ANGSTROMS
SIMULATED ROCKING CURVE
NORMALIZED INTENSITY
1.0
0.8
0.6
0.4
0.2
0.0
A
0
20
40
60
80
100
120
140
160
180
200
220
240
RELATIVE BRAGG ANGLE (SECS)

Figure 10.4 - 3

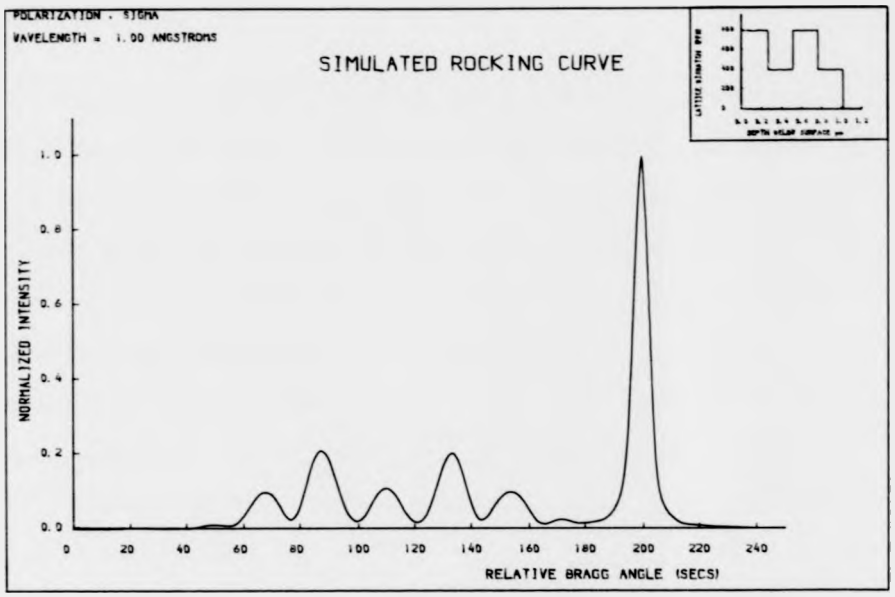

Figure 10.5 - 1

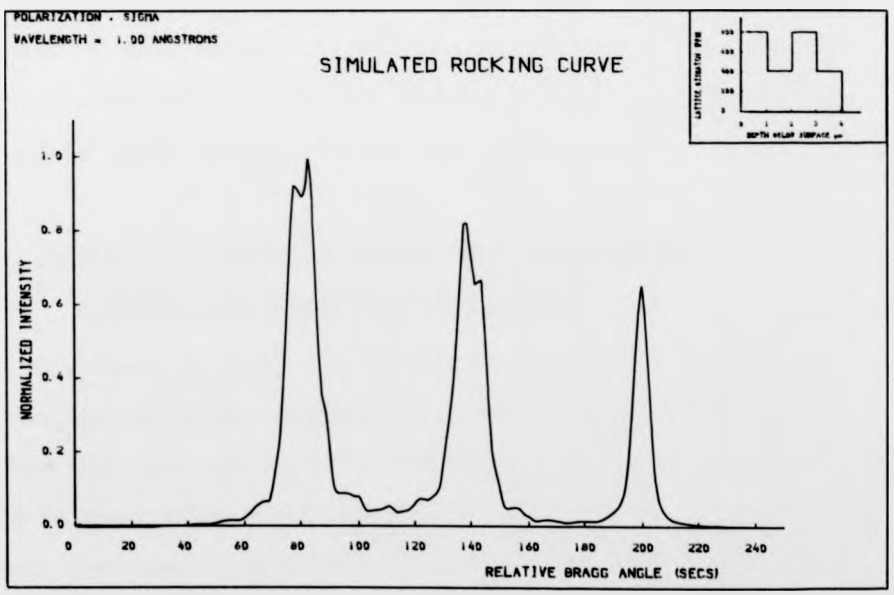

Figure 10.5 - 2

and the cap layers are usually thin, about 0.3μm or so but the cladding layers and buffer layers are thick, about 2μm and 2-4μm respectively and as long as compositional changes during growth of quaternary layers are avoided (unless intentionally graded) an experimental rocking curve can be satisfactorily simulated. Even if there is some complexity in the shape of the rocking curve, it is possible to have a satisfactory fit, as is demonstrated in the following section. It is however generally agreed that in view of the complex pattern of rocking curves from multilayer structures as seen in Figures 10.4 and 10.5 and also of the fact that in a double heterostructure laser, several parameters of the hetero-epitaxial layers are available for adjustments in order to fit experimental rocking curves, one has to proceed with great caution in interpreting experimental rocking curves from such structures. In spite of the complexity, a remarkable agreement of the simulated rocking curves with experimental curves has been observed in many specimens. These are described in the next section.

10.6. Theoretical Fitting of Experimental Rocking Curves

10.6.1. A double heterostructure laser, R154

This laser structure has been duly analyzed experimentally and the results of the experimental studies reported in Chapter 8. We find that this structure has a quaternary buffer layer quite close in composition to InP and with a reported thickness of greater than 6μm, a quaternary active layer, around 0.2μm thick, an InP layer ∿ 2.1μm thick and finally a ternary GaInAs cap

$\sim$ .15μm thick. As described in Chapter 8, the initial experimental analysis carried out by observing rocking curves from structures by selectively etching off each layer from the top and subsequently comparing them with rocking curves from the unetched region yielded invaluable information about the approximate composition of the layers, their mismatch values and their rocking curve widths. The mismatch parameters obtained from the experiments were duly corrected for tetragonal distortion to give a 'relaxed' mismatch parameter M that is required for the rocking curve calculation. From the experimental analysis it was suggested that the buffer layer was probably made up of two sections, one with a mismatch of around M = 250 ppm and the other with a mismatch of around M = 100 ppm. By using this data however, some of the kinks observed in the experimental curve cannot be accounted for, unless one of the sections is assumed linearly graded with mismatch between 100 and 250 ppm and the other with a constant mismatch of 250 ppm. The mismatch for the active layer, 0.2μm thick, is set at 150 ppm while the InP and GaInAs cap have been assumed lattice matched. The energy band gap of the buffer, being close in composition to InP, has been set at 1.35 eV while that of the active layer is set at 0.947 eV (corresponding to the reported emission wavelength λ = 1.31μm). With these initial parameters, rocking curves were calculated for the entire structure. It was observed that the thickness of the buffer layer had to be set at 9.0μm in order that a reasonable fit is observed. This is shown in Figure 10.6a where the comparison is made with an experimental rocking curve

from an unetched area of the specimen. Next the ternary cap is removed from the proposed model for the simulation. The calculated rocking curves are now compared with a corresponding experimental curve from a similar region. Figure 10.6b shows even a better agreement between the simulated and experimental curves. The InP layer is now removed from the simulated model leaving only the active layer and the buffer layer. The buffer layer thickness is now intentionally set at 6.0μm to see if there is any effective change. The calculated rocking curve does not however seem to fit very well with the corresponding experimental curve (Figure 10.6c). The buffer layer does not seem to be thick enough to prevent the reflection from the InP substrate from appearing, as is the case in the experimental observation. Even restoring to the original buffer thickness did not seem to cut off the substrate reflection. One reason for the slight lack of agreement may be the fact that the experimental rocking curves were observed at different points on the specimen and, as pointed out in Chapter 7, there is always a possibility of a localized fluctuation in the uniformity of thickness and composition of grown layers. By increasing the buffer layer thickness to 9.8μm the rocking curves (Figure 10.6d) seem to have a better agreement. However, the tail of the peak on the left in Figure 10.6d does not still agree. An attempt to stretch the tail of this peak by giving a graded mismatch for this layer proved worse in Figures 10.6e, f and g. An attempt to increase the difference in mismatch levels in order to try to match the peak positions in Figure 10.6d resulted in a

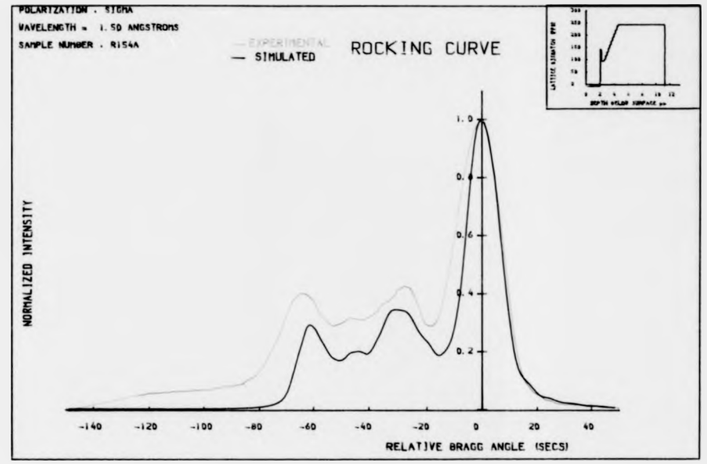

Figure 10.6a

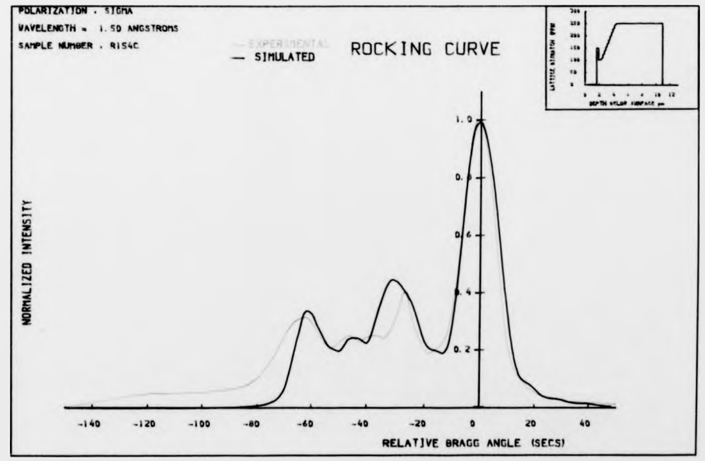

Figure 10.6b

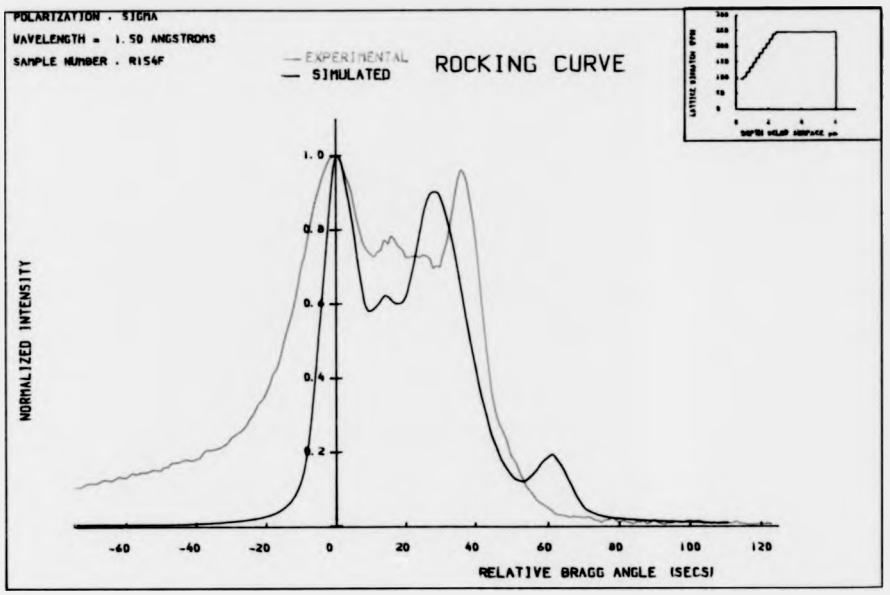

Figure 10.6c

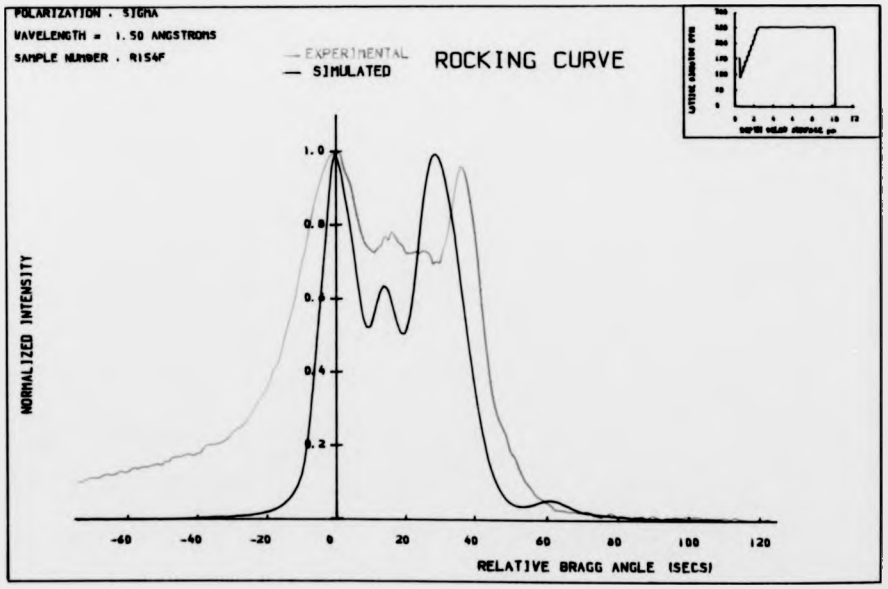

Figure 10.6d

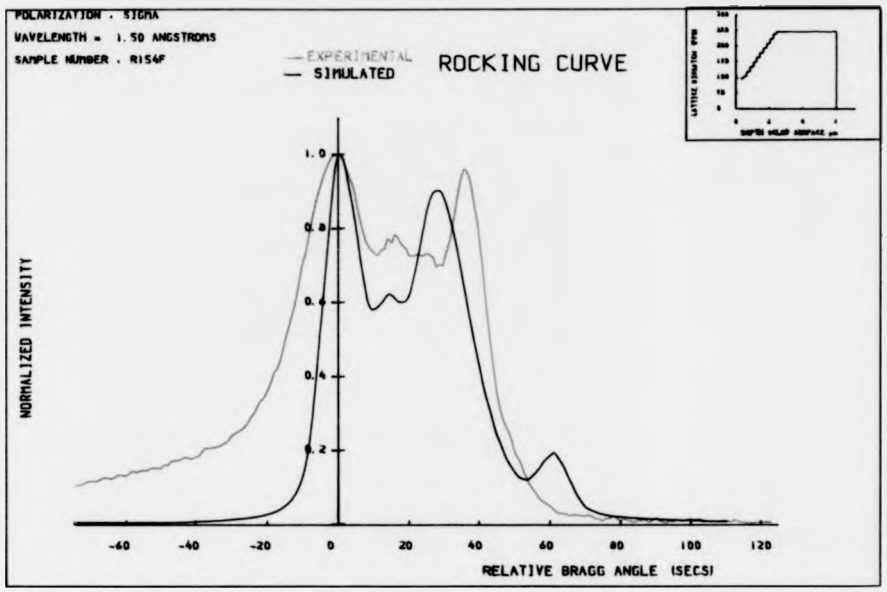

Figure 10.6c

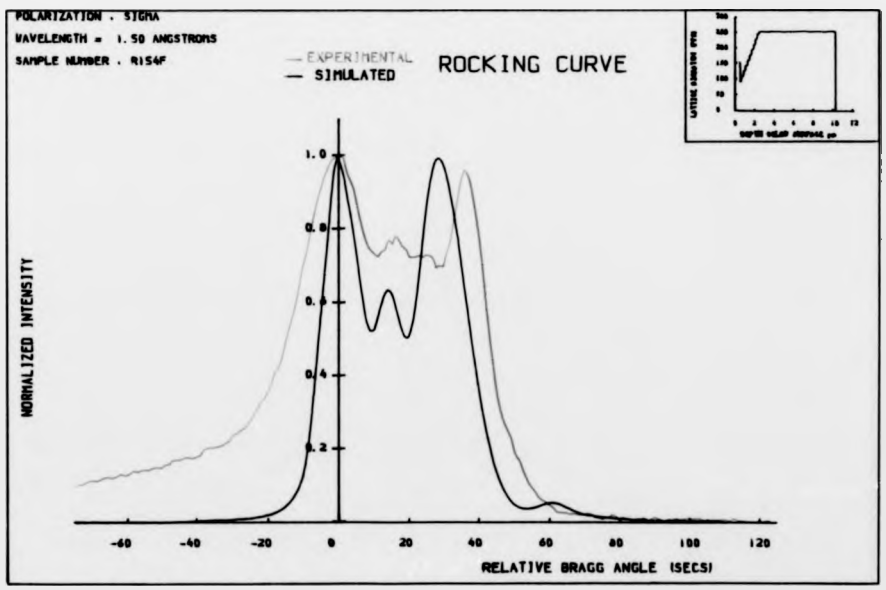

Figure 10.6d

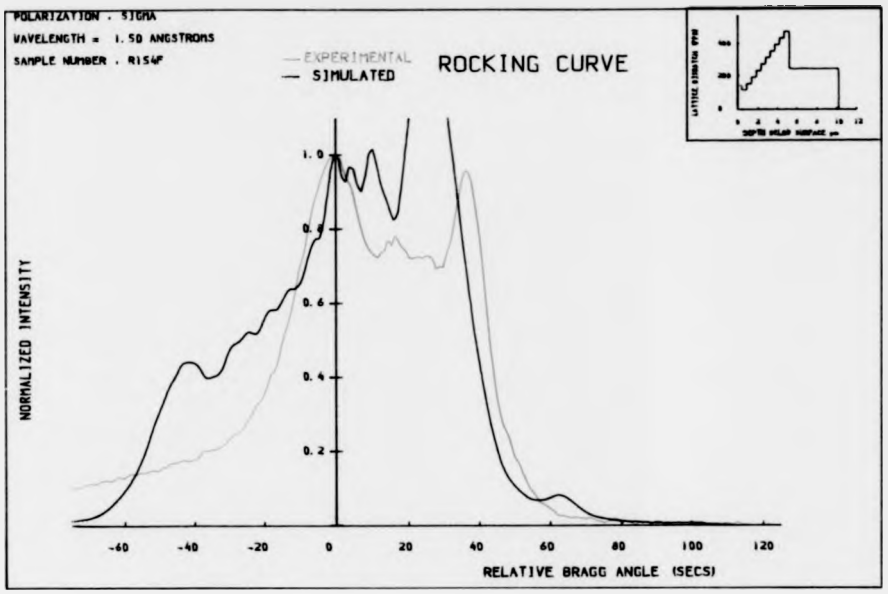

Figure 10.6e

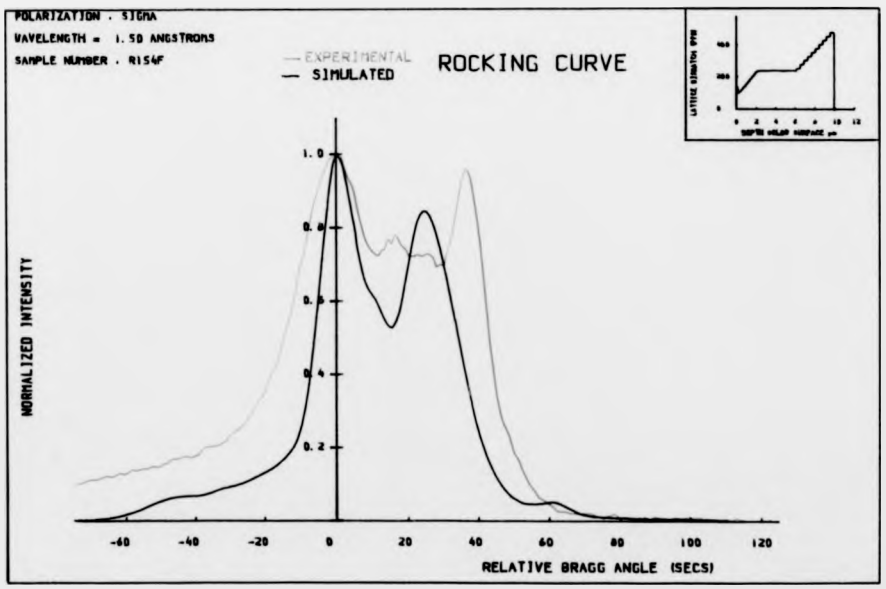

Figure 10.6f

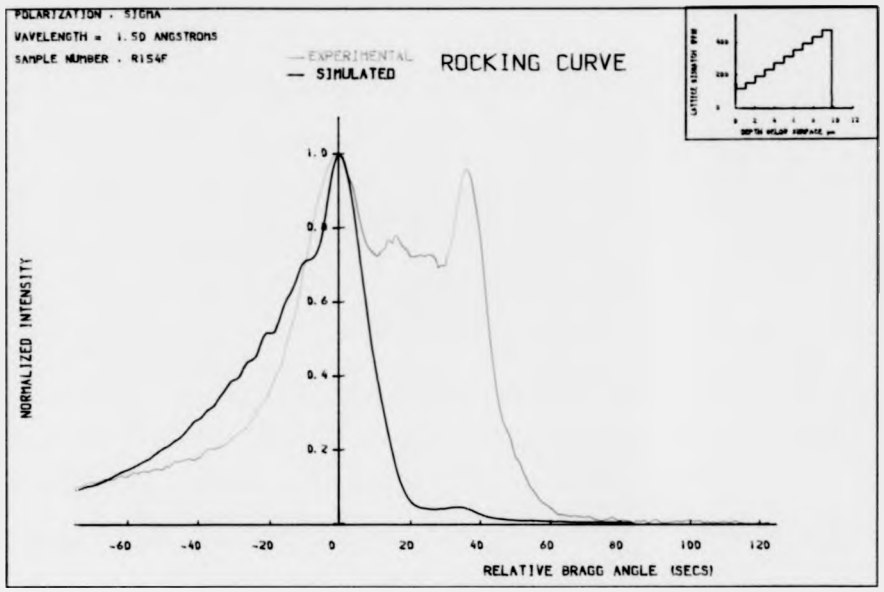

Figure 10.6g

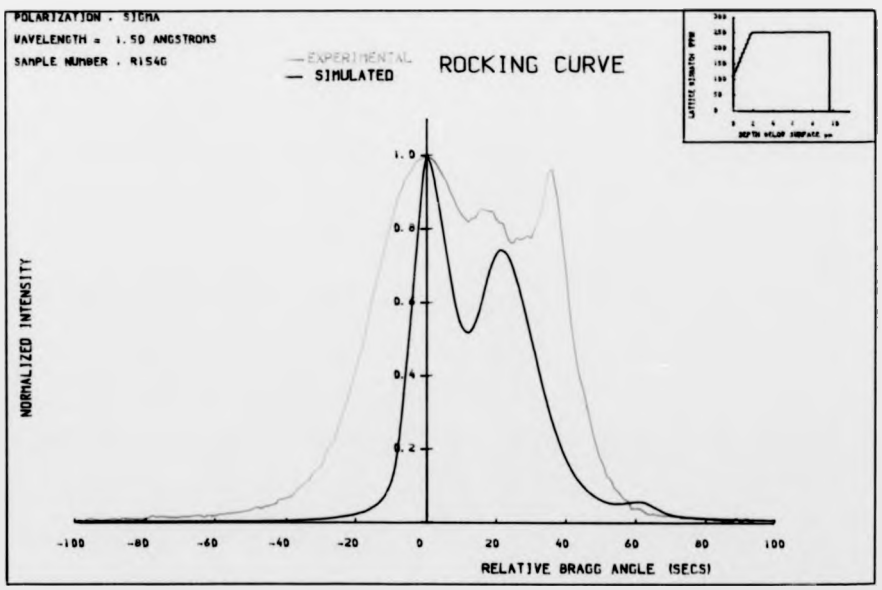

Figure 10.6h

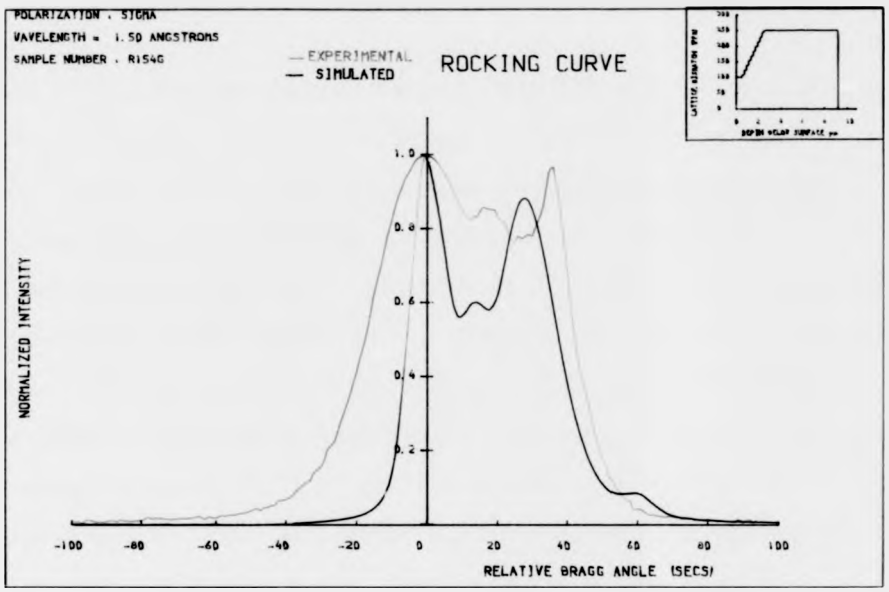

Figure 10.6i

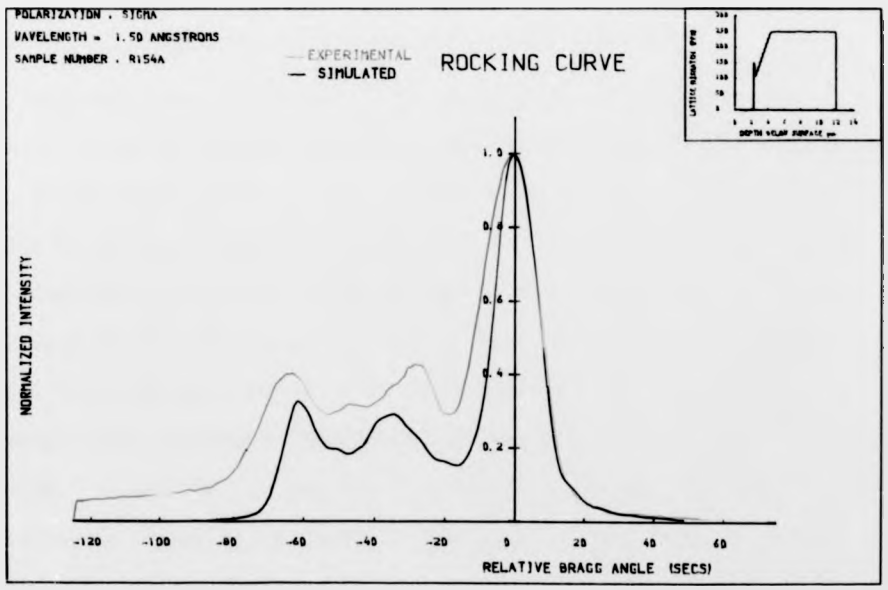

Figure 10.6j

number of oscillations between the peaks and the peak on the left reduced in height. The model in Figure 10.6d is therefore taken as the closest and a rocking curve from the buffer layer simulated in Figure 10.6h after removing the active layer. Figure 10.6h does not show good agreement, again due to fluctuation in homogeneity and uniformity of the buffer layer. Reducing the buffer layer thickness to 9.0μm (Figure 10.6i) by removing a thin section of 250 ppm layer shows a considerable improvement. A final plot is made using the ternary cap and InP layer characteristics from the plot of Figures 10.6a and b and the active layer and buffer characteristics from the plot of Figure 10.6d. This is shown in Figure 10.6j where the agreement is worse than in Figure 10.6a. This shows that the growth pattern is not the same along the layer.

10.6.2. A double heterostructure laser. Specimen M979

We refer back to Chapter 6 for details on the experimental rocking curves from this specimen. The thicknesses of the quaternary cap, p-InP layer, active layer and n-InP layers on top of the substrate have been assumed as 0.6μm, 2μm, 0.25μm and 2μm respectively. The experimental rocking curve (Figure 6.8) that will be simulated here will be the one obtained using a (100) InP on the first crystal. We see that the peak width of the experimental plot is about 45 arc seconds, The mismatch M from equation (10.22) is thus approximately 190 ppm. Figure 10.7a compares the calculated curve with the experimental curve for a constant mismatch of 180 ppm for both the active and capping layers. The peak positions do not agree. The

mismatch was then increased to 200 ppm (Figure 10.7b) which shows a better agreement in the peak positions. However the simulated quaternary peak height is still lower and narrower than the experimental curve. Hence an increase in the quaternary layer thickness as well as a graded mismatch was felt necessary. The effect of introducing a linear grading in the mismatch for the cap (Figure 10.7c) is that the quaternary peak reduces in height while the peak broadens. By increasing the thickness of the active layer (Figure 10.7d) we find that oscillations on the peak are more prominent while the peak is shifted to the right. Increasing the cap thickness (Figure 10.7e), however seems to give an improvement. The cap thickness in figure 10.7e has been assumed as 0.8μm. Increasing it to 0.9μm (Figure 10.7f) shows that the simulated peak is still lower. Figure 10.7g with a cap thickness of 1.0μm compares reasonably well. Any further increase in the cap thickness (Figure 10.7h,k) shows deviations from the experimental plot even if the grading of the cap is adjusted (Figure 10.7i). Adjustment of the grading with a cap thickness of 1.0μm does not improve on the agreement obtained in Figure 10.7g. Increasing the thickness of the active layer makes the peak shift to the right (Figure 10.7ℓ), whereas an adjustment of the grading of the cap while retaining its thickness at 1.0μm reduced the height of the peak (Figure 10.7j). Figure 10.7g has thus the nearest simulated fit to the experimental curve. The model thus assumes a thickness of the cap of 1.0μm. To verify this, a part of the ternary cap was etched off using a selective etchant of $3(H_2SO_4) : 1(H_2O_2)$:

mismatch was then increased to 200 ppm (Figure 10.7b) which shows a better agreement in the peak positions. However the simulated quaternary peak height is still lower and narrower than the experimental curve. Hence an increase in the quaternary layer thickness as well as a graded mismatch was felt necessary. The effect of introducing a linear grading in the mismatch for the cap (Figure 10.7c) is that the quaternary peak reduces in height while the peak broadens. By increasing the thickness of the active layer (Figure 10.7d) we find that oscillations on the peak are more prominent while the peak is shifted to the right. Increasing the cap thickness (Figure 10.7e), however seems to give an improvement. The cap thickness in figure 10.7e has been assumed as 0.8μm. Increasing it to 0.9μm (Figure 10.7f) shows that the simulated peak is still lower. Figure 10.7g with a cap thickness of 1.0μm compares reasonably well. Any further increase in the cap thickness (Figure 10.7h,k) shows deviations from the experimental plot even if the grading of the cap is adjusted (Figure 10.7i). Adjustment of the grading with a cap thickness of 1.0μm does not improve on the agreement obtained in Figure 10.7g. Increasing the thickness of the active layer makes the peak shift to the right (Figure 10.7ℓ), whereas an adjustment of the grading of the cap while retaining its thickness at 1.0μm reduced the height of the peak (Figure 10.7j). Figure 10.7g has thus the nearest simulated fit to the experimental curve. The model thus assumes a thickness of the cap of 1.0μm. To verify this, a part of the ternary cap was etched off using a selective etchant of $3(H_2SO_4) : 1(H_2O_2)$:

Figure	Title	Page No.
10.7. (a to l)	Comparison of the experimental and simulated rocking curves for the specimen M979. Emission wavelength for the active layer = 1.31μm. Energy band gap for the quaternary cap is 1.24 eV. Mismatch levels are as indicated in the insets in the graph. The simulated layer thicknesses (μm) for the various graphs are as follows	

	n-InP	Q-Active	p-InP	Q-cap	
a	2	0.25	2	0.6	235
b	2	0.25	2	0.6	235
c	2	0.25	2	0.3+0.3	236
d	2	0.50	2	0.3+0.3	236
e	2	0.25	2	0.2+0.5	237
f	2	0.25	2	0.2+0.7	237
g	2	0.25	2	0.2+0.8	238
h	2	0.25	2	0.2+0.9	238
i	2	0.25	2	0.3+0.8	239
j	2	0.25	2	0.3+0.7	239
k	2	0.25	2	0.4+0.8	240
l	2	0.25	2	0.4+0.7	240

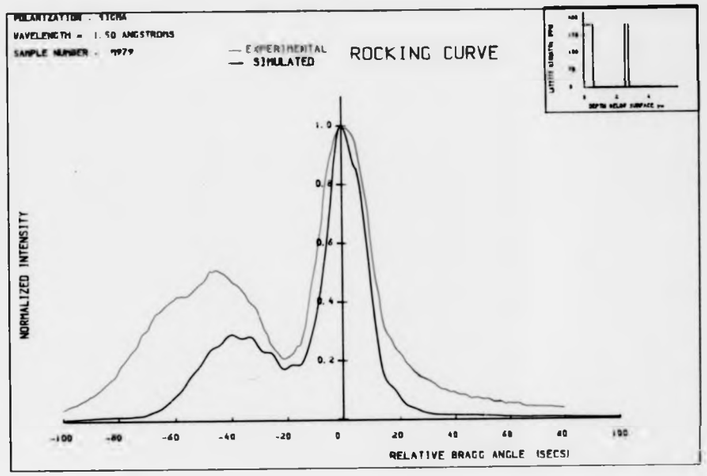

Figure 10.7a

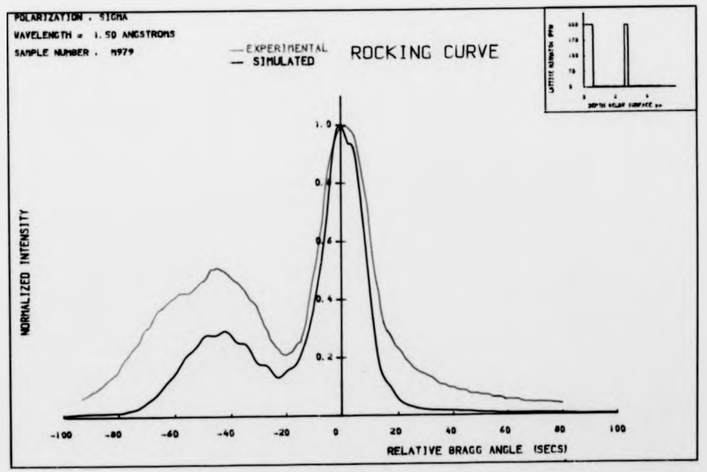

Figure 10.7b

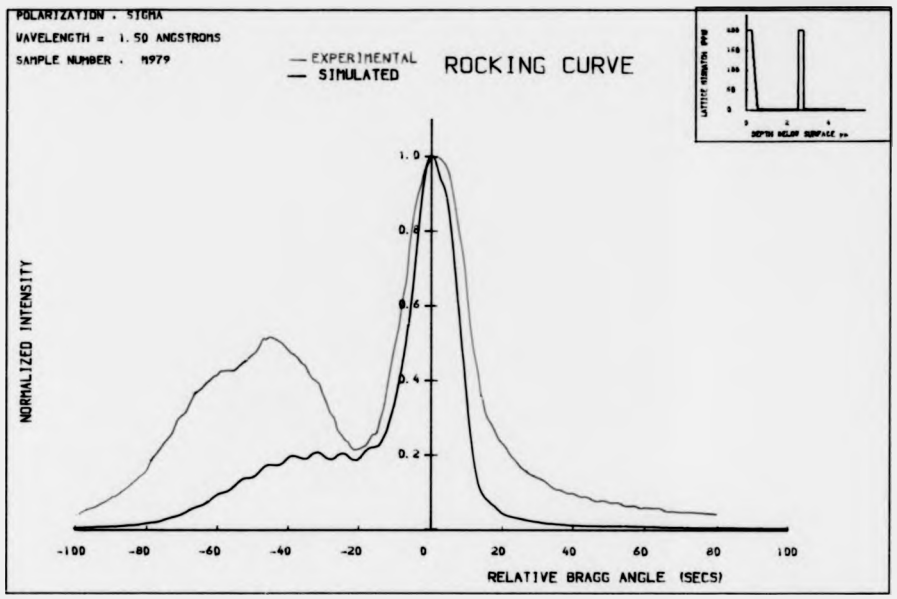

Figure 10.7c

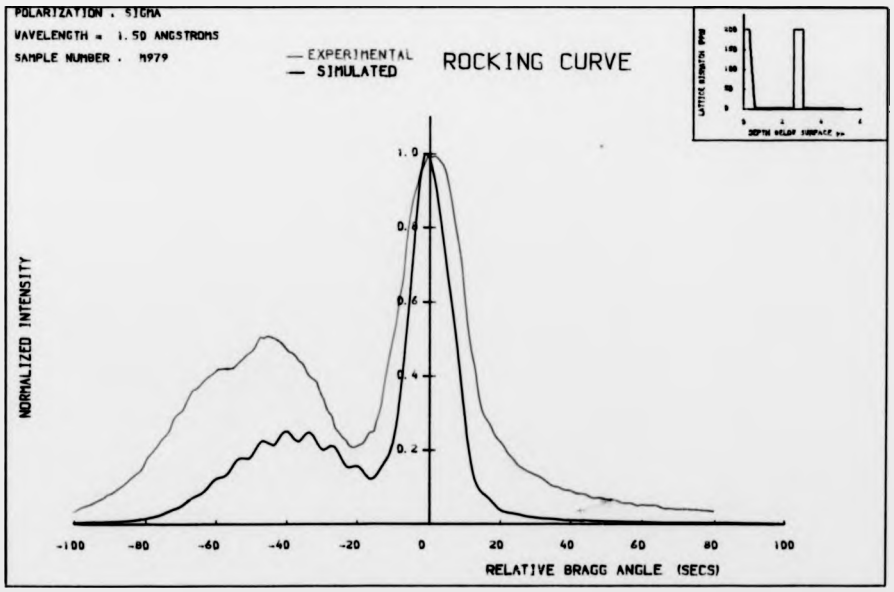

Figure 10.7d

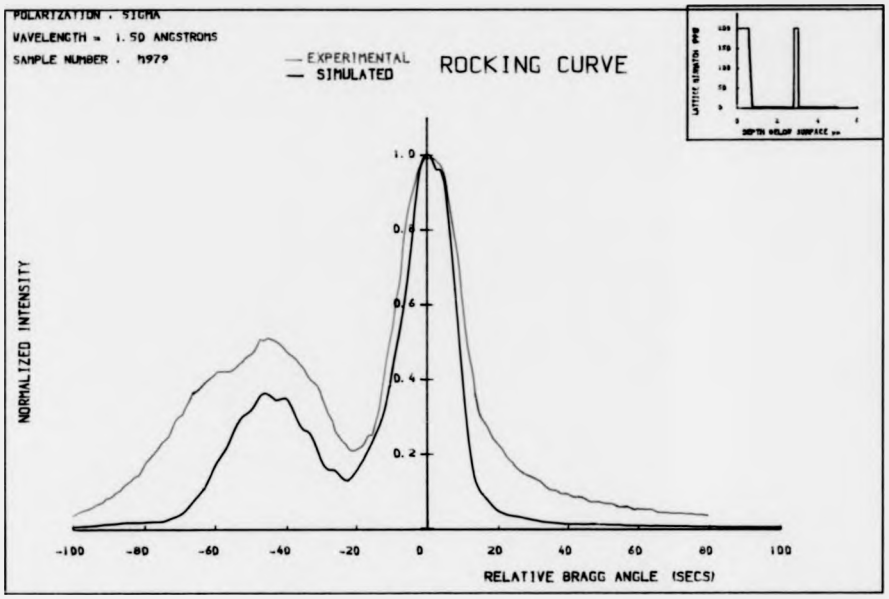

Figure 10.7e

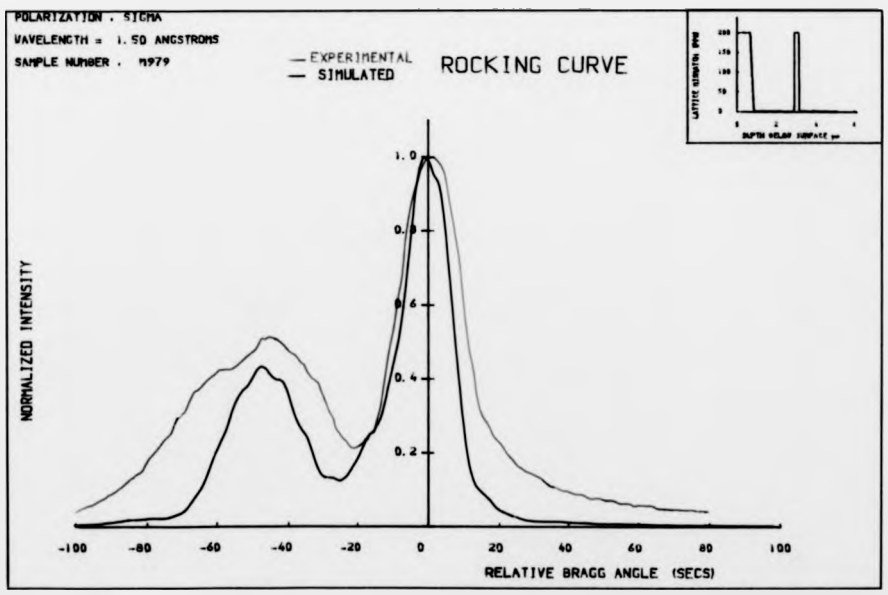

Figure 10.7f

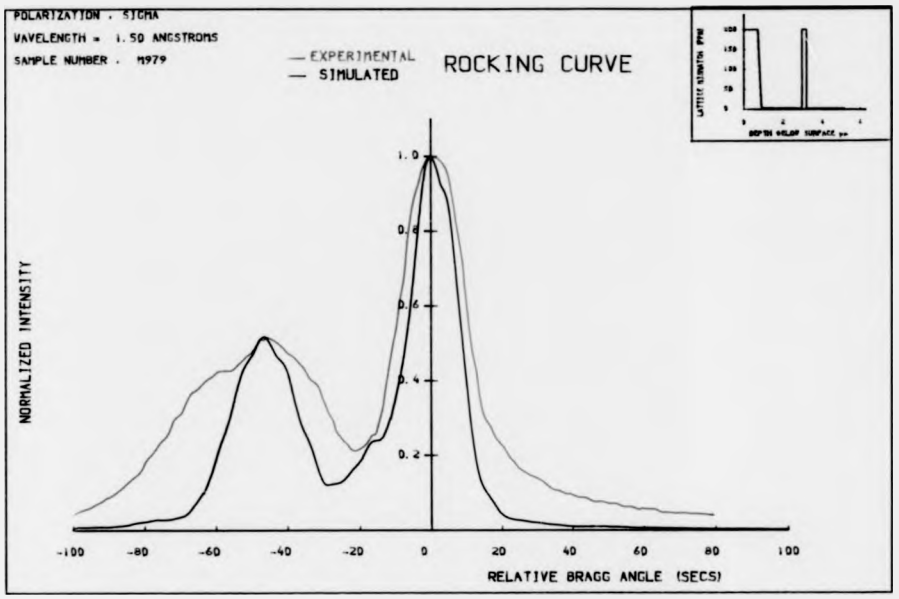

Figure 10.7g

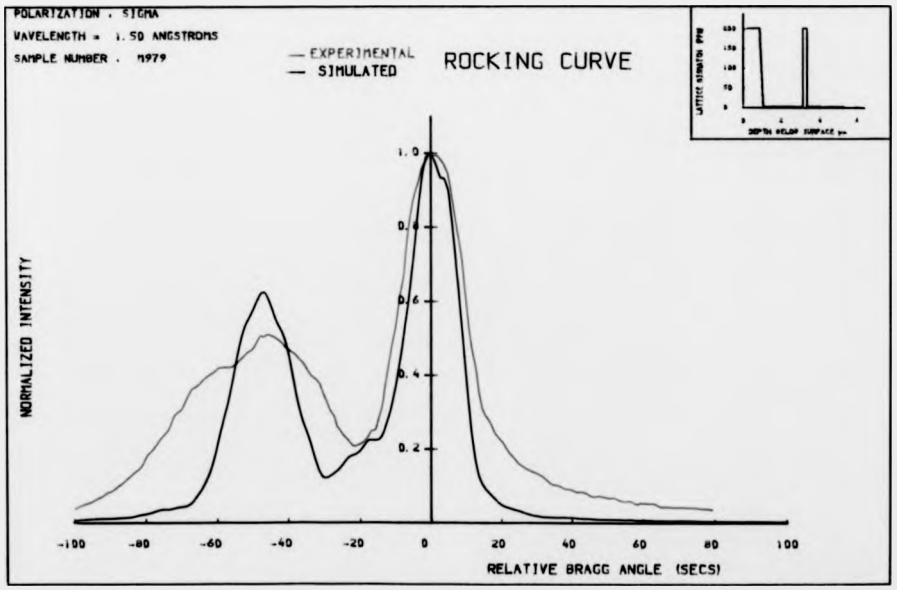

Figure 10.7h

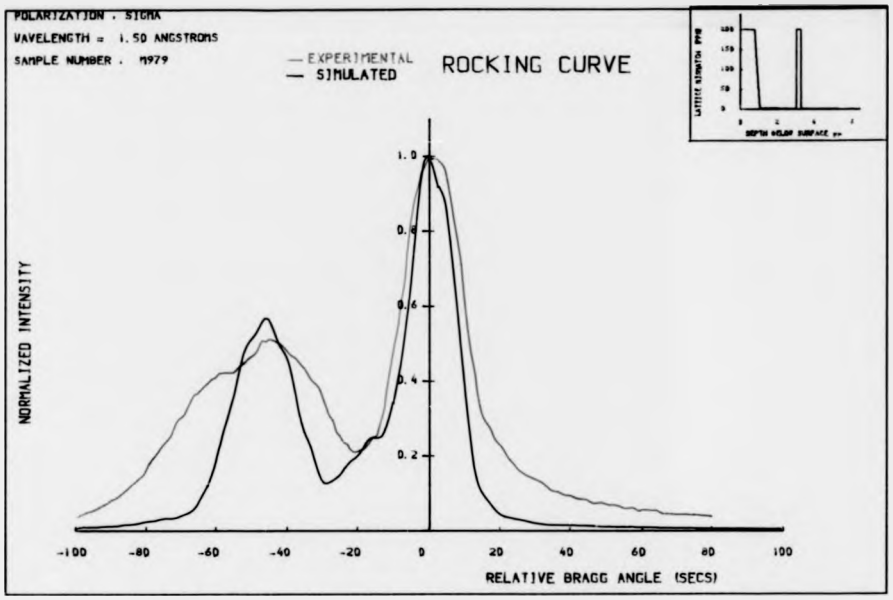

Figure 10.7i

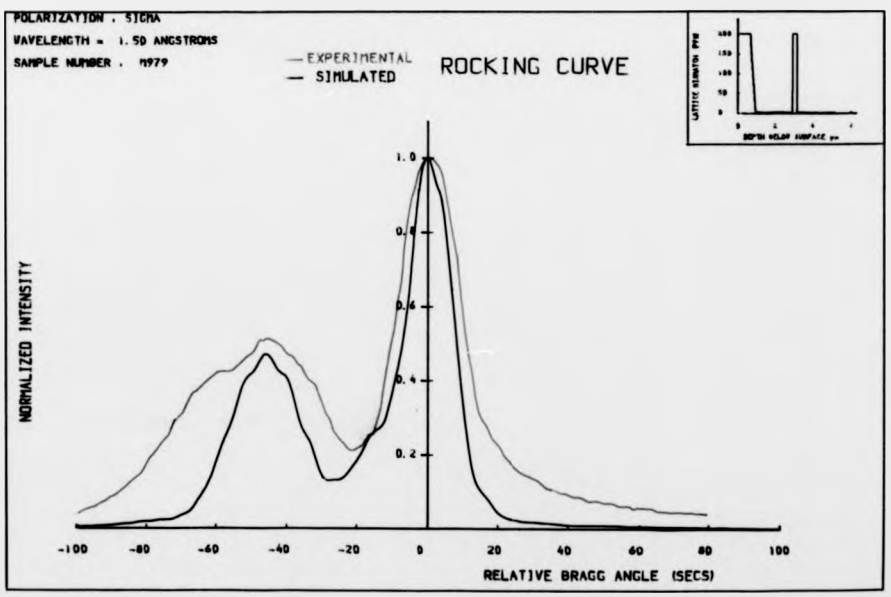

Figure 10.7j

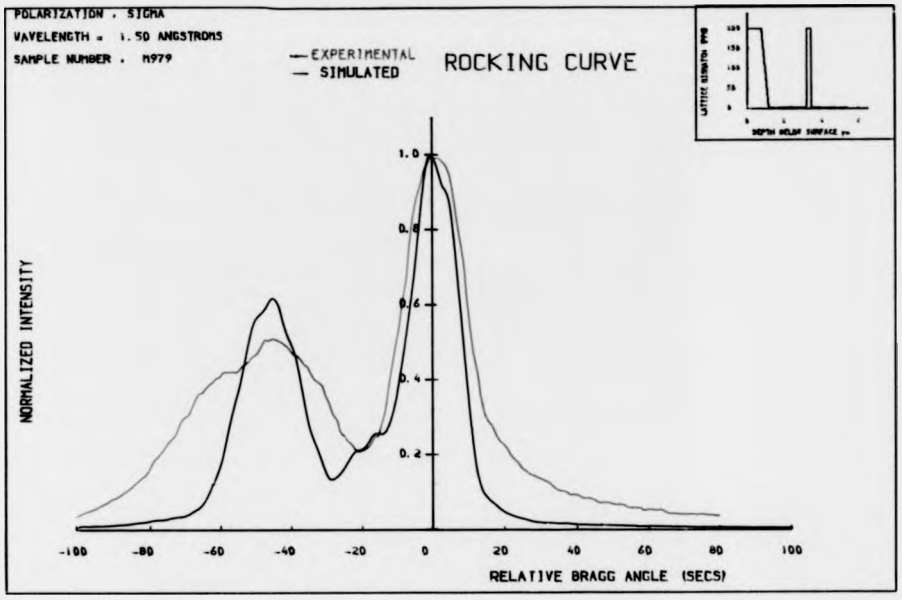

Figure 10.7k

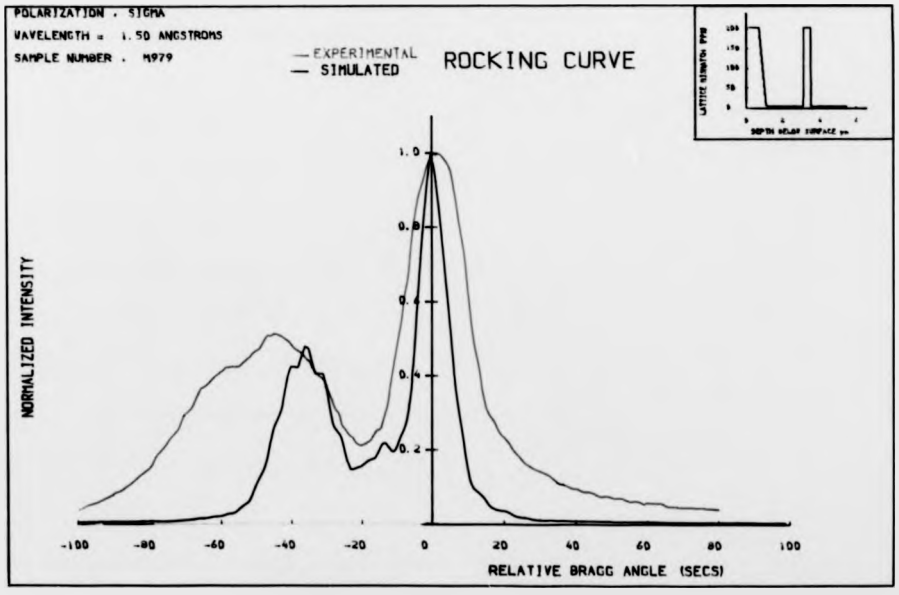

Figure 10.71

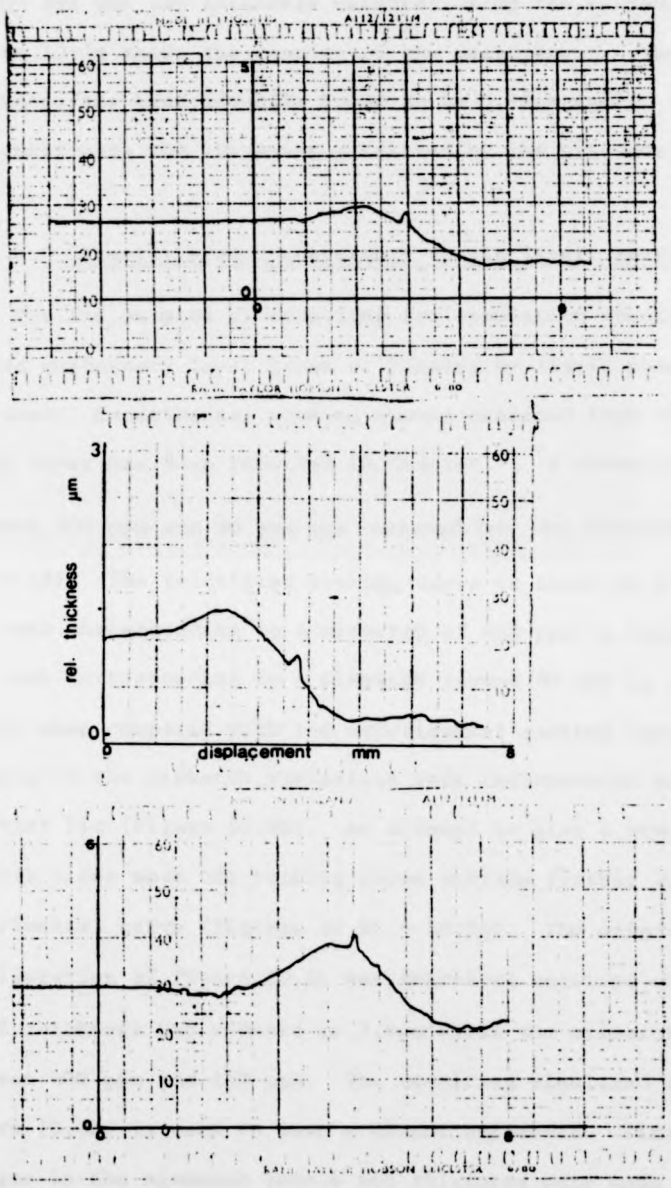

Figure 10.7m. Thickness of the ternary cap as measured at three regions using the Talysurf, are 0.95µm, 0.90µm and 0.90µm respectively, giving an average thickness of 0.92µm

1(H_2O) and the cap thickness measured using the Talysurf. Figure 10.7m shows the results of the measurement. The cap thickness has been actually found to be 0.92μm and is in good agreement with the thickness predicted by the simulated curve.

10.6.3. Linearly graded quaternary single layer, specimen L5

For the purpose of modelling for simulation studies, a linearly graded quaternary layer grown at Plessey by liquid phase epitaxy, was used. Experimental rocking curves obtained from the 4.2μm thick layer has been reported in Chapter 7. A mismatch varying between 400 ppm and 80 ppm was assumed for the experimental curve L5F. The calculated rocking curve is shown in Figure 10.8a. The peak corresponding to a mismatch of 400 ppm is elevated while the peak corresponding to a mismatch around 80 ppm is reduced in height when compared with the experimental rocking curve. So changes in the mismatch variations were incorporated to achieve a better fit (Figure 10.8b). An attempt to give a graded mismatch on both sides made the rocking curve deviate further away from the experimental curve (Figures 10.8c - 10.8g). The original configuration of Figure 10.8b was therefore retained while the total thickness was reduced to 3.6μm while the mismatch varied between 400 ppm and 110 ppm. The resulting simulated curve, Figure 10.8h, is seen to have a closer agreement. Finally minor changes in the mismatch levels and thickness were made and rocking curves calculated (Figures 10.8i, 10.8j). The most satisfactory fit is observed in Figure 10.8j where the layer thickness is set at 3.8μm and mismatch levels between 395 and 100 ppm. According

Figure	Title	Page No.
10.8. (a to j)	Comparison of the experimental and simulated rocking curves for the specimen L5. Emission wavelength for the layer is = 1.245μm. Mismatch levels are as indicated in the insets in the graphs. The simulated layer thicknesses (μm) for various graphs are as follows	

	Layer thickness	
a	4.2	243
b	4.2	243
c	4.2	244
d	4.0	244
e	4.0	245
f	4.2	245
g	4.1	246
h	3.6	246
i	3.7	248
j	3.8	247

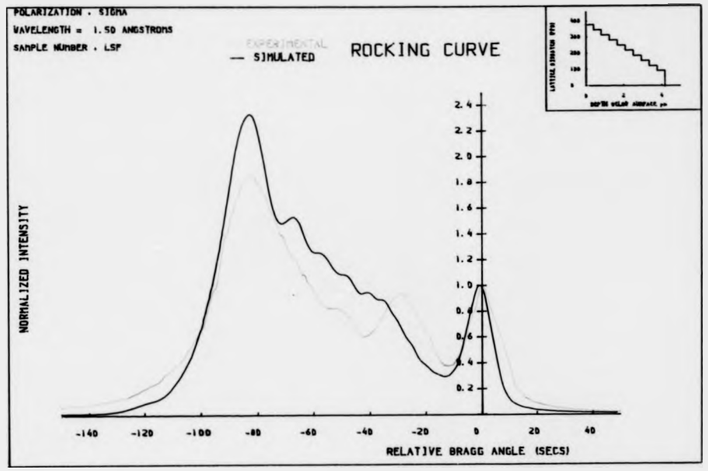

Figure 10.8a

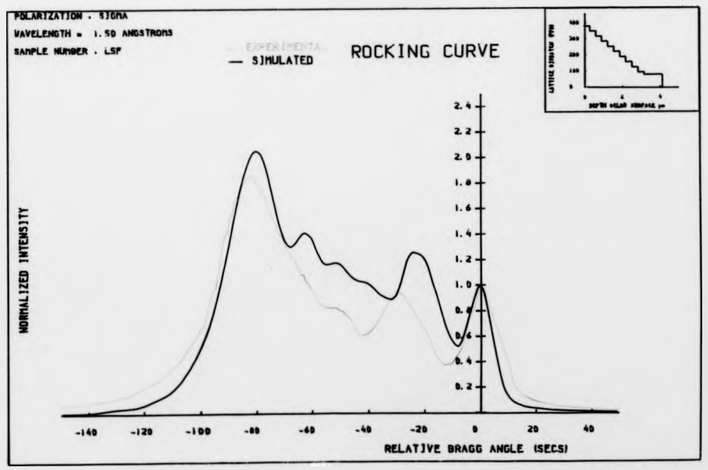

Figure 10.8b

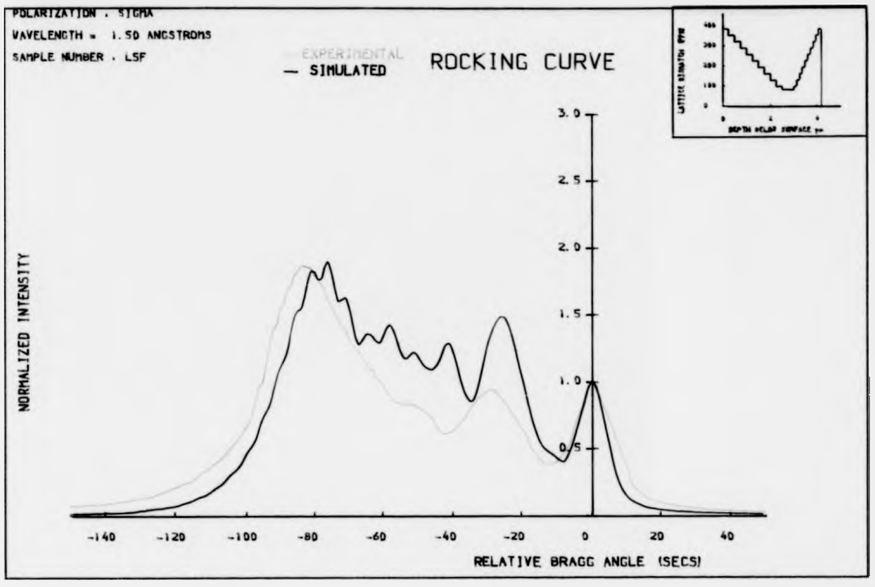

Figure 10.8c

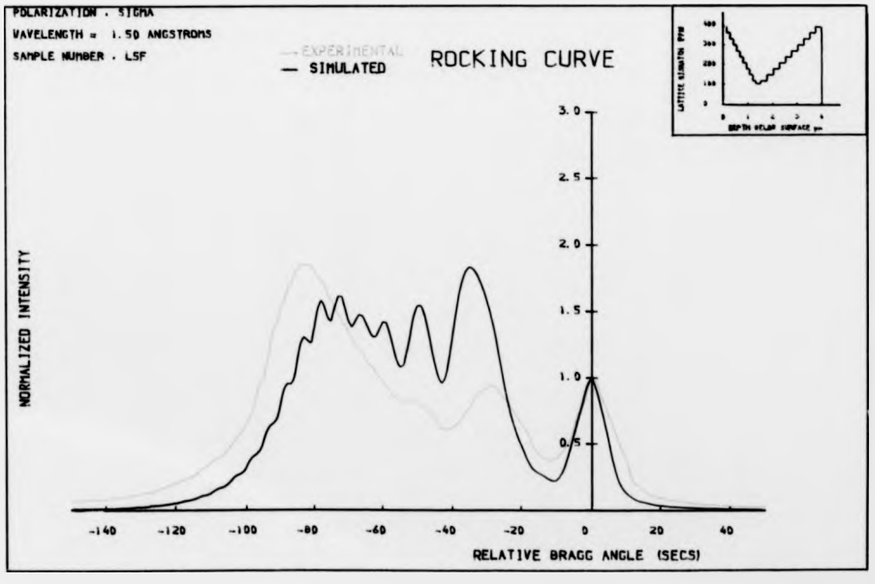

Figure 10.8d

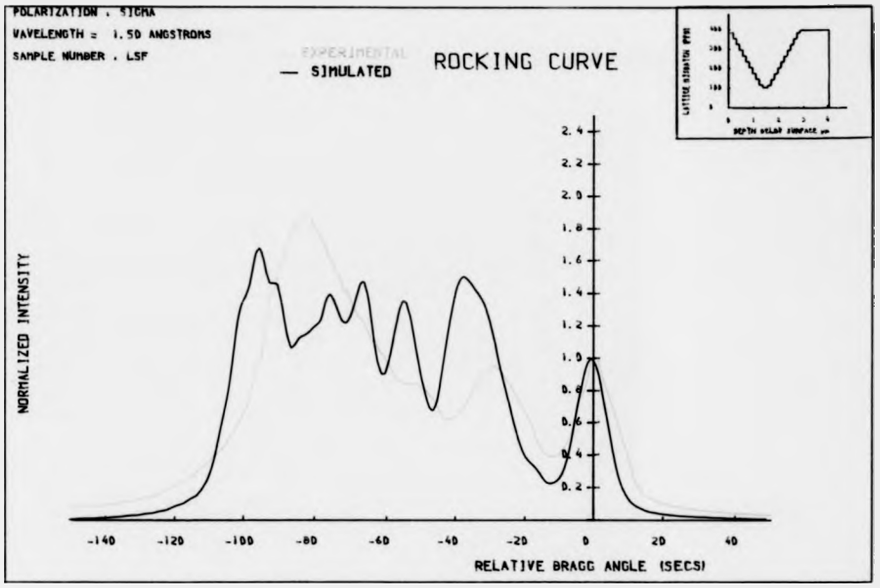

Figure 10.8e

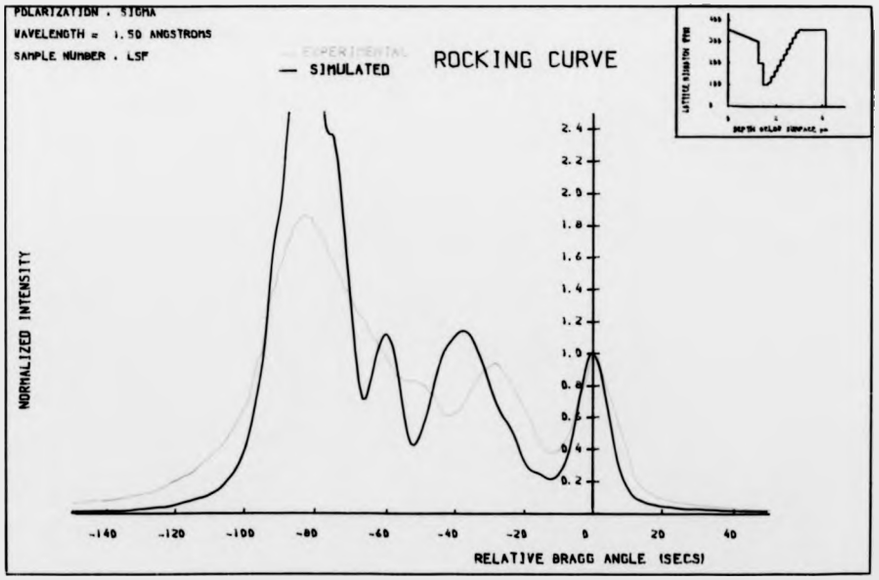

Figure 10.8f

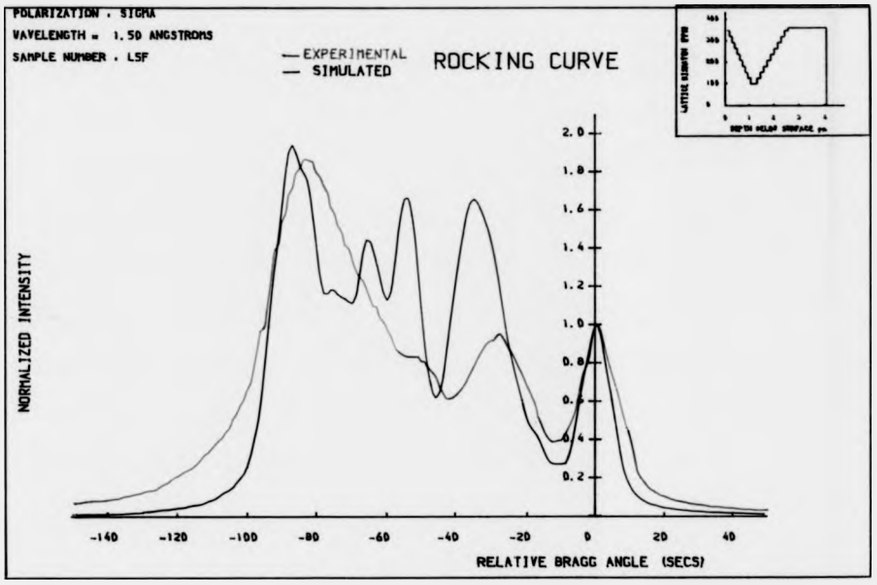

Figure 10.8g

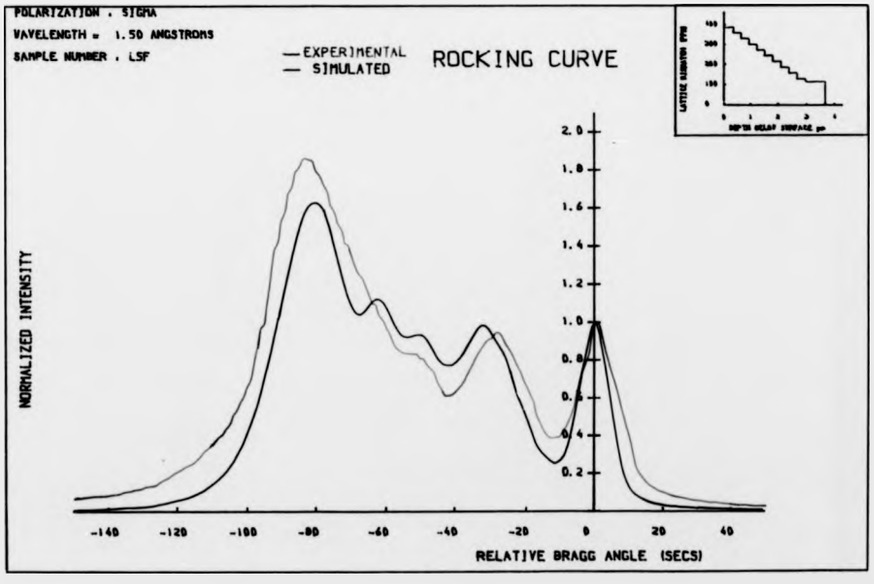

Figure 10.8h

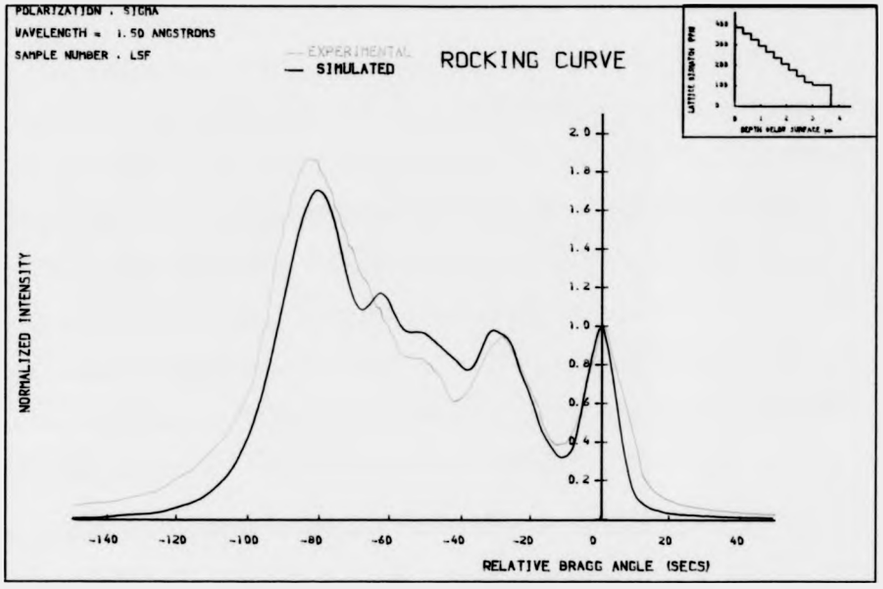

Figure 10.8i

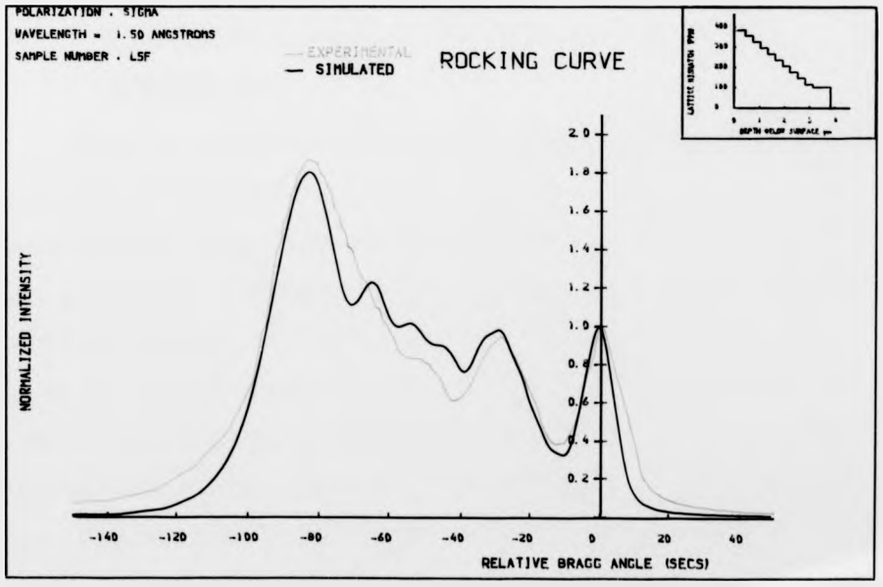

Figure 10.8j

to this model, the layer consists of two sections, the section adjacent to the substrate having a uniform mismatch of 100 ppm and is 0.7μm thick while the other section, 3.1μm thick has a linearly graded mismatch varying between 100 ppm and 395 ppm. In view of a possible variation in the thickness of the layer and a departure from a linearly graded mismatch variation at different points on the specimen, a simulation made for a different point on the specimen is likely to agree for a different thickness and mismatch variation. In fact, in Figure 10.8j, it is the experimental rocking curve at the point F (Figure 7.4) that has been simulated. Rocking curves at other points D , E and G are different and a simulation of these curves would yield different results.

10.6.4. Etched single layers of linearly graded quaternary specimen, L5.

Using the model for the linearly graded specimen L5 as proposed in Section 10.6.3, simulation of rocking curves of the same specimen after etching off parts of the layer in succession, was attempted. In Chapter 9 rocking curves were plotted for the specimen, etched to various layer thicknesses. The mismatch gradient for the chosen model being known, the limits of the mismatch variations for any etched layer can thus be calculated. Appropriate rocking curves for a successively reduced layer thickness were calculated and compared with the rocking curve at the point C (Figure 9.3a) until, for a layer thickness of 3.6μm, the

simulated curve agreed with the experimental rocking curve(Figure 10.9a) The mismatch limits for such a layer is thus between 385 and 100 ppm. The change in the thickness at D could not be properly measured (Table 9.2). An appropriate simulation for a layer thickness around 3.4μm was tried for the rocking curve at D. In figure 10.9b the calculated rocking curve for a layer thickness of 3.35μm but with a mismatch variation between 360 ppm and 100 ppm shows a reasonable agreement in the intensity levels of the peaks but not quite so in the peak separations. The expected mismatch levels for a layer of thickness 3.35μm are between 353 ppm and 100 ppm. The calculated rocking curves for the same layer with a mismatch variation between 350 ppm and 100 ppm shows a much better fit with the experimental rocking curve at D (Figure 10.9c). In a similar way, experimental rocking curves for the points E and F are compared with the curves calculated for layer thicknesses 3.2μm and 3.1μm respectively, for which the expected mismatch variations according to the model are between 338 and 100, and 328 and 100 ppm respectively. Mismatch levels between 340 and 100, and 330 and 100 ppm were therefore chosen for comparison with rocking curves at the points E and F respectively (Figure 10.9d and 10.9e). It can be seen that the layer peak height in the vicinity of 100 ppm angular position is larger than in the corresponding experimental curve. The thickness of the 100 ppm mismatch section has been assumed as .7μm in the model. If this is simply reduced to 0.6μm, the substrate peak level would rise still higher. Hence, keeping the total thickness of the layer constant but reducing the 100 ppm section to 0.6μm the rocking

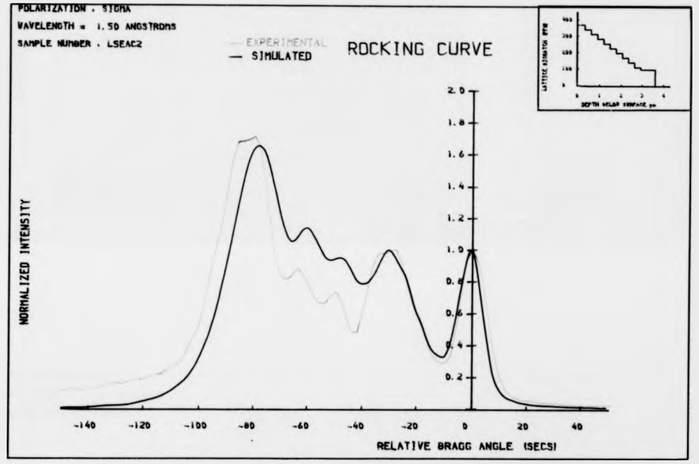

Figure 10.9a

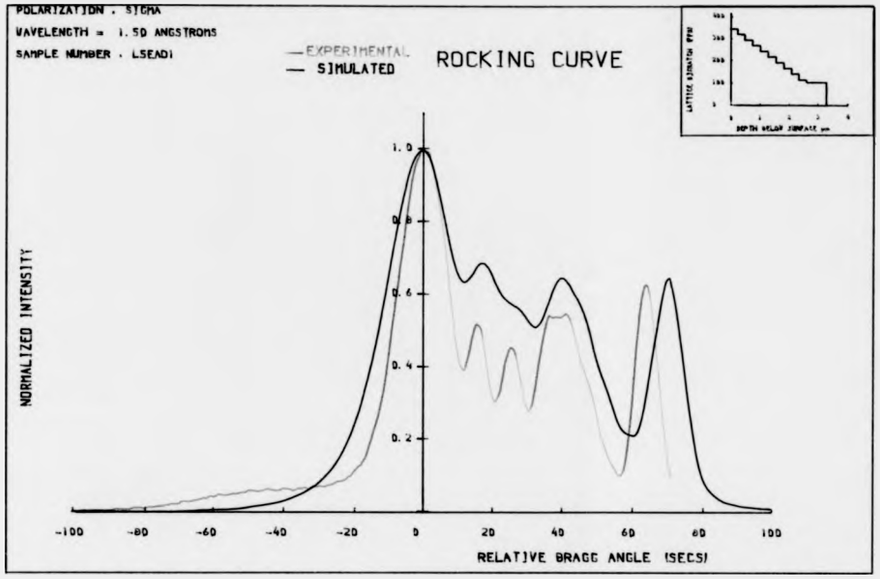

Figure 10.9b

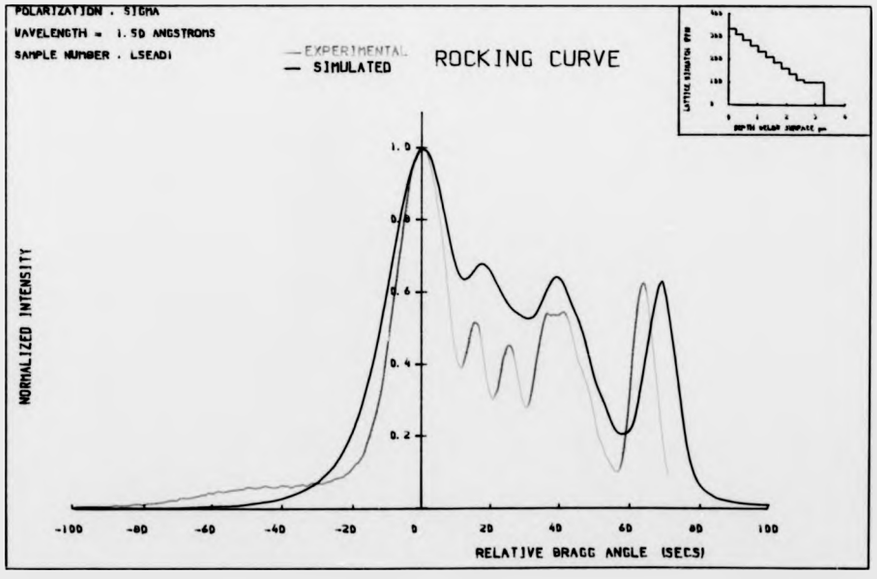

Figure 10.9c

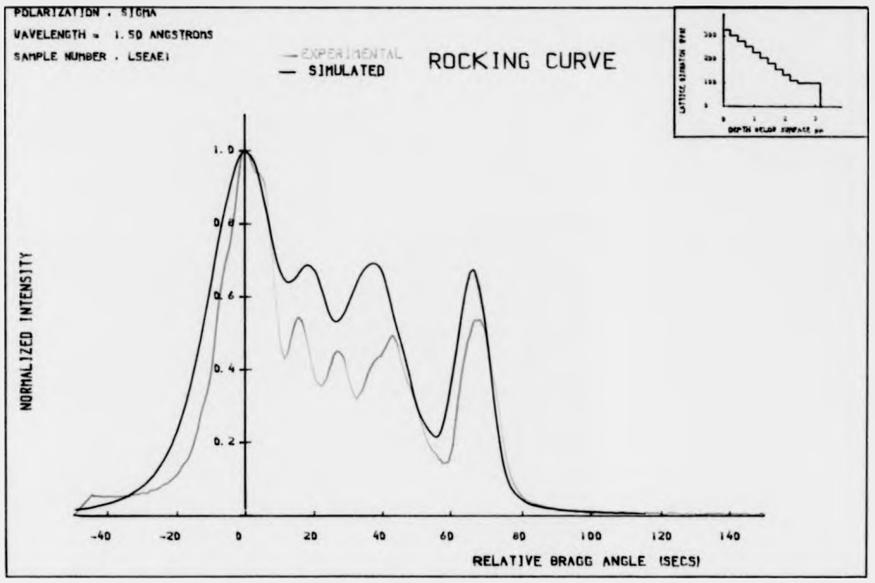

Figure 10.9d

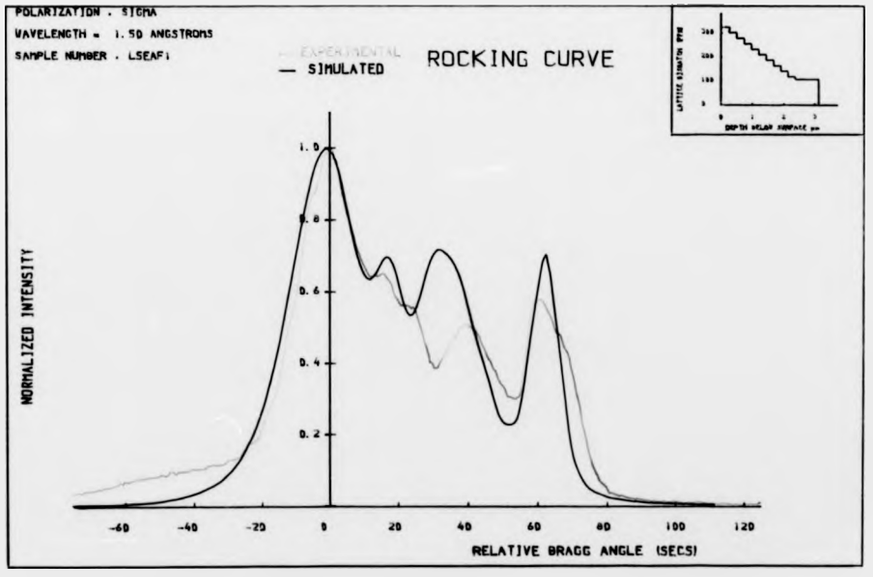

Figure 10.9e

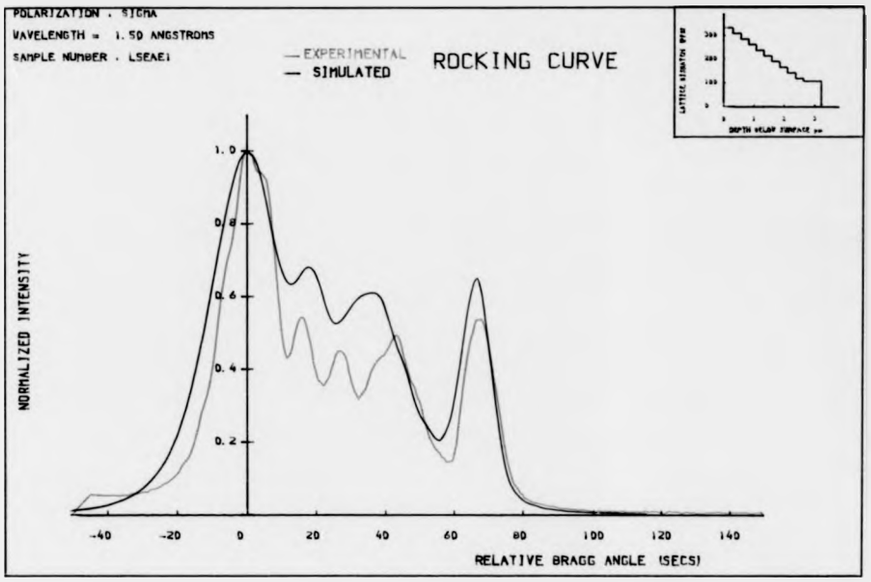

Figure 10.9f

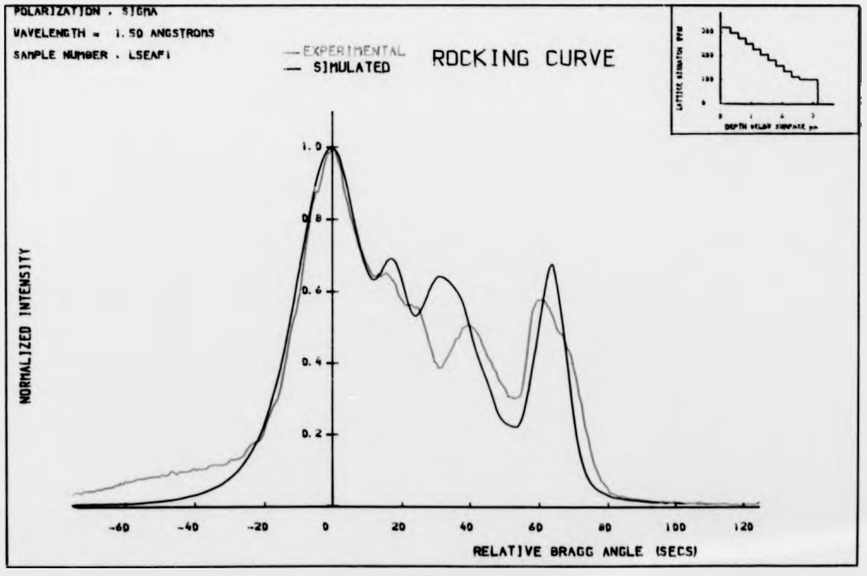

Figure 10.9g

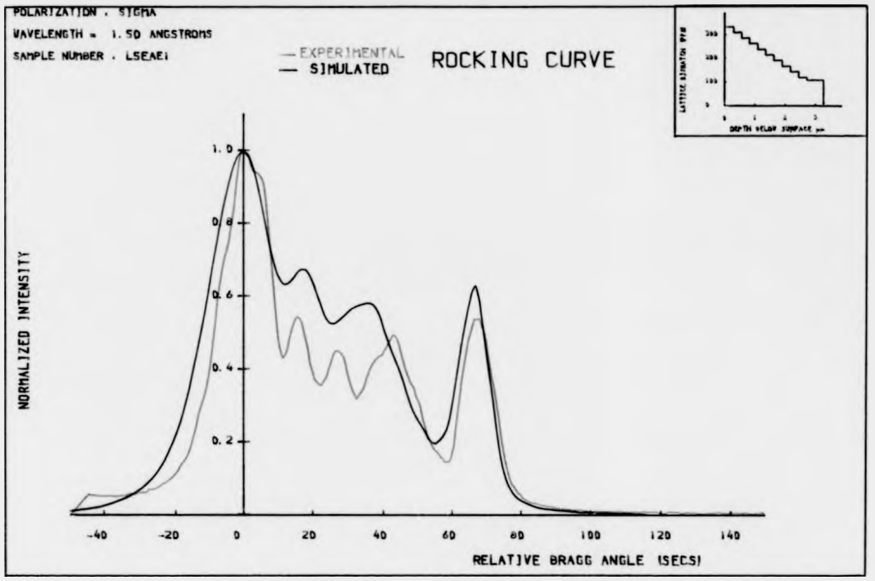

Figure 10.9h

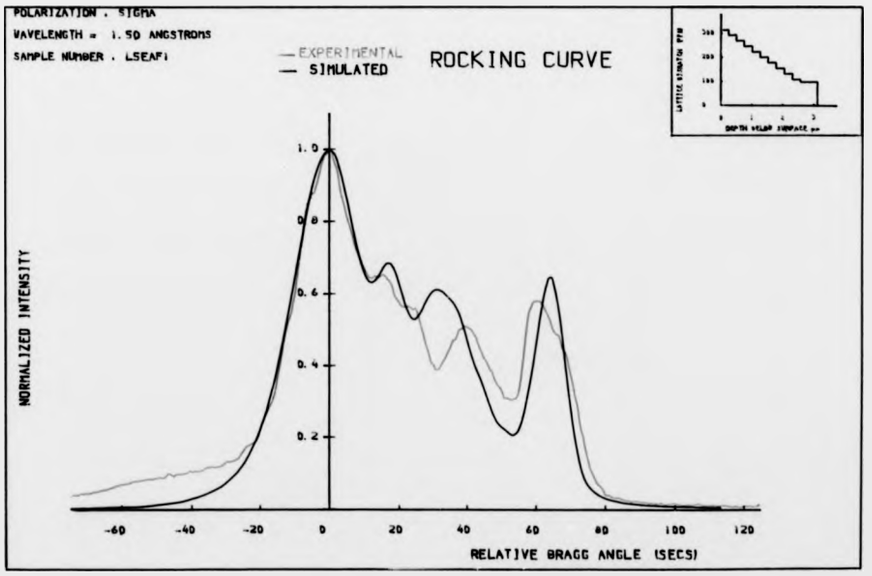

Figure 10.9i

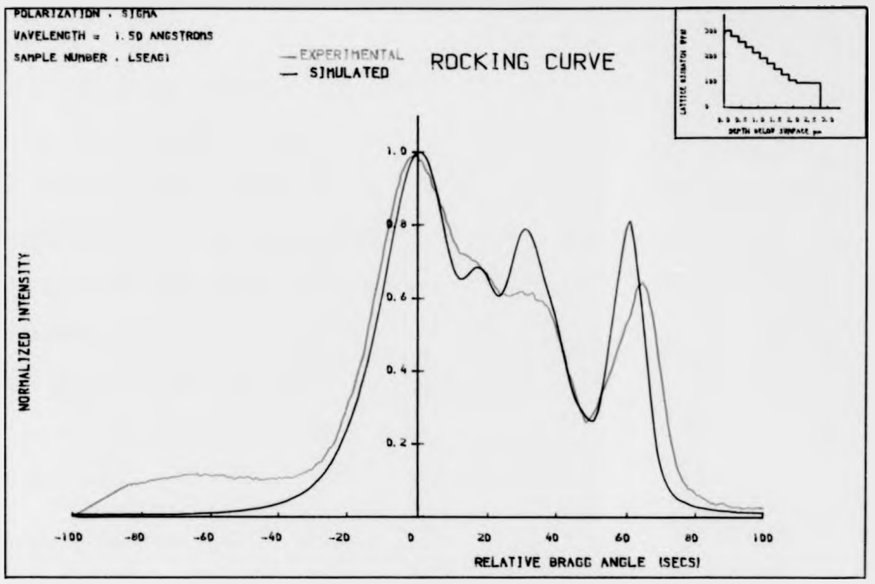

Figure 10.9j

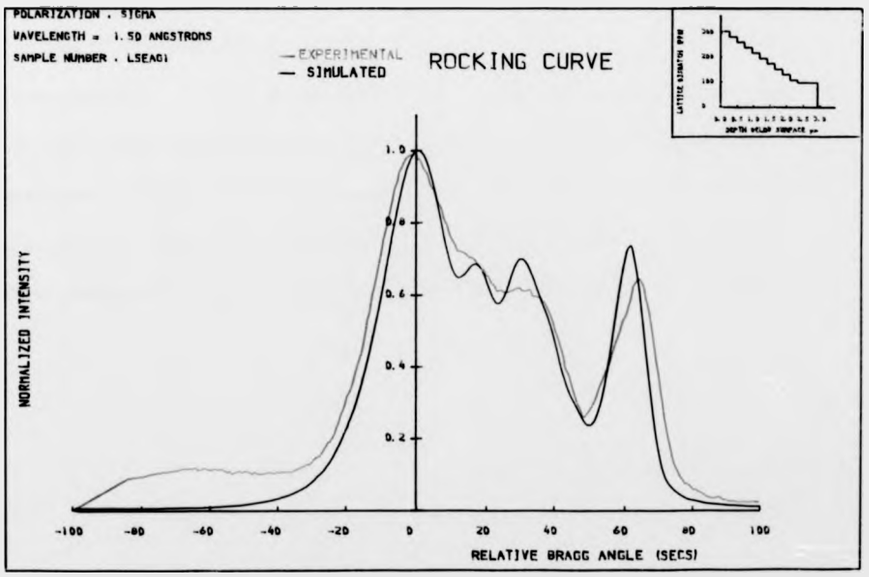

Figure 10.9k

curves were calculated. When compared with the experimental curves at E and F, (Figures 10.9f and 10.9g), they show a much better agreement. Reducing the thickness of the section still further does not show much improvement, (Figure 10.9h and 10.9i). Finally, the calculated rocking curve for the point G with layer thickness 2.8μm but with mismatch levels between 320 and 100 is compared with the experimental curve at G, (Figure 10.9j). In figure 10.9k the layer thickness has been adjusted to get a much better fit. In Table 10.1 characteristics of the layer obtained from a simulated fit at various positions C to G on the specimen, are listed. Table 10.2 compares the thickness changes obtained from Talysurf measurements with that obtained from simulation studies. According to Table 10.1, the step change in layer thickness, in microns, as one proceeds from points C to G through D, E and F is predicted to be - 0.25, - 0.15, - 0.10 and - 0.20 respectively. These are compared with the corresponding figures measured experimentally using the Talysurf. Details of the experiment can be found in Chapter 9. The results are listed in Table 10.2. The predicted thickness changes are thus found to agree reasonably well with the experimentally observed values.

Table 10.1 : Simulated characteristics of the layer for various experimental positions on the specimen, L5.

Position on the specimen	Layer details from the simulated curve					Total thickness µm
	Graded mismatch section			Constant mismatch section		
	Thickness µm	Mismatch grading between		Thickness µm	Mismatch ppm	
		Upper limit, ppm	Lower limit, ppm			
C	2.9	385	100	0.7	100	3.6
D	2.65	350	100	0.7	100	3.35
E	2.6	340	100	0.6	100	3.2
F	2.5	330	100	0.6	100	3.1
G	2.3	320	100	0.6	100	2.9

Table 10.2 : Comparison of the step change in thickness for two adjacent points between C and G on the specimen.

Position on the specimen	Step change in thickness (μm) from one position to the next	
	Talysurf measurements (see Table 9.2)	Simulated
C	-	-
D	Value uncertain	-0.25
E	-0.14	-0.15
F	-0.15	-0.10
G	-0.21	-0.20

The object of this exercise is to show that

i) a simple mathematical model can be proposed for the mismatch characteristics of a layer.

ii) local fluctuations in homogeneity and uniformity of the layer due to uncontrolled growing techniques would mean that the actual growth may deviate from a chosen compositional grading.

iii) the actual fluctuations can in fact be accurately described by a proper simulation of experimental rocking curves. This leads us to an important conclusion that in addition to being able to point out to a crystal grower that what he thinks is the growth pattern may not be the actual growth pattern, the actual compositional variation can even be predicted. As a matter of fact the specimen L5 was originally thought of as being graded in mismatch in both directions. A systematic simulation of an experimental rocking curve from the specimen however showed that the layer was made up of two sections, one with a mismatch graded in one direction, while the other had a uniform mismatch instead of being graded in the other direction. The proposed model for the specimen was extended to verify rocking curves at several intermediate thicknesses by etching off a part of the layer. For certain positions at intermediate thicknesses, minor

deviations from the proposed model were detected. It is to be remembered that the points C, D, E, F and G refer to different positions on the specimen. Deviations from the proposed patterns only indicates a fluctuation in the homogeneity of the layer and can be quantitatively determined by the changes in layer characteristics that are required for the simulated curve to fit the experimental curves at those points.

10.6.5. A light emitting diode, VS296A

From the experimental rocking curve, a mismatch level for the quaternary was estimated as 560 ppm. Rocking curves calculated for several configurations were compared with the experimental curve (Figures 10.10a - 10.10h). The agreement is poor, particularly with respect to the width of the peaks. It is suspected that the large mismatch has resulted in a small curvature for the substrate and due to a finite beam width of the incident X-rays, this curvature would result in a broadening of the peaks. Such factors have not been accounted for in the calculated curves.

10.6. Discussion

An experimental study of X-ray rocking curves can in general, provide valuable information on the characterization of hetero-epitaxial layers. However, if a large number of thin layers is involved or if the layers are inhomogeneous, the rocking curve

Figure	Title	Page No.
10.10. (a to h)	Comparison of the experimental and simulated rocking curves for the specimen VS296A. Emission wavelength for the active layer is λ = 1.31μm. Energy bandgap of the cap layer is 1.24 eV. Mismatch levels are as indicated in the insets in the graphs. Simulated layer thicknesses (μm) for various graphs as as follows	

	N-InP	Q-Active	p-InP	Q-cap	
a	2	2	1	0.25	261
b	2	2	1	0.25	261
c	2	2	1	0.50	262
d	2	2	1	0.25	262
e	2	2	1	0.50	263
f	2	2.5	1	0.50	263
g	2	2.5	1	0.50	264
h	2	2.5	1	0.50	264

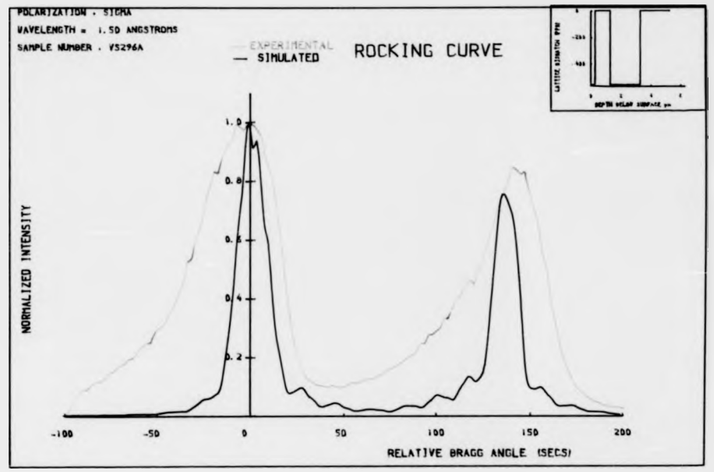

Figure 10.10a

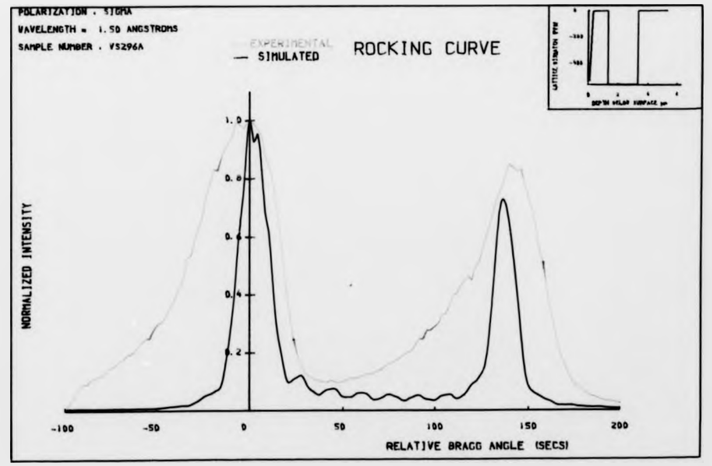

Figure 10.10b

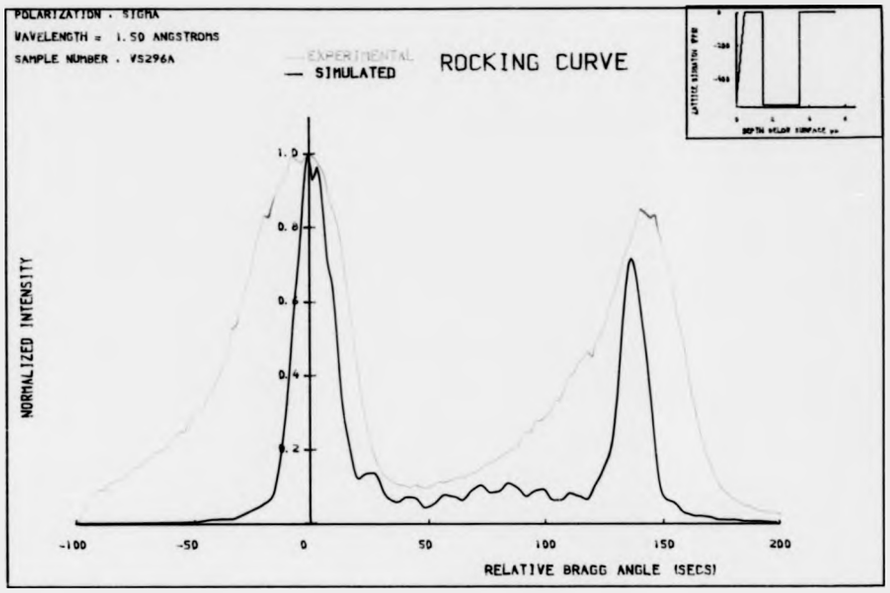

Figure 10.10c

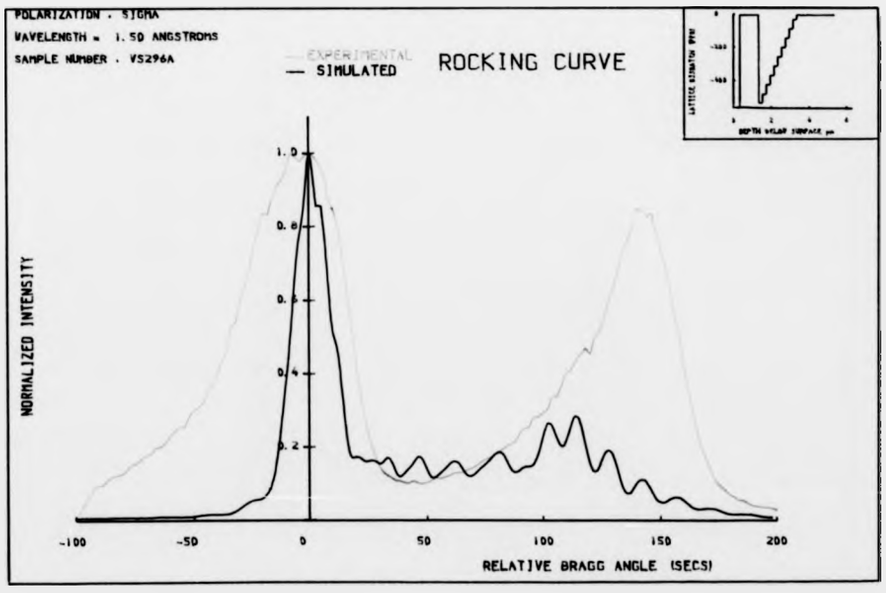

Figure 10.10d

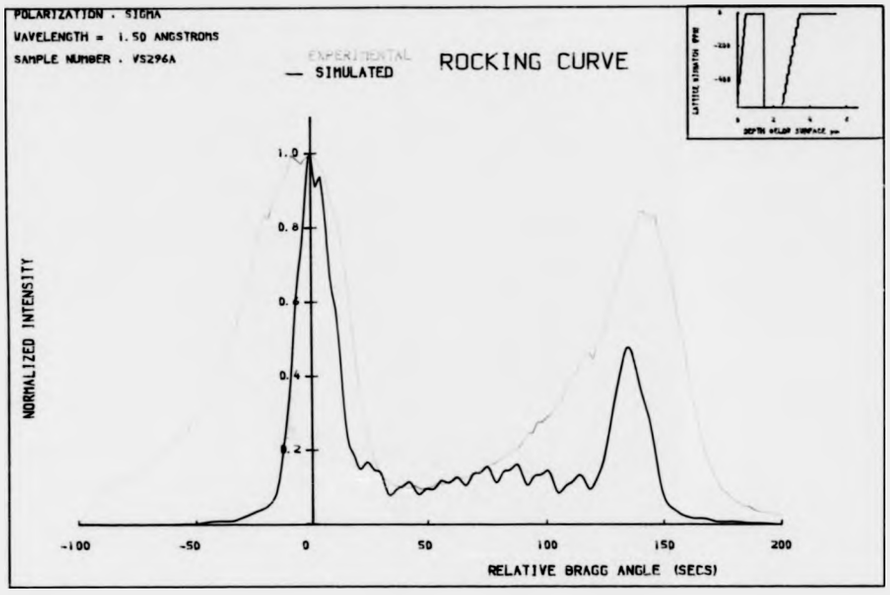

Figure 10.10e

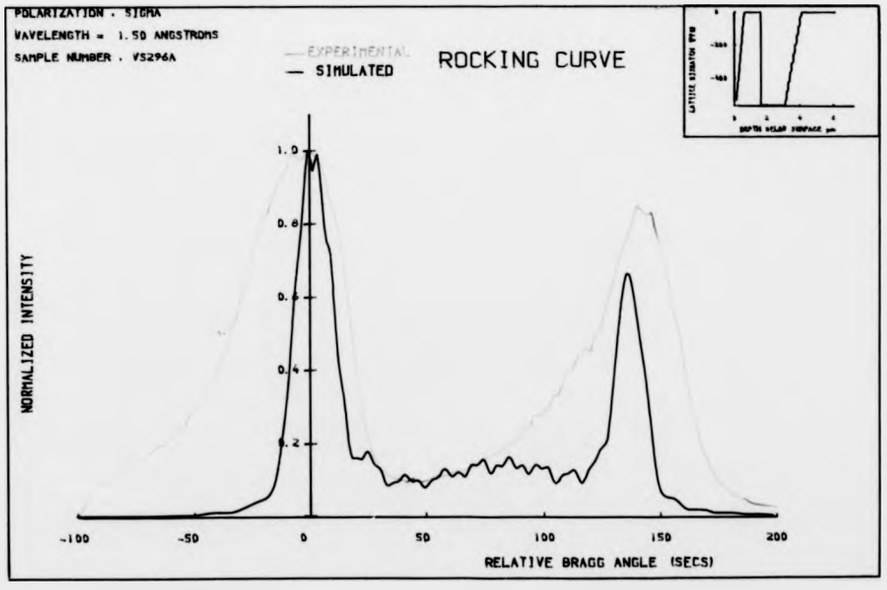

Figure 10.10f

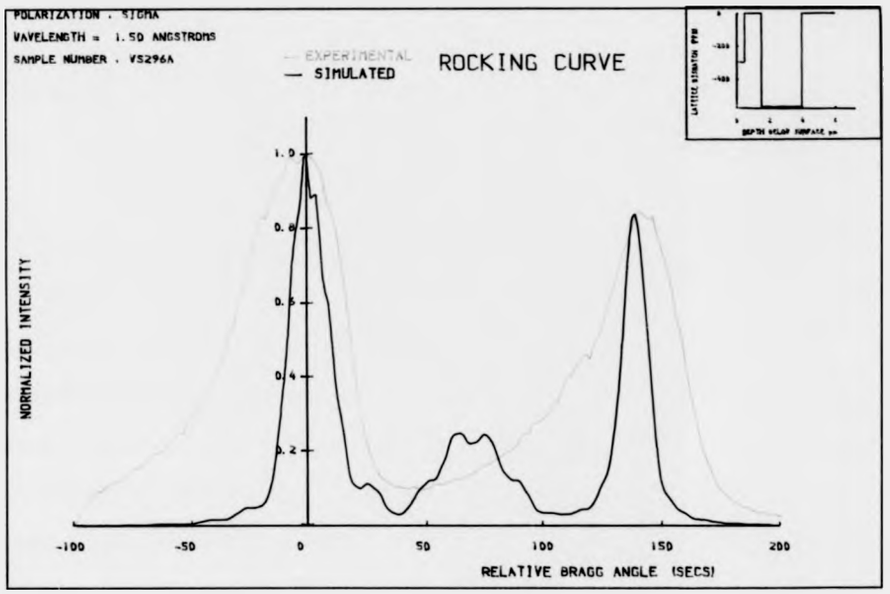

Figure 10.10g

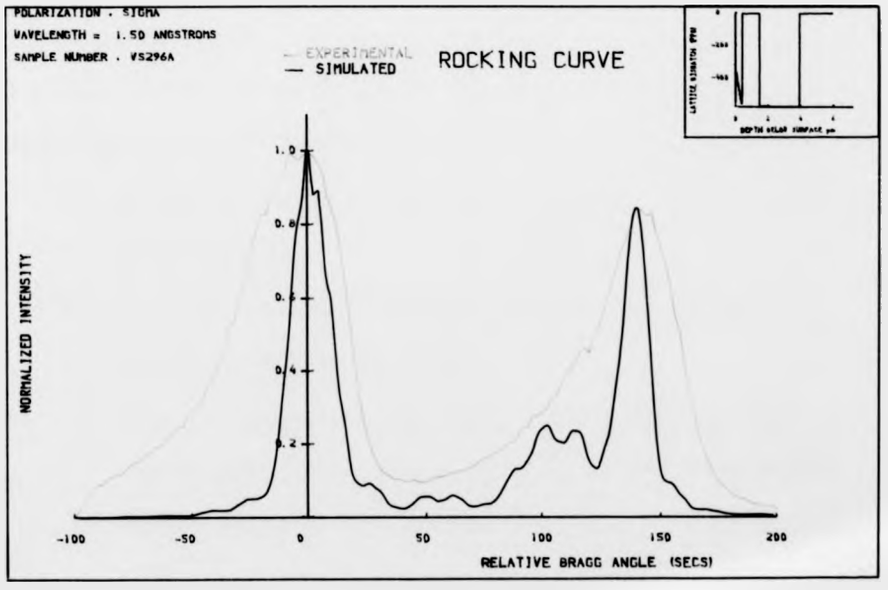

Figure 10.10h

attains a complicated shape from which it would normally be difficult to extract accurate information. Under such conditions, a preliminary experimental study of the heterostructure with one or more layers etched off would be extremely necessary so that a theoretical fit to the experimental curve could be made. Moreover, simulation studies on hypothetical multilayers have shown that unexpected peaks are observed in rocking curves. In view of this, great care is to be taken when a direct interpretation of experimental rocking curves from multilayers, is attempted. Simulation of rocking curves is extremely useful in predicting the characteristics of single layers or perfect epitaxial multilayers in which case a quick, non destructive and a detailed assessment of several of the layer parameters can be made. For inhomogeneous multilayers, interpretation of rocking curves can generally be done with the aid of some more experimental data characteristic of each layer in the multilayer structure. The supporting experimental data may involve one or more of the following

1) An SEM of a cleaved edge for a knowledge of the thickness of each layer.

2) Photo luminescence study for the band gap of the quaternary or ternary layer.

3) Electron microprobe analysis or SIMS study for the compositional variation across the layer. This method however destroys the specimen.

In short, the procedure for simulating an experimental rocking curve may be described as follows:

Essential Requirements:

i) What the substrate material is.

ii) How many epilayers are involved.

iii) What the layer materials are.

iv) An experimental rocking curve from the specimen, to compare with.

v) The hkl reflection and the wavelength for which rocking curve is obtained.

It is assumed that due precautions are taken to correct for specimen tilt and lattice plane misorientation while plotting experimental rocking curves. Once a precise experimental rocking curve is obtained, then the following procedures will have to be taken in order to simulate it:

1) Identification of Substrate reflection.

Substrates are required to be perfect crystals so that defects are not carried over to epilayers when they are grown over it. Near perfect InP crystals are also available. The reflection from such a substrate is therefore likely to be very sharp and symmetric with a rocking curve width close to the theoretically estimated value for the reflection and the X-ray wavelength, which is typically in the region of 10 arc secs. Experimental rocking curve widths are usually slightly greater than this value.

In order to identify such a peak in the experimental rocking curve it would be convenient to know the relative level of the substrate peak compared to this epilayer peak. For this, at least a rough idea of the thickness of the layers, may be required. Once it is decided as to what sort of a peak to look for and at what level, the position of the substrate reflection on the experimental rocking curve can be located. In the absence of any information about the layer thickness, the expected sharpness and symmetry of the substrate peak can itself be sufficient to identify its position. For highly perfect layers, one alternative is to etch a thin layer from a small area of the specimen and compare the rocking curves before and after etching.

2) Layer Characteristics and Simulation.

Having identified the substrate peak position, it is now necessary to have a rough idea of the mismatch characteristics of the layers. The approximate mismatch levels giving rise to one or more peaks for the layer are noted from the experimental rocking curve. Based on what the crystal grower had assumed as the growth pattern for the specimen, and on the information collected thus far, a rocking curve is computed for a particular set of thicknesses, mismatch levels and mismatch variations. A comparison with the experimental curve will indicate which of the parameters are to be varied and in what direction. The changes are made one at a time and a series of rocking curves are computed and compared with the experimental curve. A

systematic procedure is followed with a judicious choice of the relevant parameter changes in a manner outlined in previous sections, until a close fit with the experimental curve is obtained.

References

1. TAUPIN, D., Bull. Soc. Fr. Mineral Cristallogr., 87, 469 (1964).

2. TAKAGI, S., 'A dynamic theory of diffraction for a distorted crystal', J. Phys. Soc. Jpn., 26, 1239 (1969).

3. BURGEAT, J. and TAUPIN, D., Acta Cryst., A24, 99 (1968).

4. FUKUHARA, A. and TAKANO, Y., 'Determination of strain distributions from X-ray Bragg reflection by silicon single crystals', Acta Cryst., A33, 137 (1977).

5. LARSON, B.C. and BARHORST, J.F., 'X-ray Study of lattice strain in boron implanted laser annealed silicon', J. Appl. Phys., 51, 3181 (1980).

6. HALLIWELL, M.A.G., JULER, J. and NORMAN, A.G., 'Measurement of grading in heteroepitaxial layers', Microscopy of Semicond. Mater, Conf., Inst. Phys. Conf. Ser. No. 67, 365 (1983).

7. HALLIWELL, M.A.G., LYONS, M.H. and HILL, M.J., 'Interpretation of X-ray rocking curves from III-V semiconductor device structures', J. Cryst. Growth, 68, 523 (1984).

8. JAMES, R.W., 'The optical principles of Diffraction of X-rays', Bell, London (1965).

9. International Tables for X-ray Crystallography, Vol. 4., (Kynoch, Birmingham, 1974).

10. OLSEN, G.H., ZAMEROWSKI, T.Z., SMITH, R.T. and BERTIN, E.P. 'InGaAsP Quaternary alloys : Composition, refractive index and lattice mismatch', J. Elec. Mater., 9, 1977 (1980).

11. MOON, R.L., ANTYPAS, G.A. and JAMES, L.W., 'Bandgap and lattice constant of GaInAsP as a function of alloy composition', J. Elec. Mater., 3, 635 (1974).

12. NAHORY, R.E., POLLACK, M.A., JOHNSON, W.D. Jr., and BARNS, R.L., 'Bandgap versus composition and demonstration of Vegard's law for $In_{1-x}Ga_xAs_yP_{1-y}$ lattice matched to InP', Appl. Phys. Lett., 33, 659 (1978).

13. CROMER, D.T. and LIBERMANN, D., 'Relativistic calculation of anomalous scattering factor for X-rays', J. Chem. Phys., 53, 1891 (1970).

14. NYE, J.F., 'Physical Properties of Crystals', Oxford University Press, 143 (1960).

15. BRANTLEY, W.A., 'Calculated elastic constants for stress problems associated with semiconductor devices', J. Appl. Phys., 44, 534 (1973).

16. COLEMAN J.J., HOLONYAK, N.Jr., LUDOWISE, M.J. and WRIGHT, P.D. 'Yellow $In_{1-x}Ga_xP_{1-z}As_z$ double-heterojunction lasers', J. Appl. Phys., 47, 2015 (1976).

17. HILL, M.J., Physics Department, Durham University, (private communications).

18. SPERIOSU, V.S. and VREELAND, T. Jr., 'X-ray rocking curve analysis of superlattices', J. Appl. Phys., 56, 1591 (1984).

11

GENERAL DISCUSSIONS

AND

CONCLUSIONS

GENERAL DISCUSSIONS AND CONCLUSIONS

In the study of optoelectronic device materials, minute variations in the lattice parameter of different layers as each layer of the heteroepitaxial structure is grown cause lattice strain. Radiative recombination of injected minority carriers takes place in the active region of the device, hence it is extremely important that such a layer is free from lattice strain. The presence of large amounts of lattice strain promotes the growth of defects into network clusters which take the form of a cross hatch pattern of misfit dislocations at the interface. In this thesis, double crystal plane wave synchrotron radiation methods have been shown to be capable of accurately characterizing individual layers in a multilayer structure. This non destructive method can separate images of the ternary/quaternary layers from the substrate (InP), thereby identifying the location of any defects.

The advantages of a synchrotron radiation source, namely i) its ability to produce, at reasonable intensity, a low divergence beam of the order of a fraction of an arc second which acts very much like a plane wave, and ii) control of wavelength and polarization state, makes the synchrotron radiation double crystal camera a natural choice for multilayer material characterization. Separated images from the quaternary and InP layers, made possible by the double crystal method, have been shown for a light emitting diode (Figure 6.3 and Figure 6.4). Distinction between the active and the cap layers cannot however be made on the quaternary topograph

unless each layer has a different lattice mismatch. The topograph corresponding to the quaternary layers in Figures 6.3 and 6.4 shows a cross hatch network of misfit dislocations while the same is almost absent in the other topographs of Figures 6.3 and 6.4. A large quaternary mismatch, as observed from the rocking curve characteristics for the specimen, shown in Figure 6.6, is likely to result in misfit dislocation in the layer/substrate interface. The presence of these interfacial misfit dislocations can be strongly correlated to the degradation of the device as is evident from the analysis of a set of LEDs which had shown varying levels of degradation. The double crystal method is capable of accurately mapping lattice parameter changes of the order of 10^{-8}, though however, a lowest non-zero mismatch of the order of m = 220 ppm only has been detected from a routine analysis of a large number of experimental specimens. The theoretical limit of detection in the double crystal method corresponds to one single step on the fine axis motor carrying the experimental specimen, which is 0.2 arc secs. It appears that samples with lower lattice mismatch figures other than zero are probably not available.

The double crystal method also provides a fairly accurate assessment of the inhomogeneity and non-uniformity of quaternary multi-layers grown by liquid phase epitaxy. About 54% variations in the total quaternary layer thickness was observed for a double heterostructure laser by comparing a set of rocking curves at various points on the specimen. The layer composition however seemed to be almost uniform. The lattice mismatch m as measured

from the rocking curves includes the effect of tetragonal distortion. This has to be duly corrected in order to obtain the mismatch M corresponding to the relaxed layer parameter. In general $M \simeq m/2$ for coherent layers.

An accurate interpretation of layer characteristics has been made by a computer simulation of experimental rocking curves. These have been found to be extremely useful in providing a quick, non destructive and a detailed assessment of several of the layer parameters in a heteroepitaxial structure. The predicted layer thicknesses have even been found to match closely with the thicknesses measured by the Talysurf after selectively etching off a part of a layer. For multilayer structures showing complicated rocking curves, it has been demonstrated that a selective etching of the layers in sequence, helps to identify individual layer characteristics. From a theoretical calculation of rocking curves, the mismatch data for the layers obtained by selective etching has been effectively used as approximate initial values for a computer simulation of experimental rocking curves and thereby detailed characteristics of the layer were obtained.

Some of the experimental rocking curves have been obtained using a Silicon monochromator on the first axis of the double crystal camera. The calculated rocking curve in such cases would be a convolution of the reflectivity curve $R_2(\theta)$ for the specimen for a 400 reflection and the rocking curve for the monochromator for a 111 reflection at the required incident beam wavelength. A comparison of the experimental rocking curve for the same

specimen but with different reference crystals (InP or Si-monochromator) made in Figures 6.7 and 6.8, indicates that the quaternary layer and InP peakwidths for rocking curve with InP reference crystal are only slightly wider than the corresponding quantities for the rocking curve with a Si-monochromator by a factor of 1.05. This does not compare very well with the factor up to 1.32 estimated from plane wave rocking curve studies. The lack of agreement may probably be due to the positional changes in rocking curve shapes due to inhomogeneity and non uniformity of the specimen. Simulation studies made on a number of experimental rocking curves have shown a satisfactory fit. An exact fit was never achieved primarily because the rocking curve calculation assumed the layers and the substrates to be perfect. In actual practice dislocation-free InP substrates are not commercially available. The dislocation densities, though small, are sufficient to tilt the lattice planes even in a small area that is normally used in rocking curve measurements. The result is a broad rocking curve. In spite of this, the more-or-less satisfactory fit has been found to predict layer thicknesses that match closely with the thicknesses either reported by Plessey or measured separately using the Talysurf. As a course for future work, a much more generalized simulation study is needed that will take into account of the imperfections in the reference crystals as well as in the InP substrate of the specimen; a treatment that will distinguish between a silicon monochromator and the reference InP crystal. Once these changes are established, a closer fit of

the simulated curve with an experimental curve can be expected. The entire process of repeated comparison of the two curves followed by more changes in layer parameters until the simulated curve more-or-less fits the experimental curve can be left to the computer which will find out the standard deviation for the simulated plot by comparing with the standard experimental curve. By assigning a maximum deviation, a fairly accurate and fast simulation can be expected.

Since there are several layer parameters to vary in a multi-layer structure, it might appear that there are several simulations possible for a given experimental rocking curve. In the examples considered in Chapter 10, only one set of layer characteristics seemed to have a satisfactory fit with the experimental rocking curve. The question therefore arises whether a rocking curve from a multilayer structure has a unique characteristic. If that be so then a generalized computer simulation can be easily implemented to get an accurate and a non-destructive measurement of layer characteristics automatically.

In conclusion, the computer simulation of rocking curves from heteroepitaxial layers offers a powerful non-destructive method of characterization of multi-layer structures. The simulation studies have been found to offer a detailed interpretation of experimental rocking curves as regards the assessment of layer thicknesses and compositional variations. The thickness of layers predicted by simulation studies have been verified by other experimental methods in some cases. Double crystal synchrotron radiation methods on the

other hand, are capable of producing precision experimental rocking curve plots, with an angular accuracy of ± 0.1 arc sec and form an ideal experimental plot for comparison with the simulated rocking curves. The double crystal experimental technique in combination with the rocking curve simulation studies thus offer a powerful non-destructive method for optoelectronic device material characterization. In fact, active layer thicknesses of multilayer double heterostructures can be characterised to within 0.05μm from the simulation studies.

7